

**ENHANCING THE SURFACE FINISH OF SINGLE POINT DIAMOND
TURNING**

ENHANCING THE SURFACE FINISH OF SINGLE POINT DIAMOND TURNING

By

Mohammed Tauhiduzzaman

A Thesis

Submitted to the School of Graduate Studies

in Partial Fulfillment of the Requirements

for the Degree

Doctor of Philosophy

McMaster University

© Copyright by Mohammed Tauhiduzzaman, February 11, 2011

Doctor of Philosophy (2010), Mechanical Engineering

McMaster University Hamilton, Ontario

TITLE: Enhancing the surface finish of single point diamond turning

AUTHOR: Mohammed Tauhiduzzaman
B. Sc. In Mechanical Engineering (Bangladesh University of
Engineering and Technology, BUET)
M. Eng. (Research) in Mechanical Engineering (National
University of Singapore, NUS)

SUPERVISOR: Dr. Stephen C. Veldhuis

NUMBER OF PAGES: XIX, 205

ABSTRACT

Ultra precision single point diamond turning (SPDT) is a machining process used to produce optical grade surfaces in a wide range of materials. Aluminum is of primary interest as a workpiece material because it is easily diamond turnable, highly reflective and corrosion resistant. The cutting tool used is made from a single crystal diamond honed to a very sharp cutting edge. The machines used in this process are extremely precise and stiff. The nature of the cutting parameters used in SPDT changes the process physics substantially over conventional machining. The underlying reason relates to the relative size of the uncut chip thickness and the cutting edge radius of the tool in comparison to the grain size of the workpiece. When performing SPDT, there is a functional limit to the achievable surface finish. This is predominately due to material side flow and the opening up of material defects. Thus the machined surfaces have to undergo post processing operations like lapping or polishing, which increase cost and production time. Thus, the objective of this study was to improve the surface finish of the SPDT process to minimize the amount of post processing.

The approach involved addressing the ratio between the tool cutting edge radius and the microstructure. Realizing the limitations associated with sharpening a diamond tool further, efforts have been made to mechanically or thermo-mechanically induce dislocations into the workpiece to refine the microstructure and in so doing enhance

machinability. As dislocations act as a point of defect, it is observed that higher dislocation density offers less side flow and leads to better surface roughness.

A special tool with a flat secondary edge was then developed to address the remaining side flow issue for planar surfaces. The combination of thermo-mechanically produced ultra fine grained material with the special tool provided a substantial reduction in surface roughness from values typically reported at 3nm [Roblee, 2007] R_a to 0.75nm R_a . In addition to this the use of the custom designed tool can improve the productivity associated with machining a flat face by a factor of one hundred times by allowing the feed rate to be increased while still achieving the desired surface finish.

TO MY PARENTS

AND

MY WIFE

ACKNOWLEDGEMENTS

I would like to express my sincere appreciation to my supervisor Dr. Stephen C. Veldhuis for giving me the opportunity and providing me with guidance and support throughout my research. I would also like to express my sincere gratitude to my supervisory committee members, Dr. John Vlachopoulos and Dr. Ravi Selvaganapathy for their feedback and guidance.

Special thanks to Mr. Maneesh Khanna, Dr. German Fox-Rabinovich and Dr. Julia Dosboeva for their spontaneous support and feedback throughout the time. Special thanks also go to Dr. Mani Subramanian for his valuable feedback on the project. I am grateful to Mr. Andrew Biksa for proof reading my thesis and Mr. Jeremy Boyed for sharing his expertise in friction stir welding.

Special thanks to Dr. Paula Meyer, Ms. Zareena Gani, Mr. Matthias Mann, Ms. Holly Dzuba, Mr. Brian Perry, Mr. Terry Wagg, Ms. Janet Murphy and all my friends and colleagues at McMaster Manufacturing Research Institute. Special thanks to all the staff and colleagues at the Mechanical Engineering Department.

I would like to thank my wife and my in-law's for their inestimable support throughout this project. Also thanks to Dr. W. Khan and his family for their enormous support.

Finally, author would also like to thank the Natural Sciences and Engineering Research Council of Canada (NSERC) and B-Con Engineering for their financial support of this research.

TABLE OF CONTENTS

ABSTRACT.....IV

ACKNOWLEDGEMENTS VII

TABLE OF CONTENTS.....IX

LIST OF FIGURESXI

LIST OF TABLES XVII

CHAPTER 1: INTRODUCTION..... 1

CHAPTER 2: LITERATURE REVIEW 9

2.1. BACKGROUND OF PRECISION AND ULTRA PRECISION TECHNOLOGY .. 9

2.2. SINGLE POINT DIAMOND TURNING (SPDT) 12

 2.2.1. Applications15

2.3. PROCESS PHYSICS AND SIZE EFFECT IN SPDT 16

 2.3.1. Size effect and microstructure17

 2.3.2. Size effect and cutting edge radius25

2.4. SURFACE INTEGRITY IN SINGLE POINT DIAMOND TURNING..... 30

 2.4.1. Surface Roughness.....33

 2.4.1.1 The interpretation of precision machining limits and measurement sensitivities.....43

 2.4.2. Subsurface information43

2.5. DISLOCATION AND STRAIN HARDENING 46

 2.5.1. Strain Hardening49

 2.5.2. Grain boundary52

 2.5.3. Bulk Nanostructuring of metals54

 2.5.3.1 Subgrain formation58

 2.5.4. Atkin’s model and material separation criterion.....58

2.6. TOOL GEOMETRY 63

CHAPTER 3: GEOMETRICAL ANALYSIS OF SPDT 65

CHAPTER 4: EXPERIMENTAL..... 73

4.1. MACHINE TOOL..... 75

 4.1.1. Operating procedure.....78

4.2. WORKPIECE..... 81

 4.2.1. Metallography86

4.3. DIAMOND TOOL 87

4.3.1. Cutting edge radius	91
4.3.2. Flat end tool setup	92
4.4. DATA ACQUISITION SYSTEM	94
4.4.1. MiniDyn 3-Component Dynamometer: KISTLER Type 9256B1	94
4.4.2. Multi channel Charge amplifier	95
4.4.1. NI compactDAQ-9172 USB data acquisition system	96
4.5. CUTTING CONDITIONS	97
4.6. SURFACE ROUGHNESS MEASUREMENT	99
4.6.1. Roughness Parameters	101
4.6.2.1 Average roughness (R_a)	102
4.6.2.2 Root Mean Square (RMS) roughness (R_q)	102
4.6.2.3 Ten point height (R_z)	102
4.6.2.4 Peak to valley roughness (R_{th} or PV)	103
4.6.2. Filtering data	103
CHAPTER 5: RESULTS AND DISCUSSION	106
5.1. WORKPIECE MATERIAL SELECTION	107
5.1.1. Plastic side flow induced roughness	111
5.1.2. Secondary particles induced roughness	115
5.1.2.1 Brittle fracture	115
5.1.2.2 Smearing and dimple formation from secondary hard particles	117
5.2. FURTHER ENGINEERING OF FURNACE COOLED 99.87% ALUMINUM	121
5.2.1. Friction stir process (FSP)	125
5.3. TOOL GEOMETRY SELECTION	129
5.4. SURFACE ROUGHNESS	137
5.4.1. Optimum cutting parameters based on roughness	137
5.4.2. Effect of material property	141
5.4.3. Effect of tool geometry on surface roughness	166
CHAPTER 6: CONCLUSIONS AND RECOMMENDATIONS	174
6.1. CONCLUSIONS	176
6.2. SUMMARY	179
6.3. RECOMMENDATIONS	182
REFERENCE	184
APPENDIX A: PRECITECH 700G MOTIONS	192
APPENDIX B: PGM AND LABVIEW CODE	193
APPENDIX C: OBLIQUE PLOTS OF MACHINED SURFACES	195
APPENDIX D: WAVINESS AND FORCE DATA IN THE CUTTING DIRECTION	204

LIST OF FIGURES

Figure 2-1: Taniguchi Curve showing the development of ultra precision diamond turning machine positioning accuracy since yr. 1940 to yr. 2010 [After Corbett et al., 2000] 10

Figure 2-2: Application market of microproducts [After Luo et al., 2005]..... 11

Figure 2-3: Micromachining relative to other machining Processes [After Byrne et al., 2003] 13

Figure 2-4: Material Behavior as machining size reduces. (a) Continuous material. (b) Effects of grain boundary. (c) Effects of dislocation and (d) Ideal material. 18

Figure 2-5: Change in shear plane area with shear angle (a) Smaller shear angle and (b) larger shear angle 21

Figure 2-6: Minimum scale lengths of plasticity [After McDowell, 2000]..... 24

Figure 2-7: Shows a typical metal cutting zone and identifies the primary and secondary shear zones, the angles involved where ϕ : shear angle, α : rake angle and β : friction angle, t : uncut chip thickness, t_c : chip thickness, F_s , F_p and F_c are shear, cutting and frictional forces and F_q , N_s and N_c are their normal component respectively [After Shaw, 2005] 26

Figure 2-8: Change in effective negative rake angle with uncut chip thickness [Ng et al., 2006] 27

Figure 2-9: Behavior of cutting edge as the cutting dimension reduces [Moriwaki, 1989] Schematic and Merchant’s circle diagram for (a) Large uncut chip thickness and (b) Small uncut chip thickness showing an effective negative rake angle. 29

Figure 2-10: Surface topography [After Liu and Melkote, 2006] 31

Figure 2-11: True cutting geometry for diamond turning with a roundnose tool. The chip moving up the tool rake face is not shown 31

Figure 2-12: Schematic of change in cutting behavior along cutting edge..... 32

Figure 2-13: Turning operation and surface roughness 33

Figure 2-14: Roughness data on turning and facing from [After Childs et al., 2008a; 2008b] 34

Figure 2-15: Illustration of plastic side flow and plastic side flow induced roughness [After Liu and Melkote, 2006]..... 35

Figure 2-16: Size effect in cutting force and specific cutting energy for diamond turning of 7075 aluminum alloy [After Ng et al., 2006] 39

Figure 2-17: Effect of nose radius on chip thinning [After Kishawy and Elbestawi, 1999] 41

Figure 2-18: Material anisotropy and recovery [After Cheung and Lee, 2000]	42
Figure 2-19: Range of measured depth of plastically deformed layer (δ) versus uncut chip thickness (h) after machining a Te/Cu alloy with a sharp and a worn diamond tool [After Lucca et al., 1994]	45
Figure 2-20: Atomic arrangements that accompany the motion of an edge dislocation as it moves in response to an applied shear stress. (a) The extra half plane of atom is labeled A. (b) The dislocation moves one atomic distance to the right as A links up to the lower portion of plane B; in the process, the upper portion of B becomes the extra half-plane. (c) A step forms on the surface of the crystal as the extra half plane exists [After Callister, 1997]	46
Figure 2-21: Regions of compression (top) and tension (below) located around an edge dislocation [Callister, 1997]	48
Figure 2-22: Dislocation-dislocation interaction. (a) two edge dislocations of same sign lying on the same plane exert a repulsive force. (b) edge dislocations of opposite sign lying on the same plane exerts and attractive force on each other and annihilate each other and leave a region of perfect crystal [Callister, 1997]	49
Figure 2-23: Effect of strain hardening on mechanical properties showing an influence of cold work on stress-strain behavior and schematic representation of the influence of cold working on the tensile strength and ductility an alloy. [After Callister, 1997]	50
Figure 2-24: Effect of grain boundary: The motion of a dislocation as it encounters a barrier at grain boundary resulting in a discontinuous slip plane [After Callister, 1997]	52
Figure 2-25: Principles of severe plastic deformation (SPD) techniques. (a) High-pressure torsion (HPT). (b) Equal channel angular (ECA) pressing [Valiev, 2004]	55
Figure 2-26: Strength and ductility of the nanostructured metals compared with coarse grained cold rolled metals (% indicate amount of rolling) [After Valiev, 2004] .	56
Figure 2-27: Schematic illustration of friction stir processing (FSP) [After Su et al., 2006]	57
Figure 2-28: Experimental data of primary shear angle for cutting various metals [After Atkins, 2005]	59
Figure 2-29: Material separation during cutting: Piispanen’s stacked card analogy highlighting possible gap formation in the region of AB [After Atkins, 2003] ..	60
Figure 2-30: Distribution of energy during cutting [After Subbiah and Melkote, 2007] .	61
Figure 2-31: Diamond turning of Al-Mg alloy with flat end tool. (a) Tool geometry. (b) Surface roughness [After Nishiguchi et al., 1988 and Masuda et al., 1989]	64
Figure 3-1: SPDT analysis	67

Figure 3-2: Limiting feed rate.....	68
Figure 3-3: Simplified chip cross-section	69
Figure 3-4: Effective depth of cut as a function of tool nose radius and feed rate.	70
Figure 4-1: Diamond turning operation. (a) Schematic of the cutting process and force direction. (b) Schematic of the data acquisition process.....	75
Figure 4-2: Precitech freeform 700G ultra precision machining center	76
Figure 4-3: Mechanical and thermo-mechanical processes. (a) FC 99.87% aluminum. (b) 54% cold rolled 99.87% aluminum. (c) and (d) FC 99.87% aluminum after 2 passes and 15 pass of FSP with travel length of 60mm. (d) FSP at 400RPM, 68mm/min and 3.05mm depth with chilled air.....	85
Figure 4-4: Optical images of FC 99.87% aluminum after grinding and polishing. (a) Without steps 3a and 4a of Table 4.6 (b) With steps 3a and 4a of Table 4.6	86
Figure 4-5: Schematic of the cutting tools. (a) 1.5mm nose radius. (b) 0.5mm nose radius and (c) 0.5mm nose radius and flat [K & Y diamond]	90
Figure 4-6: Measurement of cutting edge radius on Zygo at camera resolution of 112nm	92
Figure 4-7: Flat end tool setup procedure	93
Figure 4-8: Kistler type 5010 dual mode charge amplifier.....	96
Figure 4-9: NI cDAQ system. (a) NI cDAQ-9172 chassis. (b) NI 9215 general purpose module and (c) cDAQ system in operation.....	97
Figure 4-10: Roughness parameters. (a) Average roughness (R_a). (b) Ten point average roughness (R_z). (c) Peak to valley roughness (R_{th} or PV). [ZYGO manual]	103
Figure 4-11: Alteration of test results by filtering from original (filter off) data [ZYGO manual]	104
Figure 5-1: Microstructure of aluminum alloys at different magnification. (a) and (b): Furnace cooled (FC) 99.87% aluminum alloy. (c) and (d): 54% cold rolled (54CR) 99.87% aluminum alloy. (e) Annealed 6061 aluminum alloy. (f) 32% cold rolled 6061 aluminum alloy	108
Figure 5-2: Variation in surface roughness (R_a , R_z and PV) for different aluminum alloys at 1000RPM, 5 μ m Depth of cut and 5 μ m/rev.	109
Figure 5-3: Oblique plot of surface roughness for different alloys at 1000RPM, 5 μ m Depth of cut and 5 μ m/rev. PV _{min} values are a. 65.05nm, b. 29.28nm, c. 62.62nm and d. 27.08nm.....	110
Figure 5-4: Side flow	111

Figure 5-5: SEM photograph of chips produced from: (a, b and c) Furnace cooled 99.87% Al, (d, e and f) Strain Hardened 99.87% Al at 1000RPM, 5 μm Depth of cut at 5 $\mu\text{m}/\text{rev}$ 112

Figure 5-6: Comparison of side flow and swelling effect on Furnace cooled and 54% cold rolled aluminum alloy at 20 $\mu\text{m}/\text{rev}$ feed rate, 1000RPM and 2 μm depth of cut 114

Figure 5-7: Brittle type of failure in 6061 Aluminum [Figure (b) from Shaw, 1995].... 116

Figure 5-8: EDS analysis of brittle type of fracture on 6061 aluminum 117

Figure 5-9: Back-Scattered Electron (BSE) image of 6061 aluminum showing brittle fracture, smearing of hard particles and dimple formation..... 118

Figure 5-10: Sign of missing particles on chips on a. Annealed 6061 Aluminum and b. Strain Hardened 6061 Aluminum. 119

Figure 5-11: Dimple induced roughness along feed (1-1') and cutting (2-2', 3-3' and 4-4') in 99.87% aluminum alloy 120

Figure 5-12 Micro hardness tests performed on a machined surface and along the cross section of a 6061 aluminum 122

Figure 5-13: Machined surface of 54% cold rolled 99.87% aluminum. (a) 1.5mm nose radius tool. (b) 0.5mm nose radius tool. (c) Tool with flat secondary edge generated at 1000rpm, 2 μm depth of cut and 1 $\mu\text{m}/\text{rev}$ feed rate. 123

Figure 5-14: 82% cold rolled (82CR) 99.87% aluminum alloy. (7500X) 125

Figure 5-15: Micro hardness values for FSP samples [Parameters in Table 4.5] 127

Figure 5-16 a1-b3: Microstructure of FSP samples at different depths (at 7500X) 127

Figure 5-16 c1-f3: Microstructure of FSP samples at different depths (at 7500X) 128

Figure 5-17 g1-i3: Microstructure of FSP samples at different depths (at 7500X) 129

Figure 5-19: Effect of nose radius on peak to valley (PV) surface roughness. 130

Figure 5-20: Chip thinning is more in larger nose radius tool..... 131

Figure 5-21: Ratio of thrust force and cutting force on FC and 54% CR 99.87% aluminum alloy for different tools 132

Figure 5-22: Chip edge serration is higher with larger edge radius tool (54%CR material) 135

Figure 5-23: Optical images of three different tools. (a) 1.5mm nose radius. (b) 0.5mm nose radius and (c) 0.5mm nose radius with 0.5mm flat secondary edge. (no scale) 136

Figure 5-24: Chips produced by 0.5mm Rn and 0.5mm flat end, 1 $\mu\text{m}/\text{rev}$ (54%CR material) 137

Figure 5-25: Effect of nominal depth of cut (DOC) on SPDT 138

Figure 5-26: Effect of RPM on SPDT	139
Figure 5-27: 3D plot for optimum RPM in SPDT. (a) for 1.5mm nose radius tool and (b) for 0.5mm nose radius tool	140
Figure 5-28: Feed rate vs roughness curve for 1.5mm nose radius tool for FC: Furnace Cooled, 54%CR: 54% Cold rolled, FSP: Friction stir processed and 82%CR: 82% cold rolled aluminum.	142
Figure 5-29: Effect of material microstructure in surface roughness	143
Figure 5-30: Oblique plot of surface profile at 1000RPM, 2 μ m depth of cut and 1 μ m/rev feed rate with 1.5mm nose radius tool for (a) FC aluminum, (b) 54%CR aluminum, (c) 82%CR aluminum and (d) FSP aluminium.....	144
Figure 5-31: Chip produced at 1000RPM, 2 μ m depth of cut and 1 μ m/rev feed rate with 1.5mm nose radius tool for (a) FC aluminum, (b) 54%CR aluminum, (c) 82%CR aluminum and (d) FSP aluminium (1000X).	145
Figure 5-32: Observations on machined 82% cold rolled and FSP 99.87% aluminum .	147
Figure 5-33: Machining of ultra-fine grained material	150
Figure 5-34: Rainbow pattern observed in FSP alloy at 5 μ m/rev	152
Figure 5-35 Feed rate vs force curves for 1.5mm nose radius tool for FC: Furnace Cooled, 54%CR: 54% Cold rolled, FSP: Friction stir processed and 82%CR: 82% cold rolled aluminum.	154
Figure 5-36: Atkins' model verification	155
Figure 5-37: Feed rate vs roughness curve for 0.5mm nose radius tool for FC: Furnace Cooled, 54%CR: 54% Cold rolled, FSP: Friction stir processed 99.87% aluminum.	157
Figure 5-38: Feed rate vs roughness curve for Flat end tool for FC: Furnace Cooled, 54%CR: 54% Cold rolled, FSP: Friction stir processed.	158
Figure 5-39: Arrest of plastic deformation resulting from micro-indentation on furnace cooled 99.87% Aluminum at grain boundaries.....	160
Figure 5-40: Grain boundary induced surface roughness in (a) and (b) on Furnace cooled 99.97% Aluminum; 1. Feed direction, 2. Cutting direction.....	161
Figure 5-41: Grain boundary induced roughness minimized in (a) 54% cold rolled alloy and eliminated in (b) Friction stir alloy	162
Figure 5-42: Micro indentation on FSP alloy	163
Figure 5-43: Machined surfaces with flat end tool. (a-c) Furnace cooled alloy. (d-f) 54% cold rolled alloy. (g) Frictions stirred alloy. (h) SEM image of a machined friction stirred alloy	166

Figure 5-44: Effect of tool geometry on furnace cooled 99.87% aluminum alloy at 1000RPM, 2 μ m depth of cut.....	167
Figure 5-45: Effect of tool geometry on 54% cold rolled 99.87% aluminum alloy at 1000RPM, 2 μ m depth of cut.....	168
Figure 5-46: Effect of tool geometry on friction stir processed 99.87% aluminum alloy at 1000RPM, 2 μ m depth of cut.....	169
Figure 5-47: Best surface achieved with FSP aluminum alloy and flat end tool at 1000RPM, 2 μ m depth of cut and 0.4 μ m/rev feed rate.....	172
Figure 5-48: New and worn tool.....	173
Figure 5-49: Effect of tool wear on surface roughness.....	173
Figure 6-1: A sample produced on 54% cold rolled alloy with flat end tool.....	180
Figure A-1: Machine tool coordinate limits and relative cutting force directions.....	192
B-1: *.PGM code	193
Figure B-2: Graphical representation of LabVIEW data acquisition program.....	194
Figure C-1: Furnace cooled 99.87% aluminum (1000RPM, 2 μ m depth, 1.5mm nose radius)	195
Figure C-2: 54% cold rolled 99.87% aluminum (1000RPM, 2 μ m depth, 1.5mm nose radius)	196
Figure C-3: FSP 99.87% aluminum (1000RPM, 2 μ m depth, 1.5mm nose radius)	197
Figure C-4: Furnace cooled 99.87% aluminum (1000RPM, 2 μ m depth, 0.5mm nose radius)	198
Figure C-5: 54% cold rolled 99.87% aluminum (1000RPM, 2 μ m depth, 0.5mm nose radius)	199
Figure C-6: FSP 99.87% aluminum (1000RPM, 2 μ m depth, 0.5mm nose radius)	200
Figure C-7: Furnace cooled 99.87% aluminum (1000RPM, 2 μ m depth, 0.5mm flat end)	201
Figure C-8: 54% Cold rolled 99.87% aluminum (1000RPM, 2 μ m depth, 0.5mm flat end)	202
Figure C-9: FSP 99.87% aluminum (1000RPM, 2 μ m depth, 0.5mm flat end)	203
Figure D-1: Zygo images of machined furnace cooled 99.87% pure aluminum alloy at 1000 RPM, 2 μ m depth of cut and 20 μ m/rev.....	205
Figure D-2: Thrust force data and frequency analysis of FC 99.87% pure aluminum at 1000RPM, 2 μ m depth of cut and 10 μ m/rev feed rate with flat end tool.....	205

LIST OF TABLES

Table 2.1: Cutting scale and uncut chip thickness [After Simoneau et al., 2006a]	14
Table 2.2: A listing of the expected electronic configurations [Callister, 1997]	15
Table 3.1: Geometric quantitative values for oblique cutting: 1.5mm nose radius tool ...	70
Table 3.2: Geometric quantitative values for oblique cutting: 0.5mm nose radius tool ...	71
Table 4.1: Stiffness of axes [Precitech Manual]	78
Table 4.2: Chemical composition of aluminum alloys	82
Table 4.3: Properties of aluminum [Callister, 1997]	82
Table 4.4: List of workpieces.....	83
Table 4.5: Friction stir process (FSP) parameters.....	84
Table 4.6: Grinding and polishing steps to reveal microstructure	87
Table 4.7: Properties of Diamond (Carbon) [Callister, 1997]	88
Table 4.8: MiniDyn 3-Component Force Dynamometer Type 9256B1	95
Table 4.9: Design of experiments	98
Table 4.10: Cutting parameters.....	99
Table 4.11: Field of view and spatial resolution at different magnification [ZYGO manual]	101
Table 4.12: Recommended cut-off ISO 4288 [Whitehouse, 2002]	104
Table 5.1: Micro hardness of aluminum workpieces.....	124
Table 6.1: Summary of results	181

NOMANCLATURE

α	Rake angle, radian
α_e	Effective rake angle, radian
β	Frictional angle, radian
φ	Shear angle, radian
μ	Friction coefficient
τ_y	Shear yield strength, Pa
D	Nominal depth of cut, μm
D_e	Effective depth of cut, μm
f	Feed rate, $\mu\text{m}/\text{rev}$ [$\mu\text{m}\cdot\text{min}^{-1}/\text{rev}\cdot\text{min}^{-1}$]; allowable step size
F_c	Frictional force, N
F_p	Cutting force, N
F_s	Shear force, N
F_q	Thrust force, N
L_{SPDC}	Tool-workpiece contact length, μm
N_c	Normal direction of frictional force, N
N_s	Normal direction of shear force, N
R	Specific work for surface formation, J/m^2
R_a	Average roughness, nm
R_e	Edge radius of tool, nm
R_n	Nose radius of tool, mm
R_{rms}	Root mean square roughness, nm
R_{th}	Peak to valley (PV) roughness, nm
R_{th}'	Corrected Peak to valley roughness, nm
R_z	Ten point average roughness, nm
t	Uncut chip thickness, μm
t_c	Chip thickness, μm
t_m	Minimum chip thickness, μm
V	Cutting speed, m/sec

w Width of cut, μm

CHAPTER 1 INTRODUCTION

Ultra precision single point diamond turning (SPDT) is a cutting tool based manufacturing technology for producing optical grade surfaces. Initial applications were in manufacturing of computer memory disks, photocopiers, printer components, infra-red optics, mass production of precision molds for compact disk lenses and LCD panels. Recent applications have been in high energy lasers and x-rays. Aluminum is of primary interest for these applications as it is easily diamond turnable, highly reflective and corrosion resistant.

Like conventional machining, diamond cutting also removes material through the relative motion between a tool and a workpiece; however, the cutting tool is a single crystal diamond honed to an extremely sharp edge. Such cutting tools have high hardness, stiffness, thermal conductivity and are able to retain a sharp edge. The average cutting edge radius of a diamond tool is approximately 100nm. The cutting edge radius of a conventional TiN coated tungsten carbide cutting tool varies from 8000~10000 nm. Moreover, a conventional precision computer numerical control (CNC) machine tool generally has a positional accuracy of ± 1000 nm whereas an ultra precision machine tool generally operates with an accuracy of $\pm 1\sim 5$ nm. Therefore due to the sharpness of the tool as well as the positional accuracy and rigidity of the machines used in SPDT, very smooth mirror like surfaces can be produced by mechanical machining.

Ultra precision machining produces a low surface roughness and is capable of removing material while moving with a very small feed rate. It has been observed that with the reduction in feed rate, the surface roughness becomes independent of the feed rate of the process and deviates from theoretically expected values based on successive passes of the tool geometry. This implies surface roughness may become near constant or possibly increase with a decrease in feed rate. It is well known in industry that an average roughness (R_a) value of less than 3nm is very difficult to achieve with aluminum alloys [Roblee, 2007]. Thus for products such as mirror surfaces, the machined surface may have to undergo post processing operations such as lapping or polishing to achieve an average surface roughness requirement as low as 0.2nm. Lapping and polishing are both time consuming operations and increase the overall capital and labor cost of the process.

One explanation for this deviation of theoretical and experimental surface roughness is based on the relative sizes of the workpiece microstructure and the cutting edge of the tool. This is often referred to as the size effect [Shaw, 2005]. With the reduction in feed rate, the workpiece material and the cutting edge radius are of the same magnitude. For example, a standard cutting parameter for a SPDT operation is 2 μ m depth of cut and 5 μ m/rev feed rate. In an ultra precision face turning operation with a typical round nosed tool, the uncut chip thickness or effective depth of cut will vary from its maximum of 250nm for 1.5mm nose radius tool and 423nm for 0.5mm nose radius tool at

the leading edge to near zero in the region where the final surface is being generated.

Thus a number of issues need to be considered:

1. Nanometric scale cutting is taking place.
2. Cutting dimensions are of the same magnitude of a single workpiece grain size.
3. The probability that the region in front of the tool will have a shear initiating defect at this scale is low in comparison to traditional cutting processes.
4. At that relative small scale, a new diamond tool cannot be assumed to be sharp, rather the rounding of cutting edge radius must be taken into account as it is of the same order of magnitude as the thin region of the chip and of the microstructural features.

Thus, a reduction in the effective depth of cut along the tool edge not only makes the tool behave as a rounded edge but also the material properties change from isotropic to anisotropic. The rounded edge exerts a hydrostatic pressure on the workpiece that causes micro extrusion of the material and promotes ploughing action during cutting. For plastic deformation to occur in SPDT there has to be defects in the form of voids, dislocations or inclusions in the cutting zone. Thus for a very small effective depth of cut, the material removal has to take place at the atomistic and/or discrete dislocation level. To form a chip the material has to undergo a high amount of plastic deformation followed by fracture, otherwise the deformed material will remain on the surface and will result in

a higher value of surface roughness. This plastic deformation is not desired; rather fracture followed by chip formation is preferable.

Thus the objective of this study is to address and understand the cutting mechanisms of SPDT of an aluminum workpiece and apply this knowledge to improve achievable levels of surface finish. The focus will be on the micro structural influence and mechanical properties of the workpiece material as it applies to SPDT. The research will incorporate changes to the microstructure of aluminum alloys with the intent of lowering the cutting forces and improving surface finish. Overall the work will focus on aiding the fracture of the aluminum and promoting a more favorable chip flow and breakage mechanism. Research to date suggests that both fracture and plastic deformation take place simultaneously in the chip formation process in SPDT. If plastic deformation can be reduced and fracture increased, this may improve the surface roughness by producing less side flow. In addition to surface finish subsurface damage also must be minimized for this application. This research will then be coupled with tool geometry optimization to produce the best possible surface quality that ideally will require no post processing such as lapping or polishing.

In this study the workpiece was strain hardened to increase the dislocation density. This made the material more prone to fracture rather than plastic deformation, which is favorable for chip formation. Defects in the form of dislocations were introduced to 99.87% pure aluminum and 6061 aluminum alloy by strain hardening using cold rolling

and grain refinement in 99.87% aluminum alloy to produce ultra-fine grained material by severe plastic deformation using a friction stir welding process. After strain hardening the mechanical properties were measured by micro hardness testing. On a microscopic scale, plastic deformation of crystalline materials corresponds to the motion of dislocations by a slip process. The ability of a metal to plastically deform depends on the ability of dislocations to move. With an increase in dislocation density, the resistance to dislocation motion increases. This is because dislocation to dislocation strain interactions are repulsive. The net result is that the motion of a dislocation is arrested by the presence of other dislocations. This mechanism results in an increase in the hardness of the material. As the material loses its ductility, it will reduce the ability of the material to plastically deform. Initial results suggest that strain hardening improves the surface roughness performance of SPDT with the 99.87% aluminum alloy performing better than the 6061 aluminum. The poorer performance of the aluminum 6061 is attributed to the increased level of impurities in the material. Four different pre-treated 99.87% aluminum samples were studied: 1. Soft, furnace cooled aluminum, 2. 54% cold rolled aluminum, 3. 82% cold rolled aluminum and 4. Friction stirred ultra fine grained aluminum. Three different diamond tools were used for the experiments: 1. 1.5mm nose radius, 2. 0.5mm nose radius, and 3. 0.5mm nose radius and 0.5mm flat secondary edge. The flat secondary edge tool was designed in the MMRI and manufactured by K&Y Diamond, Canada. All the tool-workpiece combinations were tested on a Precitech 700G ultra precision machine and surface roughness was measured using a Zygo NewView 5000 white light interferometer.

A significant improvement in surface roughness value has been achieved with the flat end tool and friction stirred sample. A R_a value as low as 0.75nm (R_z : 3.08nm; R_{th} : 4.0nm) has been achieved when measured under a lateral resolution of 0.56 μ m. The best result for all materials was achieved with the flat secondary edge tool. Another important feature of the flat end tool is an improvement in productivity compared to the round nose tools typically used for producing similar surface roughness. However issues associated with tool setup still need to be improved.

In general, the 54% cold rolled 99.87% aluminum alloy gave the best surface roughness for all the tools, while the furnace cooled 99.87% aluminum alloy gave the worst surface roughness of the samples tested. This result supports the postulated hypothesis that the microstructure can be optimized for ultra precision machining. The hypothesis is further supported by a metal cutting model developed by Atkins that allows the user to test the effects of material properties [Atkins, 2003]. The model accurately predicts the experimental observations in this case. The hypothesis is that surface finish improves with an increase in yield strength and a decrease in specific work for surface generation. This change in material properties is achieved through a strain hardening operation where a large number of dislocations are produced and as a result more slip planes are made available, which serve to enhance machinability.

The following chapters will discuss the various aspects of this study in further detail. Chapter 2 will provide a comprehensive literature review that will discuss the background material and forge the hypothesis of this work. This chapter consists of a brief introduction to the ultra precision machining process and precision technology in general. This will be followed by details on the SPDT process and its application to the production of optical grade surfaces. Process physics and details on the size effect relating the material microstructure and the cutting tool geometry will also be discussed. This is then followed by a discussion on surface quality including roughness, surface and subsurface damage. Finally a brief introduction to the importance of dislocations, strain hardening processes, bulk ultra-fine structuring of metals and material separation components in machining will be highlighted and discussed.

Chapter 3 discusses the geometrical aspects of a single point diamond turning tool. This chapter describes the coordinate geometrical equations to approximate and quantify the relative scale between the cutting tool and the workpiece material. This analysis allows one to estimate the tool-workpiece contact length, effective depth of cut or uncut chip thickness and the uncut chip area.

Chapter 4 describes the experimental procedure. This chapter includes properties of the materials, specifications and limitations of the measuring instruments as well as the machining parameters used from initial testing through to final validation.

Chapter 5 focuses on the results and discussion from the current study with focus placed on the surface roughness. A set of cutting force data is shown to verify Atkins' model [Atkins, 2003]. Further data from repeated tests are presented in the appendix.

Chapter 6 presents the conclusions and summary from this study and provides direction for future work.

CHAPTER 2 LITERATURE REVIEW

2.1. BACKGROUND OF PRECISION AND ULTRA PRECISION TECHNOLOGY

Ultra precision machining has developed significantly since the early 1980's [Franks, 1987] as the demands for miniaturization and high surface finish quality have increased. The concept of ultra precision manufacturing technology for miniaturization was first introduced in 1959 by a Noble Laureate Dr. Richard Feynman in his lecture at the California Institute of Technology entitled "There's a plenty of room at the bottom" [Feynman, 1993]. Dr. Feynman realized the huge potential of miniaturization in the early 1950's and tried to encourage researchers to concentrate on ultra precision technology. He realized for example, if one can write and read information in a small scale, this will enable the storage of large amounts of information in a small place and at the same time increase the speed of data transfer and ultimately cost. Today, precision on a similar scale is available for ultra precision machining technology. Researchers have made several attempts to define the relative scales of machining as seen in Figure 2-1 which is commonly referred to as the "Taniguchi Curve" [modified after Corbett et al., 2000]. The definitions of these scales are approximations. To add perspective to Figure 2-1, [Corbett et al., 2000] shows a size scale of various objects found in nature.

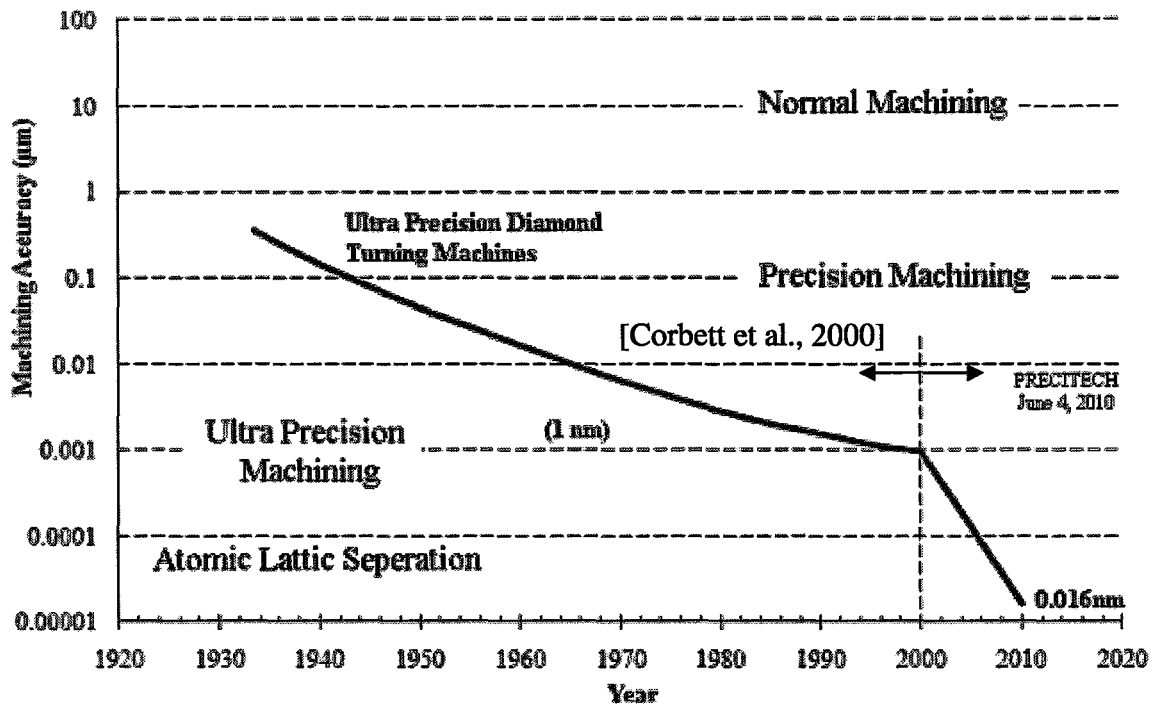


Figure 2-1: Taniguchi Curve showing the development of ultra precision diamond turning machine positioning accuracy since yr. 1940 to yr. 2010 [After Corbett et al., 2000]

According to McKeown [1996], micro machining is a branch of machining where the tolerances and dimensions of the features remain in the micro scale (in the order of 1 µm). Alting et al., [2003] states that, “micro engineering deals with the development and manufacture of products, whose functional features in at least one dimension are on the order of µm. The products are usually characterized by a high degree of integration of functionalities and components”. Recently Simoneau et al., [2006a, 2006b and 2006c] defined micro scale cutting as “the point at which the uncut chip thickness was smaller than the average size of the smallest grain size in the material micro-structure”. At present, MEMS (Micro Electro-Mechanical Systems) is the prime driving force for micro manufacturing. However, several other sectors are also using micro technology to

enhance functionality and quality. Figure 2-2 shows the market potential of different microproducts [Luo et al., 2005; Corbett et al., 2000].

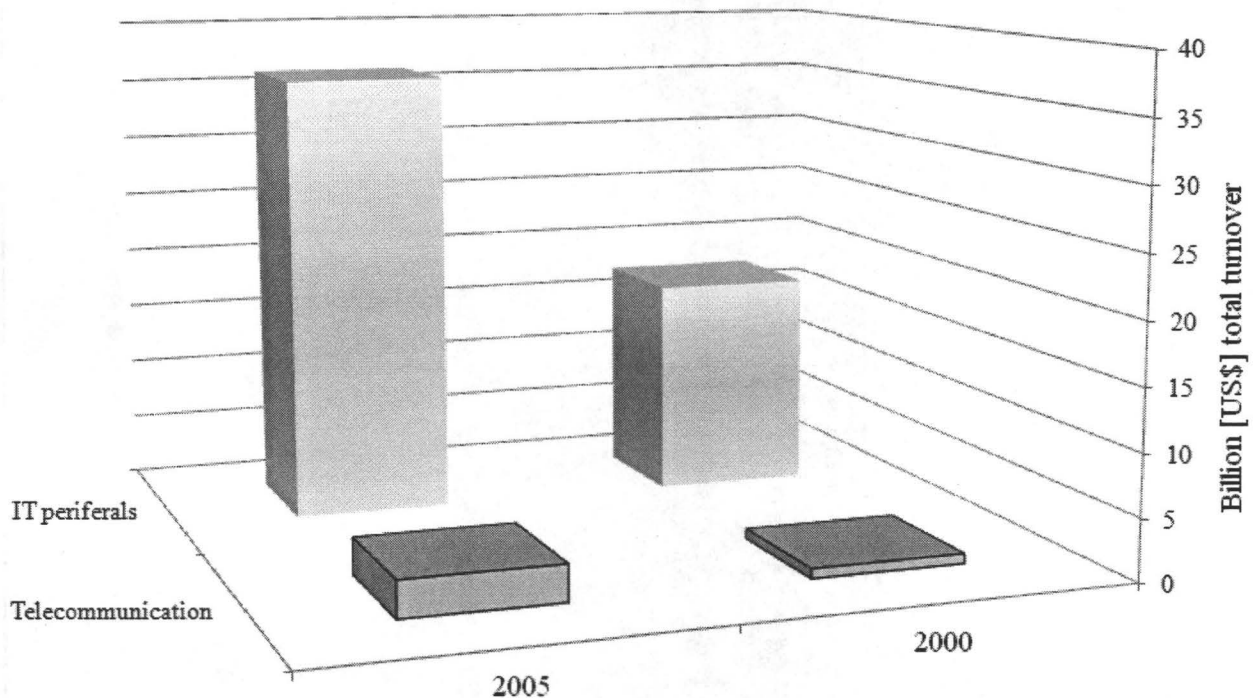


Figure 2-2: Application market of microproducts [After Luo et al., 2005]

The term “Nanotechnology” was first introduced by Professor Taniguchi in 1974 while he was trying to describe his ultra fine machining work on quartz, ceramics and silicon materials [Corbett et al., 2000]. In recent years, ultra precision machine tools have achieved position accuracy on the order of 0.016 nm [Nanoform 250 ultra, 2010]. As of the year 2000 10nm was the best accuracy achievable. Corbett et al., [2000] defined nanotechnology to be “the study, development and processing of materials, devices and systems in which structures on a dimension of less than 100 nm is essential to obtain the required functional performance.” At the same time the necessity of interdisciplinary

knowledge and development for nanotechnology is essential [Corbett et al., 2000]. However, the scope of this literature is restricted only to diamond tool based mechanical ultra precision machining which is used for the creation of two dimensional workpieces with an optical grade mirror surface finish. The review includes topics on process physics and size effects, material microstructural effects, tool geometry effects and surface integrity. The background, applications, technological advancements and opportunities for both conventional and non-conventional micro and nano technology can be found in [Corbett et al., 2000; Dornfeld et al., 2006; Byrne et al., 2003; Alting et al., 2003 and Liu et al., 2001].

2.2. SINGLE POINT DIAMOND TURNING (SPDT)

SPDT is a form of ultra precision machining technology which uses a tool based material removal process where the cutting tool is a single crystal diamond (SCD). Like conventional machining, diamond turning also removes material of a desired shape and amount through the relative motion of the tool and the workpiece. Figure 2-3 shows the capability of ultra precision machining relative to other conventional or non-conventional processes such as laser machining, Electro-Discharge Machining (EDM), grinding and LIGA which is a German acronym for X-ray lithography (Lithographie), Electroplating (Galvanoformung), and Molding (Abformung)) process. It can be seen that R_a values as low as 5 nm can be attained for features down to $1\mu\text{m}$ [Byrne et al., 2003]. The physics associated with conventional turning and diamond turning are similar up to a certain

point but differ in one key aspect. The first major difference is the size effect found in diamond turning. In ultra precision machining, single crystal natural diamond tools are usually the preferred cutting tools. They possess high hardness, stiffness, thermal conductivity as well as low friction and low relative inertness when interacting with aluminum.

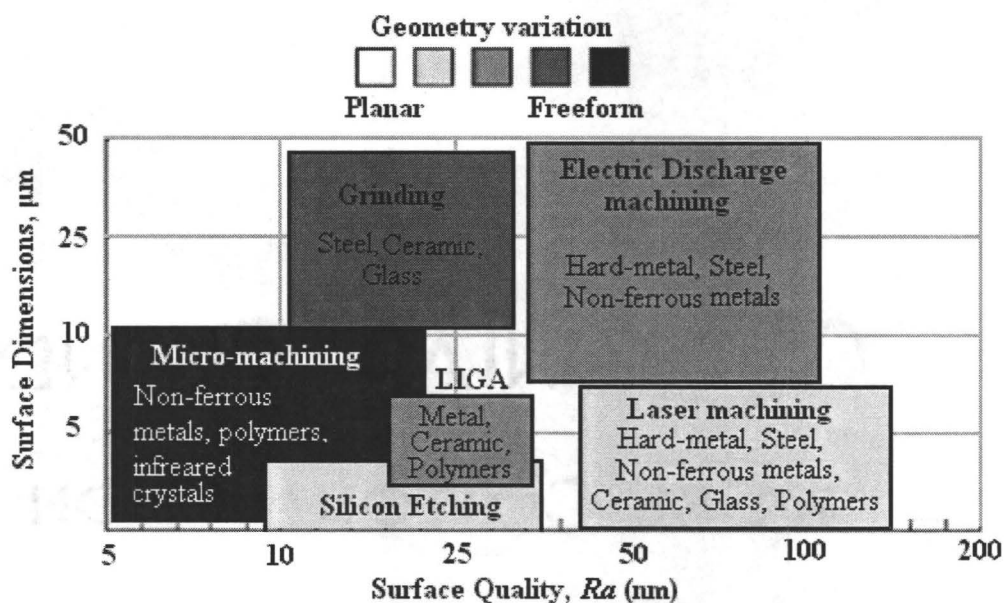


Figure 2-3: Micromachining relative to other machining Processes [After Byrne et al., 2003]

Diamond also has the ability to be sharpened to a very sharp edge and is able to hold that edge while cutting. Researchers have found that the cutting edge radius of a SCD tool varies between 10~500 nm [Ng et al., 2006; Dornfeld et al., 2006; Lucca et al., 1994; Furukawa and Moronuki, 1988; Liu et al., 2004 and Chan et al., 2001] while the cutting edge radius of a conventional TiN coated tungsten carbide varies between 8~10

micro meters [Simoneau et al., 2006a]. Based on the Taniguchi curve [Corbett et al., 2000] proposed in 1974, the single point diamond turning process can be classified as ultra-precision machining based on its machining accuracy [Dornfeld et al., 2006; Byrne et al., 2003]. Moreover, because of the sharpness of the diamond tool and the accuracy of the machine tool, the cutting process can be referred to as a nanoscale cutting process (also in Table 2.1) where the dimension of the uncut chip thickness that participates in surface generation is less than 100nm in most cases.

Table 2.1: Cutting scale and uncut chip thickness [After Simoneau et al., 2006a]

Scale	Uncut chip thickness (μm)
Macroscale	100-400
Mesoscale	30-50
Microscale	2-10
Nanoscale	<1

The single point diamond turning process is limited in general to Face Centered Cubic (FCC) materials and non-ferrous alloys such as aluminum and copper. This is due to the chemical affinity between carbon and iron, the machining of ferrous materials by diamond results in excessively high tool wear rates [Ng et al., 2006; Byrne et al., 2003]. Paul et al., [1996] proposed a hypothesis that chemical wear of diamond tools are accelerated with the presence of unpaired d-shell electrons in the metal sample being machined. For example, consider nickel and copper which have atomic number of 28 and 29 respectively and both are FCC elements. Nickel has 2 free d-shell electrons while

copper has no free electrons. It is well known that nickel is not diamond turnable [Paul et al., 1996] while copper is an ideal material for single point diamond turning [Chapman, 2010]. However, after doping nickel with phosphorous, the effect of the free d-shell electrons in nickel is eliminated and the doped material, which is commonly called electroless nickel is readily diamond turnable [Roblee, 2007]. The symbols, atomic number and electron configuration of phosphorous, nickel and copper are shown in Table 2.2 with Krypton, an inert gas [Callister, 1997]. Further work regarding diamond tool wear can be found in the recent work of Brinksmeier et al., [2006] who machined ferrous alloys (BCC) up to 4nm R_a roughness after nitriding. SPDT is also well suited for cutting single crystal materials such as germanium, silicon and also polymers [Chapman, 2010]. However, the scope of this study is limited to aluminum (FCC poly crystal: also shown in Table 2.2) which is diamond turntable with minimal chemical wear of the tool [Paul et al., 1996].

Table 2.2: A listing of the expected electronic configurations [Callister, 1997]

Element	Symbol	Atomic number	Electron Configuration
Carbon	C	6	$1s^2 2s^2 2p^2$
Nitrogen	N	7	$1s^2 2s^2 2p^3$
Aluminum	Al	13	$1s^2 2s^2 2p^6 3s^2 3p^1$
Phosphorous	P	15	$1s^2 2s^2 2p^6 3s^2 3p^3$
Iron	Fe	26	$1s^2 2s^2 2p^6 3s^2 3p^6 3d^6 4s^2$
Nickel	Ni	28	$1s^2 2s^2 2p^6 3s^2 3p^6 3d^8 4s^2$
Copper	Cu	29	$1s^2 2s^2 2p^6 3s^2 3p^6 3d^{10} 4s^1$
Krypton	Kr	36	$1s^2 2s^2 2p^6 3s^2 3p^6 3d^{10} 4s^2 4p^6$

2.2.1. Applications

Pioneering work on the design and construction of single point diamond turning machine was initiated in the 1970's at the Lawrence Livermore National Laboratory [Arefin, 2004]. One of the earliest applications of diamond turning was the machining of aluminum substrates for computer memory discs and photoreceptor components used in photocopier machines and printer applications [Chapman, 2010]. However, from the 1970s onward the large demand for infrared optics has employed diamond-turning machines for mass production. Infrared night vision systems require a range of reflective components typically machined in aluminum alloys [Chapman, 2010]. The surface roughness must be below 20nm RMS to meet the criterion for diffraction limited performance in such applications. However, the demand of optical surfaces having roughness in the range of 0.1nm arises from the requirements for high-energy laser mirrors. It is a requirement to have an extremely low surface roughness to reduce laser-induced damage and to minimize scatter in the laser and X-ray optics. However, this level of surface roughness is still only achievable by performing post machining lapping and polishing techniques [Franks, 1987].

2.3. PROCESS PHYSICS AND SIZE EFFECT IN SPDT

Various aspects of micro and nano scale cutting such as cutting force, size effect phenomenon, chip geometry and surface integrity have been studied to date. There are two primary aspects of size effect that alters the process physics of SPDT:

1. Workpiece microstructure has a significant influence on the cutting mechanism.
2. Uncut chip thickness is of the same order of magnitude as the cutting edge radius which creates a ploughing effect rather than a shearing effect.

Machining characteristics such as chip formation, surface generation, specific cutting energy, cutting forces, and surface integrity are the primary consequences of the size effect resulting from either or both of the above mentioned reasons.

2.3.1. Size effect and microstructure

Figure 2-4 provides a schematic outlining the effect of microstructure on the cutting process ranging from the macro scale to the micro scale. In conventional machining the uncut chip thickness varies from 1mm down to approximately 100 μm depending on whether the process is a roughing or finishing operation.

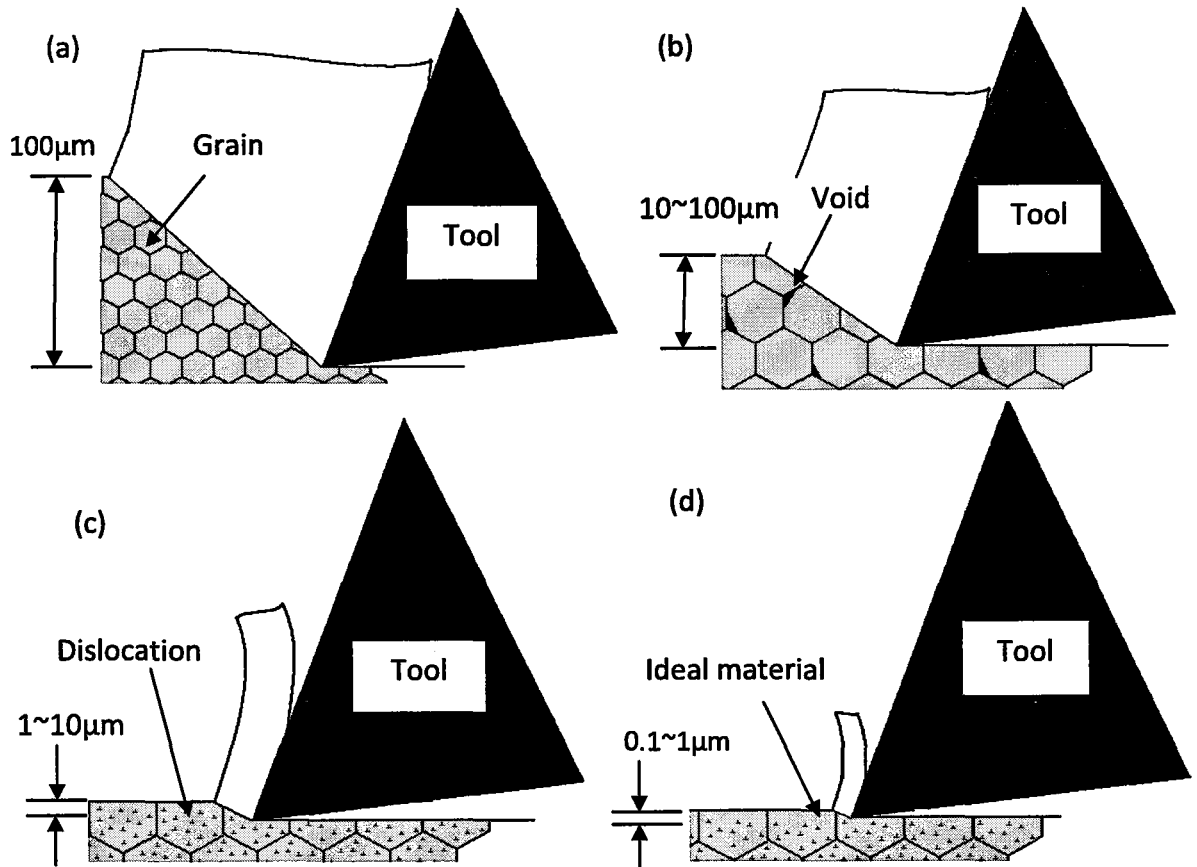


Figure 2-4: Material Behavior as machining size reduces. (a) Continuous material. (b) Effects of grain boundary. (c) Effects of dislocation and (d) Ideal material. [After Sugita et al., 1984]

The relative scale of the uncut chip thickness and cutting tool is represented in Figure 2-4(a). In conventional machining the material behaves as a continuous material and the properties of the material may be known from bulk mechanical testing performed at the macro scale. However, given the small uncut chip thickness used in ultra precision machining (mesoscale cutting in [Simoneau et al., 2006a]), the same material starts behaving differently as the voids, segregations and grain boundaries must be considered

as shown in Figure 2-4(b). With a further reduction in cutting dimension (Figure 2-4(c)), a single crystal of the same polycrystalline material becomes significant and dislocation-dislocation interactions define the material property as well as process physics in microscale cutting [Simoneau et al., 2006a]. Finally, with a further reduction in cutting dimension, the effect of dislocations becomes minimal and the material starts behaving as an ideal material as shown in Figure 2-4(d) and may be termed as nanoscale cutting.

The relationship between cutting scales and uncut chip thickness is shown in Table 2.1 adopted from [Simoneau et al., 2006a]. From Table 2.1 it can be seen that in ultra precision SPDT, the nominal uncut chip thickness is usually on the order of a few micrometers. These values are on the same order as the grain size of commonly used engineering materials such as steel and aluminum and vary between 100 nm to 100 μm [Liu et al., 2004]. In conventional machining the cutting process is isotropic in nature with material being removed through a shearing process. Because of the small uncut chip thickness used in SPDT, the cutting process takes place among the single crystals of a polycrystalline material and this is why the crystallographic orientation, alloy composition and grain structure of the workpiece material has a significant influence on the cutting mechanism, surface generation and forces in micro machining [Dornfeld et al., 2006].

Crystalline materials are known to be anisotropic in their physical and mechanical properties. One important source of material anisotropy lies in the crystallographic nature

of the metallic substrate [Lee, 1995]. Research by Furukawa and Moronuki [1988] further describes this aspect of machining. The authors [Furukawa and Moronuki, 1988] did some early investigation on polycrystal materials such as an aluminum alloy with 4% magnesium, oxygen free 99.99% copper, and germanium, as well as single crystals such as fluorite, silicon and amorphous materials like acrylic resins. They concluded that the anisotropy of crystalline materials cannot be neglected in SPDT. The authors also altered the grain size of aluminum alloys considering 160 μm , 270 μm and 620 μm by recrystallizing at various temperatures; but, no direct conclusion of their effects on surface roughness were made. However effects on cutting force at grain boundaries was reported while cutting an aluminum alloy at 100mm/sec, 6 μm depth and 40 μm feed with a 0.5mm nose radius tool and concluded that the grain boundaries have a large effect on cutting forces. This finding is in agreement with a recent observation made by Kim et al., [2008] who studied constant loading nanoscratch testing on aluminum alloys and concluded that there is an increase in the friction coefficient at the grain boundary as opposed to within the grain itself. An analogy between nanoscratch testing of Kim et al., [2008] and diamond cutting observations of Furukawa and Moronuki, [1988] thus can be made by stating that at the grain boundary, the frictional component (μ) increases, which eventually reduces the shear angle (ϕ). A reduction in shear angle results in a larger area undergoing the shearing process and thus increases the cutting or principal force as can also be seen from Equation 2.1. This is well known based on Merchant's theory [Shaw, 2005].

$$2\varphi + \beta - \alpha = 90^\circ$$

Equation 2.1

Where, φ is the shear angle, β is the friction angle and α is the rake angle of the tool. Figure 2-5 shows schematically how the shear angle affects the shear plane and shear area. A lower shear angle results in a larger shear plane and thus more cutting force.

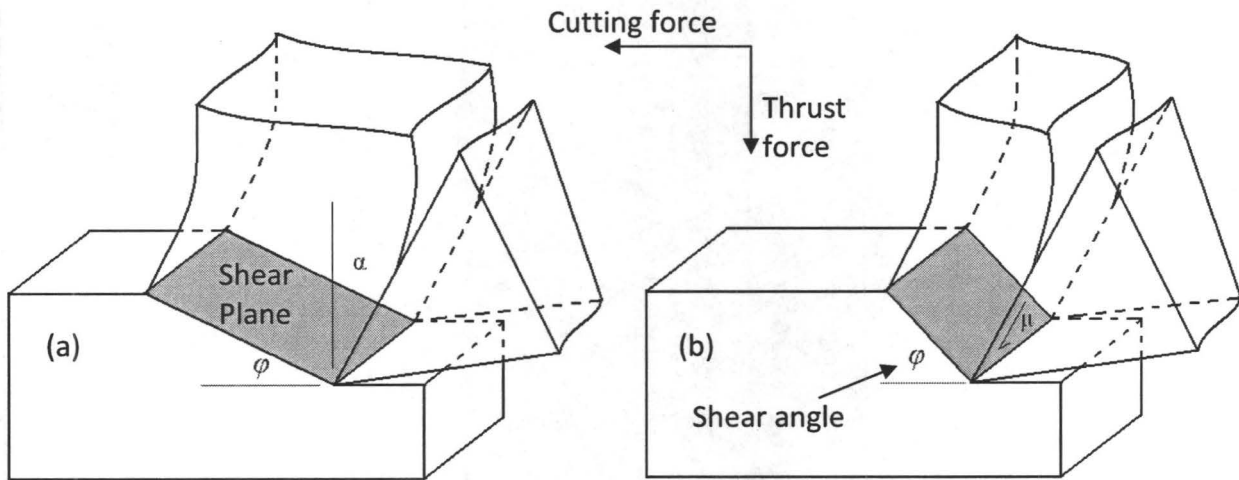


Figure 2-5: Change in shear plane area with shear angle (a) Smaller shear angle and (b) larger shear angle

According to Furukawa and Moronuki [1988], copper has a large degree of anisotropy followed by germanium and aluminum. Moriwaki [1989] studied the effect of crystal structure of copper inside of a Scanning Electron Microscope (SEM) with a depth of cut ranging from 0.1 to 5 micrometers with a cutting speed of 120mm/min and found that the shear angle reached a value as high as 60° . Ueda et al., [1980] further studied

this phenomenon and concluded that the shear angle varied from 15° to 60° for different crystallographic orientation of β -brass. A shear angle greater than 45° is generally unlikely to occur in conventional cutting; however, in single-crystal cutting such a large shear angle is possible due to the high anisotropy of single crystal materials and the ploughing effect [To et al., 1997]. To et al., [1997] studied single crystal aluminum rods with the crystallographic axes normal to the $\langle 100 \rangle$, $\langle 110 \rangle$ and $\langle 111 \rangle$ direction while varying the depth of cut from 1 to 10 micrometer. They reported that the highest cutting force was produced for the $\{110\}$ crystal orientation. This orientation also produced the worst surface finish. The testing achieved a better surface finish in the $\{100\}$ orientation while the minimum cutting force was observed in the $\{111\}$ orientation. The maximum variation in cutting force for different orientation of grains and depth of cut was only 0.05N. From fly cutting tests performed on copper, Moriwaki [1989] concluded that the steps at the grain boundaries of a machined surface are much more distinct at an uncut chip thickness of $1\mu\text{m}$ or more, while they become insignificant when the uncut chip thickness was below $0.10\mu\text{m}$ where rubbing and burnishing dominated over shear [Demir, 2008].

From the theory of plasticity applied to metal cutting it is known that for plastic deformation to occur there has to be defects in the form of voids, dislocations and/or inclusions [Gurson, 1977]. According to McDowell [2000], “plasticity is a phenomenon that is affected by kinetics and processes of dislocation generation and interactions occurring across a wide range of length scales.” There are at least five scale lengths to

describe plasticity: 1) atomistic, 2) discrete dislocations, 3) sub-grain dislocation substructures, 4) grain or 5) crystal and macro-scale as shown in Figure 2-6 [McDowell, 2000]. According to Callister, [1997] a heavily deformed metal can have a dislocation density as high as 10^9 to 10^{10} mm^{-2} while a subsequent heat treatment can reduce that number to 10^5 to 10^6 mm^{-2} . Dislocation densities as low as 10^3 mm^{-2} are typically found in carefully solidified metal crystals. However, when there is a material with no defects, for example a metal “whisker”, that is loaded in bending it shows no plastic flow and the material behaves elastically to the point of fracture so they are considered to be perfectly brittle (yield strain \geq fracture strain) [Shaw, 2005; 1995]. Thus for very small undeformed chip thicknesses the material removal is at the atomistic level and elastic spring back will occur.

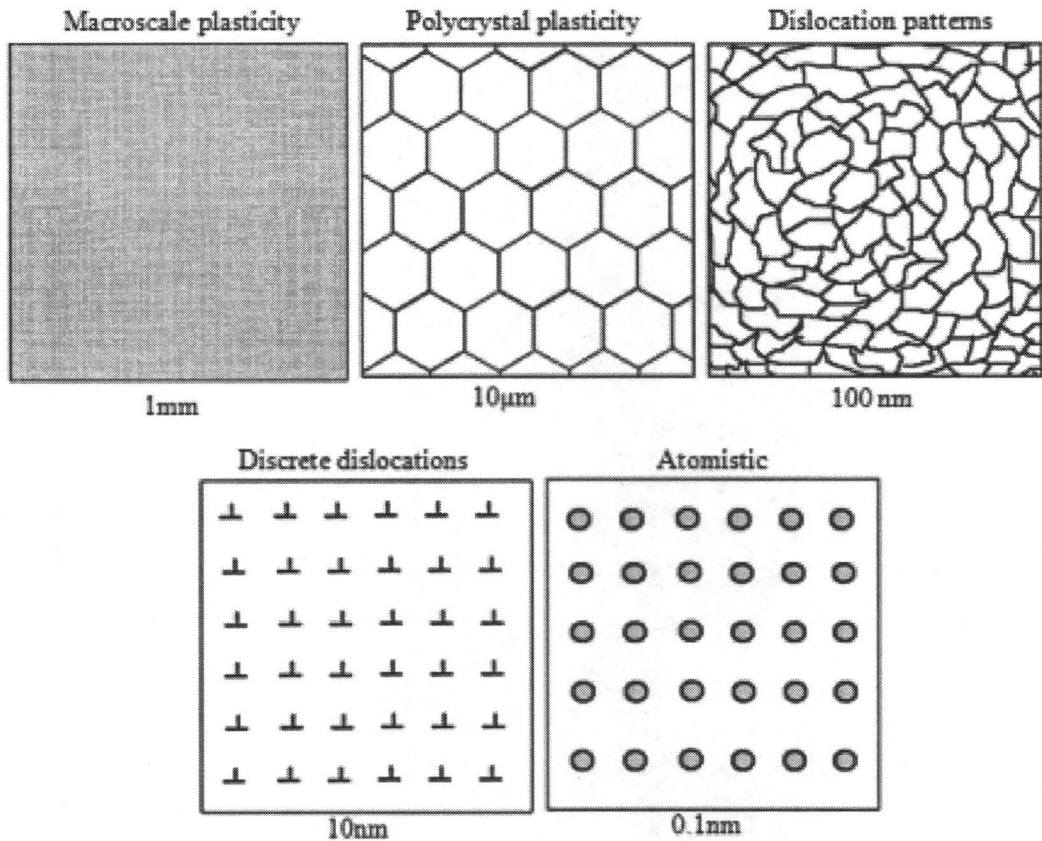


Figure 2-6: Minimum scale lengths of plasticity [After McDowell, 2000]

Thus it becomes evident that material properties will change with the decrease in cutting dimension and should reach the theoretical material property values eventually. This understanding of the change in material behavior is very important as it pertains to single point diamond turning. In a cutting process the tool has to fracture the material to form chips of a desired geometric shape to achieve a predictable dimensional accuracy. This accuracy is the key motivation of ultra precision single point diamond turning. However, it is well understood that in SPDT plastic deformation and elastic recovery may dominate over the fracture mechanism while chip formation, because of size effect as

well as its deformation and recovery, is dependent on the anisotropy of the crystalline material. Thus the choice of substrate material with the correct grain size and crystallographic orientation is of particular importance in ultra-precision machining. However, it may not be practically feasible to produce a functional surface when the crystallographic orientation is limited to one plane. Thus, when turning is required, a workpiece with an ultra-fine grain size and a weak or random crystallographic texture would be preferable to reduce the size effect [Lee, 1995].

2.3.2. Size effect and cutting edge radius

Figure 2-7 shows a typical metal cutting zone and identifies primary and secondary shear deformation zones, angles and forces involved.

different measuring techniques such as the fitting of a circle to the cutting edge image in an SEM image [Ng et al., 2006] or on a profile produced using an atomic force microscope (AFM) of the indentation that the cutting edge would make when pressed into a soft metal [Arefin, 2004]. SEM imaging techniques may result in over estimation of the edge radius due to parallax error in the setup and in the case of measuring the indentation; spring back of the soft metal may take place altering the indentation. Lucca et al., [1994] developed special instrumentation to measure the tool edge radius using an AFM by taking into account the cantilever tip radius. Due to the size effect and irrespective of the nominal rake angle (α), the effective rake angle (α_e) acts as a negative rake angle when the uncut or undeformed chip thickness, t is less than the cutting edge radius R_e as shown in Figure 2-8 [Ng et al., 2006; Fang and Zhang, 2003].

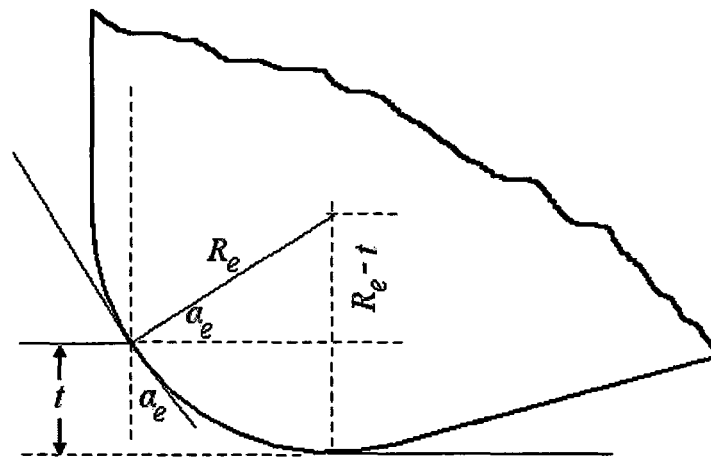


Figure 2-8: Change in effective negative rake angle with uncut chip thickness [Ng et al., 2006]

The effective rake angle is defined as the angle between the vertical axis and the tangent to the contact point between the cutting tool and the undeformed chip thickness and can be expressed as [Ng et al., 2006]:

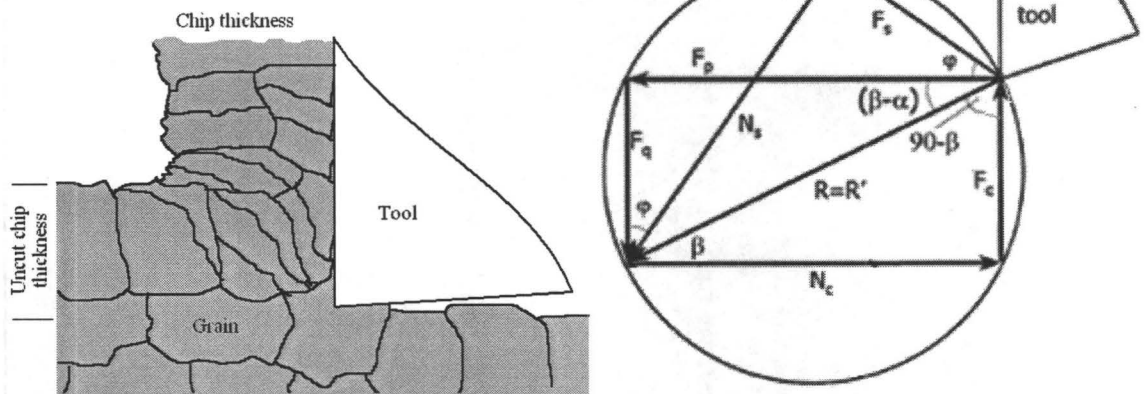
$$\alpha_e = \sin^{-1}\left(1 - \frac{t}{R_e}\right)$$

Equation 2.2

Where, α_e is the effective rake angle, t is the uncut chip thickness and R_e is the cutting edge radius.

The primary effect of a negative rake angle in a metal cutting operation is to increase the thrust force as compared to the cutting force. Figure 2-9 show this phenomenon from the orthogonal cutting force model proposed by Merchant in 1945, often referred to as Merchant's circle diagram [Shaw 2005] with the help of a cutting force model for large and small uncut chip thickness proposed by Moriwaki [1989]. Sreejet and Ngoi [2001] have shown a comparative relation between cutting force (F_p) and thrust force (F_q) for different tool workpiece interactions. According to their results on conventional cutting $F_p/F_q \approx 2$, for grinding $F_p/F_q \approx 1/2$, for SPDT at small uncut chip thickness $F_p/F_q < 1/2$ and for indentation sliding $F_p/F_q \ll 1/2$.

(a) Large uncut chip thickness



(b) Small uncut chip thickness

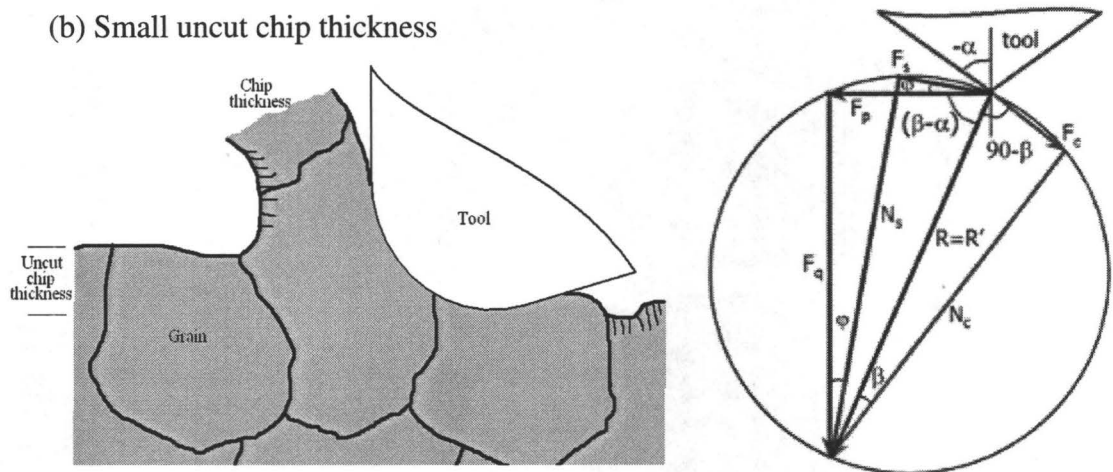


Figure 2-9: Behavior of cutting edge as the cutting dimension reduces [Moriwaki, 1989] Schematic and Merchant's circle diagram for (a) Large uncut chip thickness and (b) Small uncut chip thickness showing an effective negative rake angle.

An effective negative rake angle at a very small uncut chip thickness greatly influences the cutting process and predominantly defines the active material removal

mechanism such as cutting or ploughing and sliding with microextrusion thus impacting the resulting surface finish. In the following section the influence of size effect on surface integrity will be discussed with respect to workpiece material and tool geometry in SPDT.

2.4. SURFACE INTEGRITY IN SINGLE POINT DIAMOND TURNING

In theory, surface integrity has two aspects [Bhattacharyya, 2000]:

1. surface topography which includes:
 - a. surface roughness and
 - b. form (waviness) and
2. surface metallurgy or subsurface damage and residual stress.

The scope of the thesis is limited to surface roughness and metallurgy or subsurface information. Waviness or form of a surface topography is primarily attributed to low frequency, high wavelength machine tool vibration and is beyond the scope of this study. Here, authors assumed that the machine tool is perfectly stiff based on the observed sub-micron force and machine tool stiffness ($N/\mu\text{m}$) information available from the manufacturer. This is discussed further in the experimental setup in Chapter 4. Figure 2-10 shows a schematic of surface topography showing surface roughness as well as the

combined effect of roughness and waviness. A detailed literature review on waviness or form induced surface topographical changes is presented in [Meyer et al., 2009].

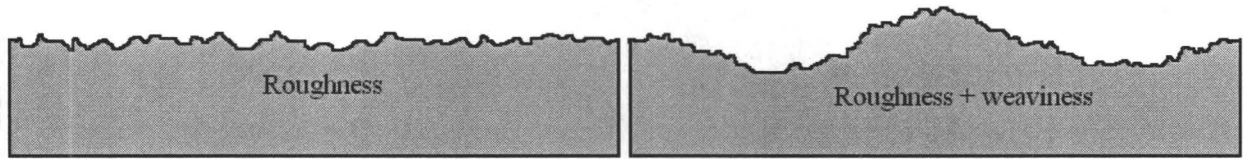


Figure 2-10: Surface topography [After Liu and Melkote, 2006]

In oblique single point diamond turning operations with round nosed tools, size effect is inevitable. Figure 2-11 shows the true cutting geometry for diamond turning with a round nose tool (not to scale).

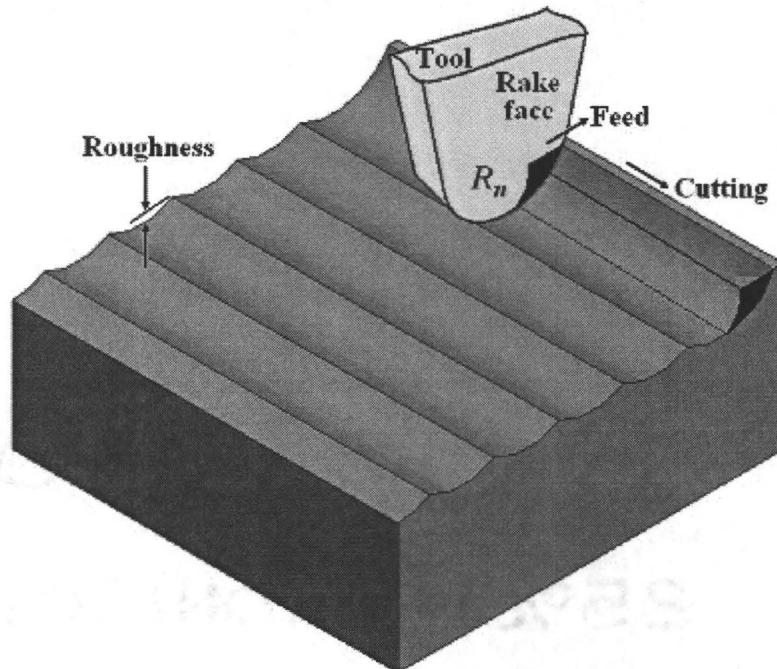


Figure 2-11: True cutting geometry for diamond turning with a roundnose tool. The chip moving up the tool rake face is not shown

The combination of cutting and feed motions produces the chip cross section projected into the uncut shoulder which is highlighted in the tool rake face. Figure 2-12 (a) is a schematic 2D representation of Figure 2-11 and Figure 2-12 (b, c, d and e) represents the right hand sectional view along the dotted lines showing the relative change in cutting edge radius and material property with a change in the effective uncut chip thickness.

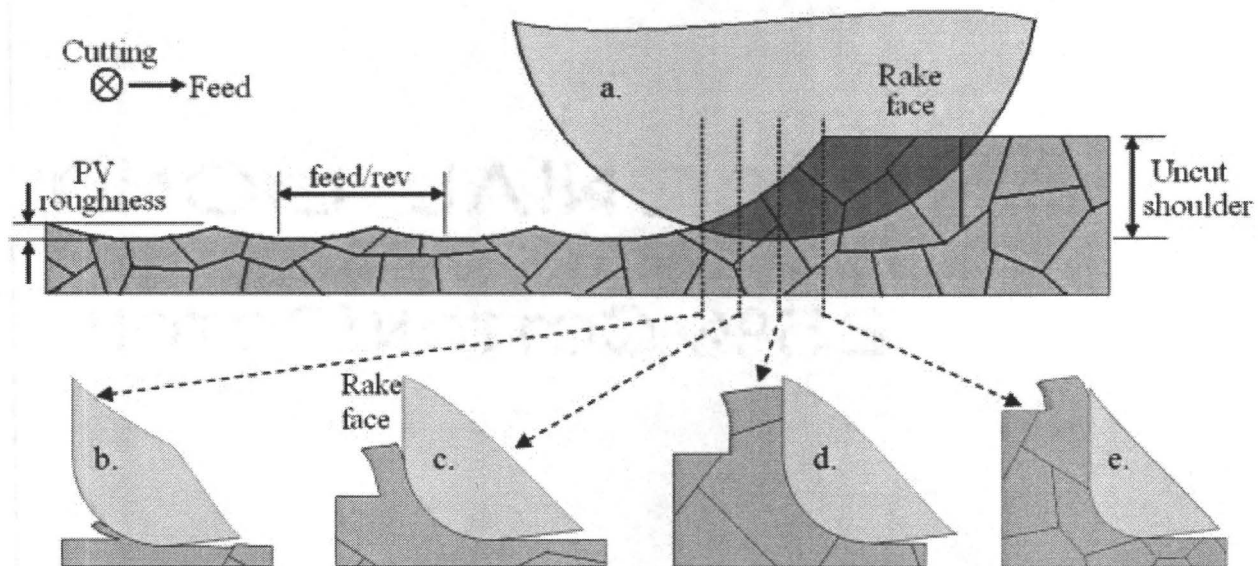


Figure 2-12: Schematic of change in cutting behavior along cutting edge

It is evident that the effective uncut chip thickness is a maximum at Figure 2-12 (e) and gradually decreases to zero at the trailing edge of the tool. For example, according to Moriwaki [1989], for a 1mm nose radius tool with feed rate of $5\mu\text{m}/\text{rev}$ and nominal depth of cut of $3\mu\text{m}$, the maximum uncut chip thickness is approximately 375nm. The effective uncut chip thickness under which the surface is generated by the tool section $5\mu\text{m}$ from the trailing edge in this case, is only 25nm. Assuming the cutting edge radius is

100nm, the effect of cutting edge radius rounding dominates near the trailing edge of the tool where the material is extremely thin and thus is potentially entirely defect free. With this basic understanding of process physics and the size effect in SPDT, the following sections will discuss how independent process parameters such as, material microstructure and tool geometry affects the micro/nano cutting mechanisms.

2.4.1. Surface Roughness

In a turning operation, the peak-to-valley (R_{th}) surface roughness usually equals or exceeds the value predicted by a geometric calculation value $f^2/(8R_n)$, where f is the feed rate (mm/rev) and R_n is the tool nose radius as shown in Figure 2-13.

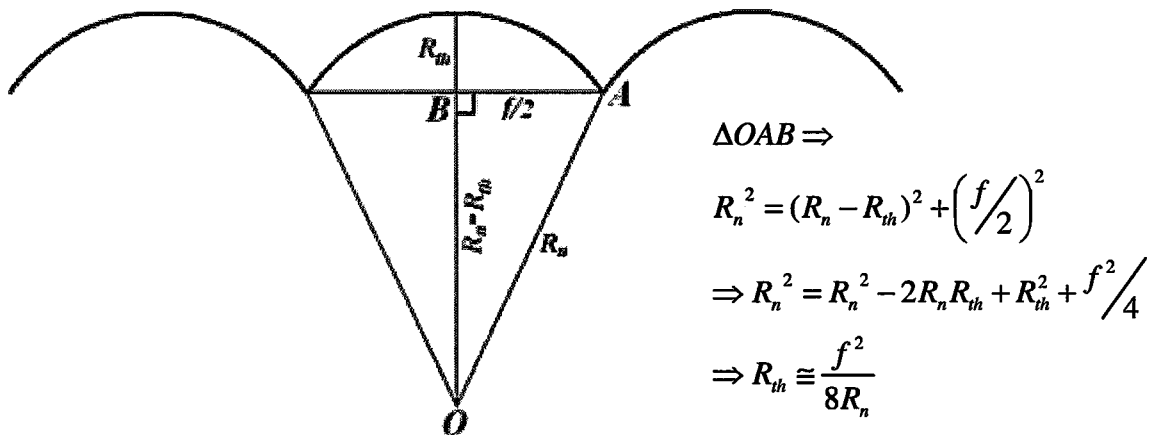


Figure 2-13: Turning operation and surface roughness

However, below a limiting value of f , R_{th} becomes independent of f and may even increase as f is reduced [Childs et al., 2008a and 2008b; Liu and Melkote, 2006; Shaw,

2005]. Figure 2-14 shows the results compiled by Childs et al., [2008a; 2008b] to date for turning and facing operations with round nose tools. The primary reason for this increased peak to valley roughness is material side flow which results from the concept of minimum chip thickness. It is thought that below a minimum value of uncut chip thickness, no chip will form [Dornfeld et al., 2006]. Kishawy and Elbestawi [1999], concluded from their hard turning experiments that the primary reason for material side flow was the squeezing of the material between the secondary edge of the tool and the machined surface when the chip thickness is less than a minimum value. Thus the direction of the side flow is opposite to the feed direction. This causes an increase in the peak-to-valley roughness as shown in Figure 2-15.

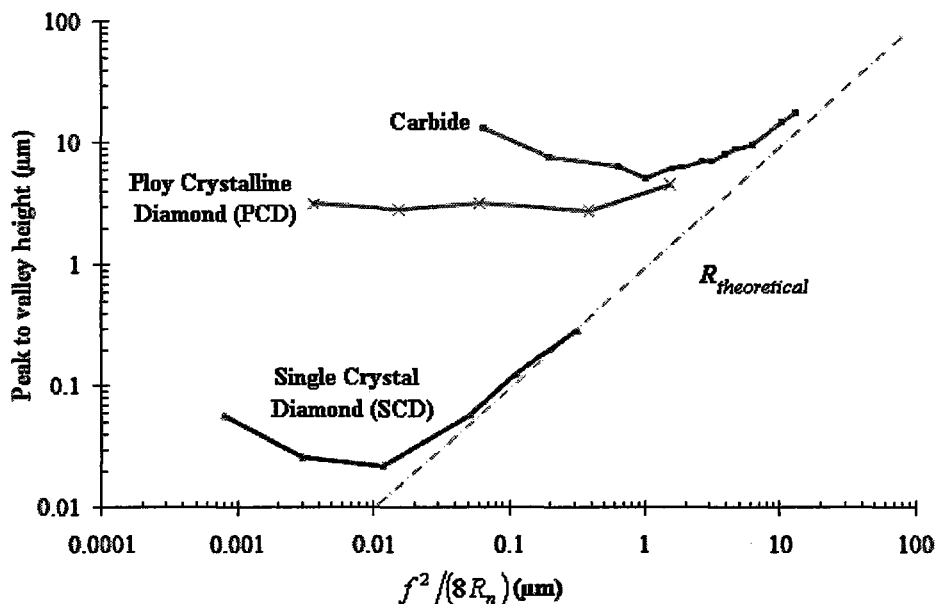


Figure 2-14: Roughness data on turning and facing from [After Childs et al., 2008a; 2008b]

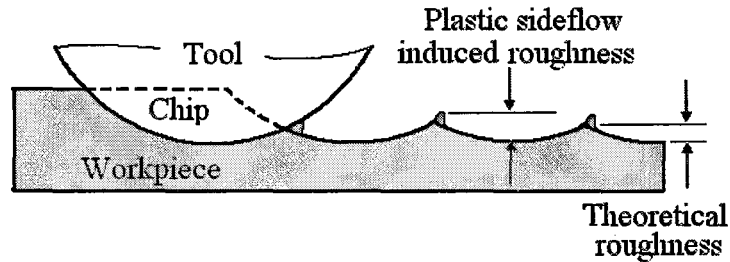


Figure 2-15: Illustration of plastic side flow and plastic side flow induced roughness [After Liu and Melkote, 2006]

The concept of minimum chip thickness was suggested by Sokolowski in 1955 [Shaw, 2005] and concluded that below a minimum chip thickness, chips will not form and rubbing will take place. The value of minimum undeformed chip thickness depends upon the radius of the cutting edge, cutting speed and the stiffness of the system. Applying this idea to the cutting edge of a turning tool, it is suggested that a small triangular portion of the material is left behind. This has been analyzed by Brammertz who called it a Spanzipfel in German. An additional geometric concept was proposed by Brammertz to supplement the kinematic surface roughness to account for the contribution of the minimum chip thickness to the surface roughness in turning as shown in Equation 2.3 [Shaw, 2005] where t_m is minimum chip thickness, R_n is the tool nose radius, R_{th} is the theoretical peak to valley roughness and R'_{th} is the corrected peak to valley roughness.

$$R'_{th} = R_{th} + \frac{t_m}{2} \left(1 + \frac{R_n t_m}{2} \right)$$

Equation 2.3

Estimating the t_m however is non-trivial as it depends on the workpiece material and cutting tool geometry. Grzesik [1996] proposed a model to estimate critical undeformed chip thickness t_m by applying a molecular-mechanical theory of friction to consider the effect of adhesion. The model predicts surface roughness with respect to the known cutting parameters and tool corner radius. However, the results are based on a conventional turning operation. Yuan et al., [1996] concluded that the diamond tool sharpness has the most important effect in realizing the minimum chip thickness. This is believed to be because of less size effect. They proposed a mathematical equation that defines the minimum chip thickness to further support their conclusion. This is shown in Equation 2.4.

$$t_m = R_e \left(1 - \frac{F_q + \mu F_p}{\sqrt{(F_p^2 + F_q^2)(1 + \mu^2)}} \right)$$

Equation 2.4

Where, R_e is the cutting edge radius, μ is the friction coefficient; F_p and F_q are cutting force and thrust force respectively. However, exact determination of F_p and F_q and μ at that scale is experimentally very difficult unless the orthogonal cutting case is considered. Moreover the effect of material property is ignored in Equation 2.4. The effect of tool edge roughness on surface roughness in turning has also been studied and can be neglected as it has minimal effect on traditional machining [Childs et al., 2008a, 2008b; Liu and Melkote, 2006]. Sata et al., first studied the material swelling effect in 1985. This work was followed by a more complete definition given by Cheung and Lee [2000].

According to the body of work by [Cheung and Lee, 2000; Sata et al., 1985] the swelling effect is a combined effect of material side flow, the burnishing effect and the elastic recovery of the machined surface that will cause deeper tool marks. Elastic recovery occurs in the region below the chip where the workpiece material left behind the front clearance of the tool springs back or recovers after burnishing. According to Sata et al., [1985] the amount of swelling depends on the properties of the material being cut and is higher for softer and more ductile material. For example Sata and Shaw [in Liu and Melkote, 2006] have studied the influence of material side flow on surface finish and have found that this component of roughness is minimal for a brittle material such as brass, but may contribute up to 6 μm to the peak to valley roughness value when alloy steel is machined.

According to Childs et al., [2008a; 2008b] with the decrease in feed rate, the surface roughness is proportional to the cutting edge radius and independent of the feed rate but is limited to the precision of the machine tool. However, not only does the machine tool and cutting edge radius limit the achievable surface roughness but also the proper selection of the workpiece material plays a major role in achieving the lowest surface roughness. The machine tool plays a vital role in the form error, which is a low frequency vibration signature left on the final machined surface [Roblee, 2007]. Knuefermann and McKeown [2004] studied and simulated the oblique cutting operation and discovered that there is a change in relative cutting scale along the tool axis in the feed direction. Knuefermann and McKeown [2004] separated the chip formation

mechanism into three primary processes based on local chip thickness, chip removal, plastic deformation and elastic deformation. However, the effect of cutting edge radius was neglected in the study and primarily attributed to conventional machining with Cubic Boron Nitride (CBN) tools. Chan et al., [2001] studied the surface generation in diamond turning of an Al6061/SiC_p metal matrix composite and reported the effect of SiC_p particles on the surface generation. However, the literature does not sufficiently explain the effect of secondary particles of the matrix on surface roughness. Lee et al., [1999] studied the material induced vibration and performed a framework of a model based simulation system to quantify the surface topography of a diamond turned surface. However, it is difficult to analyze the crystallographic orientation of a polycrystalline material and moreover, the framework does not include the ploughing effect.

It can thus be concluded that the explanation for minimum chip thickness is a combined size effect of material microstructure and cutting edge radius as discussed in Sections 2.3.1. and 2.3.2. This part of the relative uncut chip thickness and cutting edge radius generates the surface that has a roughness essentially higher in value than the geometrically predicted value. This is the hypothesized reason why in cutting operations, the thrust force and specific cutting energy [Figure 2-16] increases with a decrease in uncut chip thickness and is an indication of the size effect [Shaw 1995; 2005].

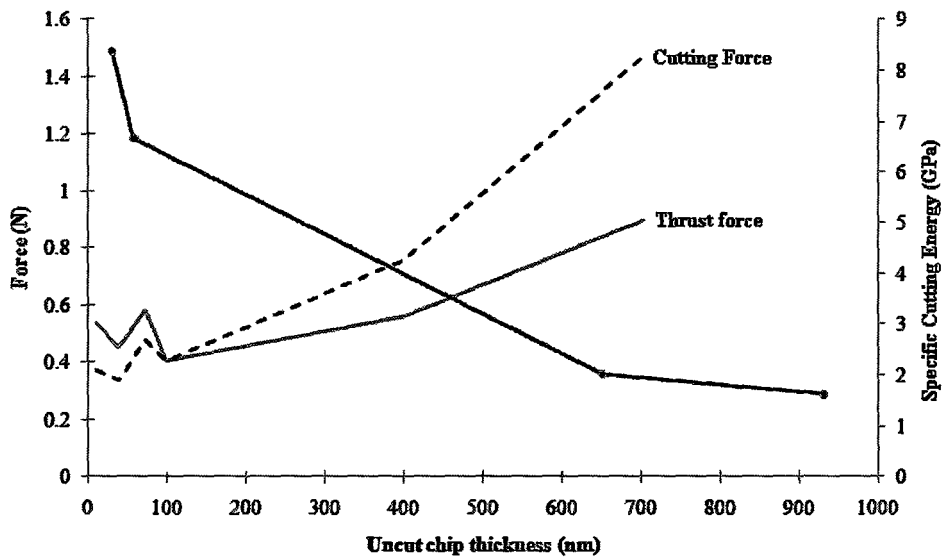


Figure 2-16: Size effect in cutting force and specific cutting energy for diamond turning of 7075 aluminum alloy [After Ng et al., 2006]

According to Shaw [1995; 2005], this increase in specific cutting energy increases rapidly as the feed decreases, which in turn causes more plastic side flow along the secondary cutting edge. Moriwaki [1989] observed that below a $0.2\mu\text{m}$ depth of cut, rubbing and burnishing become more dominant than shear during machining polycrystalline copper. However, the cutting edge radius plays an important role which is evident from Figure 2-14. For a conventional cemented carbide tool, the typical edge radius R_e is in the range of $10\text{--}20\ \mu\text{m}$ and for single crystal diamond (SCD) tools, the edge radius is around $0.1\ \mu\text{m}$. On this basis, the departure from kinematic roughness in Figure 2-14 as found from $f^2/[8R_n]$ varies from 2 to $8\ \mu\text{m}$ for carbide and 0.02 to $0.08\ \mu\text{m}$ for SCD inserts. This mechanism suggests a change in roughness at a ratio of f^2/R_n to R_e in the range of $1\text{--}5\ \mu\text{m}$ [Childs, 2008a]. Figure 2-14 may also be considered directly in

terms of its minimum ranges of peak-to-valley height (2–8 μm for cemented carbide and 0.02–0.08 μm for SCD inserts) to be 0.1–0.5 R_e . According to [Childs, 2008b] at the lowest feed rates, peak to valley roughness becomes independent of feed and is proportional to cutting edge radius. However, Childs [2008a] also observed the dependency of roughness on microstructure while machining 0.45% carbon steel and hypothesized that the roughness was determined perhaps by the microstructure of the material rather than by the insert edge radius. However, the conclusions are limited to tribological compatibility of different tool-workpiece combinations such as PCD and CBN which are two different materials with different frictional characteristics and influences on the cutting process. Moreover, material property and chip formation mechanisms have not been addressed in this work. Lastly, repeatability and accuracy in measuring the cutting edge radius of SCD tools is very challenging and not generally done.

According to Kishawy and Elbestawi [1999] the material side flow was increased when using a large nose radius tool. During cutting with a large nose radius tool, a greater part of the chip will have a chip thickness less than the minimum chip thickness value which will increase the ploughing force and will lead to more material side flow. In analyzing the chip morphology, authors noticed that an increase in the nose radius increased the chip edge serration. Due to the nose radius, the chip thickness is decreased gradually to zero and causes high pressure at the trailing edge. Thus, the material at the trailing edge of the tool, where the chip thickness is a minimum, is subjected to high

stress which causes tearing on the weakest edge of the chip. In addition, the variation in the chip particle velocity facilitates the non-uniform displacement along the chip width and, hence, leads to chip edge serration. Chip edge serration indicates that some part of the material is being left behind on the machined surface for conservation of mass and will become a signature of side flow on the freshly machined surface. Figure 2-17 (a and b) schematically shows that more chip thinning is occurring when machining with larger nose radius tools that generates more chip edge serration compared to a smaller one. It is also believed that because of the chip thinning along the edge of the round nose tool, the effective rake angle and shear angle will vary along the cutting edge leading to a strain gradient which further promotes side flow. Size effect in micro-cutting shows that the specific cutting energy increases nonlinearly as the uncut chip thickness is decreased. If the material directly in front of the tool face is strengthened more so than the material on the side, increased plastic side flow will occur and the roughness due to plastic side flow will be increased [Liu and Melkote, 2006].

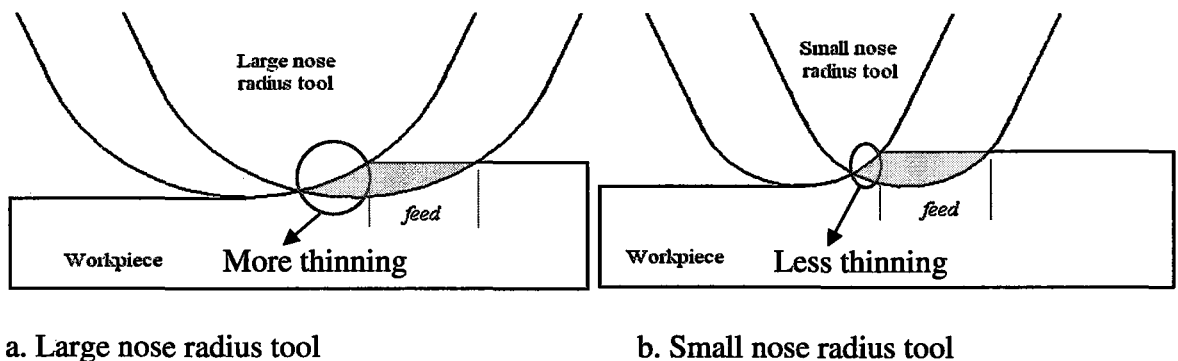


Figure 2-17: Effect of nose radius on chip thinning [After Kishawy and Elbestawi, 1999]

As a follow up to the work of Sata et al., [1985], Cheung and Lee [2000] concluded from their multi-spectrum analysis that material anisotropy also plays an important role in defining surface roughness that results from material induced vibration. Figure 2-18 shows schematically the variation in recovery of different crystal orientations as proposed by Cheung and Lee. However, their results are based on the frequency spectrum of space domain data while cutting in a specific crystallographic direction and it is not possible to correlate with the real time machining operation where there is minimal control on the directional property with respect to the cutting direction.

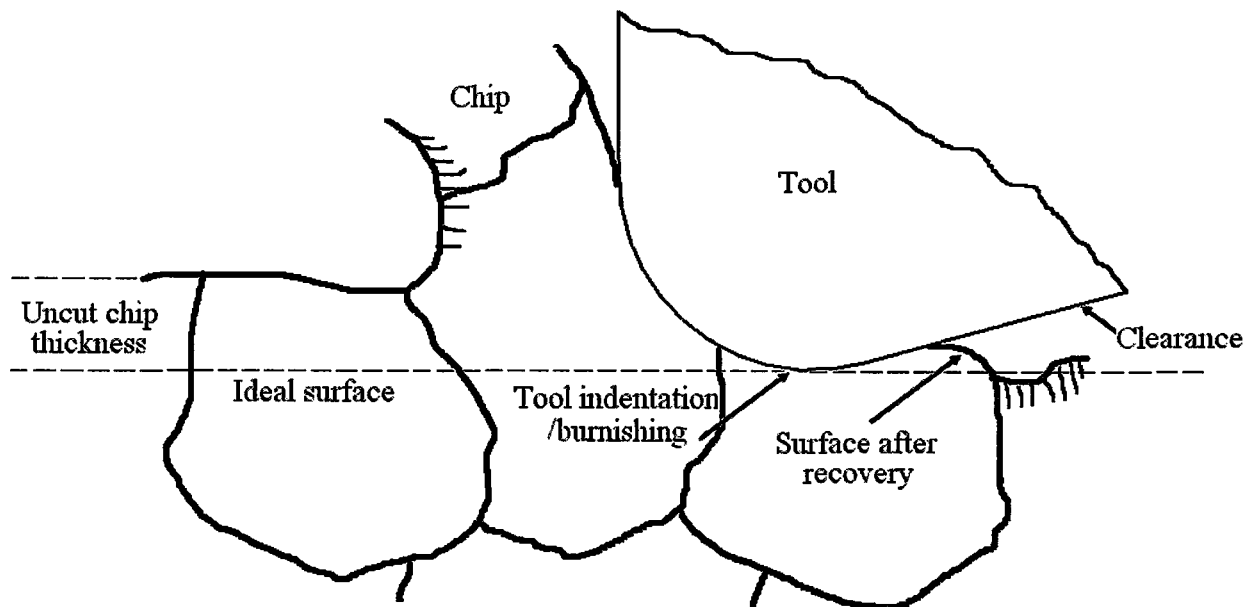


Figure 2-18: Material anisotropy and recovery [After Cheung and Lee, 2000]

2.4.1.1 The interpretation of precision machining limits and measurement sensitivities

It is of utmost importance to interpret the data quoted in different literature related to the measurement of precision surfaces. Most of the surface roughness figures reported in the literatures are based on amplitude resolution without mentioning surface wavelength. Instruments based on optical interferometers or mechanical styli have amplitude sensitivity on the order of 0.1nm; however, their surface wavelength or lateral resolution may vary by many orders of magnitude. Thus without mentioning lateral resolution, the amplitude data should taken as an undefined average. The concept of the amplitude and lateral resolution relationship is of fundamental importance in interpreting surface roughness measurements [Franks, 1987]. In optical interferometry the lateral resolution can be selected by changing the field of view while the number of pixels is fixed. A relative change in lateral resolution with field of view is shown in Table 4.11 for the Zygo Newview 5000 white light interferometer.

2.4.2. Subsurface information

Relative roundness of the cutting edge radius at a very small effective depth of cut results in a very large negative effective rake angle that causes micro extrusion of the material. To form a chip, material has to undergo a high amount of plastic deformation followed by fracture to produce a small chip, or else deformed workpiece material will remain on the surface. This is a similar concept to the minimum chip thickness approach.

When the material is heavily deformed because of the roundness of the tool, it generates a plastic deformation zone and if there is any defect present in the plastic deformation zone, a crack generates causing significant subsurface damage. Lucca et al., [1994] experimentally investigated the depth of the plastically deformed layer, which is oftentimes referred to as the subsurface damage region, by carefully polishing and etching the cross-section of the machined surface (Te/Cu alloy) after orthogonal ultra precision machining with the range of uncut chip thicknesses on the order of 0.01–10 μm . Two tools with near similar nominal geometry but with differing edge geometries were used. This result indicates that the deformed layer is essentially independent of uncut chip thickness as shown in Figure 2-19 and varies between 1~4 μm . Lucca developed a sliding indentation model and estimated the subsurface damage for aluminum to be 0.31-0.81 μm for depths of cut of 0.1-1 μm , respectively, which are very close to the X-ray results reported by [Demir, 2008]. To and Lee [2001] concluded from their micro indentation tests on aluminum that the mean depth of the deformation layer in diamond turning lies in the range 0.1-0.4 μm .

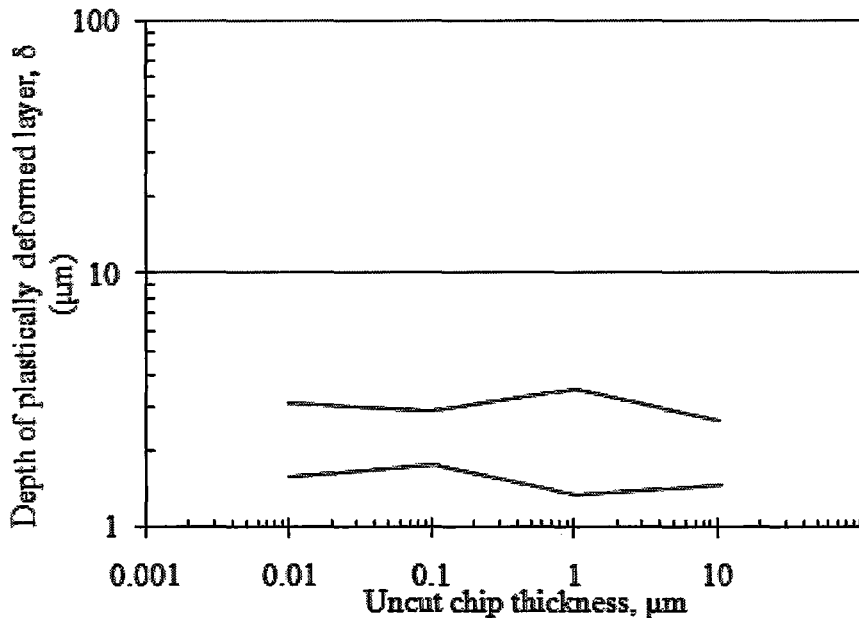


Figure 2-19: Range of measured depth of plastically deformed layer (δ) versus uncut chip thickness (h) after machining a Te/Cu alloy with a sharp and a worn diamond tool [After Lucca et al., 1994]

Thus a conservative conclusion may be drawn that, the specific cutting energy would be higher if there is no dislocation or dislocation generating defect present for an aluminum alloy. One approach to improve machinability is thus by increasing the dislocation density of the workpiece material. This will lead to better chip formation, less surface generation energy and less side flow. However, no literature could be found that tests the effect of increasing dislocation density to address surface roughness when SPDT aluminum alloys.

2.5. DISLOCATION AND STRAIN HARDENING

Due to the minimum chip thickness effect, the micromachining process is affected by two mechanisms—chip removal and ploughing/rubbing [Liu et al., 2004]. Both mechanisms are essentially subject to plastic deformation behavior of material. However, chip removal leads to fracture followed by plastic deformation and ploughing/rubbing leads to elastic-plastic deformation. It is well known from theory [Callister, 1997] that the ability of a metal to plastically deform depends on the ability of the dislocations to move. The mechanism of the motion of dislocation is represented in Figure 2-20. The process by which plastic deformation is produced by dislocation motion is termed as slip and the crystallographic plane along which the dislocation line traverses is termed a slip plane as shown in Figure 2-20 and the direction is termed a slip direction.

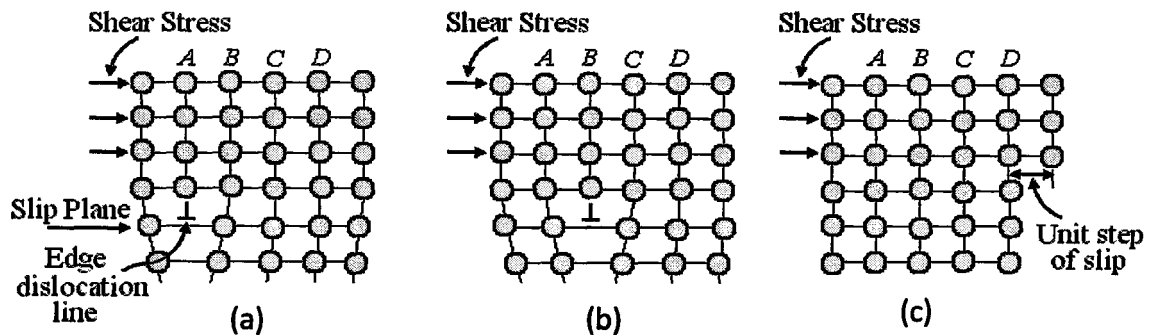


Figure 2-20: Atomic arrangements that accompany the motion of an edge dislocation as it moves in response to an applied shear stress. (a) The extra half plane of atom is labeled A. (b) The dislocation moves one atomic distance to the right as A links up to the lower portion of plane B; in the process, the upper portion of B becomes the extra half-plane. (c) A step forms on the surface of the crystal as the extra half plane exists [After Callister, 1997]

The combination of the slip plane and slip direction is termed a slip system. Dislocations do not move with the same degree of ease on all crystallographic planes of atoms rather for a particular crystal structure the slip plane is that plane having the densest atomic packing. Face Centered Cubic (FCC) metals have 12 possible slip systems composed of four unique $\{111\}$ planes and within each plane, three independent $\langle 110 \rangle$ directions. Metals with FCC (example: copper, aluminum, nickel, silver, gold etc.) and Body Centered Cubic (BCC; example: α -iron, potassium, tungsten etc.) crystal structures have a relatively large number of slip systems numbering at least 12 and are quite ductile. Conversely, Hexagonal Close-Packed (HCP; example: cadmium, zinc, magnesium, titanium etc.) metals have few active slip planes (3 or 6) and are normally quite brittle [Callister, 1997]. Several characteristics of dislocations are important with regard to the mechanical properties of metals such as lattice strain or strain fields that exist around dislocations. Lattice strain is influential in determining the mobility of the dislocations as well as their ability to multiply. For example, atoms immediately above and adjacent to the dislocation line are squeezed together and are in compression and directly below the half plane, the effect is exactly opposite as shown in Figure 2-21.

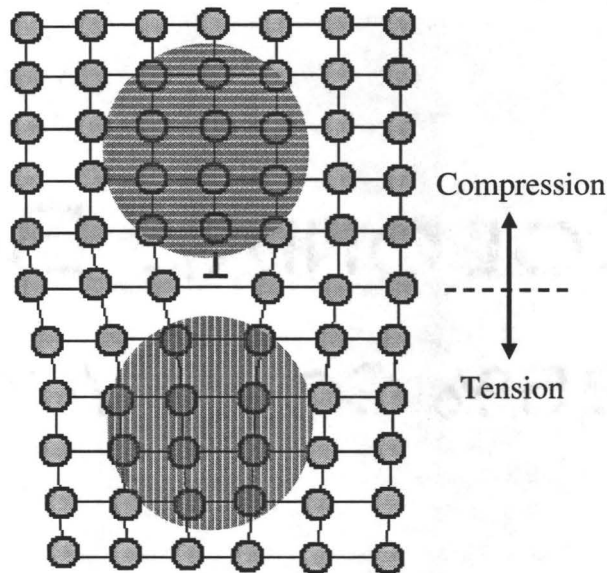


Figure 2-21: Regions of compression (top) and tension (below) located around an edge dislocation [Callister, 1997]

The strain extends to the surrounding atoms and its magnitude decreases with radial distance from the dislocation. Thus, the strain field interactions may take place with surrounding isolated dislocations in close proximity. The possible outcome of this interaction may be either repulsion or annihilation of dislocations depending on the relative position of compressive or tensile field stress as shown in Figure 2-22. These strain fields and associated forces are important for the strengthening mechanisms of metals. During plastic deformation, the number of dislocations increases dramatically from multiplication of existing dislocations, grain boundaries and stress concentration defects.

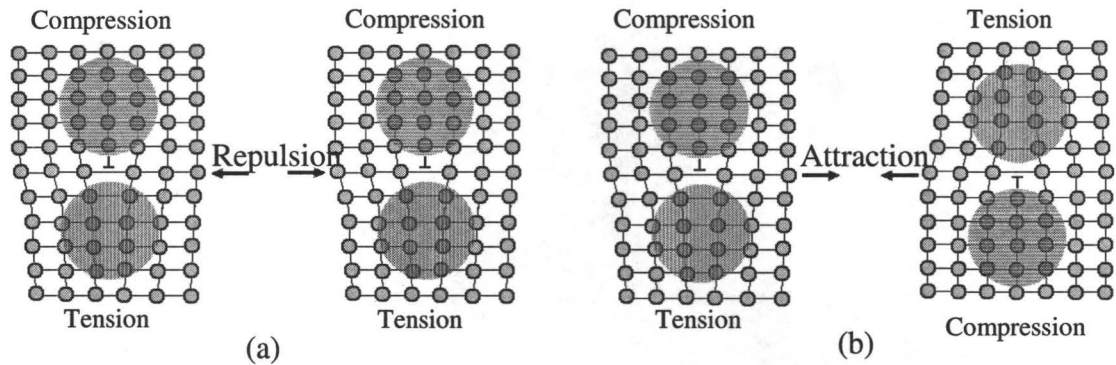


Figure 2-22: Dislocation-dislocation interaction. (a) two edge dislocations of same sign lying on the same plane exert a repulsive force. (b) edge dislocations of opposite sign lying on the same plane exerts and attractive force on each other and annihilate each other and leave a region of perfect crystal [Callister, 1997]

2.5.1. Strain Hardening

Strain hardening is the phenomenon whereby a ductile material becomes harder and stronger as it is plastically deformed below its re-crystallization temperature. Sometimes it is also called work hardening or cold working/cold rolling. In general, “restricting or hindering dislocation motion renders a material harder and stronger” [Callister, 1997]. Since strain hardening increases the hardness and strength of metals, the phenomenon can be explained from dislocation-dislocation strain field interactions as discussed in Figure 2-21 and Figure 2-22. According to Callister [1997], the dislocation density in metals increases with cold working by dislocation multiplication or formation of new dislocations. Thus the average distance between dislocations decreases. On the average, dislocation-dislocation strain interactions are repulsive thus the presence of other dislocations hinders the motion of a dislocation. With the increase in dislocation

density achieved by cold working, the resistance to dislocation motion by other dislocations becomes more pronounced and the imposed stress necessary to deform metal increases. Thus a metal becomes more prone to fracture than plastically deform by losing ductility. Strain hardening effects can be removed through an annealing heat treatment. Figure 2-23 shows the influence of cold work on the stress-strain behavior of any metal alloy and the changes in ductility and tensile strength with strain hardening operation.

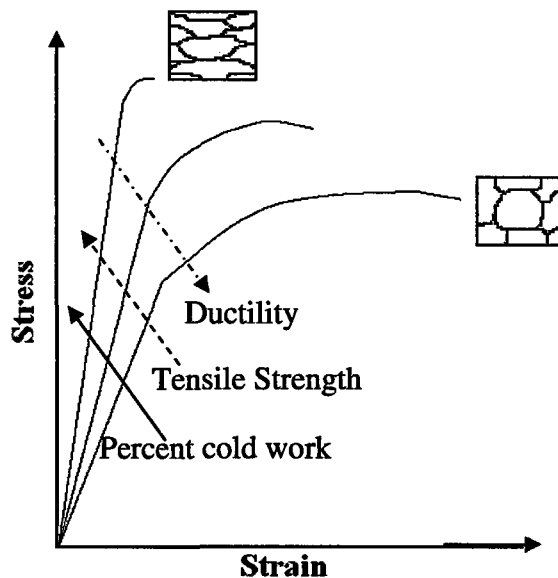


Figure 2-23: Effect of strain hardening on mechanical properties showing an influence of cold work on stress-strain behavior and schematic representation of the influence of cold working on the tensile strength and ductility an alloy. [After Callister, 1997].

The annealed or furnace cooled alloy shows more ductility and less tensile strength and the cold worked sample shows the opposite of this phenomenon. Approximate grain pattern is also shown in Figure 2-23 for cold worked and non-cold worked alloy. However, deformation and slip in polycrystalline materials is not that straight forward because of the random crystallographic orientations of numerous grains

and the variation in the slip direction from one grain to another. Instead, gross plastic deformation of a polycrystalline material corresponds to the comparable distortion of individual grains by means of slip.

During deformation, grain boundaries do not come apart and mechanical coherency and integrity are maintained. As a result, each individual grain is constrained to some degree and the manner in which grains distort is then a result of gross plastic deformation. Before deformation the grains are equiaxed and the grains become elongated in the direction the specimen was extended as shown in Figure 2-23. Polycrystalline metals are stronger than their single-crystal equivalents because of geometrical constraints that are imposed on the grains during deformation *i.e.* grain boundaries. Even though a single grain may be favorably oriented with the applied stress for slip, it cannot deform until the adjacent and less favorably oriented grains are capable of slip and requires higher applied stress levels. This is where the anisotropic behavior of material is observed in single point diamond turning as reported by To et al., [1997]. In addition to slip, deformation of some material also occurs by mechanical twinning especially on BCC and HCP crystal structures at low temperature and for shock loading conditions under which the slip process is restricted.

2.5.2. Grain boundary

Based on the above discussion it is understandable that the size of the grain diameter in polycrystalline metals influence the mechanical properties. Adjacent grains normally have different crystallographic orientations; however, a common grain boundary as shown in Figure 2-24.

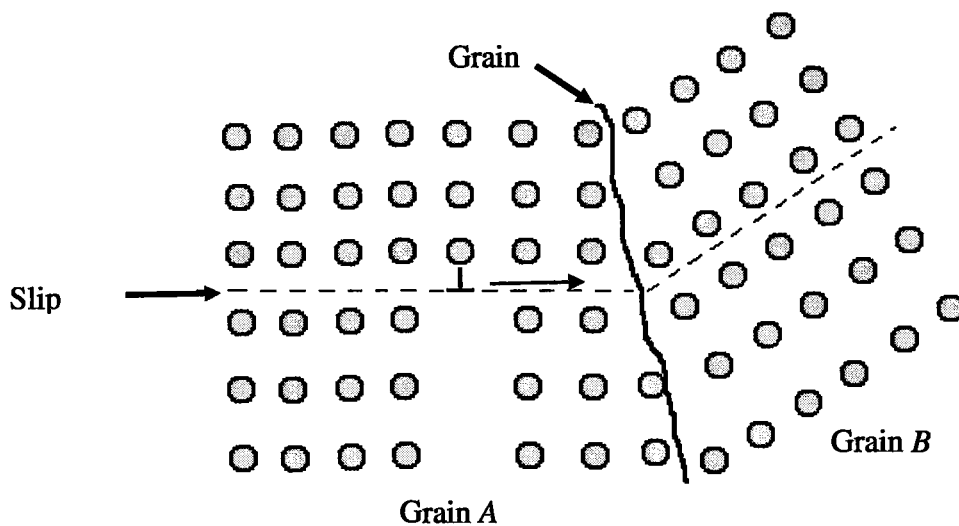


Figure 2-24: Effect of grain boundary: The motion of a dislocation as it encounters a barrier at grain boundary resulting in a discontinuous slip plane [After Callister, 1997].

During plastic deformation, slip or dislocation motion must take place across this grain boundary which acts as a barrier to dislocation motion for two reasons:

- a. A dislocation passing into grain B has to change direction to address the different orientation of grains.

- b.* Atomic disorder within a grain boundary results in discontinuity in the slip plane.

During plastic deformation, it may not be the case that dislocations traverse grain boundaries during deformation; rather, a stress concentration ahead of a slip plane in one grain may activate sources of new dislocations in an adjacent grain. This may explain the observation of Furukawa and Moronuki [1988] where they observed an increase in cutting force at a grain boundary (approximately 2 times) compared to the grains (Section 2.3.1). While machining Al-Mg alloy with a flat end diamond tool Nishiguchi et al., [1988] observed severe tearing on the machined surface at certain orientations and concluded that those tears were generated mostly at the grain boundaries.

A fine-grained material is harder, stronger and tougher than coarse grained material since the former has a greater total grain boundary area to hinder dislocation motion. Grain size may be regulated by the rate of solidification and also by plastic deformation. The effect of plastic deformation has been discussed previously in section 2.5.1. Recently few techniques have been developed in producing nanostructured metals with nanometric grain size and will be discussed in section 2.5.3.

2.5.3. Bulk Nanostructuring of metals

The concept of developing nanocrystalline materials was proposed in early 80's by Herbert Gleiter who proposed that nanomaterials will give high strength, toughness, prolong fatigue life and increase wear resistance. Earlier studies focused on fabricating nanostructure materials by inert gas condensation (ultrafine grains with a size down to 10 nm) with dimensional constraint of only up to 10 mm in diameter and up to 1 mm in thickness. The presence of porosities resulted in very low ductility [Valiev, 2004]. Realizing the potential of nanostructure metals and drawbacks of previous methods, new techniques for grain refinement of bulk materials were adopted by Valiev [2004; 2000] and Valiev and Alexandrov [1999] using severe plastic deformation (SPD) processes. The work reported two techniques to achieve SPD: 1. High-pressure torsion (HPT) and 2. Equal Channel Angular (ECA) pressing. HPT is a torsional straining process conducted under high pressure where a sample with diameter ranging from 10 to 20 mm and thickness of 0.2-0.5mm is put between anvils and compressed under applied pressure of several GPa while one anvils turns slowly as shown in Figure 2-25 (a).

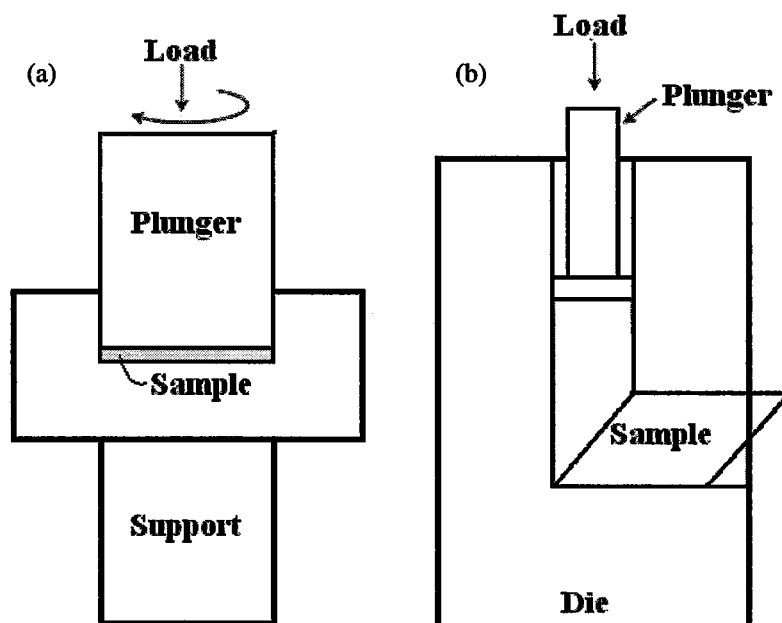


Figure 2-25: Principles of severe plastic deformation (SPD) techniques. (a) High-pressure torsion (HPT). (b) Equal channel angular (ECA) pressing [Valiev, 2004]

In ECA pressing, the ingot is pressed in a special die through two channels with equal cross-section intersecting at an angle such that each pass imparts a supplementary strain as shown in Figure 2-25 (b). Titanium billets up to 60mm diameter and 200mm long have been successfully processed. It has also been reported that strength and ductility can be improved in a bulk nanostructured material as shown in Figure 2-26 for coarse grain copper with varying percentage of cold rolling and nanostructured copper [Valiev, 2004]. A detailed report on these two methods can be found in an article by Valiev et al., [2000].

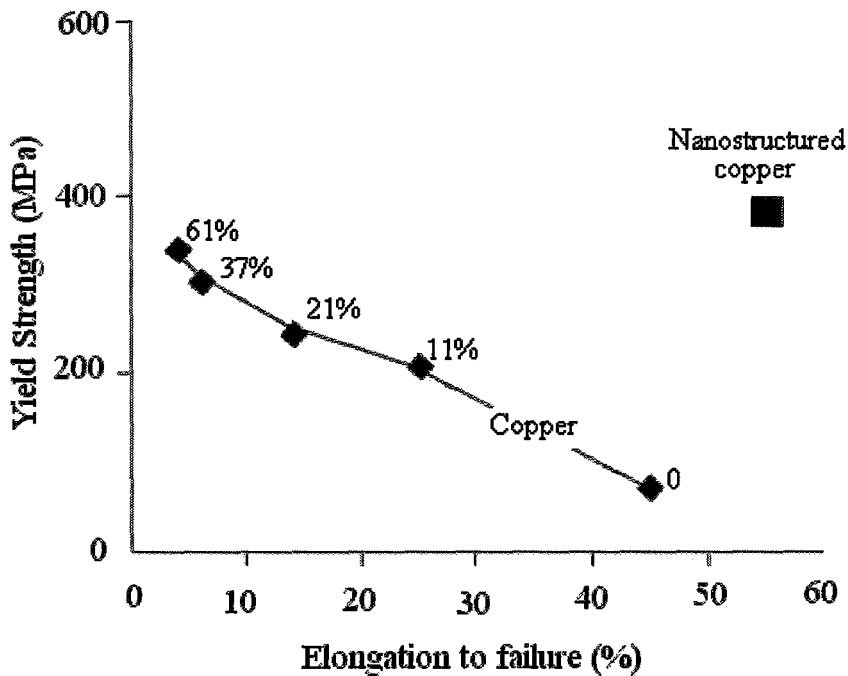


Figure 2-26: Strength and ductility of the nanostructured metals compared with coarse grained cold rolled metals (% indicate amount of rolling) [After Valiev, 2004]

However, despite the interesting properties, nanostructured materials have found limited application as a result of high cost of preparation and small dimension of the final product [Su, 2003]. Su et al., in 2003 has reported that the friction stir process (FSP) can be adopted to produce bulk nanostructured ultrafine grains. Authors have reported grain size as small as ~100nm, 180nm, 300nm and 500nm produced from 7075 aluminum using FSP technique [Su, 2003; Su et al., 2006]. The friction stir process (FSP) has been developed by adopting friction stir welding (FSW) [Mishra et al., 2000]. FSP is a thermo-mechanical process where a cylindrical rotating tool with a pin and shoulder is plugged in

the material to be processed, and traverses along the line of interest as shown in Figure 2-27.

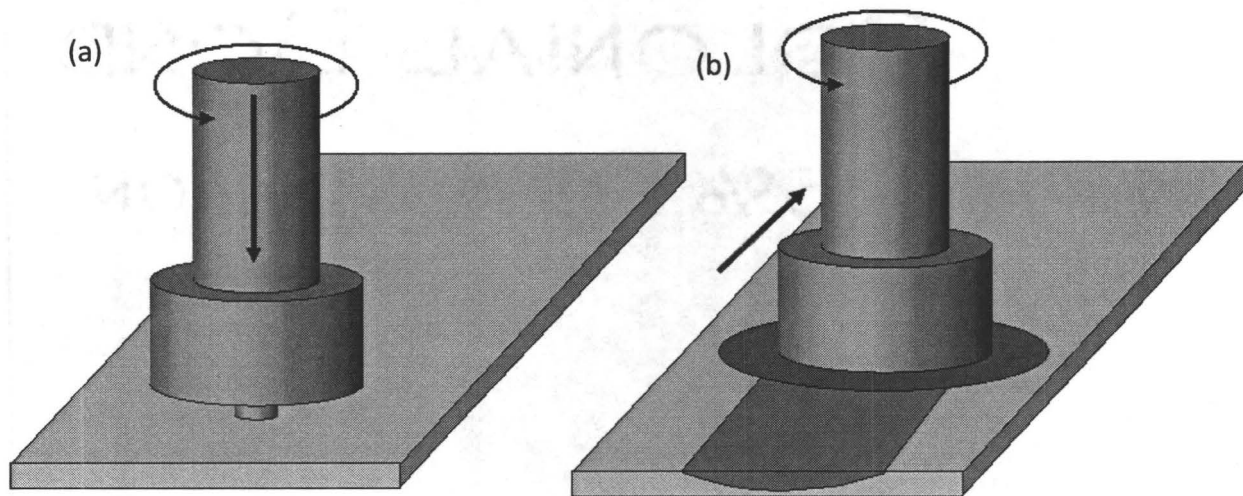


Figure 2-27: Schematic illustration of friction stir processing (FSP) [After Su et al., 2006]

Su et al., [2006] studied the effect of cooling rate on the grain structure of aluminum alloys for a single pass and concluded that a nanocrystalline structure was formed in the sample corresponding to the highest cooling rate. Slower cooling rates result in large grains with recovery structures. Unfortunately, quantitative measurement of strain, strain rate and temperature generation is difficult and has not been reported during FSP. However, according to Rajeswari [2004], FSP parameters also play a vital role in defining grain size and according to this body of work a lower rotational speed and a higher traveling speed reduces the grain size. Other notable contributions on

friction stir welding can be found in work done by Sutton et al., [2002] and Hirata et al., 2007. The conclusion was that the formability of FSW aluminum alloys was improved through the refinement of grain size.

2.5.3.1 Subgrain formation

The formation of subgrains in the course of plastic deformation is in fact, the buildup of dislocations during deformation. At a high rate of work hardening, secondary slip becomes active where dislocations lie on different mutually intersecting slip planes. An appropriate choice of different primary slip systems in a neighboring region is done by virtue of compatibility. These neighboring regions self-organize and undergo different lattice rotations thus constituting subgrains. The volume fraction of ideal subgrain boundaries is nearly negligible as a subgrain boundary has a width on the order of a dislocation spacing in the boundaries. However, it is more difficult for the dislocations to squeeze through small subgrains than through large ones with the size-effect in the subgrain hardening thus dominating the process [Sedláček et al., 2002].

2.5.4. *Atkin's model and material separation criterion*

In the 1940's, Ernst and Merchant developed a model for orthogonal cutting where undeformed material was shown to shear after passing through a primary shear zone with a shear angle ϕ to form a chip. Piispanen likened this effect to shearing of a

deck of stacked cards inclined at an angle ϕ [Robinson and Jackson, 2005; Shaw, 2005]. For minimum energy of cutting, Merchant's model can estimate the shear angle according to Equation 2.1. It is evident from Equation 2.1 that shear angle ϕ is not a function of the material property; however, experimental results indicate that the workpiece material plays a vital role in determining shear angle. The argument is further supported in Figure 2-28 where Ernst-Merchant's theory over estimates shear angle irrespective of the material being cut.

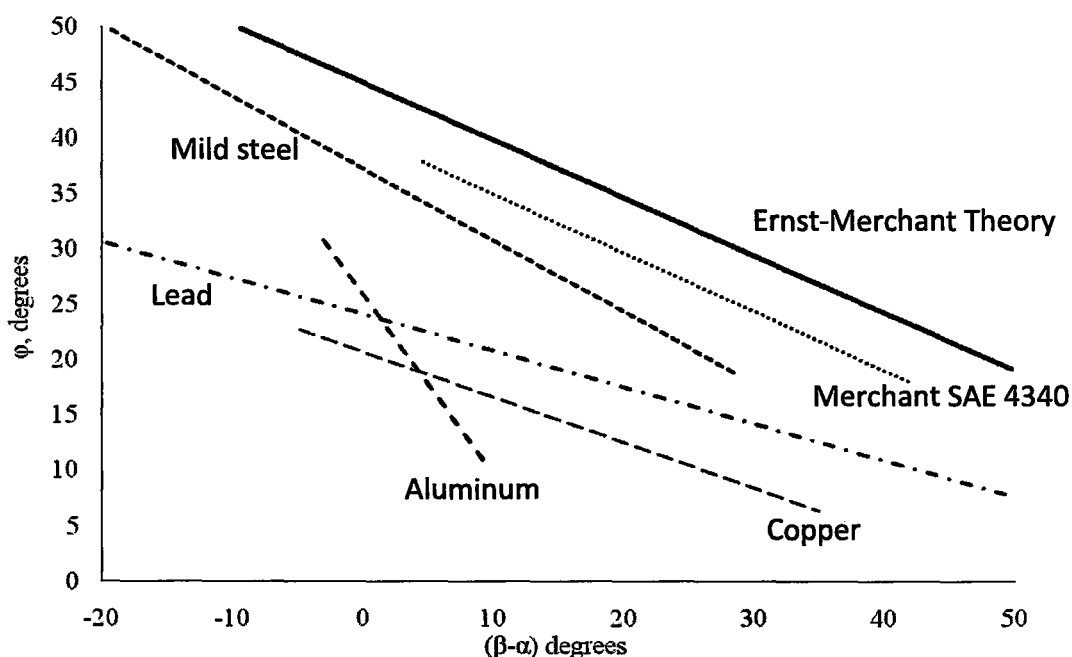


Figure 2-28: Experimental data of primary shear angle for cutting various metals [After Atkins, 2005]

The recent work of Atkins [2003] argued that in the classical model, the work required for material separation during cutting is underestimated. The argument is based

$$F_c V = (\tau_y \gamma)(t_o w V) + [F_c \sec(\beta - \alpha) \sin \beta] \frac{V \sin \phi}{\cos(\phi - \alpha)} + R_w V$$

Or

$$\frac{F_c}{w \tau_y t_o} = \frac{\cos(\beta - \alpha)}{\sin \phi \cos(\phi + \beta - \alpha)} \left[1 + \frac{R \cos(\alpha - \phi) \sin \phi}{\tau_y t_o \cos \alpha} \right]$$

Equation 2.5

Where, F_c is the cutting force, w is the width of cut, t_o is the uncut chip thickness, τ_y is the shear yield strength (Hardness) of the material, R is the specific work of surface formation (fracture toughness; J/m^2), β the friction angle, α the rake angle, and V is the cutting speed.

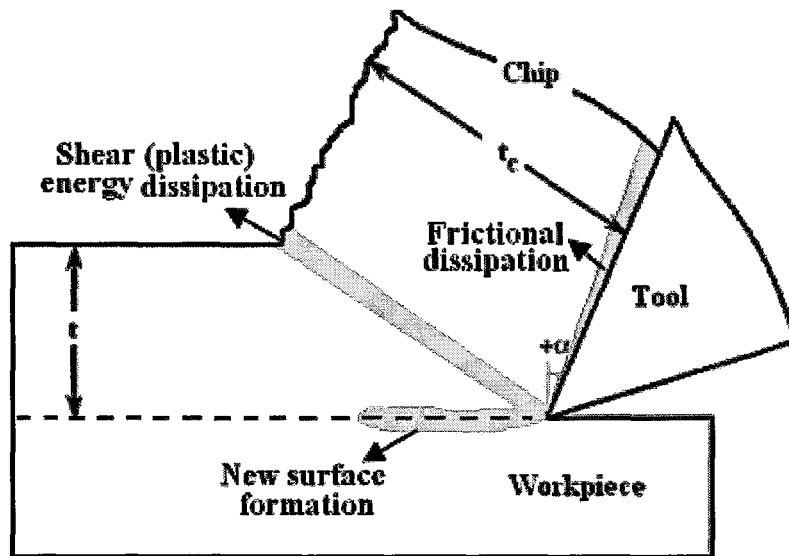


Figure 2-30: Distribution of energy during cutting [After Subbiah and Melkote, 2007]

By differentiating Equation 2.5 for minimum work done, it may be shown that φ for the lowest value of F_c satisfies the following equation:

$$\left[1 - \frac{\sin \beta \sin \varphi}{\cos(\beta - \alpha) \cos(\varphi - \alpha)} \right] \left[\frac{1}{\cos^2(\varphi - \alpha)} - \frac{1}{\sin^2 \varphi} \right] =$$

$$- [\cot \varphi + \tan(\varphi - \alpha) + Z] \left[\frac{\sin \beta}{\cos(\beta - \alpha)} \left\{ \frac{\cos \varphi}{\cos(\varphi - \alpha)} + \frac{\sin \varphi \sin(\varphi - \alpha)}{\cos^2(\varphi - \alpha)} \right\} \right]$$

Equation 2.6

Equation 2.6 is solved numerically in [Atkins, 2003] where $Z = R/\tau_y t_o$ is the dimensionless parameter which makes the shear angle φ material dependent. The parameter R representing the specific work of surface formation defines the material separation criterion. For example, it is expected that mechanical treatment of metals through cold working would increase the hardness (or τ_y) and would have lower R values than annealed metal. The new model predicts this behavior and shows from previously reported data that for pure copper the value of R/τ_y is 1.8×10^{-3} and 3×10^{-4} for annealed and prestrained metal respectively ($Z_{\text{annealed}}=8.9$ and $Z_{\text{prestrained}}= 1.5$). However, no work has been reported on ultra precision diamond turning of aluminum to verify the model and all the results are based on conventional machining.

2.6. TOOL GEOMETRY

A significant portion of the work on diamond turning operations is limited to round nose tools and a detailed literature on this topic has been completed in Section 2.4. However, according to the author's knowledge, only two literature sources have been found reporting surface generation with a flat end secondary edge diamond tool [Nishiguchi et al., 1988; Masuda et al., 1989]. The authors used a sharp corner diamond tool to observe the tool orientation effect with respect to workpiece material and tool wear while machining Al-Mg alloy at $50\mu\text{m}/\text{rev}$ feed rate and $10\mu\text{m}$ depth of cut. Authors [Nishiguchi et al., 1988; Masuda et al., 1989] have concluded that tearing and burr formation are the main reason for deterioration of the surface roughness. The minimum peak to valley surface roughness reported is 20nm and tear marks are reported to be reduced with a corresponding improvement in surface roughness because of the effect of growth of cutting edge recession with increasing cutting length. The geometry of the cutting tool and generated surface roughness for different tool setting angles is shown in Figure 2-31. However, the effect of primary edge roundness and parallel setup has not been studied, which theoretically should produce a surface with minimum surface roughness.

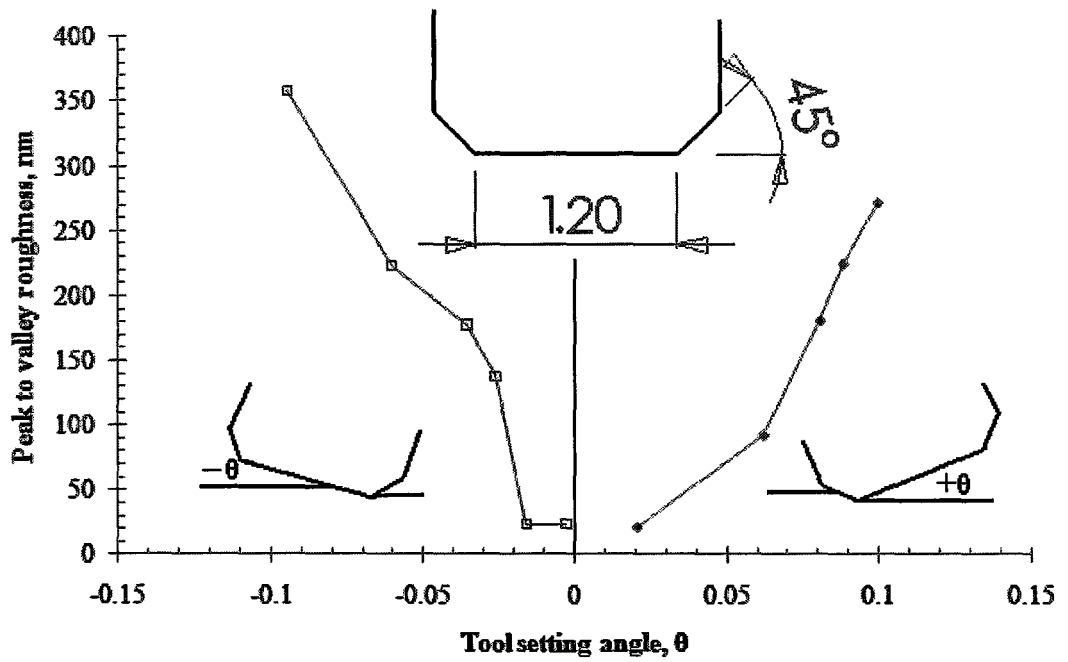


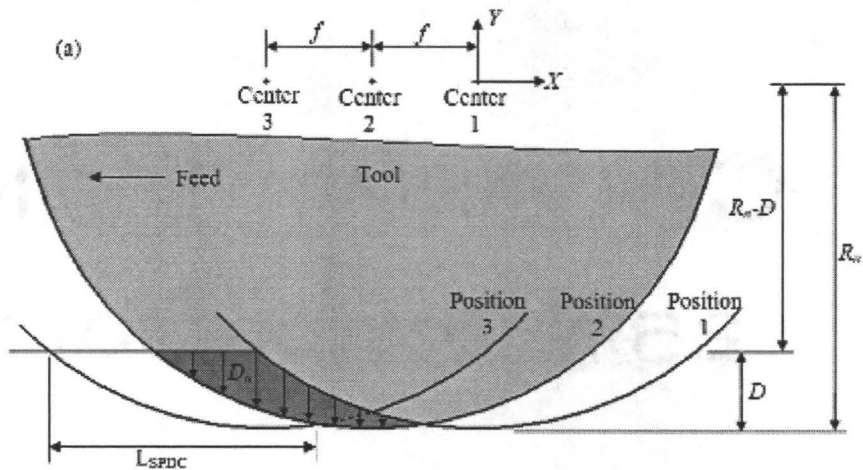
Figure 2-31: Diamond turning of Al-Mg alloy with flat end tool. (a) Tool geometry. (b) Surface roughness [After Nishiguchi et al., 1988 and Masuda et al., 1989]

CHAPTER 3 GEOMETRICAL

ANALYSIS OF SPDT

Figure 2-11 provides a schematic diagram of an SPDT process showing the rake face of the tool having a nose radius (R_n), feed rate (f) and depth of cut for a turning operation. Figure 2-12 shows the change in cutting behavior along the cutting edge due to the relative scaling of the edge and the effective depth of cut. According to the literature, there are at least five scale lengths to describe plasticity: 1) atomistic, 2) discrete dislocations, 3) sub-grain dislocation substructures, 4) grain or 5) crystal and macro-scale. Figure 2-4 and Figure 2-12 give an approximation on how these scale transitions take place along the tool-workpiece contact length and are briefly described in Section 2.3.1. This understanding of the change in relative scale of cutting edge and material is very important for this study. With the reduction in effective depth of cut not only does the tool behave as a rounded edge but the material properties change with location. Thus it is very important to have a quantitative understanding of the process based on tool geometry and cutting parameters such as nominal depth of cut, tool nose radius and feed rate. This analysis is primarily completed to highlight that the nominal axial depth of cut is misleading to understand the actual cutting process in the oblique SPDT process. Rather, effective depth of cut (D_e) is found to be the more effective approach to define uncut chip thickness which will again vary along the tool-workpiece contact length

(L_{SPDC}). Nose radius and feed rate have the greatest influence on effective depth of cut. With a larger nose radius tool and low feed rate, severe chip thinning may occur and may result in aggressive size effects. This will be discussed in this chapter. The effective depth of cut approaches zero at the tip of the tool. Figure 3-1 shows three successive positions of the tool with a nose radius of R_n and feed (f) in a Cartesian 2D coordinate system.



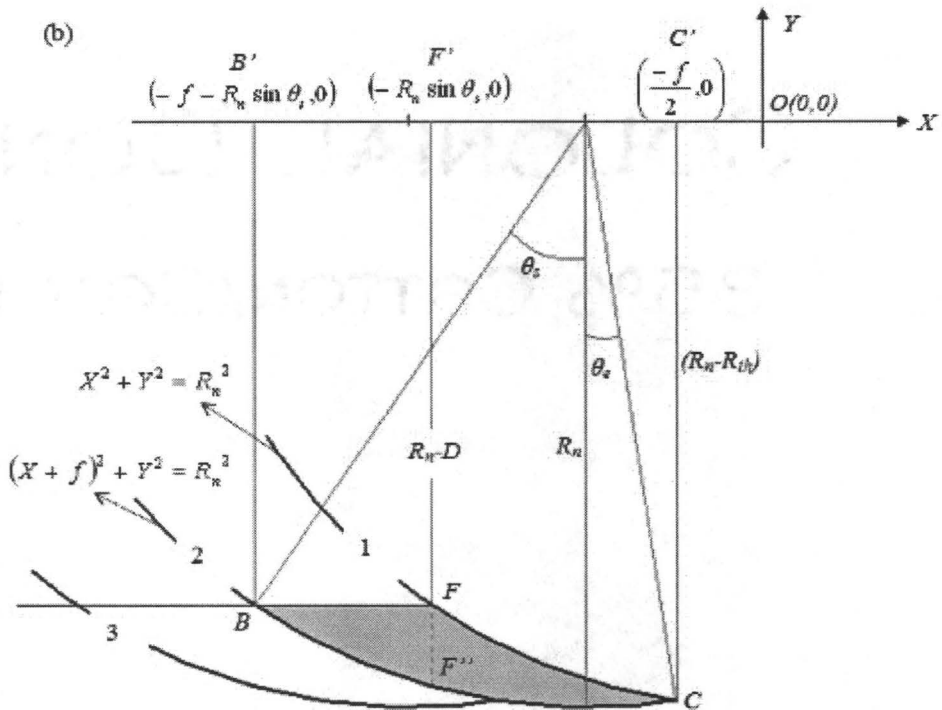


Figure 3-1: SPDT analysis

From Figure 3-1, the allowable step size (f) and tool - workpiece contact length for Single Point Diamond Cutting, SPDC (L_{SPDC}) can be estimated as shown in Equation 3.1 and Equation 3.2 respectively. If the value of feed rate is greater than the value of Equation 3.1, a surface as shown in Figure 3-2 (a) will form. If the values are equal, then a surface like that shown in Figure 3-2 (b) will form. It is very unlikely to form a surface as shown in Figure 3.2 (a) and (b) in SPDT. For example for a 1.5mm nose radius tool and 0.5mm nose radius tool with $2\mu\text{m}$ depth of cut; Equation 3.1 estimates the limiting feed rate of these 2 cases, to avoid exposing any pre-machined surface, as $155\mu\text{m}$ and $89\mu\text{m}$ per revolution respectively.

$$f = 2R_n \sin \theta_s = 2R_n \sin \left\{ \cos^{-1} \left(1 - \frac{D}{R_n} \right) \right\}$$

Equation 3.1

$$L_{SPDC} = (\theta_s + \theta_e)^c \times R_n = \left[\cos^{-1} \left(1 - \frac{D}{R_n} \right) + \sin^{-1} \left(\frac{f}{2R_n} \right) \right]^c \times R_n$$

Equation 3.2

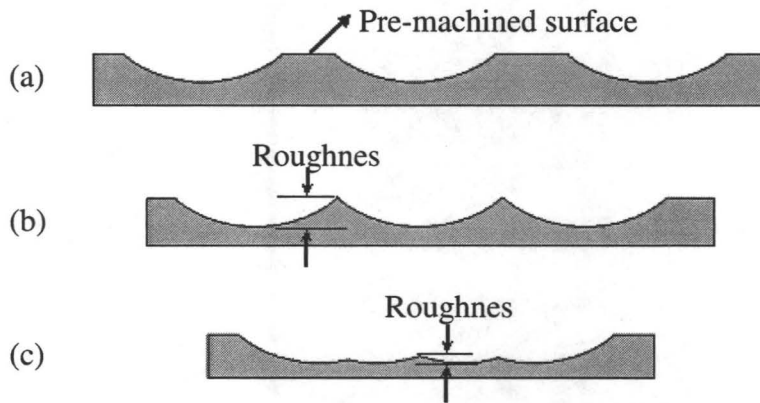


Figure 3-2: Limiting feed rate

This analysis may become significant when the nose radius is very small. The analysis, as can be seen from Equation 3.2, can estimate the tool workpiece contact length simply by knowing the tool geometry and cutting parameters. However, it is clear from Figure 3-1 that the nominal depth of cut D is not constant and the depth is varying along the cutting edge. In this study, an effective depth of cut (D_e) is assumed in the axial depth of cut direction. It can be seen from Figure 3-1 that the effective depth of cut is

“zero” at point C, then linearly increases, reaching a maximum of FF'' and then decreases linearly again to “zero” at point B. This is illustrated in Figure 3-3.

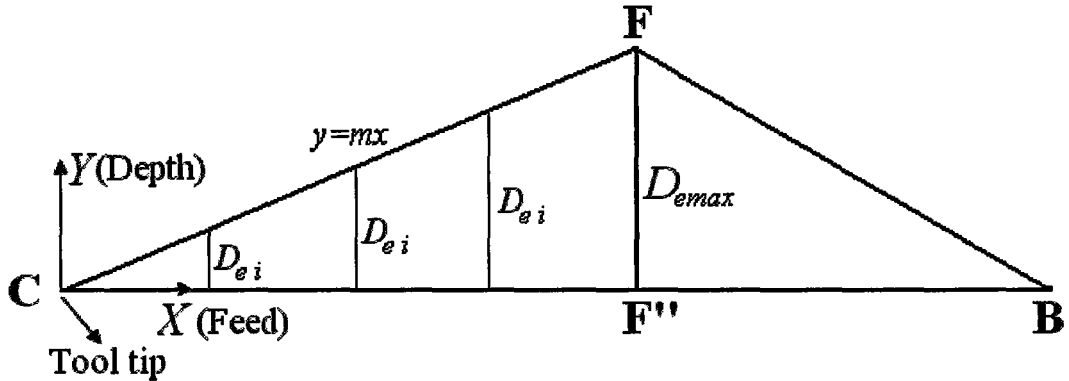


Figure 3-3: Simplified chip cross-section

According to Figure 3-1, coordinate of F (x,y) is $F(-R_n \sin \theta_s, R_n - D)$. Coordinate of $F''(X,Y)$ can be determined for X and Y by solving the following system of intersecting equations.

$$X = -R_n \sin \theta_s$$

$$(X + f)^2 + Y^2 = R_n^2$$

Equation 3.3

Once the coordinate of $F''(X,Y)$ is known, D_{emax} can be calculated to determine the positive slope, m (X from C to F''). Slope and effective depth information is redundant in $F''B$ section as this is a part of the chip. Using the positive slope m , effective depth of cut (D_{ei}) at any point in the feed direction (X) can be known by multiplying feed and slope, m i.e. $y = mx$. Table 3.1 and Table 3.2 shows the maximum effective depth of cut

(D_{max}), tool-workpiece contact length (L_{spdt}), total chip area and effective depth of cut at feed *i.e.* up to the point of surface generation for $2\mu\text{m}$ of nominal depth of cut (D). Figure 3-4 clearly shows the difference in effective depth of cut for 1.5mm and 0.5mm nose radius tool at different feed rate for nominal depth of cut, $D=2\mu\text{m}$.

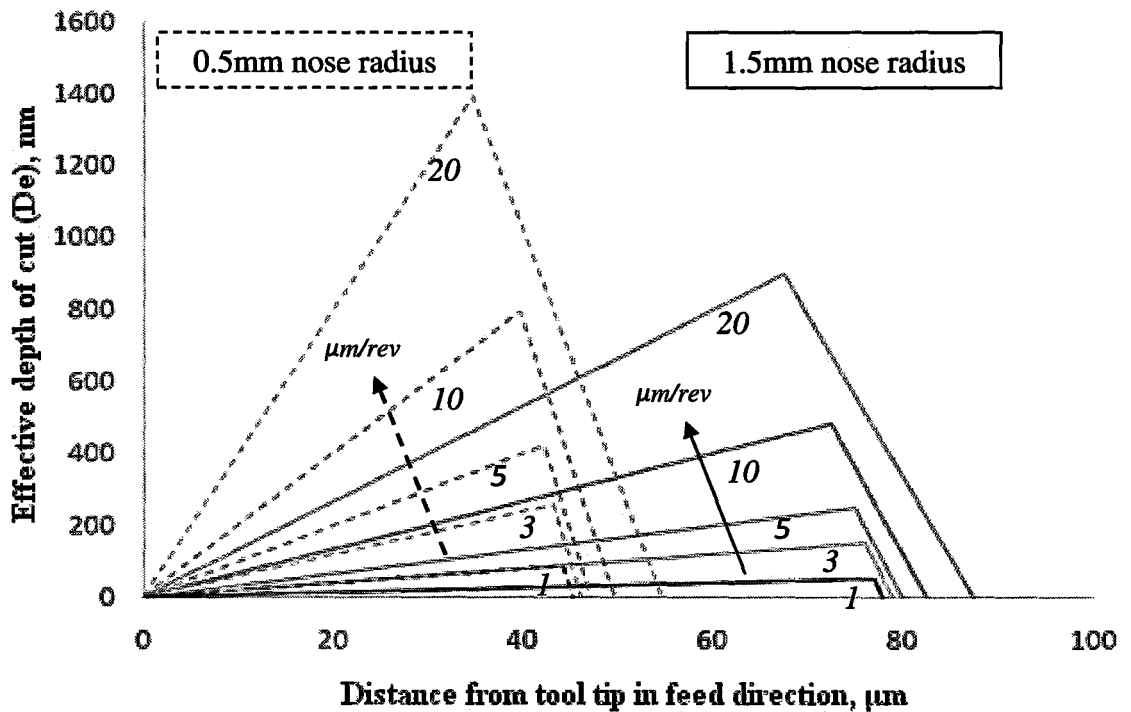


Figure 3-4: Effective depth of cut as a function of tool nose radius and feed rate.

Table 3.1: Geometric quantitative values for oblique cutting: 1.5mm nose radius tool

1.5mm tool					
Feed $\mu\text{m}/\text{rev}$	D_{emax} nm	Slope $m=\tan\theta$	L_{spdt} μm	Total chip area μm^2	D_e at feed nm
20	900.0479	0.0133	87.46835	39.36285	266
10	483.459	0.0067	82.46829	19.93502	67
5	250.0921	0.0033	79.96828	9.999717	16.5
3	152.0627	0.002	78.96828	6.004066	6
1	51.35683	0.0007	77.96828	2.002102	0.7
0.8	41.139	0.0005	77.86828	1.601712	0.4
0.6	30.89441	0.0004	77.76828	1.201303	0.24
0.4	20.62305	0.0003	77.66828	0.800878	0.12
0.2	10.32491	0.0001	77.56828	0.400443	0.02

Table 3.2: Geometric quantitative values for oblique cutting: 0.5mm nose radius tool

0.5mm tool					
Feed $\mu\text{m}/\text{rev}$	D_{emax} nm	Slope $m=\tan\theta$	L_{spdt} μm	Total chip area μm^2	D_e at feed nm
20	1390.693	0.0401	54.73695	38.06115	802
10	796.0829	0.0201	49.73636	19.79713	201
5	423.2801	0.01	47.23629	9.997091	50
3	260.0322	0.006	46.23628	6.011461	18
1	88.70016	0.002	45.23628	2.006233	2
0.8	71.12202	0.0016	45.13628	1.605092	1.28
0.6	53.46293	0.0012	45.03628	1.203886	0.72
0.4	35.72291	0.0008	44.93628	0.802627	0.32
0.2	17.90193	0.0004	44.83628	0.401328	0.08

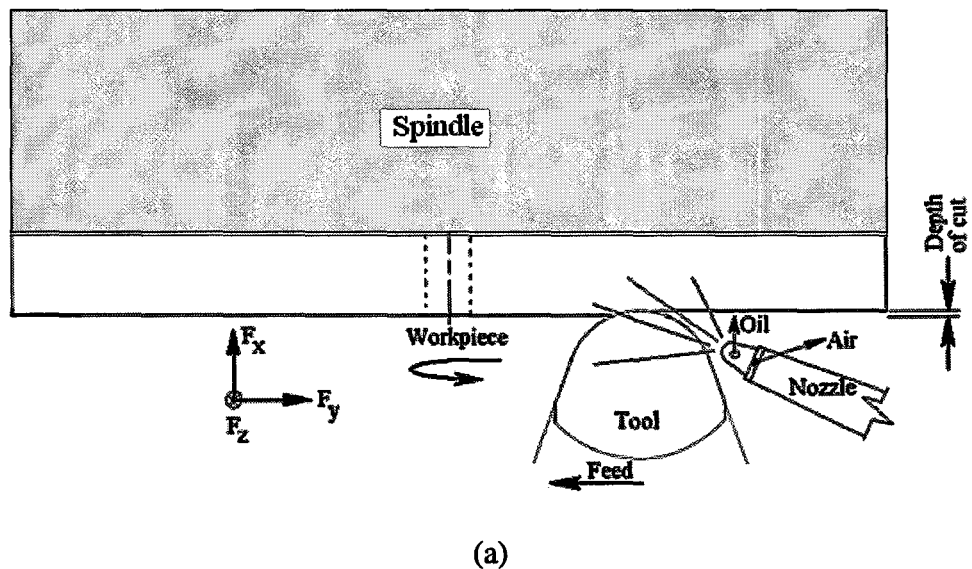
It is clear from the above analysis that uncut chip thickness is inversely related to nose radius of the tool. In this case a higher nose radius results in a smaller uncut chip thickness or effective depth of cut for a fixed feed rate. The data in Table 3.1 and Table

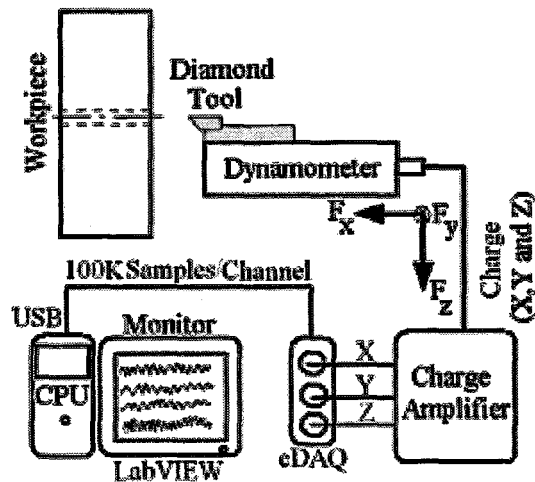
3.2 further supports the concept of size effect in SPDT. Tables 3.1 and 3.2 show that when the cutting parameters are at the micron scale, the real time cutting dimensions can reach the nanometer range and the material may behave in a crystal manner. Thus it is evident that cutting edge radius and material micro structural effects cannot be neglected or avoided. Values of Table 3.1 and Table 3.2 can be further extended by dividing the effective depth of cut and tool cutting edge radius. A ratio of uncut chip thickness and tool edge radius is a direct indication of size effect. A value less than one indicate severe size effect may be observed below this uncut chip thickness for a particular tool with a definite edge radius. This it can be concluded here that a larger nose radius tool have more size effect due to severe chip thinning as shown in Figure 3-4 compared to smaller nose radius tool assuming both the tools have same cutting edge radius. However, the cutting edge radius is difficult to measure and is difficult to repeatably manufacture. Thus, addressing the microstructure of the material to alter the size effect by changing the relative size between the edge radius and grain size may contribute some fundamental understanding to the process and provide a mechanism to improve surface finish. A details drawing of tool geometry are shown in Chapter 4 in Figure 4-5.

CHAPTER 4 EXPERIMENTAL

The experiments of this thesis were conducted on a 5 axis Precitech 700G ultra precision machine tool. Single crystal diamond tools were used to perform the face turning operation. Two of the tools used had a cutting nose radius of 1.50 mm and 0.5mm. The third tool had a specially designed 0.5mm nose radius with a 0.5mm flat secondary edge. Annealed and strain hardened 6061 aluminum, furnace cooled and strain hardened 99.87% aluminum and friction stirred 99.87% aluminum samples were used as workpiece materials. A white light interferometer was used to measure the surface roughness. All the roughness parameters reported were completed at 400X (Field of View: 0.36 X 0.27mm, Camera Resolution: 0.56 μm) with the removal of any planar form with no filtering (Exceptions specified). A minimum of 16 points were measured for roughness in each machining test as an array of four sets of points 90° apart (*i.e.* 0°, 90°, 180° and 270°). Several measurements have also been completed at 45° orientations. Mist coolant (mixture of air and vegetable oil) was used for the lubrication and chip removal from the cutting zone. Cutting parameters were selected carefully to achieve minimum surface roughness. A few fly cutting tests (50m/min cutting speed, 6 μm depth of cut) have also been performed on an as received 6061 aluminum to perform surface metallurgy investigations and to collect subsurface damage information. Chips were collected and observed under an SEM (Scanning Electron Microscopy) followed by EDS

(Energy Dispersive X-ray Spectroscopy) analysis. Micro hardness tests were also completed at 25gf load with 10 seconds of dwell time on a CLIMEX CMT 5.0 micro-indentation tester. Tool wear has been observed after every pass on the rake face with the white light interferometer at 800X magnification and then finally observed under the SEM. Cutting forces have been measured for all the cutting conditions and a schematic of the cutting and data acquisition process is shown in Figure 4-1 where the rotation, feed and depth of cut is programmed in the machine tool.





(b)

Figure 4-1: Diamond turning operation. (a) Schematic of the cutting process and force direction. (b) Schematic of the data acquisition process

4.1. MACHINE TOOL

The Precitech freeform® 700 series machine is a high performance, ultra-precision computer controlled machining center suitable for optical and mechanical component manufacture. The machine utilizes three linear axes (X, Y, Z), in conjunction with optional rotational axes (B, C) as shown in Figure 4-2. Schematic of the motion of the axes and relative position of the force dynamometer is shown in APPENDIX A.

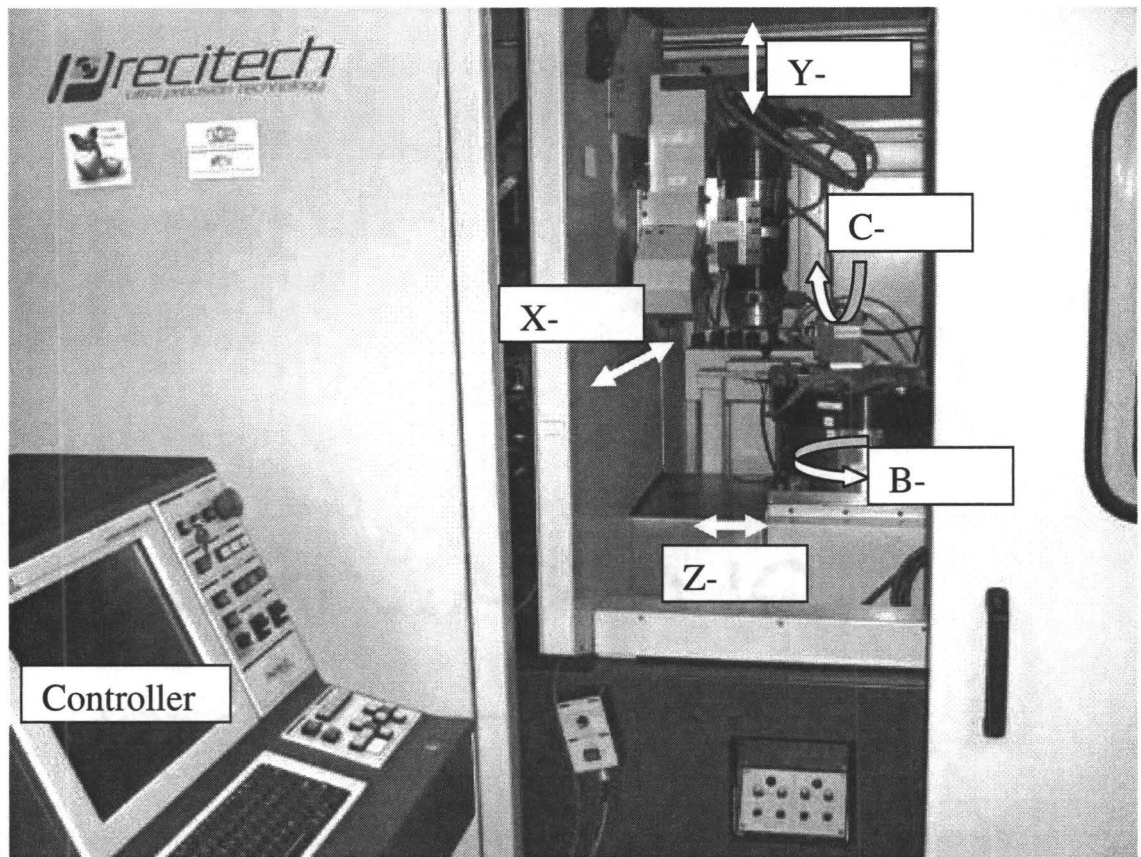


Figure 4-2: Precitech freeform 700G ultra precision machining center

The linear axes are suspended on hydrostatic oil bearing slide ways, fitted with linear glass scale for positioning feedback. The positional feedback is obtained using a laser holographic linear encoder athermally mounted on the slides with 8.6nm resolution (X, Y axes) with 1.4nm resolution (Z axis). Rotary motion for the workpiece is provided through the use of an air bearing spindle (maximum 15000RPM). The maximum spindle speed used in this study is 1000RPM. The machine is controlled through the use of a Precitech Ultrath™ digital signal processor based machine control system. Fully constrained hydrostatic bearings slide in a “T” configuration so that the X, Y and Z axes

can provide a high degree of smoothness, accuracy, repeatability and stiffness. The linear slides are driven with multi-phase linear motors and the home position is sensed by an ultra precision Linear Variable Differential Transformer (LVDT) transducer. A thick epoxy granite bed assures high rigidity and long term stability. The bed is completely isolated from the machine frame by isolation pads. The frame is mounted on four leveling/isolation feet. The straightness of the X, Y and Z slide is within $0.5\ \mu\text{m}$ over a travel distance of 150mm. The temperature controller of the machine is a stand-alone heater/cooler for maintaining the environmental conditions inside the machine enclosure. The system utilizes closed-loop temperature control with a Programmable Logic Controller (PLC) and a Resistance Temperature Detector (RTD) that can hold temperature within 0.1°C [Precitech Manual]. The operating temperature of the machine fixed at 20°C where the room temperature is always maintained at $20\pm 1^\circ\text{C}$. The axes of the machine are stiff enough to keep deflection within the nm range under the sub-newton forces generated during machining. The stiffness values of the different axes are shown in Table 4.1.

Table 4.1: Stiffness of axes [Precitech Manual]

Axis	Direction	Stiffness, N/ μ m
X (Linear)	Vertical / Horizontal	438N/ μ m / 438N/ μ m
Z (Linear)	Vertical / Horizontal	438N/ μ m / 438N/ μ m
Y (Linear)	Z-direction / X-direction	263N/ μ m / 263N/ μ m
B (Rotary, Tool holder)	Axial / Radial	1750N/ μ m / 525N/ μ m
C (Rotary, Work holding air-bearing spindle)	Axial / Radial	228 N/ μ m / 88N/ μ m
Spindle (RPM)	Axial / Radial	70N/ μ m / 26N/ μ m

The maximum load the C-Axis (*i.e.* workpiece mass) can carry is 68Kg (150 lbs.) at the spindle nose and 48 Kg (105 lbs.) 50mm (2") out from the spindle nose [Precitech Manual].

4.1.1. Operating procedure

1. Completion of homing sequence (“RESET” phase motor and then “HOME” axes).
2. Mounting (Dialing) the workpiece on the spindle with the vacuum chuck.
 - a. The workpiece has to be centered to avoid eccentricity of mass while it is rotating. Eccentric loading on the spindle causes imbalance and radial runout compromises the performance of the machine and the safety of the operator and equipment.

- b. Centering the workpiece is completed by setting the vacuum pressure for “LOW” and then tapping the workpiece on the spindle from radial directions to address the amount of runout from the dial gauge by rotating the workpiece 360°. Once completed, the vacuum pressure is set to “HIGH”.
 - c. A runout no more than 2.54 μm is recommended [Precitech Manual].
 - d. Circumference of the circular workpiece has to have a true relationship (90°) with the back face of the workpiece to be considered sufficiently dialed in.
3. The cutting tool was mounted in the tool holder, which was installed on the B-axis. The tool holder is fixed on the dynamometer to measure the cutting force exerted on the cutting tool. The B-axis can be rotated to the angle needed to achieve the desired contact between the cutting tool and workpiece.
4. Once the B-axis is orientated correctly, the X, Y and Z axis are then positioned approximately and the machine is now ready to find the X position where the tool just touches the top surface of the workpiece.
5. Touching the workpiece requires precision as a high feed or depth of cut may break the tool or destroy the workpiece. In this experimental setup we have mounted a video camera in the workspace that is focused on the tool tip and can partially see the workpiece to gauge when it is close to the tool. Rotation of the workpiece is initiated by the controller while the X axis is moved to close the distance between the workpiece and the tool. Once they are close, incremental

feed steps of 2 μm are given with an in feed rate of the X axis not more than 1mm/min. As soon as the tool touches the workpiece, chip formation can be seen by the camera and a spike in the force signature appears. In this way the ordinate of the X axis is known.

6. The center of the workpiece (Y-axis) relative to the tool axis is then determined approximately by positioning the axis and observing the location with the camera.
7. Once the position of the X, Y and B-axes are known; the travel distance of the Z axis (feed) is then determined to have a clean cut of the desired surface (face turning).
8. A *.PGM program is written and saved in the controller hard-drive to load and perform the cutting. B Axis (tool approach angle), Y axis (tool-workpiece center), C-axis (Normal position of the workpiece with respect to tool axis) are kept constant and only the X axis (Depth of cut), RPM and Z axis feed rate is changed to achieve the desired experimental parameters. A typical *.PGM code is shown in APPENDIX B.
9. The coolant nozzle is pointed at the tool tip to remove any chips from the machining operation. Positioning the coolant is of utmost importance as chip clogging may severely damage the cutting performance and generate misleading results. It is believed that coolant primarily does chip removal and improves lubricating effect.

10. The top surface of the workpiece is then marked with a permanent marker. Once the marks are removed by running the machine several times with changing X values; the setup is then ready to perform final machining operations.

4.2. WORKPIECE

Two alloys of aluminum have been selected for this study: 1. Pure (99.87%) aluminum and 2. 6061 aluminum. However, most of the study was conducted on pure aluminum because the alloying elements of 6061 aluminum were found to increase the unpredicted deterioration of the surface and addressing this issue is beyond the scope of the present study. Different mechanical and thermo-mechanical treatments have been applied on the same bulk material to ensure similar chemical composition; however, with a different mechanical property. It is important to keep the same chemical composition to study the effect of variation in microstructure and mechanical properties by thermo-mechanical processes. The chemical composition of the alloys has been shown in Table 4.2 and the general properties of aluminum are shown in Table 4.3.

Table 4.2: Chemical composition of aluminum alloys

Element	Pure aluminum	6061 aluminum [suppliersonline.com]
Aluminum	99.8746%	95.85% (min)
Chromium	2.98ppm	0.04 - 0.35%
Copper	0.01102%	0.15 - 0.4%
Iron	0.0418%	0 - 0.7%
Magnesium	-	0.8 - 1.2%
Manganese	-	0.15% max
Nickel	0.00109%	-
Silicon	0.00756%	0.4 - 0.8%
Strontium (Sr)	0.00294%	-
Tin (Sn)	0.01307%	-
Titanium	0.00493%	0.15% max
Zinc	0.0427%	0.25% max

Table 4.3: Properties of aluminum [Callister, 1997]

Symbol	Al
Atomic Number	13
Atomic weight (amu)	26.98
Density of solid	2.71 g/cm ³
Crystal Structure	Face Centered Cubic (FCC)
Slip System	Slip Plane {111}; Slip Direction $\langle 1\bar{1}0 \rangle$; No. of slip systems= 12
Atomic Radius	0.1431 nm
Ionic Radius	0.053 nm
Most Common Valance	+3
Electron Configuration	1s ² 2s ² 2p ⁶ 3s ² 3p ¹
Melting Point	660.4 °C
Recrystallization temperature	80 °C (99.999 wt%)
Bonding type and energy	Metallic; 324 kJ/mol
Mechanical Properties	E= 69 GPa, G= 25 GPa (also for alloys)
Electrical Conductivity	3.8 X 10 ⁷ [(Ω-m) ⁻¹]
Thermal conductivity	247 W/m-K (Al); 180 W/m-K (6061 Alloy)

Mechanical and thermo-mechanical processes adopted in this study are annealing, strain hardening and a friction stir process. A bulk sample of as received pure furnace cooled aluminum was used. The 6061 aluminum was a regular commercial material. The bulk annealing of the commercial 6061 Aluminum was done by heating it to 415°C and holding it for 2.5 hours followed by controlled cooling at 10°C per hour down to 260°C, then air cooled [suppliersonline.com]. The pieces were then taken out of the furnace, cooled to room temperature and finally strain hardened by a cold rolling technique. The pure aluminum samples were cold rolled with a reduction in thickness of 54% and 82% and for 6061 aluminum a reduction of approximately 30%. Another piece of FC pure aluminum was friction stirred to produce ultra-fine grained nano structured material with multiple passes of a friction stirring process (FSP) resulting in 6 different workpieces with 2 chemical composition of aluminum. The list of the workpieces and their final dimensions is shown in Table 4.4 and a sample photograph of the cold rolling process and FSP of FC 99.87% pure aluminum is shown in Figure 4-3.

Table 4.4: List of workpieces

Aluminum alloys	Thermo-mechanical Process	Outer diameter (mm)
99.87% pure aluminum	Furnace cooled	100.0
	54% cold rolled	100.0
	82% cold rolled	45.00
	Friction stir process (FSP)	50.00
6061 aluminum (commercial)	Annealed	100.0
	30% cold rolled	100.0

The friction stir process (FSP) was completed on a Fadal VMC4020 Five Axis Machining center with a 10HP spindle. Maximum speed and feed rates are 10000RPM and 20m/min respectively. Nominal pin (probe) diameter and height was 3.5mm and 3.00mm respectively. Chilled air (-35°C) was used to cool the tip of the probe as shown in Figure 4-3 (e). Nine different single pass combinations of RPM, feed and depth of cut were tried before reaching an optimal FSP condition for less void formation and ultra-fine grains. The FSP parameters are shown in Table 4.5. The length of one FSP travel was 60mm with the optimal parameters found during earlier testing of 400RPM, 68mm/min and 3.05mm depth and the step between two successive pass was 3.2mm with a total of 16 passes. Thus the total volume of material that was friction stirred was approximately 60mm X 52mm X 3.05mm. Finally a cylindrical piece from this volume was taken out and fixed with a 100mm holder. Grain sizes of Furnace cooled, 54% cold rolled and Friction stirred 99.87% aluminum was found approximately 300 μ m, 10 μ m and less than 0.50 μ m respectively.

Table 4.5: Friction stir process (FSP) parameters

Sample No.	RPM	Feed (mm/min)	Depth (mm)
1	600	60	2.75
2	1000	100	2.9
3	800	100	2.9
4	800	100	3.05
5	600	100	3.05
6	500	85	3.05
7	400	68	3.05
8	500	62.5	3.05
9	500	50	3.05

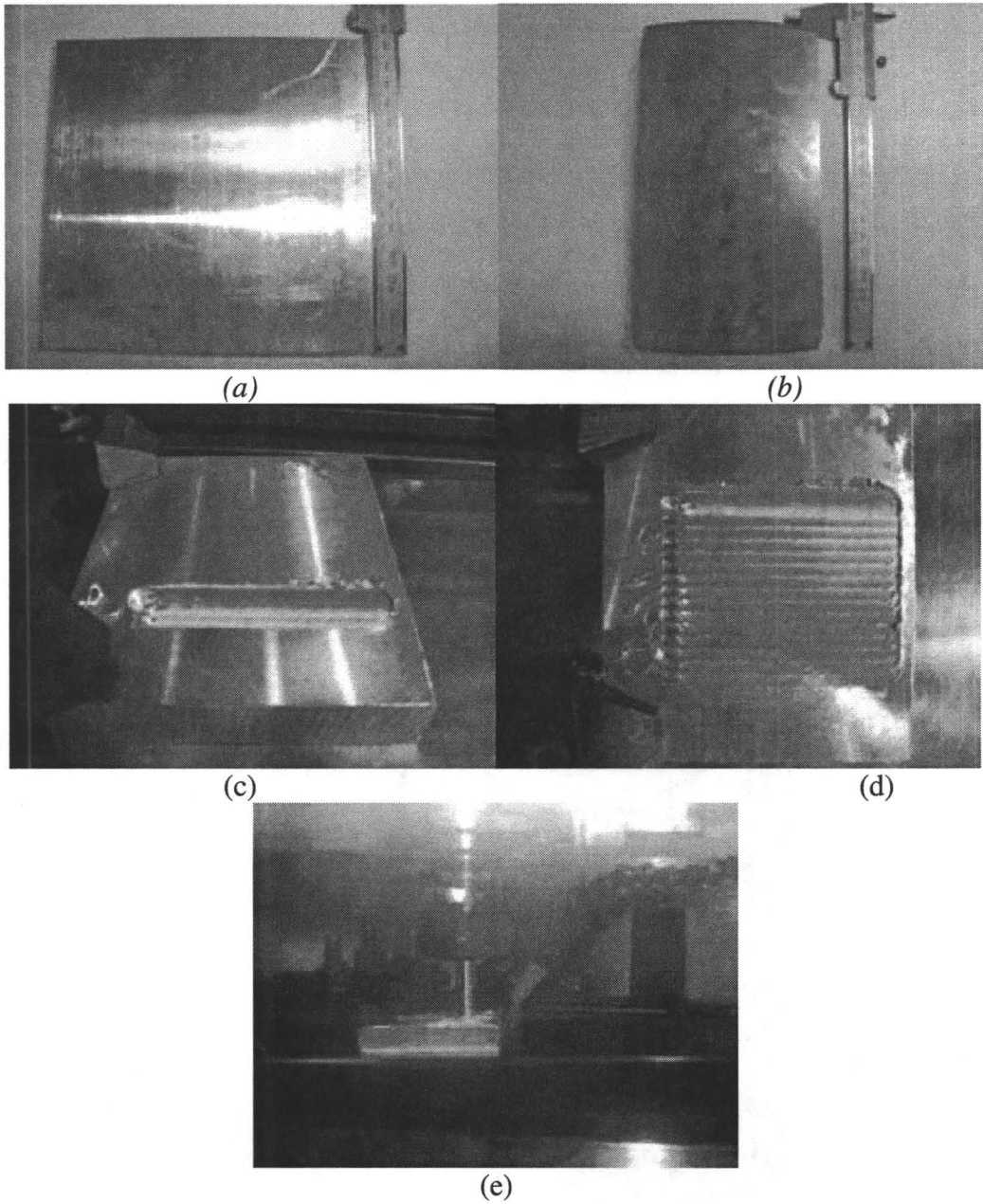


Figure 4-3: Mechanical and thermo-mechanical processes. (a) FC 99.87% aluminum. (b) 54% cold rolled 99.87% aluminum. (c) and (d) FC 99.87% aluminum after 2 passes and 15 pass of FSP with travel length of 60mm. (d) FSP at 400RPM, 68mm/min and 3.05mm depth with chilled air.

4.2.1. Metallography

It was important to characterize the microstructure and micro hardness properties of the different aluminum samples that were prepared for this study. This could be completed by mechanical grinding followed by diamond polishing and chemical etching. These processes were performed on an automatic polisher dedicated to metallographic studies. It was found that following the programmed steps of the polisher exactly does not always reveal the microstructure due to the presence of embedded SiC particles on the metal matrix. However, this problem was solved by adding a few steps manually during the process as indicated by 3a and 4a in Table 4.6. Figure 4-4 (a) shows the embedded SiC particles as black dots; however, the actual matrix is represented by Figure 4-4 (b).

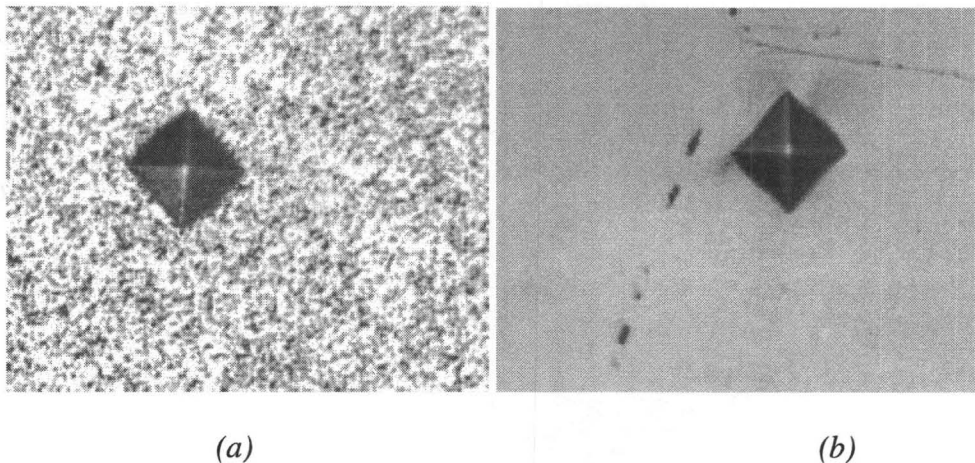


Figure 4-4: Optical images of FC 99.87% aluminum after grinding and polishing. (a) Without steps 3a and 4a of Table 4.6 (b) With steps 3a and 4a of Table 4.6

Table 4.6: Grinding and polishing steps to reveal microstructure

Step#	Surface	Suspension	Lubricant	Time (min)	Force (N)	RP M	Direction
1	800 grade SiC	--	Water	1:30	20	300	>>
2	1200 grade SiC	--	Water	1:30	20	300	>>
3	4000 grade SiC	--	Water	1:30	15	300	>>
3a					10		
4	MD/DP-Dac	3 µm diamond particles	Blue	5:00	20	150	<<
4a				10:00	10		
5	MD/OP-Nap	1 µm Colloidal	Blue	5:00	20	150	<<
6	MD/OP-Chem	Silica+10% H ₂ O ₂	--	5:00	15	150	<<

4.3. DIAMOND TOOL

Diamond is an ideal tool for ultra precision machining because of its hardness, the ability to hone it to produce and hold a sharp edge, chemical inertness with aluminum, high strength and thermal conductivity. The properties of diamond are summarized in Table 4.7.

Table 4.7: Properties of Diamond (Carbon) [Callister, 1997]

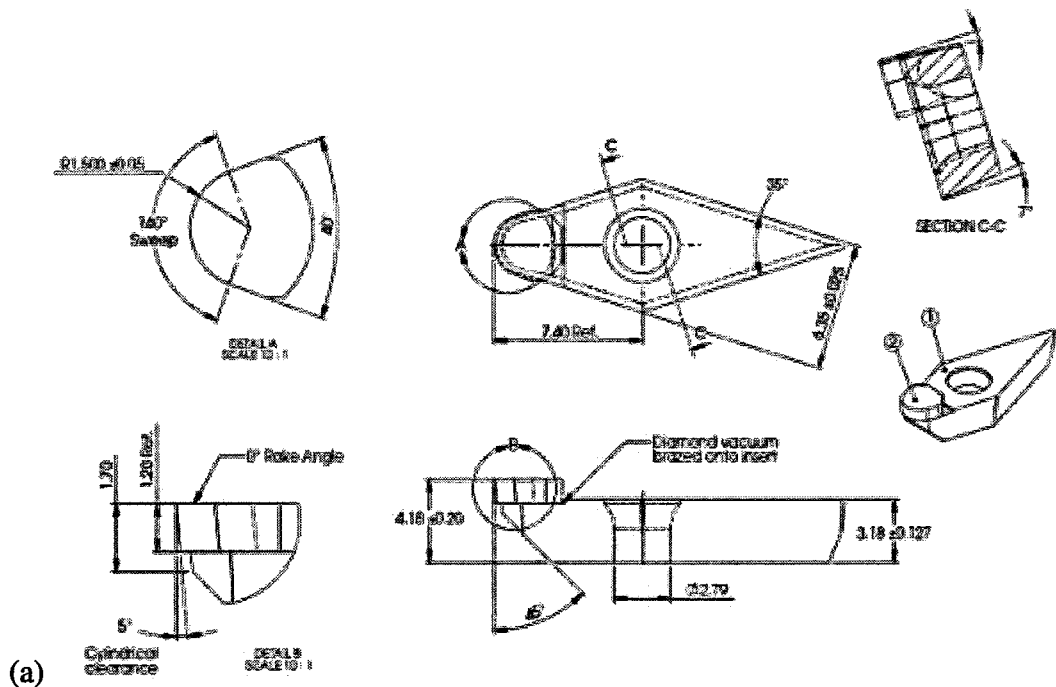
Symbol	C
Atomic Number	6
Atomic weight (amu)	12.011
Hardness	7000 Knoop Hardness (WC=2100 Knoop Hardness)
Density	3.51 g/cm ³
Most Common Valance	+4
Electron Configuration	1s ² 2s ² 2p ²
Melting Point	>3550 °C
Bonding type and energy	Covalent; 713 kJ/mol
Mechanical Properties	E= 1035 GPa
Electrical Conductivity	10 ⁻¹⁴ [(Ω-m) ⁻¹]
Thermal conductivity	2000-2500 W/m-K

Three different geometries of diamond tool have been studied. All the diamond tools have been supplied by K & Y diamond located in Quebec, Canada. The tools used in this study are:

1. 1.50 mm nose radius tool
2. 0.50 mm nose radius tool and
3. 0.5 mm nose radius with 0.5 mm flat secondary edge tool.

The 1.5mm and 0.5mm nose radius tools are commercially available; however the 0.5 mm nose radius tool with a 0.5 mm flat secondary edge tool was specially designed and modified in the MMRI with the consent of the manufacturer. All the tools were manufactured carefully with tight quality control. The tools were certified as chip free by optically viewing them at 800X magnification, which is standard industrial practice. Thus, during experimentation, before re-using diamond tools, they were examined at 800X to

ensure that the tool tips were chip free. The tool was considered to be worn and thus not used if chipping of the cutting edge was observed at 800X magnification. Proper handling of the diamond tool is very important as the diamond cutting edge is honed to such a sharp edge that it is very delicate and can be susceptible to attack from oils on your hands. For optical examination, the tools were first cleaned by air jets, followed by an alcohol cleaning wipe and rubbing with a rubber eraser. For SEM imaging, the tools were cleaned ultrasonically in an alcohol (Methanol /isopropanol) bath. Figure 4-5 shows the schematic drawing of the tools.



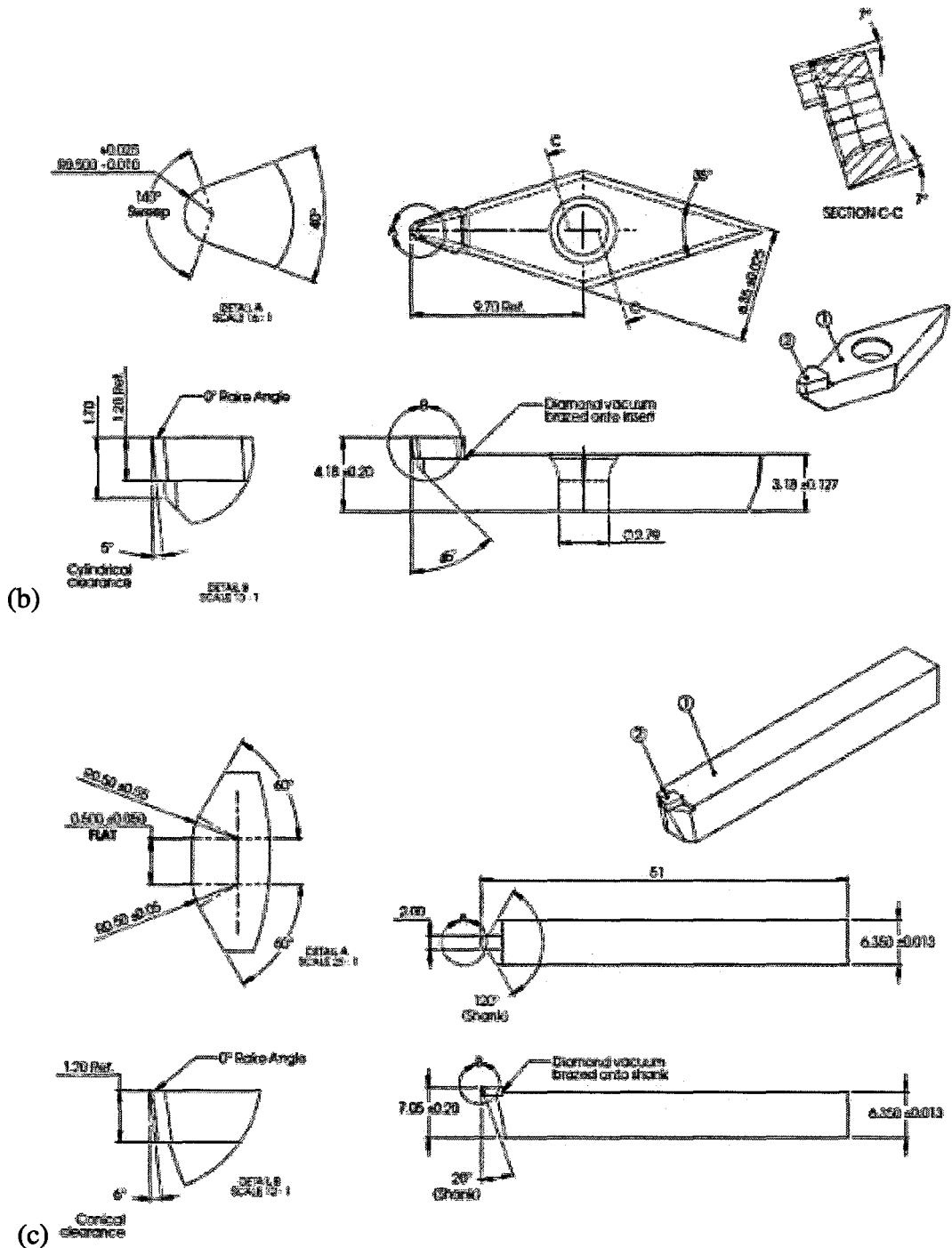


Figure 4-5: Schematic of the cutting tools. (a) 1.5mm nose radius. (b) 0.5mm nose radius and (c) 0.5mm nose radius and flat [K & Y diamond]

4.3.1. Cutting edge radius

Unfortunately tool makers do not provide a value for the cutting edge radius when supplying the tool, standard practice is to inspect the edge with an optical microscope at 800X magnification. Estimating the cutting edge radius must be completed by the end user. Efforts have been made in this study to measure the cutting edge radius using the zygo white light interferometer; however, because of the angle of inclination of the rake face and clearance face of the tool, it is very difficult to focus on the edge of the tool. Thus this thesis adopted the technique of Arefin [2004] by indenting the tool on a polished pure aluminum sample and then measuring the indentation profile at very high magnification (2000X) with lateral resolution of 112nm and vertical resolution of 0.1nm in the zygo white-light interferometer. The measurements are shown in Figure 4-6. The profile data in Figure 4-6 (a) is then extracted from the Zygo metropro software and three different values of X and Y data have been selected around the indentation from the Cartesian co-ordinate system *via* (X_1, Y_1) , (X_2, Y_2) and (X_3, Y_3) . These three values are then inserted into the three sets of equations (Equation 4.1) and the cutting edge radius (R_e) is estimated to be around 200nm~300nm for the K & Y Diamond tools, which is in agreement with reported values. Edge radius was measured once and extensively observed by microscope at 800X every time after re-lapping the tool and after machining every time.

$$\begin{aligned} X_1^2 + Y_1^2 &= R_e^2 \\ X_2^2 + Y_2^2 &= R_e^2 \\ X_3^2 + Y_3^2 &= R_e^2 \end{aligned}$$

Equation 4.1

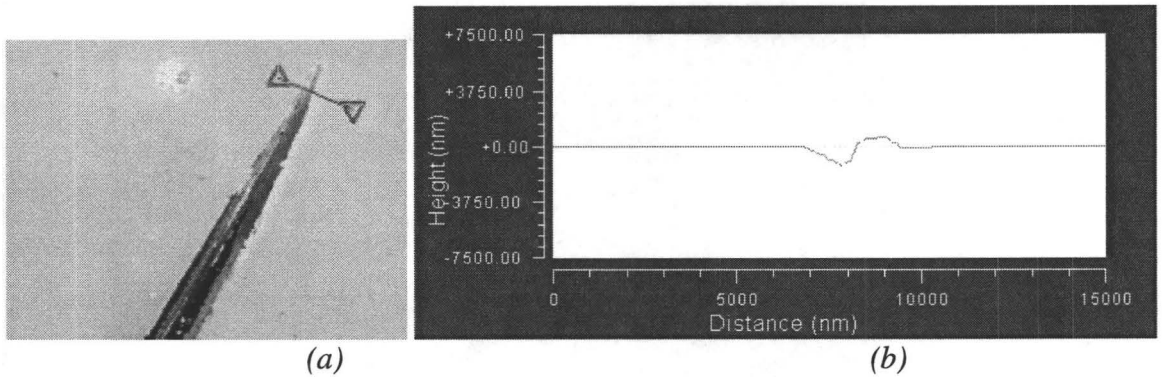


Figure 4-6: Measurement of cutting edge radius on Zygo at camera resolution of 112nm

4.3.2. Flat end tool setup

It is critical that the flat end of the tool is parallel to the machining surface. This parallelism can only be achieved by a rotational tool holder axis (B-axis). The Precitech 700G series machine tool has a rotational B-Axis with a 0.0001° resolution. The flat cutting edge of the tool has a nominal 90° relation with one side of the shank. The shank is dialed along its length with the B-axis rotated to setup the tool face perpendicular to the workpiece. Once dialed, the tool is then slowly fed against the workpiece to have a full impression of the cutting edge. The impression is then measured in the Zygo as shown in Figure 4-7.

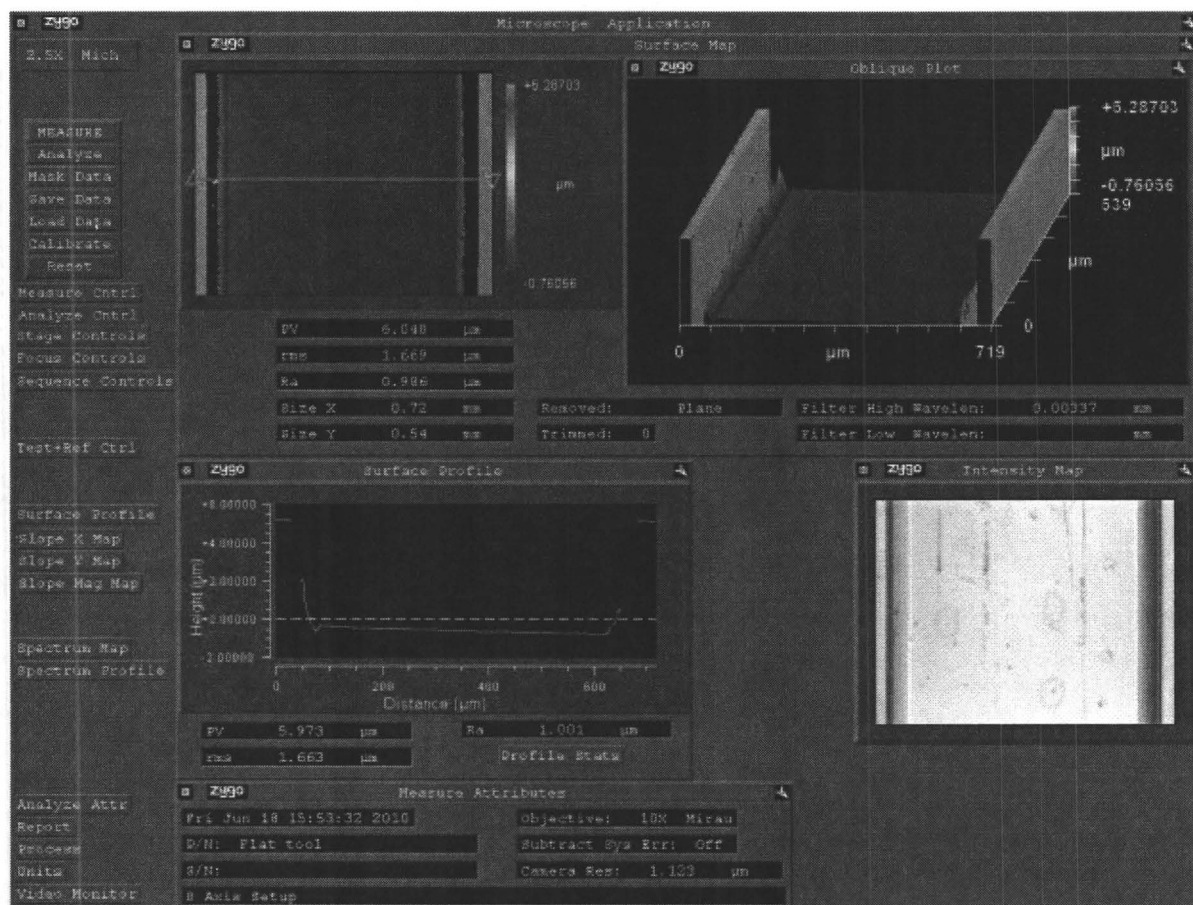


Figure 4-7: Flat end tool setup procedure

By removing form error, the angle of inclination is then measured manually to correct the B-Axis angular position. However, it has been observed that after this procedure, the tool and workpiece may not be parallel. A cutting test with higher feed rate (30 μm/rev) was usually performed to fine tune the angular position by measuring the surface in the Zygo and repeating the same procedure. This setup procedure is time consuming and it is thus not recommended to remove the tool between tests as repeatability of the results will be compromised. It has been observed that even a small misorientation of 0.014° can result a comparable result to that of a round nose tool.

4.4. DATA ACQUISITION SYSTEM

The force generated during a micro machining process is an important parameter and reflects the machining conditions. Maintaining the cutting tool in good condition is more critical in ultra-precision machining than in conventional machining processes. With a cutting force acquisition system, the cutting process can be monitored easily. The data acquisition (DAQ) system used in this study is composed of a MiniDyn 3-Component Dynamometer (Kistler 9256B1), a dual mode multi-channel charge amplifier (Type 5010) and NI compactDAQ-9172 USB data acquisition system with 4 channel analog input module (NI 9215) with universal serial bus (USB) cable. The force data is analyzed using National Instruments (NI) LabVIEW software. The schematic of the data acquisition system is shown in Figure 4-1 (b).

4.4.1. MiniDyn 3-Component Dynamometer: KISTLER Type 9256B1

The cutting tool was mounted on the KISTLER Type 9256B1 dynamometer. The characteristics are summarized in Table 4.8.

Table 4.8: MiniDyn 3-Component Force Dynamometer Type 9256B1

Technical Category	Notation	Unit	Type 9256B1
Measuring Range	F_x, F_y, F_z	N	-250 ... 250
Overload	F_x, F_y, F_z	N	-300/300
Sensitivity	F_x, F_z	pC/N	≈ -11
	F_y	pC/N	≈ -13
Crosstalk		%	$\leq \pm 2$
Rigidity	c_x, c_z	N/ μm	>250
	c_y	N/ μm	>300
Operating Temperature range		$^{\circ}\text{C}$	0 ... 70
Natural frequency	f_{nx}	KHz	5.1
	f_{ny}		2.5
	f_{nz}		5.6

4.4.2. Multi channel Charge amplifier

When the tool is cutting the workpiece, the force will be applied to the dynamometer through the tool-holder. A Kistler type 5010 dual mode (Charge or Voltage) multi channel charge amplifier was used in charge mode to convert the input charge signal into a voltage proportional to the measurement. The sensitivity (pC/N) of the three channels are selected according to the recommended values given in the dynamometer manual as shown in Table 4.8 (Row 4) for F_x , F_y and F_z . The output voltage range of the amplifier is ± 10 Volt. Thus, it is very important to select the “scale” (N/Volt) in charge amplifier depending on the applied load on the dynamometer. In this experiment, the “scale” was selected to be 1N/Volt to capture the sub-Newton force in the charge amplifier. The output data is in volts and the force value can be calculated by multiplying the voltage with the scale. The LabVIEW software can be manually programmed to address the value of the “scale” on the amplifier to give the force data automatically. The

sensitivity of the amplifier is set to its most sensitive setting of 0.01pC/N. The small dynamic force changes were measured by setting the time constant to “short” on the charge amplifier [National Instruments]. Figure 4-8 shows the photograph of the charge amplifier used in this experiment.

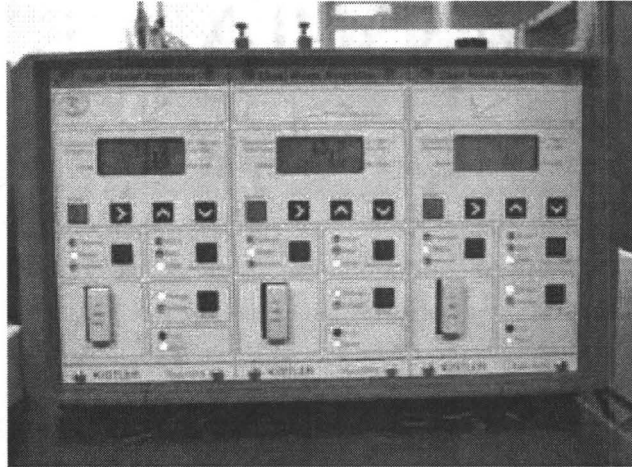


Figure 4-8: Kistler type 5010 dual mode charge amplifier

4.4.1. NI compactDAQ-9172 USB data acquisition system

National Instruments (NI) compact DAC system has two components. The first is the NI cDAQ-9172 chassis with high speed USB connection cable to the PC with a power input of 11 to 30VDC at 15W with 8 module slots as shown in Figure 4-9 (a). The chassis is versatile for different types of modules; however, the general purpose module type NI 9215 (Figure 4-9 (b)) was used in this experiment to measure force. The module has an operating voltage range of $\pm 10V$ with accuracy of 0.003V and a simultaneous sampling in four channels at a maximum sampling rate of 100kS/sec. Operating temperature range of the module is $-40^{\circ}C$ to $70^{\circ}C$. Labview is used to process the data.

A graphical representation of the data acquisition program is shown in Appendix Figure B-2.

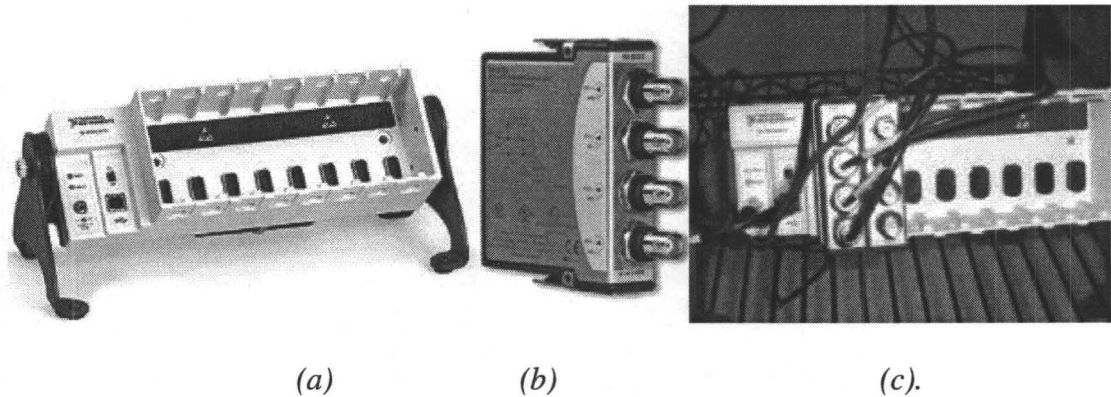


Figure 4-9: NI cDAQ system. (a) NI cDAQ-9172 chassis. (b) NI 9215 general purpose module and (c) cDAQ system in operation

4.5. CUTTING CONDITIONS

One hundred and twenty two (122) experimental conditions were tested in this study to characterize and improve surface roughness in SPDT for the different combinations of workpiece materials (6 types; Table 4.4), cutting tools (3 types; Figure 4-5) and cutting parameters (RPM, Depth and feed). Eight (8) preliminary tests were done on FC 99.87% aluminum, 54% cold rolled (CR) 99.87% aluminum, annealed 6061 aluminum and 32%CR 6061 aluminum at 1000RPM, 5 μ m nominal depth of cut and 5 μ m/rev feed rate with a 1.5mm nose radius tool. The cutting parameters were selected based on published values used to produce mirror like surfaces. Based on the results of this testing, 54%CR 99.87% aluminum was selected to run a design of experiments to

find a good set of cutting conditions that provides a minimum surface roughness for both the 1.5mm and 0.5mm nose radius tools. As feed rate is directly related to the roughness it was set to a nominal value and RPM as well as depth of cut were varied to find an optimal value. The final conditions were repeated for a minimum of 3 times to ensure repeatability of the data and to monitor the progression of tool wear and its relationship with roughness data. The complete set of experiments for optimum depth of cut and RPM is shown in Table 4.9. For the 1.5mm nose radius tool and 54%CR 99.87% aluminum, depth of cut has been selected at 1000RPM and 5 μ m/rev for different depths of cut: 5, 3, 2 and 1 μ m (symbol “*”). Different RPMs (500, 800, 1000, 1200 and 1500) and feed rates (20, 10, 5, 3 and 1 μ m/rev) have been used to find the best performing RPM. Similar experiments have been conducted with the 0.5mm nose radius tool. With the selected RPM and depth of cut determined, a larger matrix of experimental parameters were tested on four alloys of 99.87% aluminum with all three tools to find the feed rate that provided the minimum surface roughness as shown in Table 4.10.

Table 4.9: Design of experiments

54% cold rolled 99.87% aluminum							
		RPM		Depth (μ m)		Feed (μ m/rev)	
1.5mm radius	Nose	500	#	5	*	20	# ‡
		800	#	3	*	10	# ‡
		1000	* # ‡	2	* # ‡	5	* # ‡
		1200	#	1	*	3	# ‡

		1500	#		1	#	‡
		RPM		Depth (µm)		Feed (µm/rev)	
0.5mm Radius	Nose	500	#	5	*	20	# ‡
		800	#	3	*	10	# ‡
		1000	* # ‡	2	* # ‡	5	* # ‡
		1200	#	1	*	3	# ‡
		1500	#			1	# ‡

Table 4.10: Cutting parameters

	Furnace cooled (FC) 99.87% aluminum	54% cold rolled 99.87% aluminum	82% cold rolled 99.87% aluminum	Friction Stirred 99.87% aluminum
	Depth of cut:2µm	Depth of cut:2µm	Depth of cut:2µm	Depth of cut:2µm
	RPM: 1000	RPM: 1000	RPM: 1000	RPM: 1000
	Feed (µm/rev):	Feed (µm/rev):	Feed (µm/rev):	Feed (µm/rev):
1.5mm Nose radius	20, 10, 5, 3, 1, 0.8, 0.6, 0.4 and 0.2	20, 10, 5, 3, 1, 0.8, 0.6, 0.4 and 0.2	20, 10, 5, 3, 1, 0.8, 0.6, 0.4 and 0.2	20, 10, 5, 3, 1, 0.8, 0.6, 0.4 and 0.2
0.5mm Nose Radius	20, 10, 5, 3, 1, 0.8, 0.6, 0.4 and 0.2	20, 10, 5, 3, 1, 0.8, 0.6, 0.4 and 0.2	---	20, 10, 5, 3, 1, 0.8, 0.6, 0.4 and 0.2
0.5mm Nose radius and 0.5mm flat secondary edge	20, 10, 5, 3, 1, 0.8, 0.6, 0.4 and 0.2	20, 10, 5, 3, 1, 0.8, 0.6, 0.4 and 0.2	---	20, 10, 5, 3, 1, 0.8, 0.6, 0.4 and 0.2

4.6. SURFACE ROUGHNESS MEASUREMENT

The Zygo NewView 5000 is a general purpose, three dimensional, surface structure analyzer. It provides graphical images and high resolution numerical analysis to accurately characterize the surface of test parts as a surface map and profile data. The

NewView uses scanning white light interferometry to image and measure the topography of surfaces in three dimensions. The NewView 5000 system can be broken down to two basic subsystems- the microscope and the computer. The microscope provides raw data needed for analysis and includes the microscope itself, a granite base, a stable gantry column, motorized focus control, manual image zoom from 0.4 to 2.0 with manual 5 position turret for different magnification objective lens and 4-axis motorized stage with tip, tilt, X and Y axes and a high resolution camera with selectable resolution up to 640X480 pixels. The computer controls the measurement process, performs calculations and displays measurement results on a color monitor. The computational analysis of the data is done and displayed by the Zygo supplied software called “MetroPro”.

The NewView system uses scanning white light interferometry to image and measure test part surfaces and provides surface structure analysis without contacting the surface. Light from the microscope divides within the interferometric objective: one portion reflects from the test surface and another portion reflects from an internal, high quality reference surface in the objective. Both portions are then directed onto a solid-state camera. Interference between the two light wave fronts results in an image of light and dark bands, called fringes that indicate the surface structure of the part being tested. The test part is scanned by vertically moving the objective with a piezoelectric transducer (PZT). As the objective scans, a video system captures intensities at each camera pixel. These intensities are converted into images by the MetroPro software.

Measurements are three dimensional. Lateral measurements, in the plane of the surface, are performed by calculating the pixel size from the field of view (FOV) of the objective in use. Depths up to 150 μm with 0.1nm Frequency Domain Analysis (FDA) resolution and 0.4nm RMS repeatability can be imaged (independent of objective magnification). There is a tradeoff between objective power and lateral resolution. Higher magnification results increased lateral resolution; however provide a smaller field of view. The NewView objective chart in Table 4.11 shows the specification with a standard high speed camera (640X480 pixels= 307200 pixels) for the objectives used in this study (10X and 50X) [ZYGO manual].

Table 4.11: Field of view and spatial resolution at different magnification [ZYGO manual]

Magnification/Design	Field of View (FOV) (mm X mm)		Spatial Resolution (μm)	
	<i>10X/Mirau</i>	<i>50X/Mirau</i>	<i>10X/Mirau</i>	<i>50X/Mirau</i>
Field zoom lenses				
0.5X	<i>1.41 X 1.06</i>	<i>0.28 X 0.21</i>	<i>2.21</i>	<i>0.44</i>
0.75X	<i>0.94 X 0.70</i>	<i>0.19 X 0.14</i>	<i>1.47</i>	<i>0.29</i>
1.0X	<i>0.70 X 0.53</i>	<i>0.14 X 0.11</i>	<i>1.10</i>	<i>0.22</i>
1.5X	<i>0.47 X 0.35</i>	<i>0.09 X 0.07</i>	<i>0.73</i>	<i>0.15</i>
2.0X	<i>0.35 X 0.27</i>	<i>0.07 X 0.05</i>	<i>0.55</i>	<i>0.11</i>

4.6.1. Roughness Parameters

There are different units to measure the surface roughness and ZYGO newview is capable of measuring almost all of them. A few of the parameters measured in this study are discussed below.

4.6.2.1 Average roughness (R_a)

The average roughness or deviation of all points from a plane fit to the test part surface and is expressed as $R_a = \frac{1}{L} \int_0^L |y(x)| dx$ and shown in Figure 4-10 (a) [ZYGO manual].

4.6.2.2 Root Mean Square (RMS) roughness (R_q)

R_q is the RMS parameter corresponding to R_a [ZYGO manual] and can be expressed as $R_q = \sqrt{\frac{1}{L} \int_0^L y^2(x) dx}$.

4.6.2.3 Ten point height (R_z)

R_z is the average absolute value of the five highest peaks and the five lowest valleys over the evaluation length and can be expressed as $R_z = \frac{(P1 + P2 \dots + P5) - (V1 + V2 \dots + V5)}{5}$ and shown in Figure 4-10 (b) [ZYGO manual].

4.6.2.4 Peak to valley roughness (R_{th} or PV)

The vertical distance between the top of the highest peak and the bottom of the deepest valley within the sampling length. It is the maximum of all the peak-to-valley values as shown in Figure 4-10 (c) [ZYGO manual].

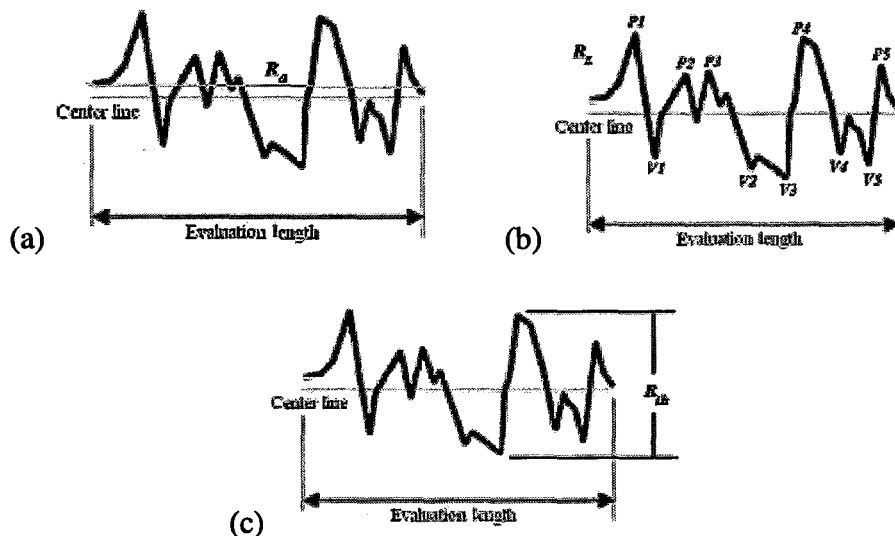


Figure 4-10: Roughness parameters. (a) Average roughness (R_a). (b) Ten point average roughness (R_z). (c) Peak to valley roughness (R_{th} or PV). [ZYGO manual]

4.6.2. Filtering data

Metropro offers digital filtering of the test data thus enabling the surface characteristics to break down to waviness, roughness and high frequency data. There are five types of digital filtering options and they are: 1. *Off*, 2. *Low pass*, 3. *Band pass*, 4. *High pass* and 5. *Band reject*. In *low pass* filtering low frequency or waviness data is highlighted *i.e.* roughness is removed. *Highpass* filtering allows the high spatial

frequency components to pass through the filter *i.e.* waviness is removed. In band pass filtering, data in the center of the band is analyzed and for band reject filtering, data at the center is rejected. Caution should be taking when filtering data, as it can drastically alter the test results as can be seen from Figure 4-11. There are some recommended cut-off values from ISO 4288 as shown in Table 4.12; however, considering the dimension of the field of view (0.35mm X 0.27mm), no filtering (filter *off*) has been applied in any of the reported data.

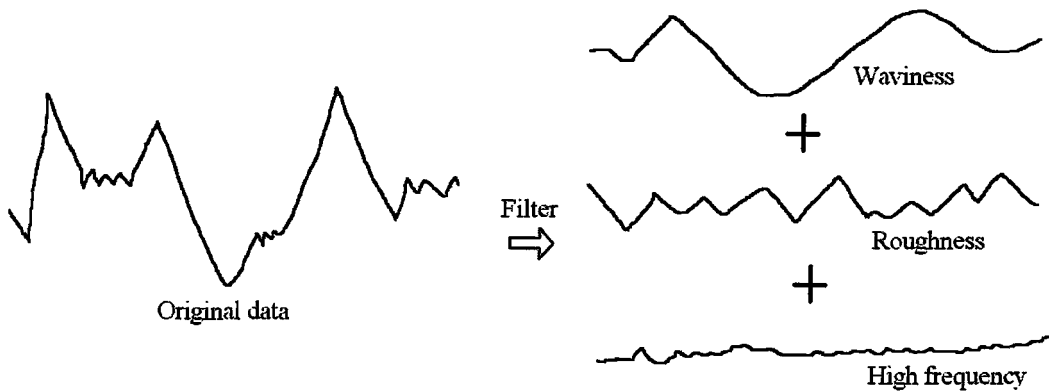


Figure 4-11: Alteration of test results by filtering from original (filter *off*) data [ZYGO manual]

Table 4.12: Recommended cut-off ISO 4288 [Whitehouse, 2002]

Roughness R_a (μm)	Cut-offs λ_c (mm)	Evaluation length $\lambda_c l$ (mm)
to 0.02	0.08	0.08/0.4
>0.02 to 0.1	0.25	0.25/11.25
>0.1 to 2	0.8	0.8/4
>2 to 10	2.5	2.5/12.5
>10	8	8/40

CHAPTER 5 RESULTS AN DISCUSSION

The objective of this study is to enhance the machinability of different aluminum alloys to achieve superior surface roughness that will require minimum or no post processing such as polishing or lapping. Achieving improved surface roughness by SPDT is a long standing problem in industry and average roughness less than 3nm is very difficult to achieve with aluminum. Thus the objective was to achieve an average roughness less than 10nm; however, desired roughness benchmark was less than 3nm average. Realizing the benefit of SPDT, the issue of surface roughness is addressed from two fundamental directions for SPDT process in this study.

1. Workpiece material considerations (for example., alloy composition, mechanical properties) and
2. Tool geometry considerations (for example., round nose and flat secondary edge tool).

The effect of workpiece material was studied by engineering different alloys of aluminum like 6061 aluminum and 99.87% aluminum. Initially study was focused on the selection of an alloy composition. Alloy selection was followed by engineering the selected alloy to enhance machinability. Pre-processing techniques like strain hardening

and friction stir welding were performed to engineer the alloys. Care was given while pre-processing the workpieces to keep it economical. Pre-processing cost of strain hardening or friction stir welding is almost negligible compared to other pre-processing techniques like rapid solidification and post-processing techniques like lapping and polishing. All the engineered alloys were then machined with different cutting tool geometries to draw conclusions.

5.1. WORKPIECE MATERIAL SELECTION

Initially, two different alloys of aluminum (Annealed 6061 aluminum and Furnace cooled 99.87% aluminum) were turned with single point diamond tools and the surface roughness was observed to be higher than the theoretical value primarily because of:

- i. plastic side flow,
- ii. brittle failure,
- iii. smearing and dimple formation from secondary hard particles and
- iv. grain boundary induced roughness.

Effort has been made to reduce the surface roughness by engineering these materials by strain hardening to increase the number of active slip planes by increasing the dislocation density. Annealed 6061 aluminum and FC 99.87% aluminum were cold rolled with a reduction of thickness of 30% and 54% respectively. Figure 5-1 shows the microstructure

of the four alloys at different magnification and Table 5.1 provides the micro hardness values. Figure 5-1 (d) shows the formation of sub-grains in response to deformation (cold rolling) process as discussed in Section 2.5.3.

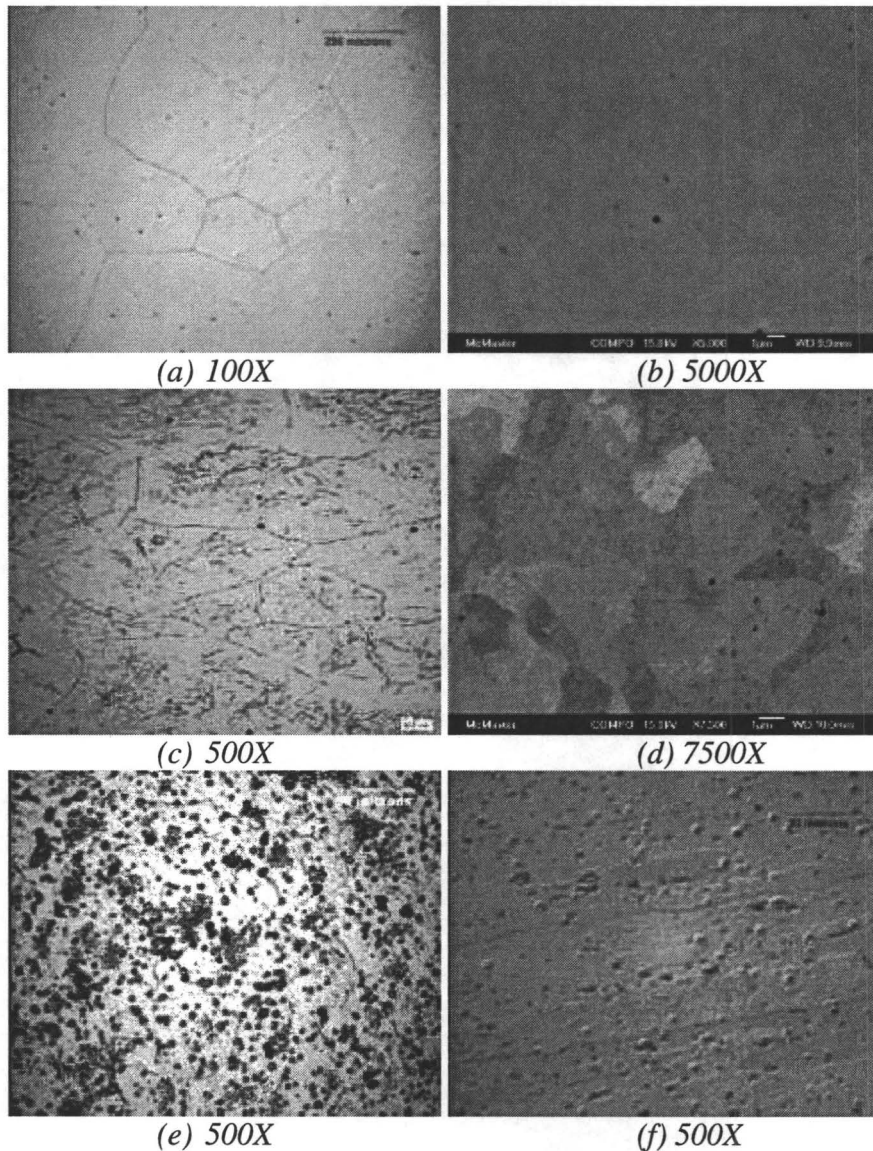


Figure 5-1: Microstructure of aluminum alloys at different magnification. (a) and (b): Furnace cooled (FC) 99.87% aluminum alloy. (c) and (d): 54% cold rolled (54CR) 99.87% aluminum alloy. (e) Annealed 6061 aluminum alloy. (f) 32% cold rolled 6061 aluminum alloy

All four workpieces are then diamond turned with a 1.5mm nose radius tool at 1000RPM and 5µm depth of cut and 5µm/rev feed rate. Figure 5-2 shows the average surface roughness at 16 different points on the surface for all the workpieces at four different diameters, 90° apart from one another. It is to be mentioned here that this study is not limited only to these alloys. Different other microstructures have been produced and studied. Methods of changing microstructure and their optical and SEM images are discussed in this chapter in appropriate sections.

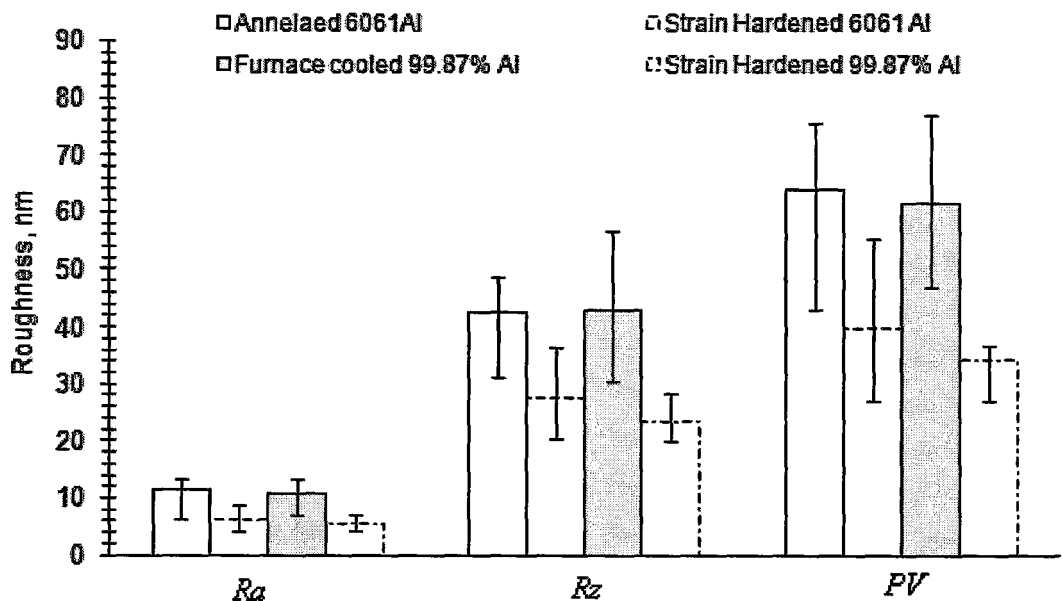


Figure 5-2: Variation in surface roughness (R_a , R_z and PV) for different aluminum alloys at 1000RPM, 5 µm Depth of cut and 5 µm/rev.

The reason for this averaging is based on the observation made by Wang et al., [in Shaw, 2005] and Roblee [2007] which stated that cutting speed has no effect on surface

roughness in single point diamond turning. This observation has also been confirmed in this study. However, Figure 5-2 clearly shows that strain hardening improves the surface roughness by reducing the peak to valley roughness (PV or R_{th}) by 27nm and 23.8nm, R_a by 5.34nm and 5.06nm and R_z by 19.5nm and 14.9nm for 99.87% pure aluminum and 6061 aluminum respectively. Figure 5-3 shows the oblique 3D plot of the machined surface of different workpiece materials and shows minimum PV value from these plots. However, geometrical roughness using the equation $R_{th} = f^2 / (8R_n) = 2.08\text{nm}$ leads to a poor surface roughness estimation and cannot be used in this study. This finding has also been concluded by other researchers [Childs et al., 2008a; 2008b; Grzesik, 1996; Liu and Melkote, 2006; Knuefermann and McKeown, 2004; Shaw, 2005; Ng et al., 2006].

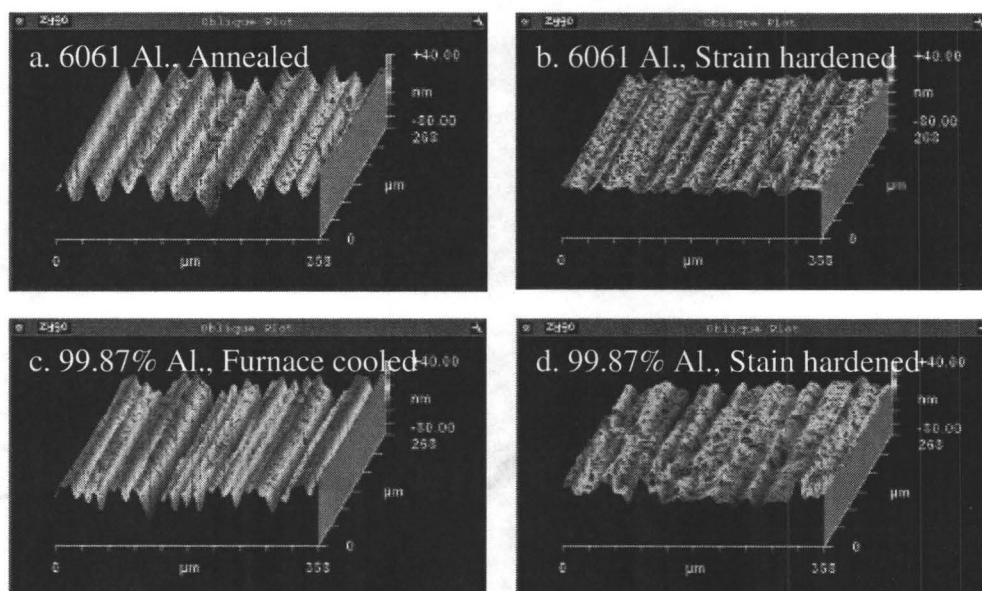


Figure 5-3: Oblique plot of surface roughness for different alloys at 1000RPM, 5 μm Depth of cut and 5 $\mu\text{m}/\text{rev}$. PV_{min} values are a. 65.05nm, b. 29.28nm, c. 62.62nm and d. 27.08nm.

In this study it has been repeatedly observed and concluded that deterioration in the surface roughness and its deviation from theoretical value takes place not only in the feed direction but also in the cutting direction. This deviation results from the combination of plastic side flow opposite to feed direction, smearing of hard secondary particles into the surface and formation of prows and dimples as well as subsurface damage because of secondary particles (brittle type of failure) in the cutting direction, and response to grain boundaries and grain orientation induced surface roughness.

5.1.1. Plastic side flow induced roughness

The most dominant factor in SPDT is plastic side flow as can be seen from Figure 5-3. Figure 5-4 shows the SEM image of material side flow while machining 6061 aluminum. However, side flow induced surface roughness is less when the workpiece is strain hardened as can be seen from Figure 5-3.

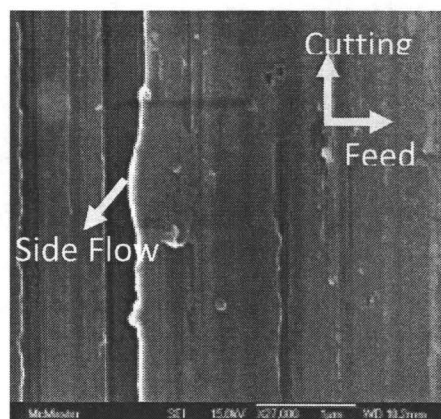


Figure 5-4: Side flow

The reason behind this is that in a strain hardened material, dislocation density is higher which results in increased hardness of the material. This makes the material prone to fracture as opposed to plastic deformation. This statement can further be supported by SEM study of the chips. Figure 5-5 shows SEM images of the chips for furnace cooled 99.87% aluminum (a, b and c) and strain hardened 99.87% aluminum (d, e and f).

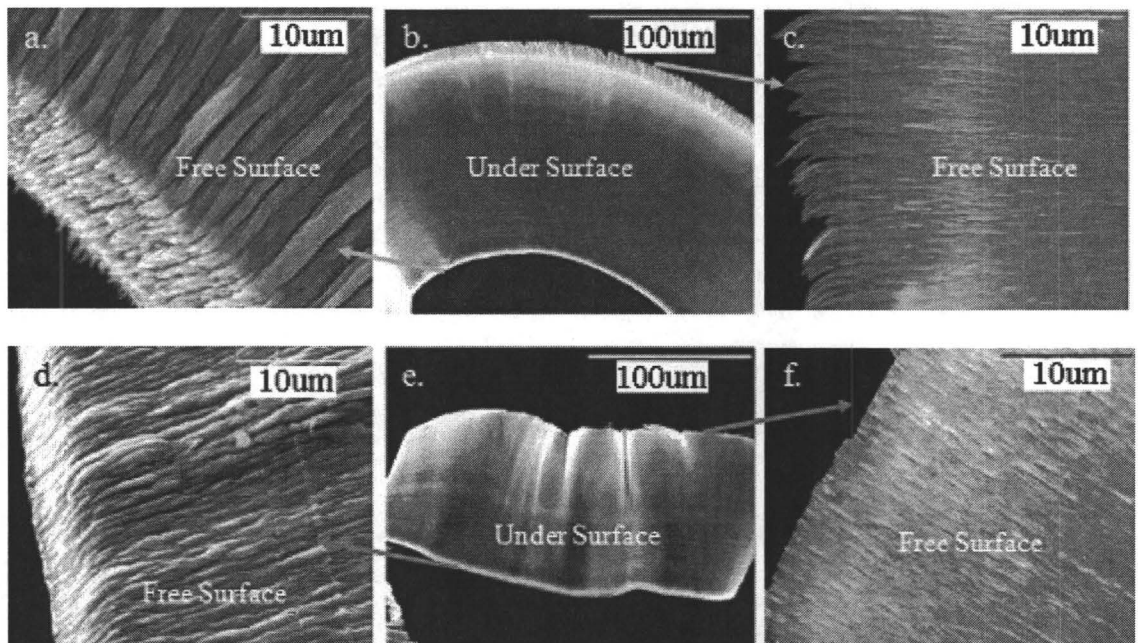


Figure 5-5: SEM photograph of chips produced from: (a, b and c) Furnace cooled 99.87% Al, (d, e and f) Strain Hardened 99.87% Al at 1000RPM, 5 µm Depth of cut at 5 µm/rev.

It is clear that furnace cooled aluminum chips have more edge serration than the strain hardened material which results from the reduction in actual chip thickness near the trailing edge. Edge serration indicates side flow. This is because less material is participating in chip formation and remains on the freshly machined surface in the form of plastically deformed side flow. Near the trailing edge, the effective depth of cut is very

small and is comparable to the cutting edge radius of the tool. For example, the effective depth of cut is only 16.5nm at a distance of 5 μ m from the tip of the tool with a 1.5mm nose radius tool as shown in Table 3.1. Thus the material at the trailing edge of the tool is subjected to high stress or in other words “size effect” that causes tearing of the weakest section of the chip [Shaw, 2005; Kishawy and Elbestawi, 1999]. However, strain hardening introduces dislocations and dislocations reduce the serration of the chip and allow the material to fracture easily. Another reason for chip serration is the strain gradient plasticity or the chip particles velocities gradient along the chip width [Liu and Melkote, 2006; Kishawy and Elbestawi, 1999] as shown in Figure 2-12, Figure 3-3 and quantified in Table 3.1. It is clear from Figure 5-5 that 99.87% furnace cooled aluminum has less response to variation in chip particle velocity than the strain hardened sample as the chip deforms itself and facilitates the reduction of chip serration in the latter case. This self-deformation of chips of strain hardened material also indicates that there is less adhesion at the chip/tool interface. Higher hardness of the workpiece material could lead to the following: the seizure formation is accompanied by intensive (around 50%) plastic deformation of surface layers [Fox-Rabinovich and Totten, 2007]. Owing to higher hardness of the strain hardened workpiece material the zone of plastic deformation is concentrated within the very thin (nano-scale range) surface layer with minimal subsurface layer involvement in the process of intensive deformation. This may result in a decrease of seizure intensity eventually reducing the surface roughness. Again the back-free surface of the chips shows a lamella structure which is a sign of the shearing process [Shaw, 2005]. The deck of card model is based on this observation. However, the

spacing between active slip planes are smaller in a strain hardened aluminum than the furnace cooled aluminum as can be seen from Figure 5-5 (a) and (d). In furnace cooled 99.87% aluminum, the spacing between active slip planes are approximately 4367 atomic diameters and for 54% strain hardened 99.87% aluminum is approximately 1664 atomic diameters where the atomic diameter of aluminum is 0.2862nm [Callister, 1997]. Sata et al., [1985] noted that softer materials have a more pronounced swelling effect, but did not explain this observation. However, this observation is explained with the results from the present study with the help of dislocation-dislocation interaction for an alloy. Figure 5-6 clearly shows the severity of the swelling effect on the furnace cooled 99.87% aluminum as opposed to the cold rolled one for 1000RPM, 2 μ m depth of cut and 20 μ m feed rate for a 1.5mm nose radius tool. Simulated surface was obtained simply by offsetting a 1.5mm radius by amount to feed rate which is 20 μ m in this case.

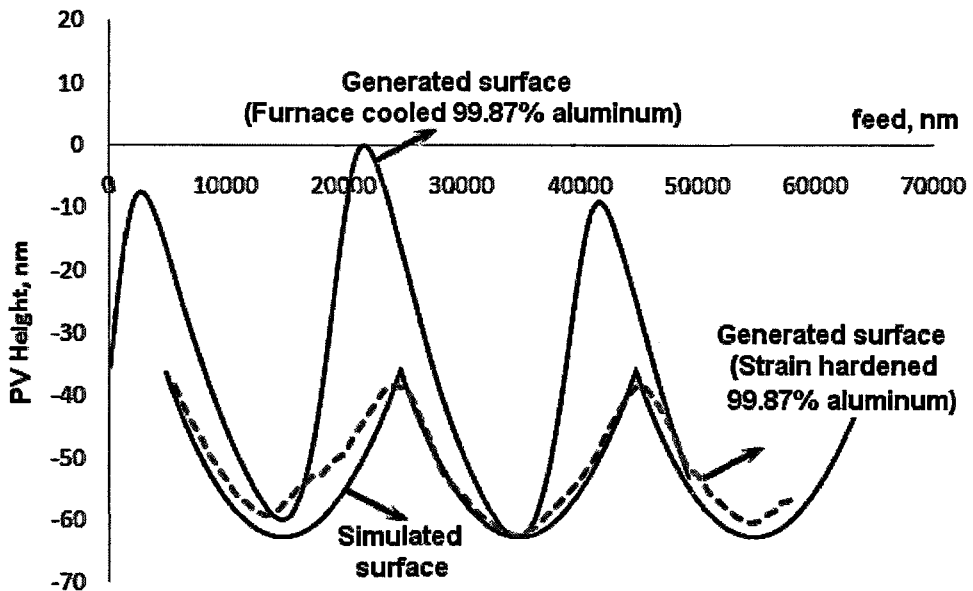


Figure 5-6: Comparison of side flow and swelling effect on Furnace cooled and 54% cold rolled aluminum alloy at 20 μ m/rev feed rate, 1000RPM and 2 μ m depth of cut

5.1.2. Secondary particles induced roughness

5.1.2.1 Brittle fracture

Brittle fracture is observed while studying surface metallurgy and has a strong influence on the surface roughness and cannot be neglected while generating mirror surfaces with a nanometer range of surface roughness. This mode of failure is prominent in the cutting direction in aluminum 6061 metal matrix composite. The cutting process generates a plastic deformation zone due to the roundness of the tool into the material and if there is any crack generating defects present on the plastic deformation zone a brittle type of failure will occur [Shaw, 1995]. Figure 5-7 (a) and (b) show an interpretation of this phenomenon with observations from the present study. Wherever there is a micro crack formation by brittle failure, the presence of magnesium, silicon and iron is observed from the EDS analysis which may be acting as a source of defect or void by strain mismatch as shown in Figure 5-7 (c). Detail EDS observation of Figure 5-7 (c) is shown in Figure 5-8 highlighting the spot in Figure 5-8 (a) on the machined surface. It is clear from Figure 5-8 that Si, Mg and Fe are causing those additional defects generating from alloying elements in 6061 aluminum.

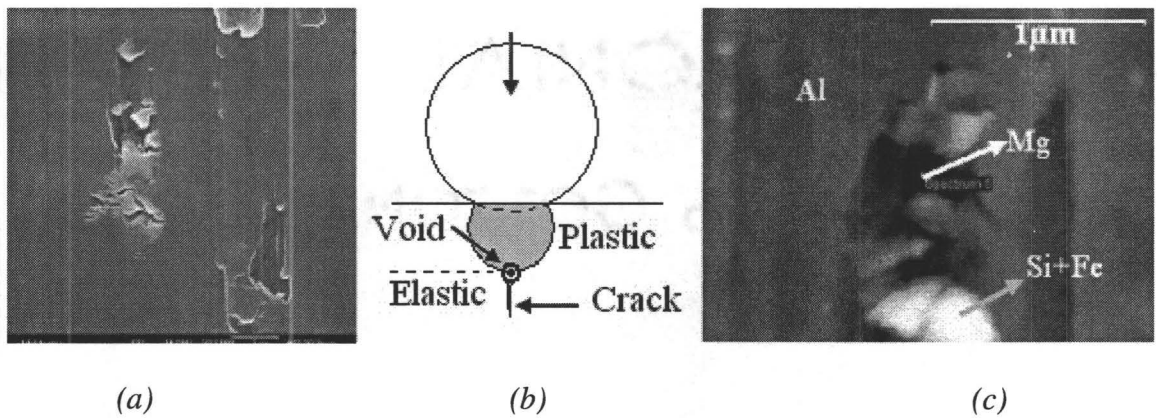
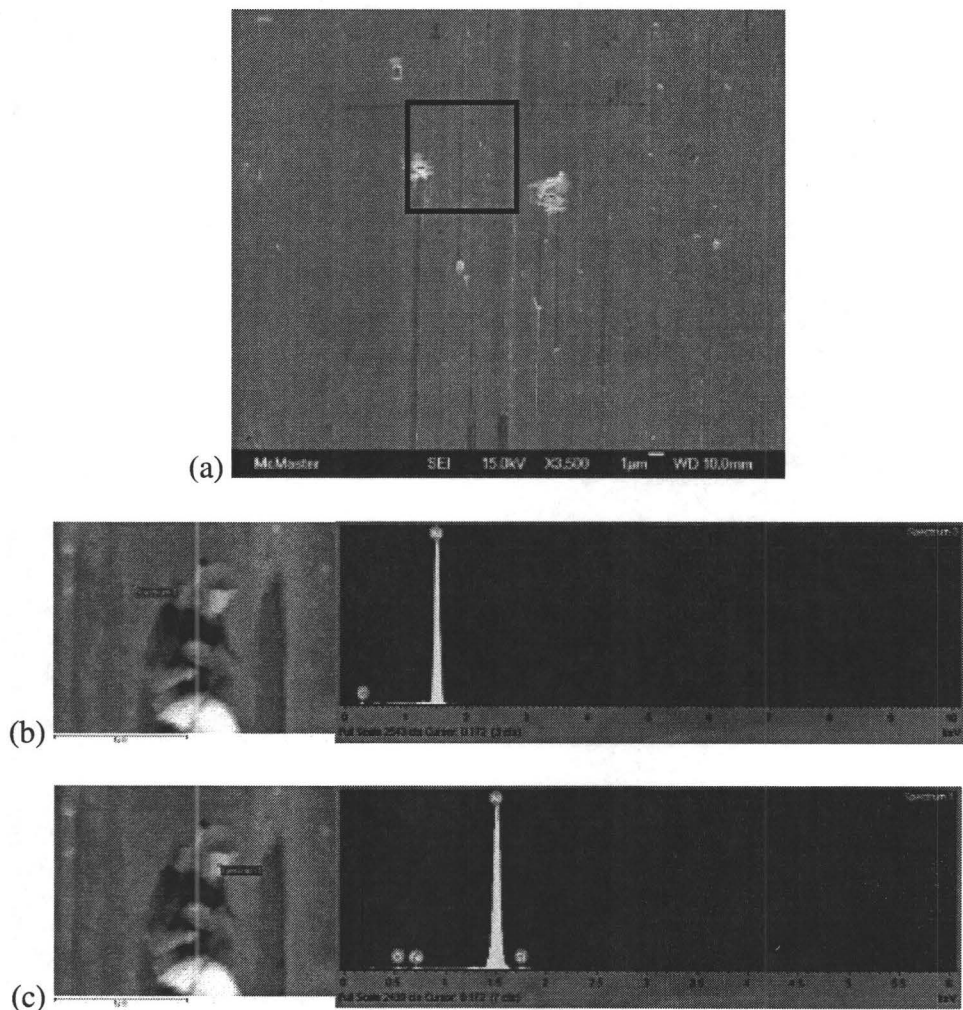


Figure 5-7: Brittle type of failure in 6061 Aluminum [Figure (b) from *Shaw, 1995*]



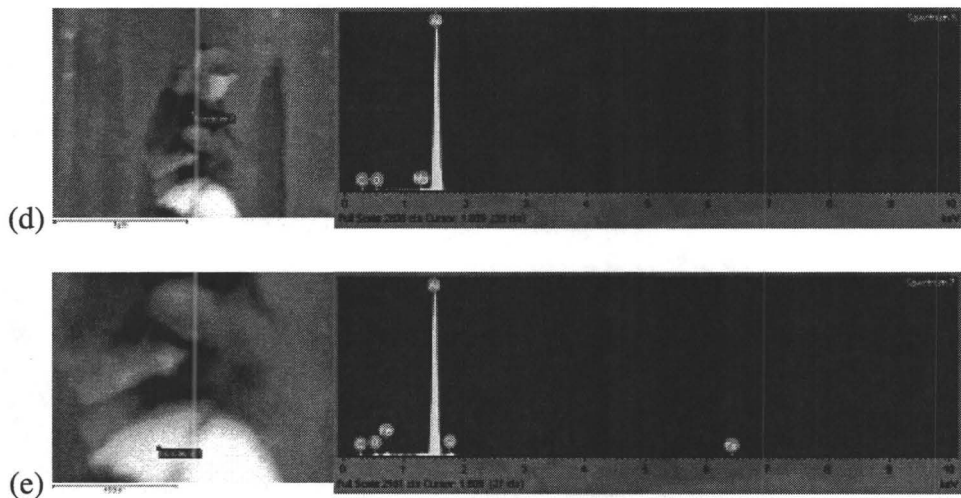


Figure 5-8: EDS analysis of brittle type of fracture on 6061 aluminum

5.1.2.2 Smearing and dimple formation from secondary hard particles

Smearing and dimple formation occurs simultaneously because of hard secondary particles which are present in the material microstructure and are more dominant in the cutting direction. Figure 5-9 (a) and Figure 5-9(b) shows the smearing of the secondary hard particles on the surface from secondary and back-scattered electron (BSE) images respectively that result in a groove along the cutting direction of a 6061 aluminum workpiece. EDS analysis shows that the smearing of the particles is mainly due to hard silicon and/or iron particles present in a soft aluminum matrix as shown in Figure 5-8.

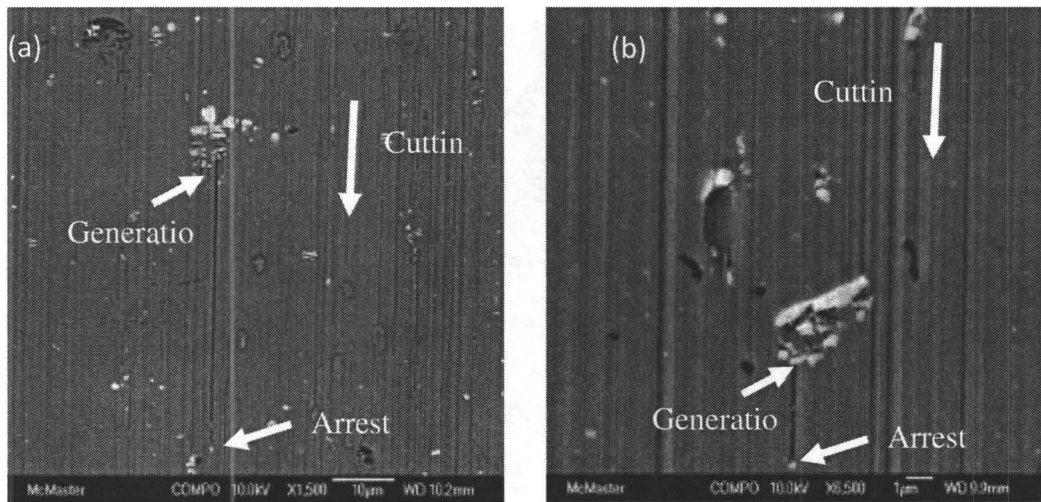


Figure 5-9: Back-Scattered Electron (BSE) image of 6061 aluminum showing brittle fracture, smearing of hard particles and dimple formation.

Smearing takes place predominantly near the trailing edge of the chip where the micro-extrusion process takes place due to tool roundness and when the tool encounters a particle having a dimension smaller or on the order of the cutting edge radius. The tool drags the particle along with it in the cutting direction. However, at the thicker section of the chip, those secondary particles are integrated into the chip and have minimal effect on the surface generation. Figure 5-10 shows chips produced from annealed 6061 and strain hardened 6061 aluminum where it is evident that some voids or missing particles are near the trailing edge of the chips which are not present at the thicker section of the chip.

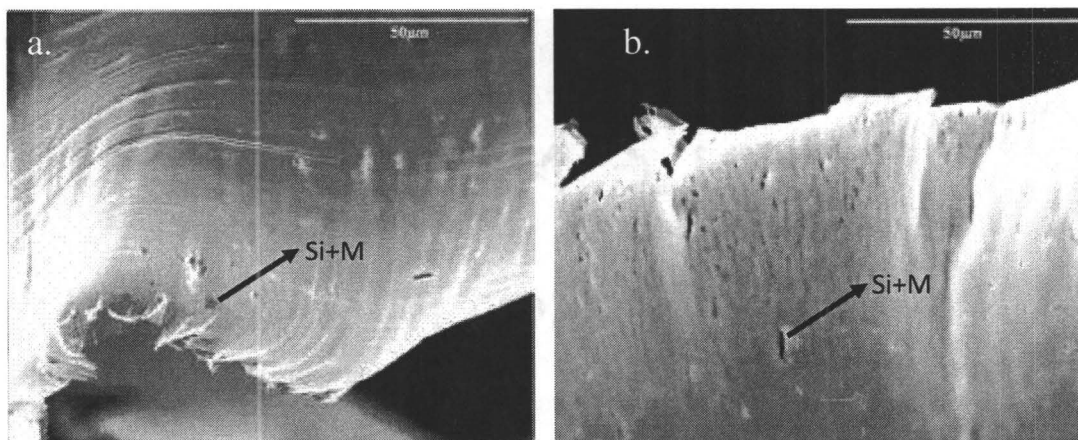


Figure 5-10: Sign of missing particles on chips on a. Annealed 6061 Aluminum and b. Strain Hardened 6061 Aluminum.

It has been observed that near the voids there is a presence of Magnesium and Silicon which indicates that they have remained on the machined surface which eventually leads to smearing of those particles on the machined surface which may result in added surface roughness. Dimples form when the hard particles leave the machined surface with chips at the trailing edge. It has been observed that there is a pileup of material adjacent to the hard particles in the cutting direction. This is because during the cutting process, the material deforms plastically and dislocations move ahead of the tool tip. The density of these dislocations pile up near the hard particle as it works as a seizure to dislocation motion. Once this hard particle moves with the chip, it forms a dimple. Peak-to-valley roughness generated by material pile-up and dimple formation may be as high as 75nm as shown in Figure 5-11 for a 99.87% aluminum alloy at the site where alloying element iron is present.

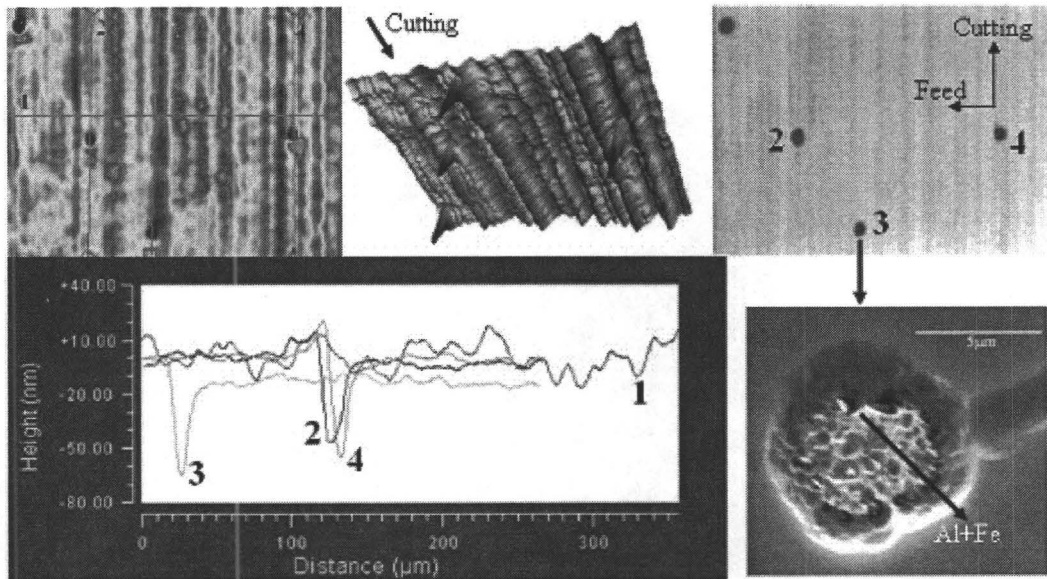
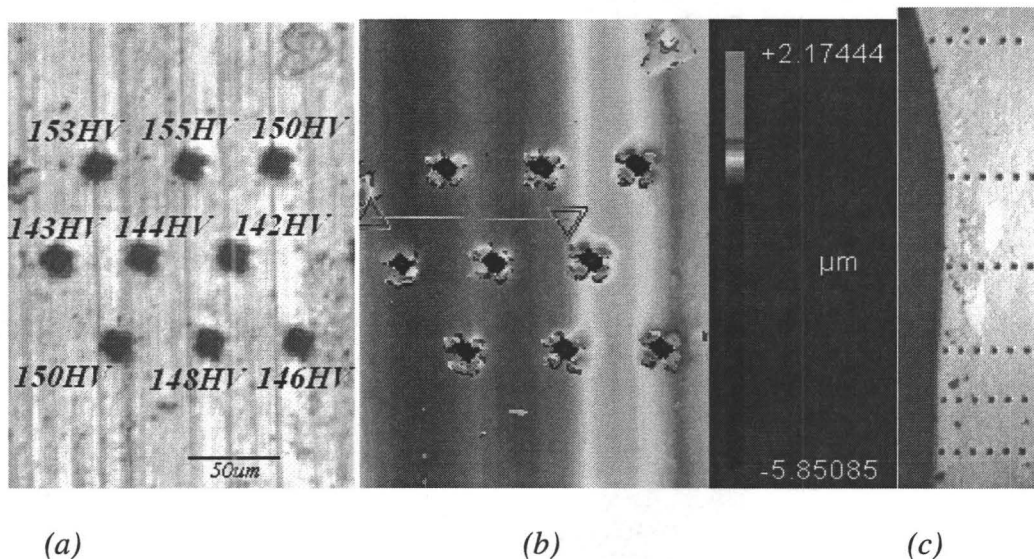


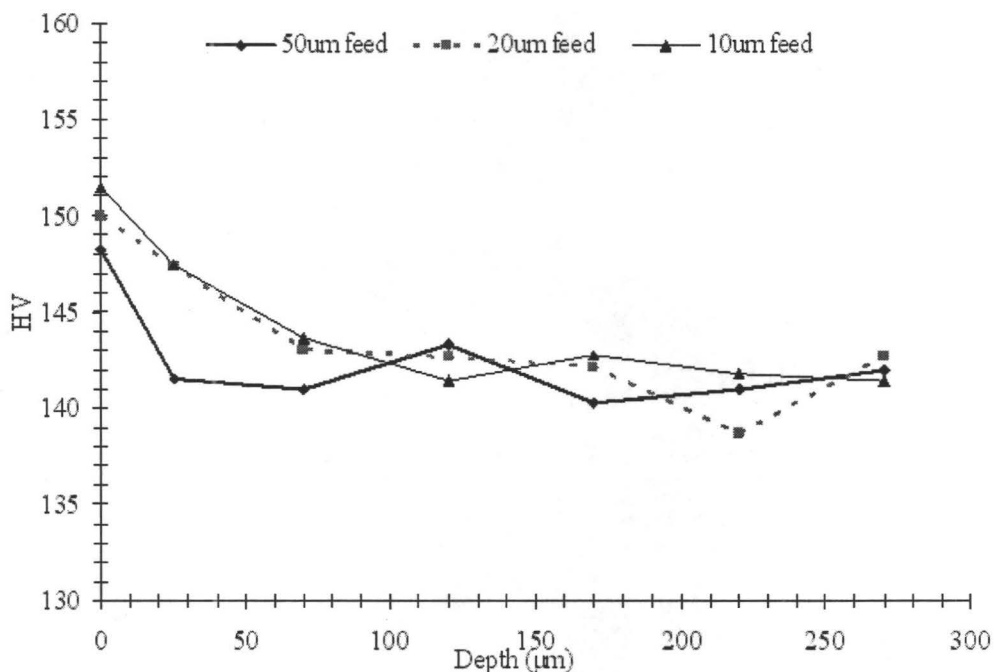
Figure 5-11: Dimple induced roughness along feed (1-1') and cutting (2-2', 3-3' and 4-4') in 99.87% aluminum alloy

Smearing and dimple formation is process independent and primarily depends on the material microstructure and tool edge roundness. This is why it is very difficult to achieve a surface roughness better than $3\text{nm } R_a$ [Roblee, 2007] with aluminum alloys. However, 6061 aluminum alloy has more secondary hard particles than the 99.87% pure aluminum and eventually has more unpredictable roughness induced from smearing and dimple formation. Thus, 99.87% pure aluminum was selected as a workpiece to address the side flow issue of surface roughness by further changing its mechanical properties by plastic deformation. A further source of surface roughness is generated at grain boundaries and due to the anisotropic nature of the polycrystals observed in this study. A detailed observation and discussion on this topic is provided in Section 5.4.2.

5.2. FURTHER ENGINEERING OF FURNACE COOLED 99.87% ALUMINUM

While machining commercial 6061 aluminum, an increase in hardness on the deformed machined layer is observed at different feed rates. Figure 5-12 (a) and (b) show the micro hardness measured on the top surface of a machined sample and Figure 5-12 (c) shows the micro hardness measurement along the cross section of the machined sample. The average of the measured roughness profile is shown in Figure 5-12 (d) for different feed rates from the top surface along the cross section at different depths. These results further support the observation made by [Lucca et al., 1994; To and Lee, 2001; Demir, 2008]. These findings are believed to be occurring from the severe plastic deformation during the cutting process.



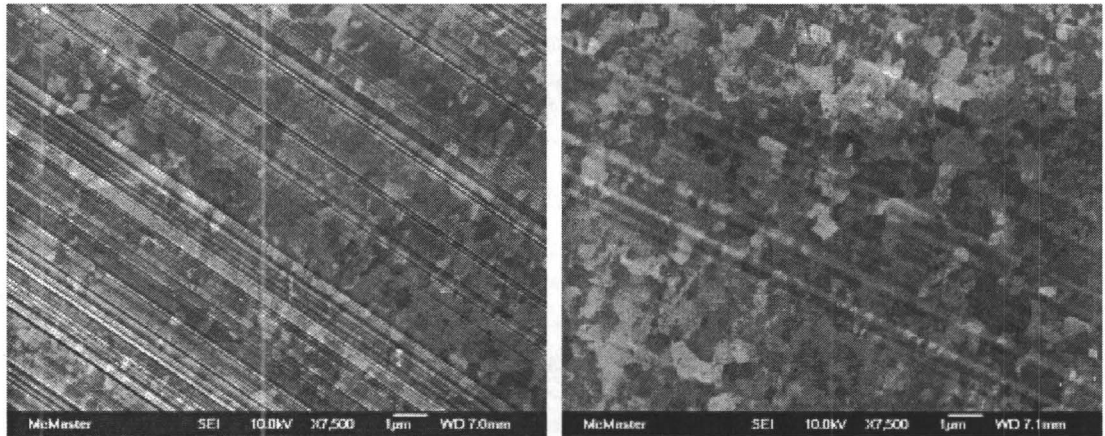


(d)

Figure 5-12 Micro hardness tests performed on a machined surface and along the cross section of a 6061 aluminum

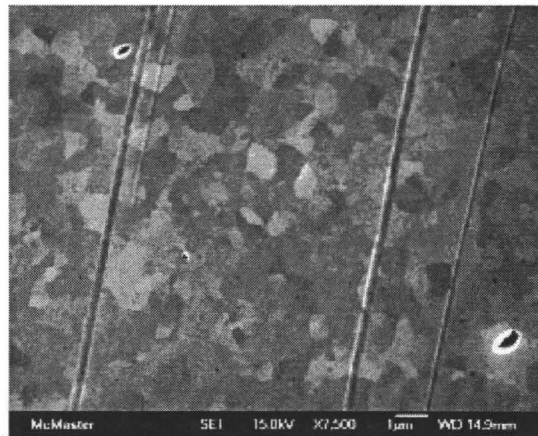
Moreover, Figure 5-12 (a) and (b) suggest that because of the severely deformed plastic zone, hardness is higher where the material side flow is occurring. For example, average micro hardness is around 153HV near the side flow and is 143HV near the valley where there is no side flow. This observation also suggests that erosive wear at the trailing edge of the cutting tool may occur [Kishawy and Elbestawi, 1999]. A similar observation and conclusion can be made while machining the other workpiece materials in this study. A clear observation of sub-grain refinement is observed while machining

54% cold rolled 99.87% aluminum irrespective of tool geometry as shown in Figure 5-13 and can be compared with Figure 5-1 (d).



(a)

(b)



(c)

Figure 5-13: Machined surface of 54% cold rolled 99.87% aluminum. (a) 1.5mm nose radius tool. (b) 0.5mm nose radius tool. (c) Tool with flat secondary edge generated at 1000rpm, 2µm depth of cut and 1µm/rev feed rate.

The smallest grain observed in 54% cold rolled aluminum is approximately 3 μ m (Figure 5-1) where the smallest grain size on a machined sample is approximately 300~500nm (Figure 5-13). There is also an increase in micro hardness on the machined surface (Table 5.1).

Table 5.1: Micro hardness of aluminum workpieces

Aluminum alloys	Process	Micro Hardness (HV)
99.87% pure aluminum	Furnace cooled	23
	54% cold rolled	29
	54% cold rolled machined	36
	82% cold rolled	54
	Friction stir process (FSP)	Figure 5-15
6061 aluminum (commercial)	Annealed	50
	30% cold rolled	64

Micro hardness of 54% cold rolled 99.87% aluminum is 29HV while the hardness is 36HV when machined. Thus strain hardening by cold rolling improves surface roughness (Figure 5-2) while further refining the grain structure during machining (Figure 5-1 (d) and Figure 5-13). This observation has prompted the author for further grain refinement of the workpiece realizing that due to micro extrusion, a thin layer of machined surface undergoes severe plastic deformation because of size effect. The thin layer of the material then organizes into a suitable state by further grain refinement. It is evident from micro hardness data that machined surfaces have a larger dislocation density. Hence, if one can generate a pre-machined surface with a similar micro-structure, it should enhance machinability by improving the chip formation process. Thus furnace

cooled 99.87% aluminum was cold rolled to a thickness reduction of 82%. The microstructure of the surface is shown in Figure 5-14. The smallest grain size of approximately 300nm can be observed. However, the microstructure shows micro porosities (voids) generated through plastic deformation and the grains are not uniform.

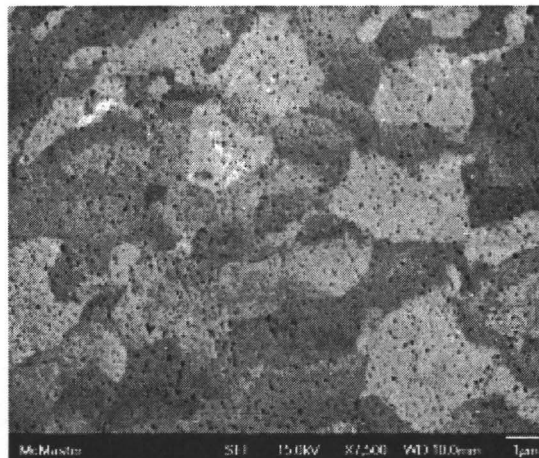


Figure 5-14: 82% cold rolled (82CR) 99.87% aluminum alloy. (7500X)

5.2.1. Friction stir process (FSP)

In this process a carbide tool with a shoulder and a probe is pressed against the workpiece. The motions involved are rotation and feed of the tool across the workpiece. This process stirs the material in contact to refine the grains of the workpiece. There is heat generation involved in this process; however, the heat generated can be minimized by carefully selecting the operating parameters. In general, a lower RPM and higher feed rate results in less heat generation and finer grain refinement (Section 2.5.3.). Nine (9)

FSP parameters selected in this study are shown in Table 4.5. All the parameters were performed for a single pass followed by microstructure and micro hardness analysis along the cross section from 200 μ m up to a 4mm depth from the stirred surface. Micro hardness values and the microstructure of different friction stirred samples are shown in Figure 5-15 and Figure 5-16 respectively. FSP was done on 99.87% furnace cooled pure aluminum. It may be concluded from Figure 5-16 that the optimal RPM of 400 and feed rate of 68mm/min providing 0.17mm/rev results in the most refined microstructure (FSP7). It is critical to have a uniform grain refinement up to a depth of 3mm in this study to allow for the repeat of the experiments on a single sample. Other FSP parameters were not considered in this study because of irregularities as shown in Figure 5-16. FSP1, FSP2, FSP3, FSP4, FSP8 and FSP9 have coarse grains while FSP5 and FSP6 have voids. However, FSP8 and FSP9 may be candidates for future studies. FSP7 was selected for the workpiece in diamond turning. It is important to note that as FSP refines the grains in the material, there was no observed presence of large grains as was the case with the FC 99.87% aluminum or 54%CR 99.87% aluminum in Figure 5-1. As discussed, grain boundaries play a vital role in SPDT and thus FSP material may offer new opportunities for SPDT.

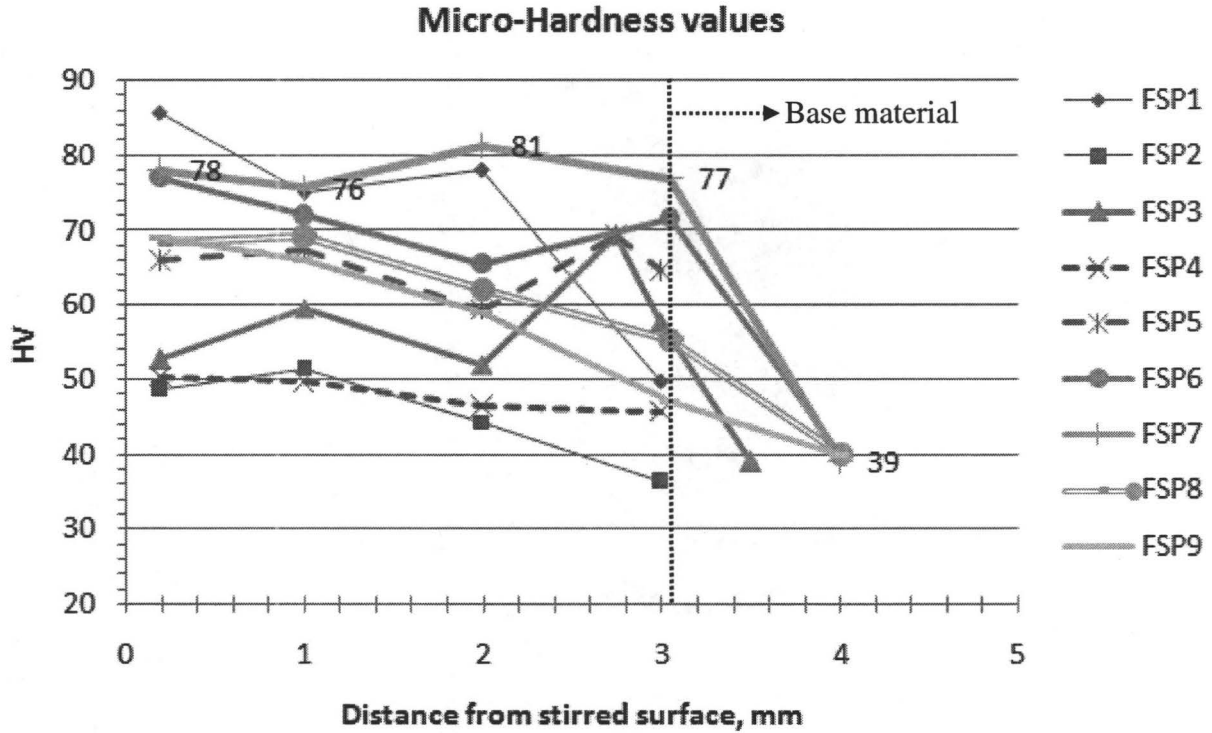


Figure 5-15: Micro hardness values for FSP samples [Parameters in Table 4.5]

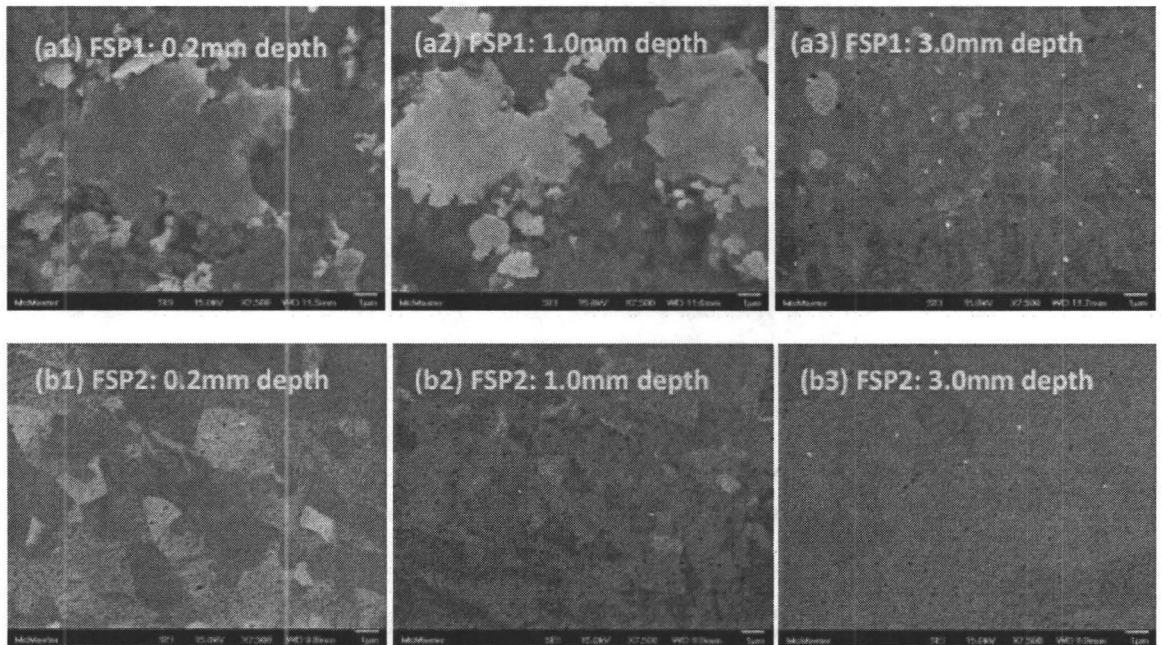


Figure 5-16 a1-b3: Microstructure of FSP samples at different depths (at 7500X)

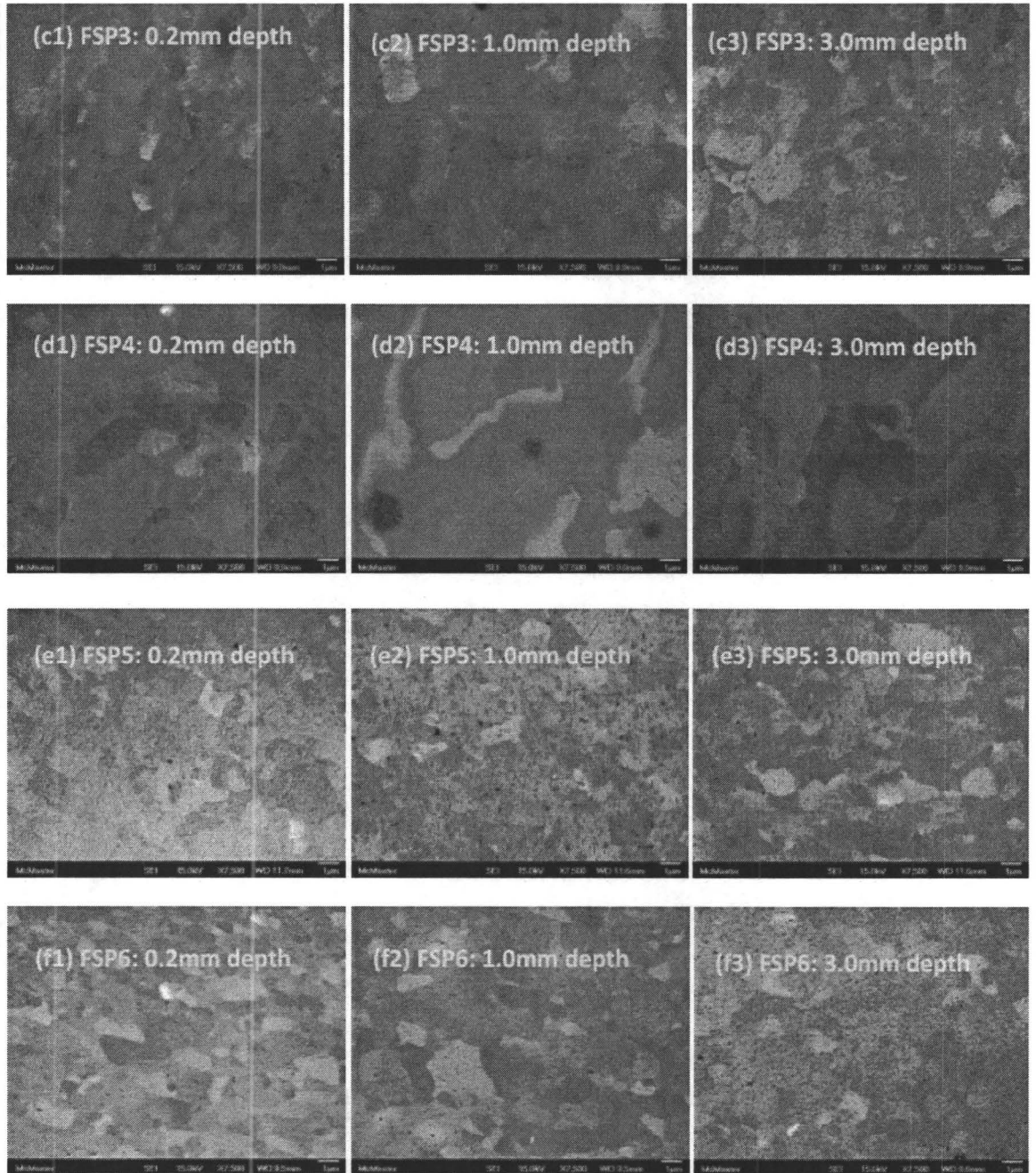


Figure 5-17 c1-f3: Microstructure of FSP samples at different depths (at 7500X)

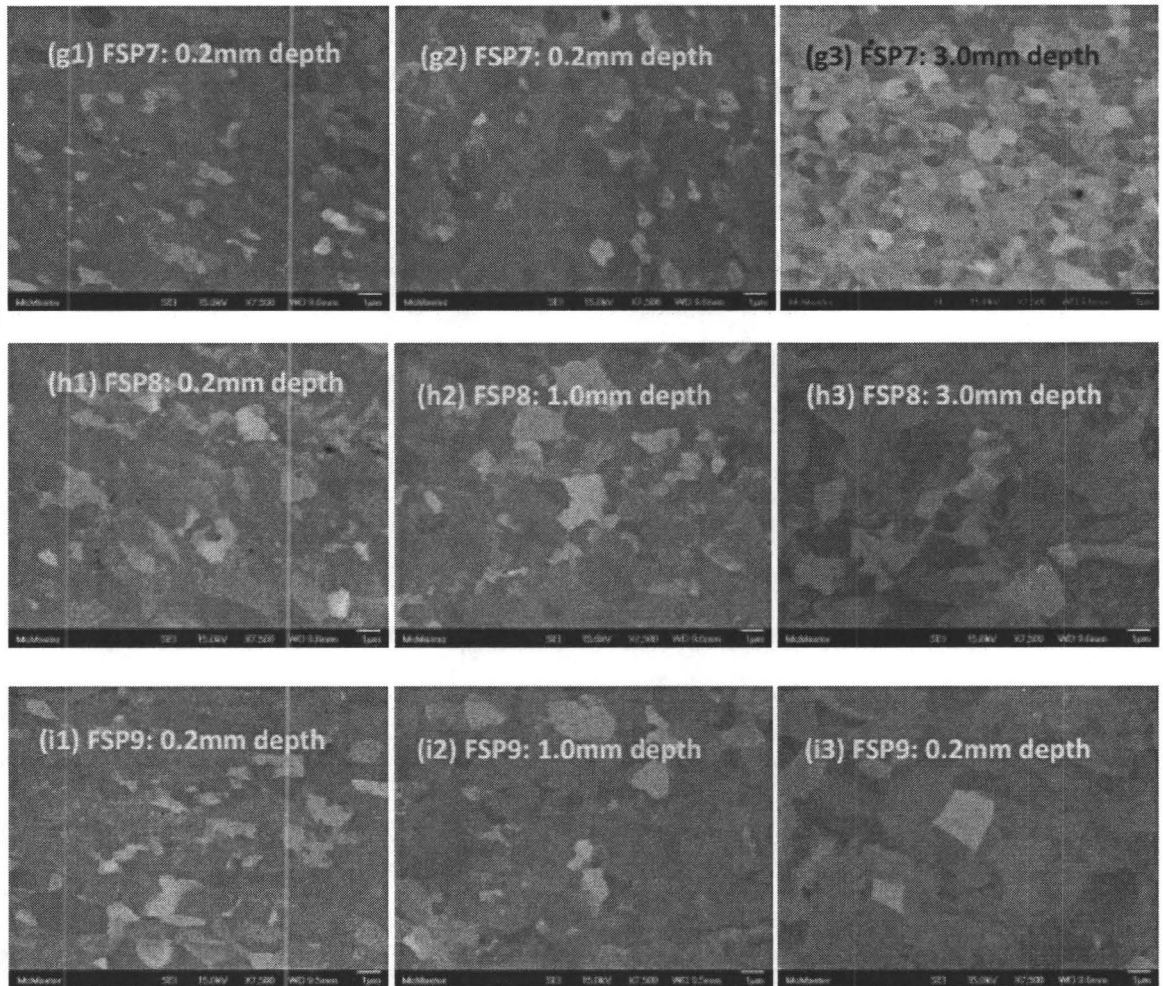


Figure 5-18 g1-i3: Microstructure of FSP samples at different depths (at 7500X)

5.3. TOOL GEOMETRY SELECTION

It is known that an approximation to surface roughness is $R_{th} = f^2 / (8R_n)$. Thus with an increase in R_n (nose radius), the peak to valley surface roughness should theoretically decrease. This statement is true to a certain extent. It has been observed that

the nose radius has minimal influence in surface roughness below a limiting feed rate. The limiting feed rate depends on the workpiece material properties. For example depending on material surface properties, surface roughness may increase with a larger nose radius tool. This observation has generally not been widely observed in SPDT to date based on the author’s knowledge. Figure 5-19 shows the theoretical peak to valley surface roughness and measured peak to valley surface roughness for a 1.5mm nose radius tool and 0.5mm nose radius tool at 20µm/rev and 1µm/rev feed rate on a 54% cold rolled sample.

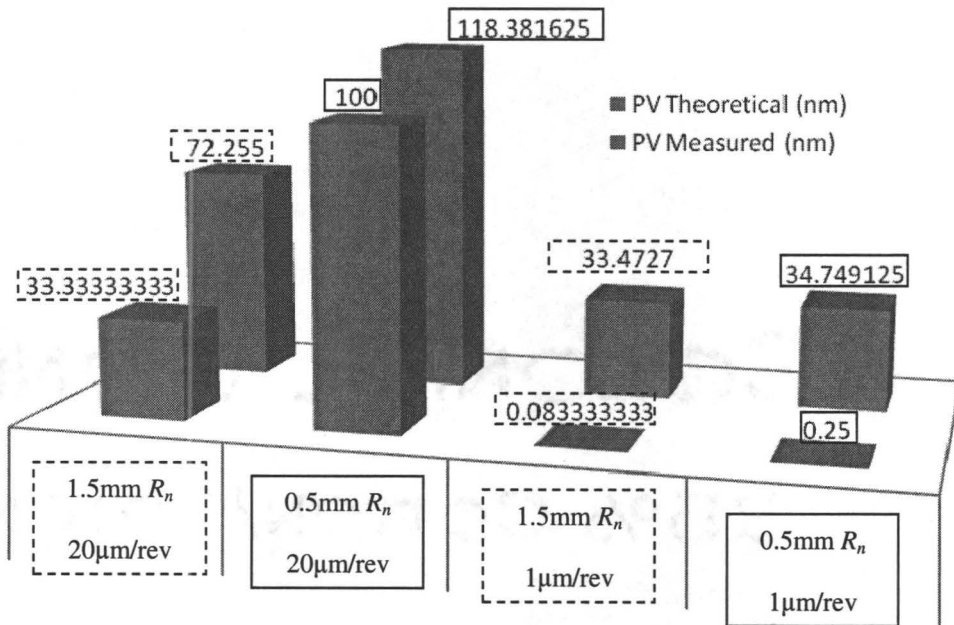


Figure 5-19: Effect of nose radius on peak to valley (PV) surface roughness.

It is worth noting that at a higher feed rate ($20\mu\text{m}/\text{rev}$), the measured and theoretical surface roughness follows a trend; however, the difference between these values is a minimum when a smaller nose radius is used. At a lower feed rate, the measured values are nearly equal despite a deviation from the theoretical value. This paradox on the effect of nose radius can be explained by looking at the scale of material being cut by the tools. In a larger nose radius, severe chip thinning takes place, opposed to a larger nose radius tool as can be seen from Figure 5-18.

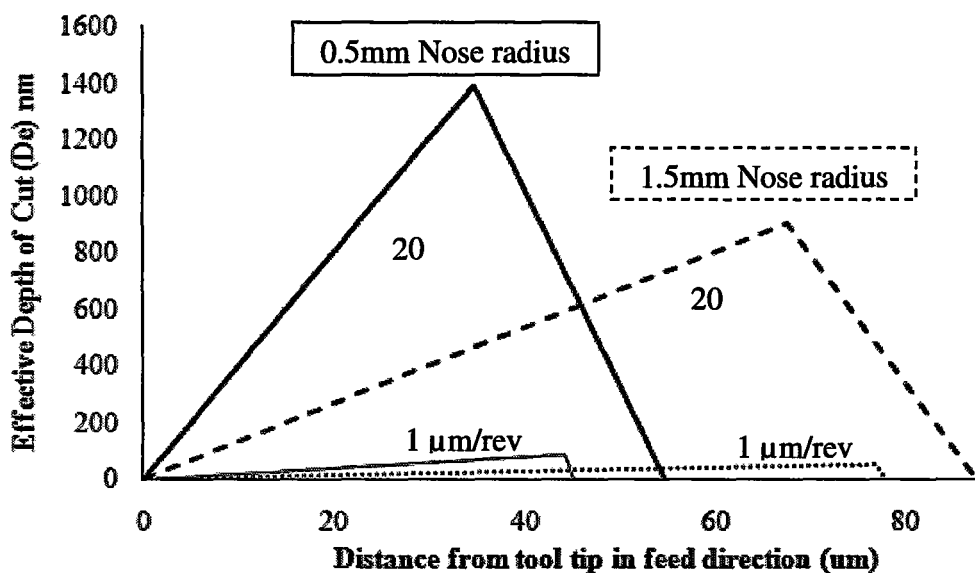


Figure 5-20: Chip thinning is more in larger nose radius tool

Thus a larger fraction of the tool / workpiece contact zone will experience a negative rake angle and a larger nose radius tool will generate more thrust force compared to cutting force as shown in Figure 5-21 for 1.5mm and 0.5mm nose radius tool when

machining furnace cooled and 54% cold rolled 99.87% aluminum alloy at 1000RPM and 2 μ m depth of cut.

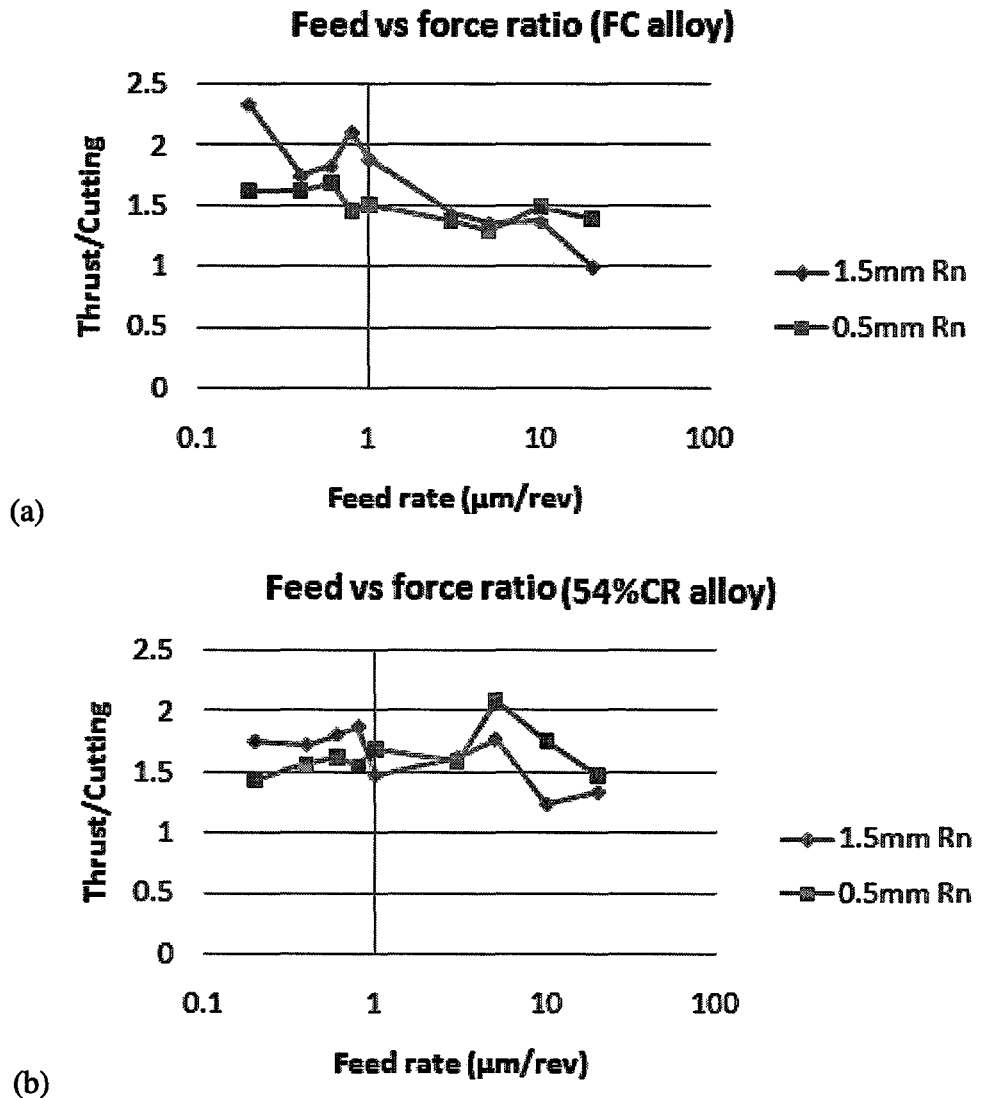
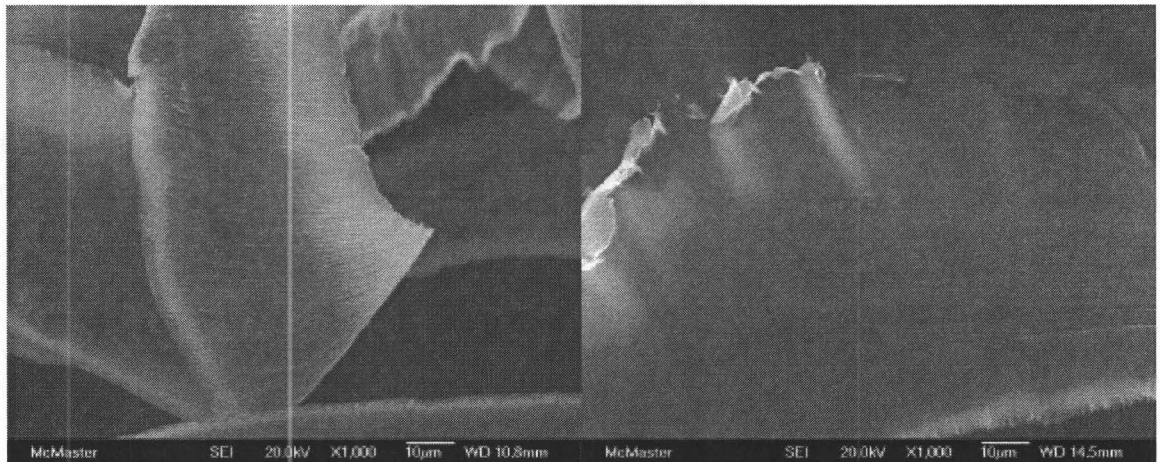


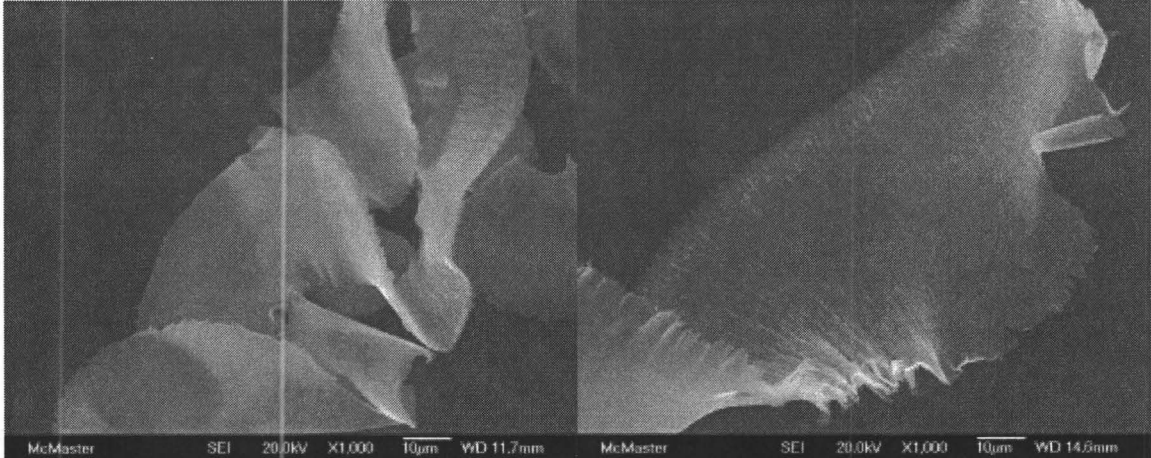
Figure 5-21: Ratio of thrust force and cutting force on FC and 54% CR 99.87% aluminum alloy for different tools

With the reduction in feed rate the uncut chip thickness decreased resulting in an increased thrust force. Thus a thin section of the workpiece will have less stress concentrating defects to produce a chip. This will eventually result in side flow. Moreover, in a carefully solidified alloy with fewer defects present will result in poor surface roughness when a larger nose radius tool is used at a lower feed rate. Figure 5-22 shows chips produced from two different tools at 1000RPM, $2\mu\text{m}$ depth of cut and at different feed rates from a 54% cold rolled alloy. It is observed from Figure 5-22 that larger nose radius tools will generally result in an increased amount of edge serration on the chip. Edge serration increases with a reduction in feed rate. Details on the effect of tool geometry on surface roughness will be discussed further in Section 5.4.3.



(a). 0.5mm Rn, $20\mu\text{m}/\text{rev}$

(b). 1.5mm Rn, $20\mu\text{m}/\text{rev}$



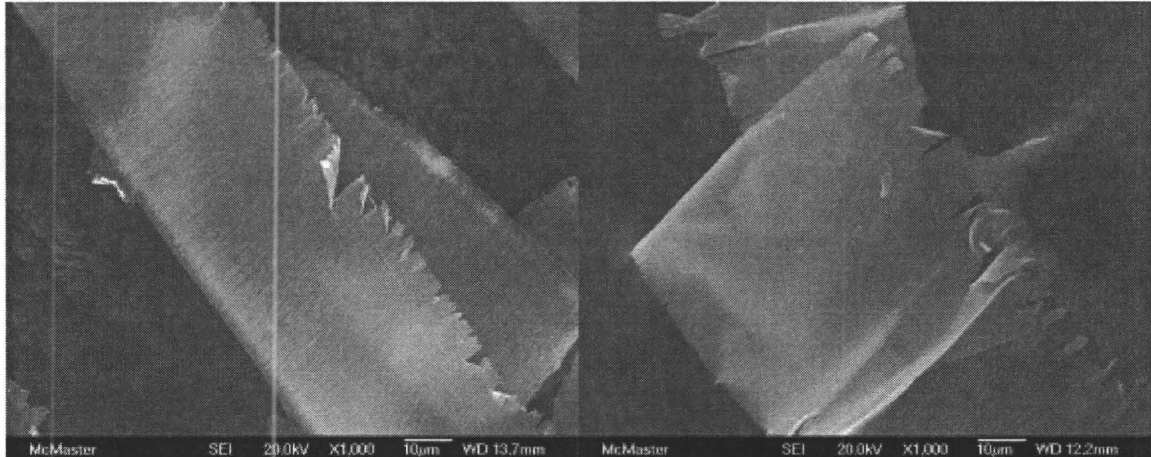
(c). 0.5mm Rn, 10µm/rev

(d). 1.5mm Rn, 10µm/rev



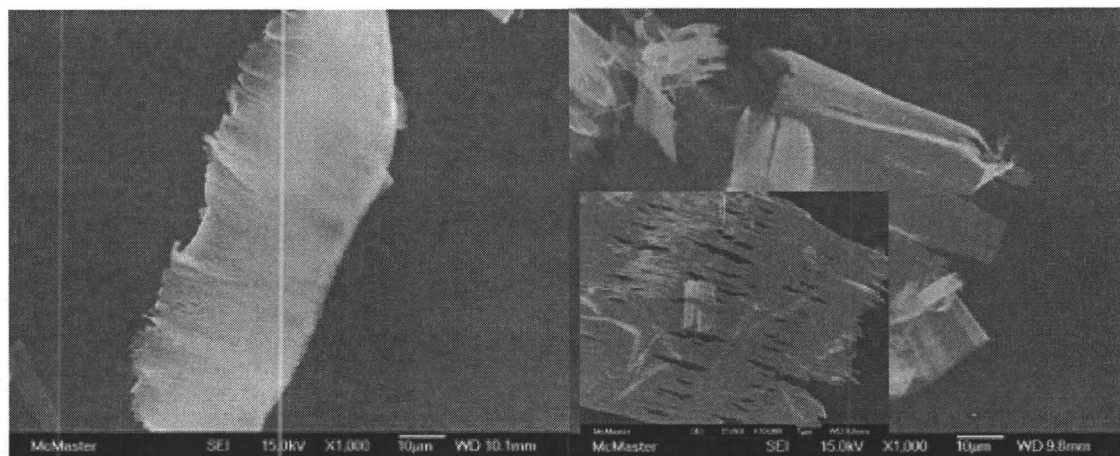
(e). 0.5mm Rn, 5µm/rev

(f). 1.5mm Rn, 5µm/rev



(g). 0.5mm Rn, 3µm/rev

(h). 1.5mm Rn, 3µm/rev



(i). 0.5mm Rn, 1µm/rev

(j). 1.5mm Rn, 1µm/rev

Figure 5-22: Chip edge serration is higher with larger edge radius tool (54% CR material)

The effect of tool nose radius has been considered when designing the 3rd special diamond tool within the MMRI. Previously reported flat end tools had a length of 1.2mm and a pointed corner (Section 2.6.) and were primarily used to study the effect of orientation angle between the tool and workpiece [Nishiguchi et al., 1988; Masuda et al., 1989]. However, the motivation of this thesis is different from the previous studies. In this case the flat end tool was designed to address the side flow of the material. Thus the tool and workpiece need to be parallel. The flat edge of the tool should remove any side flow which has a higher peak to valley difference. Thus it is critical to have the tool setup parallel to the workpiece. This was achieved by the rotation of the B-Axis of the machine tool. Moreover, as the flat end tool will have multiple points of contact; tool wear can be ignored for a longer period of time as there will be a greater probability of a fresh edge available to perform the machining. When designing such a tool, the flat

secondary edge was selected to be of 0.5mm length. The reason for this value is based on the discussion with the manufacturer in terms of capabilities for honing the tool, supporting the edge and considerations for the setting up of the tool. The length should be large enough to address the feed rate of the process. However the tool cannot be shorter than a certain value as it becomes difficult to measure the parallelism of the tool and workpiece. Based on the conclusions drawn from Figure 5-19 and Figure 5-18, a radius of 0.5mm has been selected as the nose radius as the smaller nose radius tool results in less chip thinning as well as less side flow. This radius will provide enough strength as a tool with similar nose radius has been successfully tested in this study. The three tools used in this study are shown in Figure 5-23. Figure 5-24 shows chips produced using a flat end tool on a 54% cold rolled aluminum alloy. It can be seen from Figure 5-24 that the flat end tool is capable of removing excess side flow material. Without side flow, the chip shape is very similar to the 0.5mm round nose tool as shown in Figure 5-22 (i).

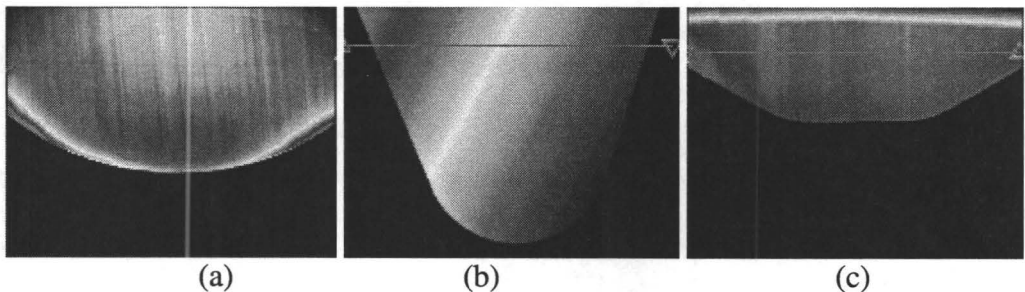


Figure 5-23: Optical images of three different tools. (a) 1.5mm nose radius. (b) 0.5mm nose radius and (c) 0.5mm nose radius with 0.5mm flat secondary edge. (no scale)

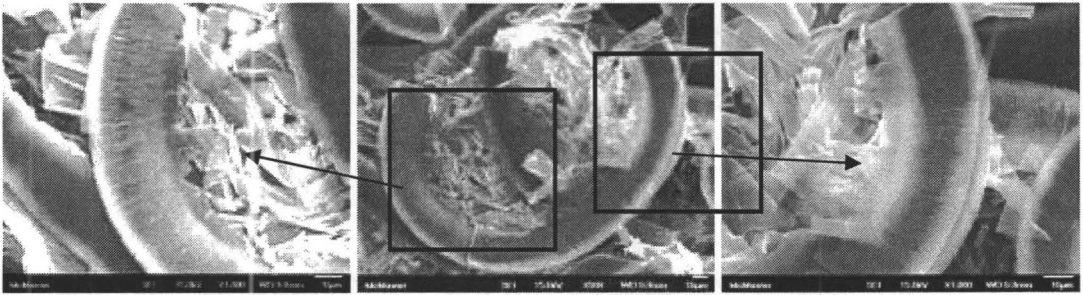


Figure 5-24: Chips produced by 0.5mm Rn and 0.5mm flat end, $1\mu\text{m}/\text{rev}$ (54% CR material)

5.4. SURFACE ROUGHNESS

Once the workpiece material and cutting tools have been designed and selected, it is important to select the appropriate cutting parameters such as RPM, depth of cut and feed rate. Among the cutting parameters, feed rate has a direct influence on surface roughness. Thus the initial experiments were performed on a 54% cold rolled 99.87% aluminum sample to optimize the depth of cut and RPM for a 1.5mm and 0.5mm nose radius tools. Once the depth of cut and RPM were fixed, series of tests were conducted with different feed rates for different tool/workpiece combinations to find the optimized surface roughness.

5.4.1. Optimum cutting parameters based on roughness

Initial tests were conducted at 1000RPM and $5\mu\text{m}/\text{rev}$ at different depths of cut ($1\mu\text{m}$, $2\mu\text{m}$, $3\mu\text{m}$ and $5\mu\text{m}$) on a 54% CR 99.87% aluminum with the 1.5mm and 0.5mm nose

radius tool. It was observed that at 2 μm of depth of cut both tools produce improved surface roughness as shown in Figure 5-25.

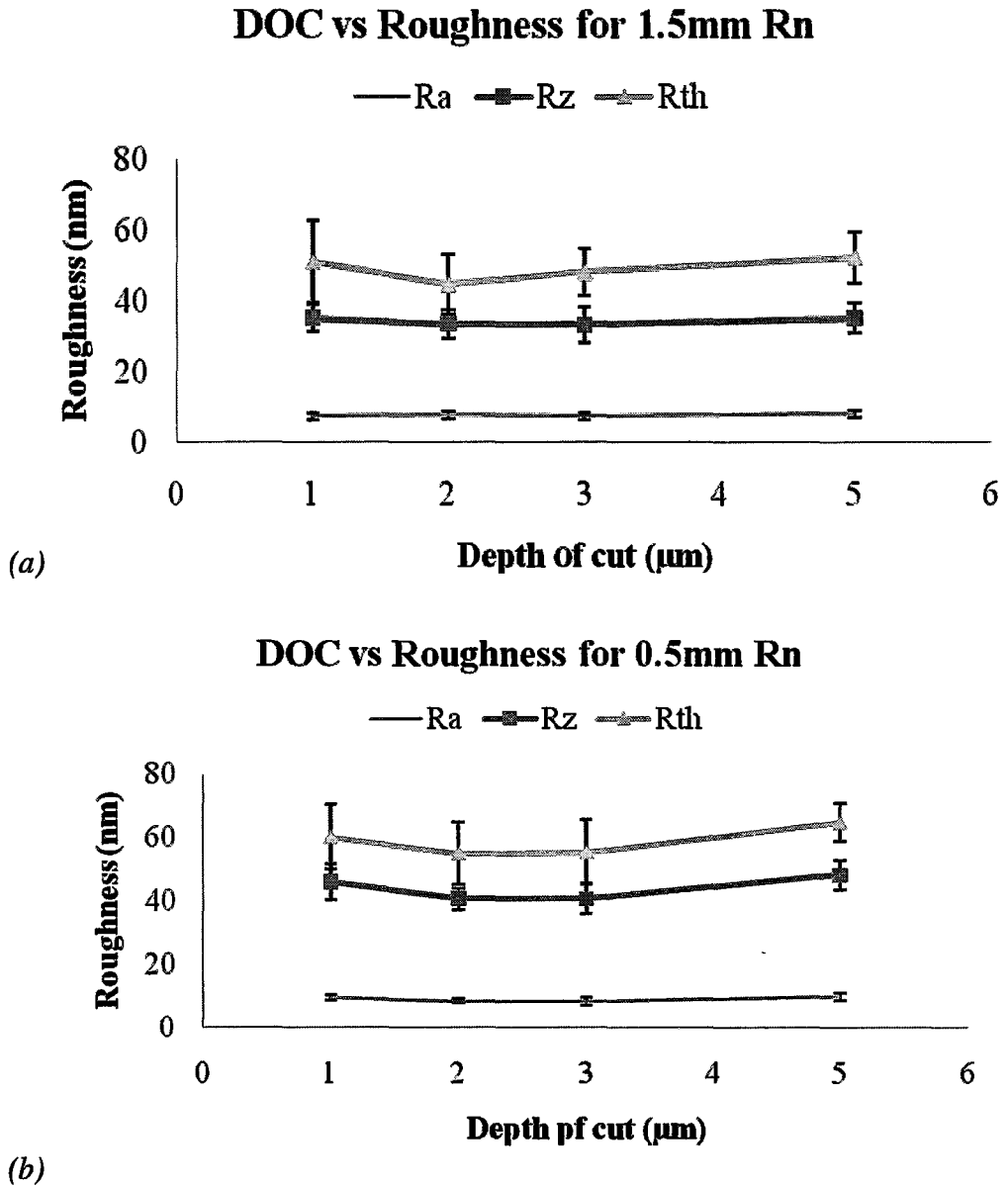


Figure 5-25: Effect of nominal depth of cut (DOC) on SPDT

Several other cutting tests have been performed to select the optimum RPM (500RPM, 800RPM, 1000RPM, 1200RPM and 1500RPM) while depth of cut was kept fixed at $2\mu\text{m}$ while varying the feed rate ($20\mu\text{m}/\text{rev}$, $10\mu\text{m}/\text{rev}$, $5\mu\text{m}/\text{rev}$, $3\mu\text{m}/\text{rev}$ and $1\mu\text{m}/\text{rev}$). It is well known from various experiments and reports that cutting speed or RPM has minimal effect on surface roughness in SPDT [Roblee, 2007]. Similar trends have been observed in this study as shown in Figure 5-24.

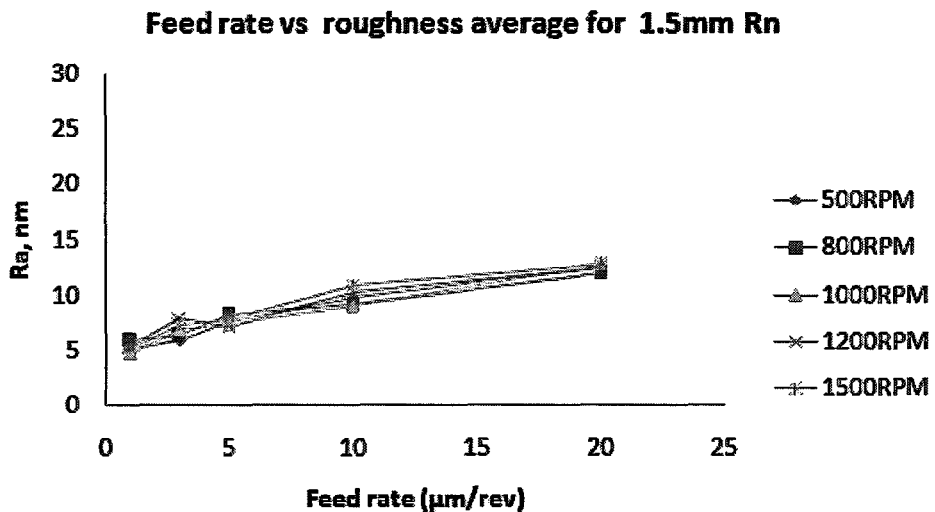


Figure 5-26: Effect of RPM on SPDT

This observation is very important and answers a very common question regarding single point diamond face turning operations where cutting speed is continuously changing throughout the process. The variation in cutting speed does not have a significant effect on surface roughness on SPDT. The advantage of keeping the speed constant is that it is easier to keep the thermal and dynamic profile of the machine constant over the whole cut. This is very important to achieve the desired form accuracy.

Figure 5-25 shows a 3D plot of surface roughness at different feed rates and RPMs for a 1.5mm and 0.5mm nose radius tool at 2 μ m depth of cut. It has been observed that 1000RPM is the best choice of cutting speed for both tools. However, Figure 5-24 also suggests a trend of improved surface roughness with a decrease in feed rate. Thus a further study was conducted with a wide range of feed rates at 1000RPM and 2 μ m depth of cut for all possible tool workpiece combinations.

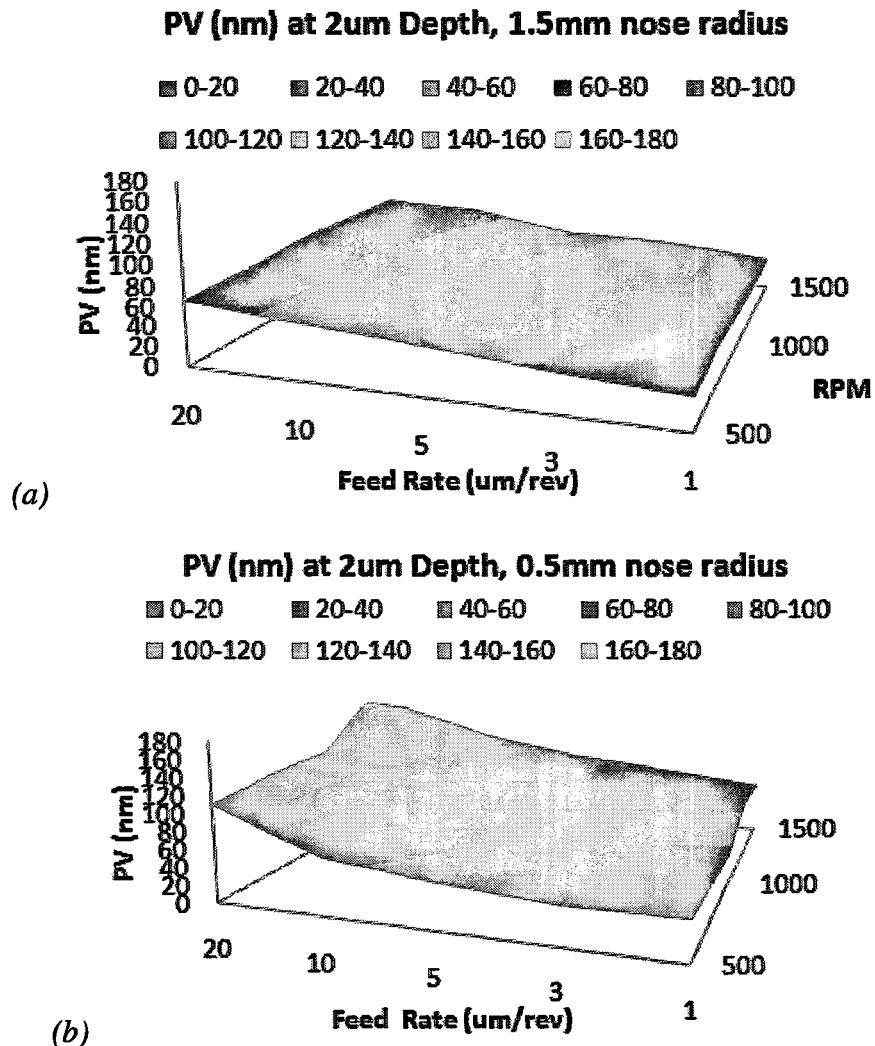
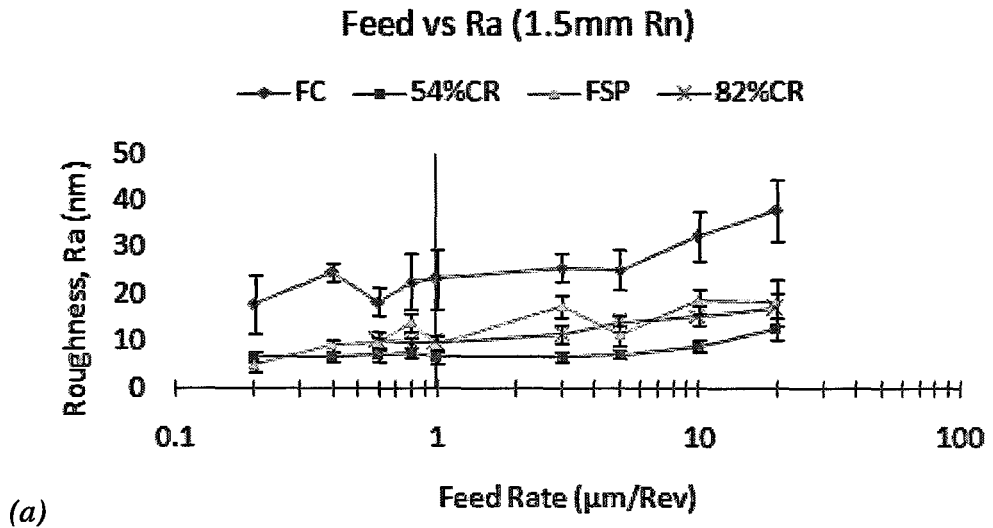


Figure 5-27: 3D plot for optimum RPM in SPDT. (a) for 1.5mm nose radius tool and (b) for 0.5mm nose radius tool

5.4.2. Effect of material property

Figure 5-28 (a), (b) and (c) show the semi-log plot of average (R_a), ten point average (R_z) and peak to valley (R_{th}) surface roughness respectively for furnace cooled, 54% cold rolled, friction stirred and 82% cold rolled 99.87% aluminum alloy for different feed rates at 1000RPM and 2 μ m depth of cut with a 1.5mm nose radius tool.



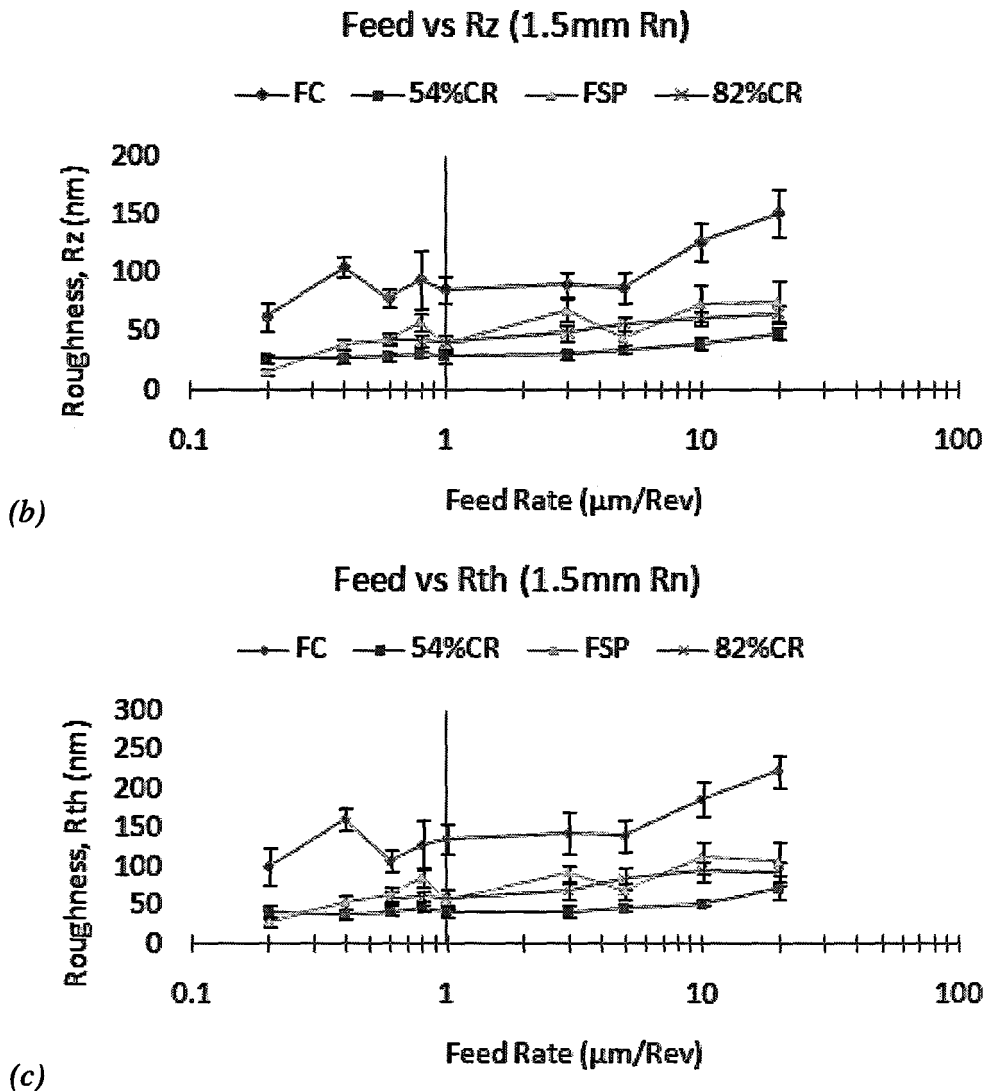


Figure 5-28: Feed rate vs roughness curve for 1.5mm nose radius tool for FC: Furnace Cooled, 54% CR: 54% Cold rolled, FSP: Friction stir processed and 82% CR: 82% cold rolled aluminum.

It is clear from Figure 5-28 that the 54% cold rolled alloy shows the most consistent and best surface roughness up to a 0.4 $\mu\text{m}/\text{rev}$ feed rate. Friction stirred samples show a slight improvement in surface roughness at 0.2 $\mu\text{m}/\text{rev}$. Irrespective of feed rate;

the furnace cooled sample shows the worst surface roughness. Interestingly the 82% cold rolled alloy does not improve the surface roughness. This result was not expected. This suggests that there is a limit to the degree of cold rolling that leads to an improvement in surface finish. Error bars are drawn for 1 standard deviation. To further elaborate on the material microstructure, Figure 5-29 has been redrawn from Figure 5-28, highlighting the 1 μ m/rev feed rate and Figure 5-28 shows the corresponding oblique surface plot. Figure 5-29 and Figure 5-28 clearly show that 54% cold rolled sample gives the most promising surface roughness and is comparable to the FSP aluminum sample.

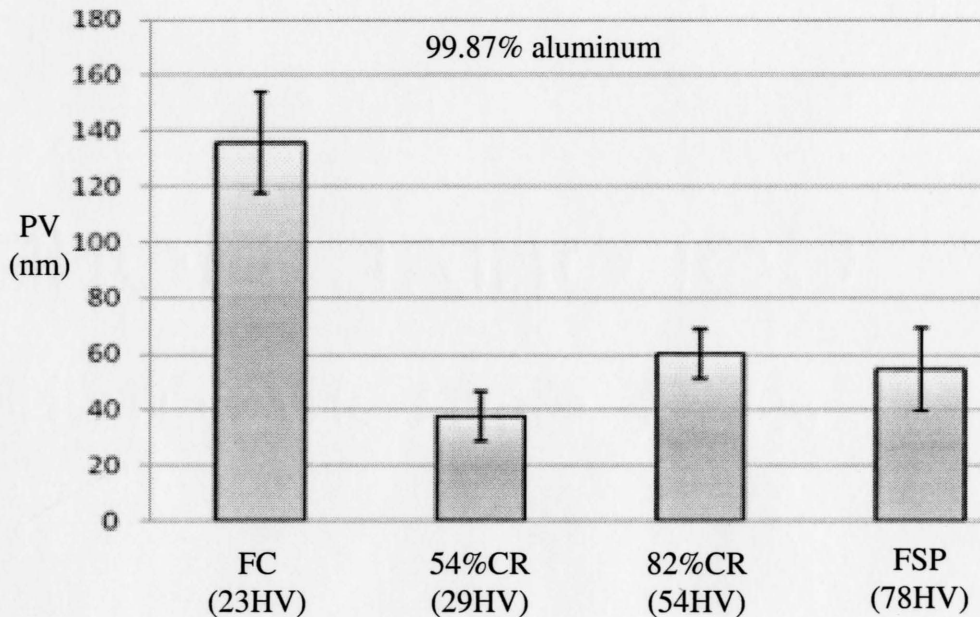


Figure 5-29: Effect of material microstructure in surface roughness

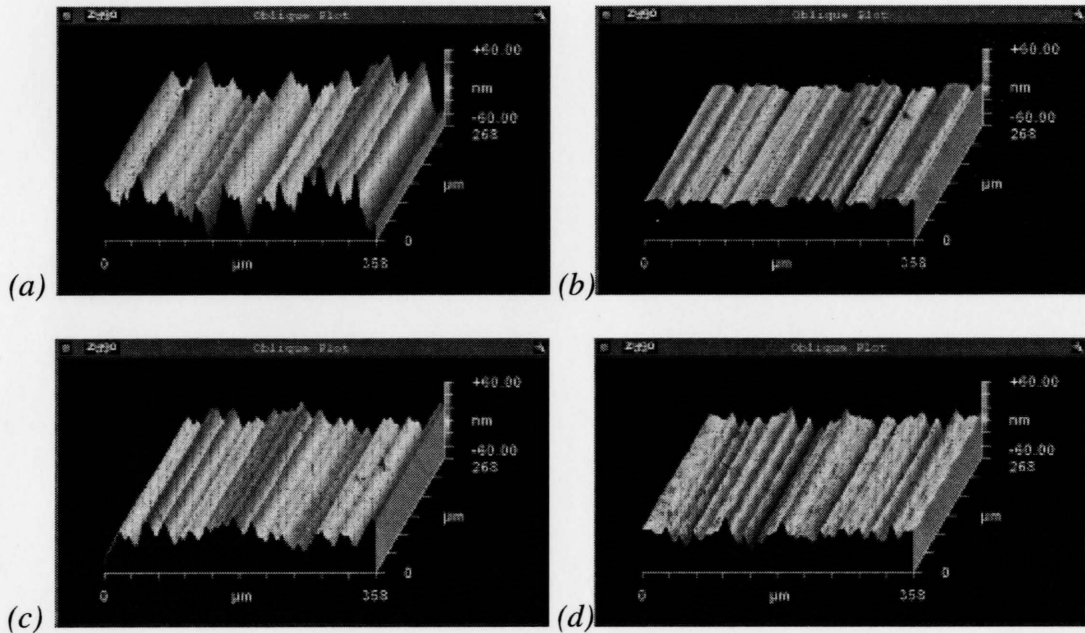


Figure 5-30: Oblique plot of surface profile at 1000RPM, 2 μ m depth of cut and 1 μ m/rev feed rate with 1.5mm nose radius tool for (a) FC aluminum, (b) 54% CR aluminum, (c) 82% CR aluminum and (d) FSP aluminum.

The reason why FC and FSP aluminum gives better surface roughness can be explained by using micro structural aspects of the materials. As stated before (Section 2.3.1), it is well known that dislocation density is minimized on a carefully solidified material and increases with heavy deformation. It has also been discussed that dislocation-dislocation interactions are repulsive and hinder dislocation motion. This increases the strength of the material but represents a loss of ductility. Thus a less ductile material is prone to fracture and it can be assumed that a close geometrical tolerance should be achieved on a strain hardened workpiece material as opposed to a carefully solidified one by producing chips of definite shape. This should reduce the side flow and so improve the surface roughness. This concept is supported from the roughness data

(Figure 5-28 and Figure 5-29) and can be further supported by chip analysis. Figure 5-29 shows the chips produced in the SPDT process of all the four alloys at 1000X magnification.

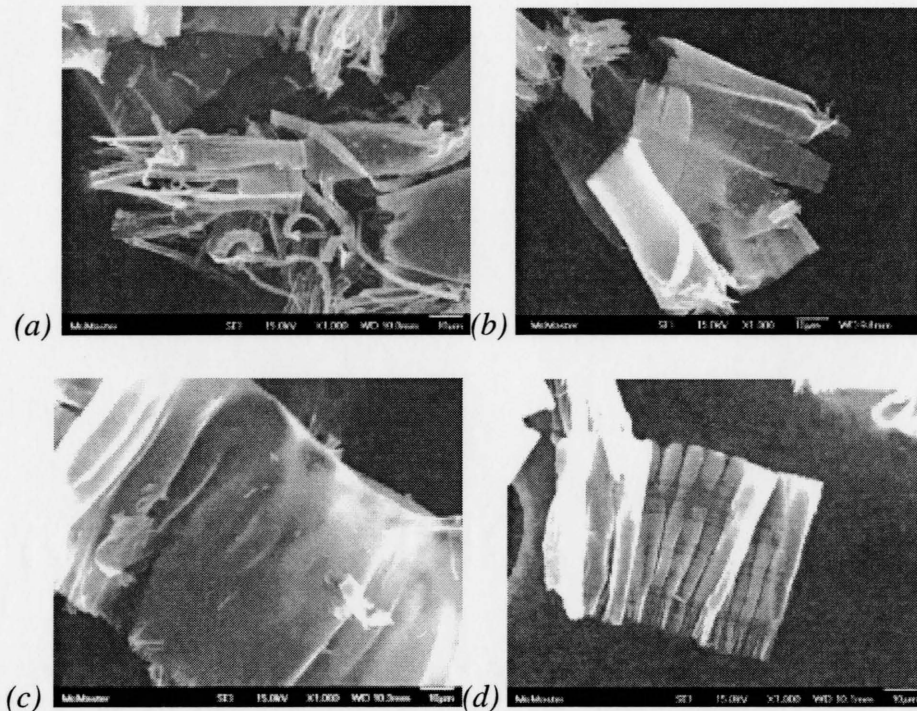


Figure 5-31: Chip produced at 1000RPM, 2µm depth of cut and 1µm/rev feed rate with 1.5mm nose radius tool for (a) FC aluminum, (b) 54% CR aluminum, (c) 82% CR aluminum and (d) FSP aluminium (1000X).

In the FC aluminum alloy, the probability of encountering any defect during chip formation is minimized compared to other alloys. This results in the serration of the chip trailing edge causing the tool to not produce a well-defined chip. Chip serration at the trailing edge is a strong indication of material side flow. For conservation of mass, if the material is not coming out with the chip, some must remain on the machined surface as a

pile up material that eventually leads to a higher peak to valley surface roughness. Figure 5-29 (a) clearly shows the severity of trailing edge chip serration and higher peak to valley roughness as shown in Figure 5-6 and Figure 5-28 (a). This is the result of material pile up or side flow. As the severity of strain hardening increases, the chip edge serration reduces as can be seen from Figure 5-29 (b), (c) and (d). Moreover, self-deformation of the chips also takes place in a response to the velocity gradient along the cutting length of the tool. This will eventually reduce the sticking of the workpiece material to the tool.

Despite the 82% cold rolled alloy generating a more promising chip shape, it does not produce promising surface roughness because of inherent defects induced by the severe cold rolling process. It has been observed that micro fractures are present on the machined surface causing a deterioration of the surface. Figure 5-32 (a) shows micro voids produced from the machining operation. It is believed that the material failed by ductile tearing through void formation and coalescence due to the stress generated in the cutting process. Figure 5-32 (b) shows the back scatter image and where it can be concluded that the void formation took place in the aluminum matrix. Figure 5-32 (c), (d) and (e) show micro cracks at the point of defects on the surface and Figure 5-32 (f) shows that the defects are in the metal matrix. Similar observations are made on FSP aluminum alloy as shown in Figure 5-32 (g).

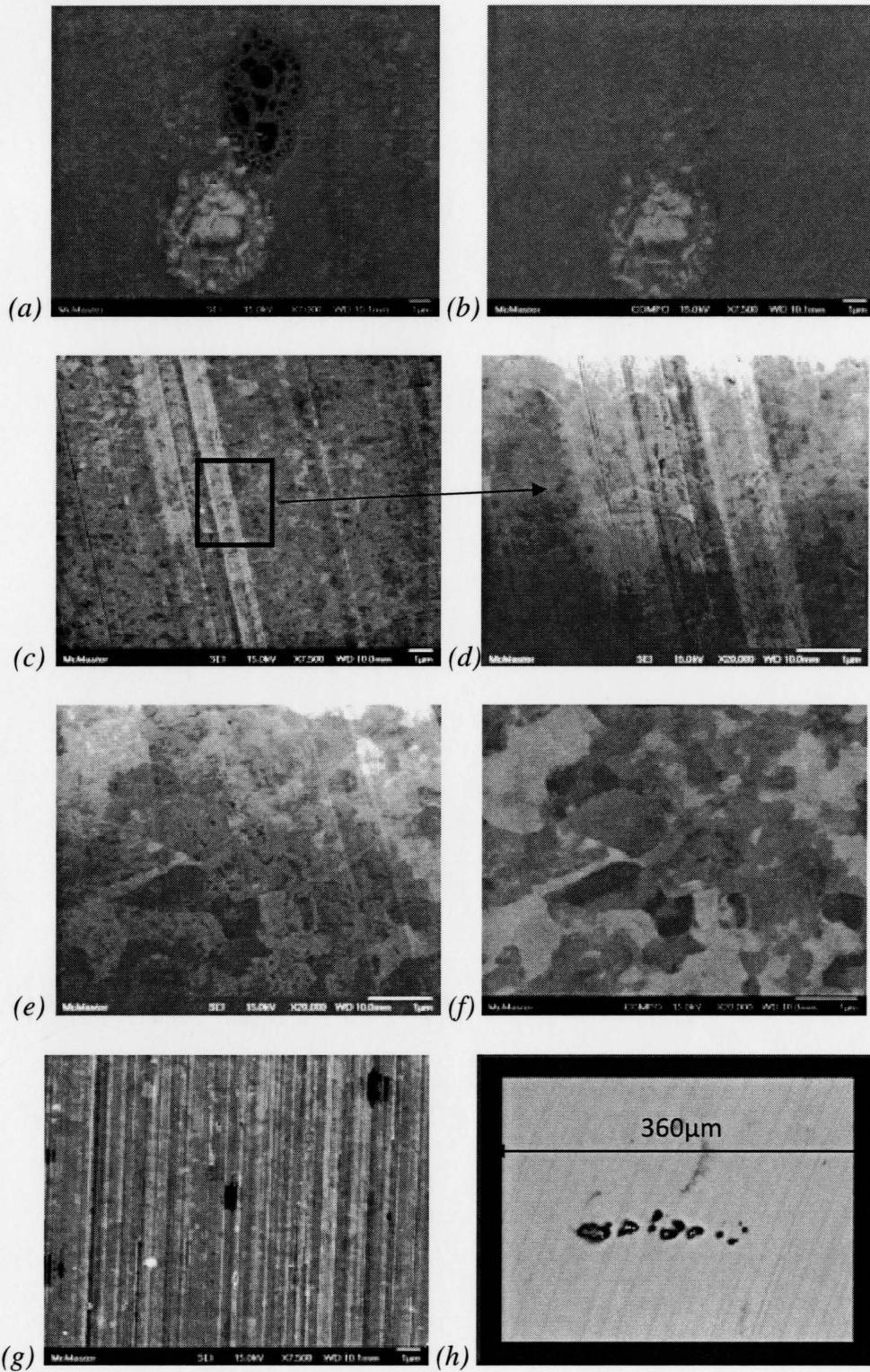


Figure 5-32: Observations on machined 82% cold rolled and FSP 99.87% aluminum

There is ductile tearing by void growth and coalescence. This phenomenon of ductile tearing (or material separation component) has been introduced by Atkins [2003]. Melkote and Subbiah experimented with this concept to validate Atkins model [Subbiah, 2006]. Micro cutting of aluminum was investigated in their study and the oblique chip root was studied using a quick stop device. However, their depth of cut for orthogonal cutting was around 15 μ m with an HSS tool. Strands at the chip-tool interface suggest a failure by ductile tearing leading to chip formation which leaves tearing marks on the machined surface and can be compared with Figure 5-32 (a) and (g) [Subbiah, 2006]. Figure 5-32 (h) shows cracks or voids on the surface. Such voids are usually seen in tensile tests before failing near the necking zone. This is a result of void formation followed by void coalescence that eventually leads to gross failure of the metal. Thus, it is concluded that there is a limit to the degree of cold working up to which there will not be any subsurface damage coming from the mechanical process. If the pre-processing induced defects are present in the surface region, it remains as a signature even after machining and eventually deteriorates the surface quality.

Surface quality is another important aspect while machining the FSP alloy where the grains are in the nanometer range. It has been observed that surface roughness is comparable for 54% cold rolled and friction stir processed (FSP) 99.87% aluminum alloy; however, there is a rainbow pattern in the machined FSP alloy. It is known from conventional machining practice that a rainbow color represents a good surface roughness where the cusp heights are in agreement with the tool nose geometry and

causes a diffraction of light which produces a rainbow of colors. It can be seen from Figure 5-32 (g) that $1\mu\text{m}$ feed marks and ductile tearing is visible under high magnification in the SEM image of the machined FSP alloy. However, it is interesting to note that with FSP grain refinement side flow is completely eliminated. On the other hand, $1\mu\text{m}$ feed marks are not visible for any other workpiece for the same cutting parameters due to side flow. Thus these observations lead to the following question: if side flow is minimized or eliminated, then why does FSP not produce promising surface roughness and generate a rainbow color?

The generation of a rainbow of color can be explained with the help of size effect and redefinition of single point diamond turning (SPDT) for roughing and finishing. Roughing operations in face turning with a round nosed tool can be assumed to be taking place when the relative length of the maximum uncut chip thickness is greater than the average grain size of the workpiece. That is the workpiece is behaving as a continuous material and effects of grain boundaries may exist. On the other hand, when the maximum uncut chip thickness is less than the average grain size of the material, a finishing operation takes place. In most of the polycrystalline materials, grain sizes are large enough to be assumed to be a SPDT with finishing operation. However, in a nano-structured FSP alloy, grain sizes are so small that the process behaves as if a conventional or roughing operation is taking place. This is why while machining FSP alloy, the roughness of the machined surface is comparable with 54% cold rolled alloy mainly because of the fine feed marks. This definition and relative scaling of grain size and

cutting depth can be explained from the perspective of Figure 2-4. Figure 5-33 has been re-drawn from Figure 2-4. If one assumes that the average grain size of a material is approximately $30\mu\text{m}$, then the size effect can be easily discussed as in Section 2.3.1. However, in a nano structured material (say 500nm grain size), the size effect can only be explained by Figure 5-33 (a) and (b).

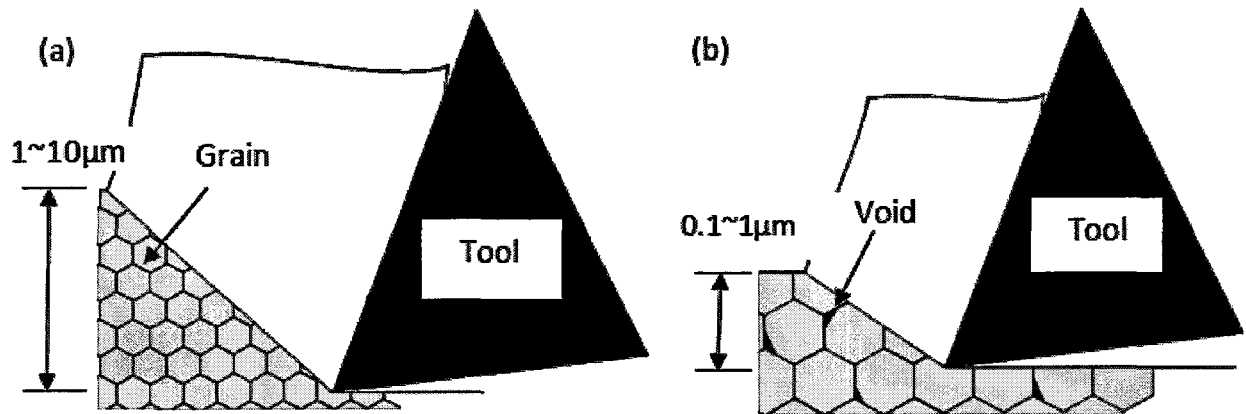
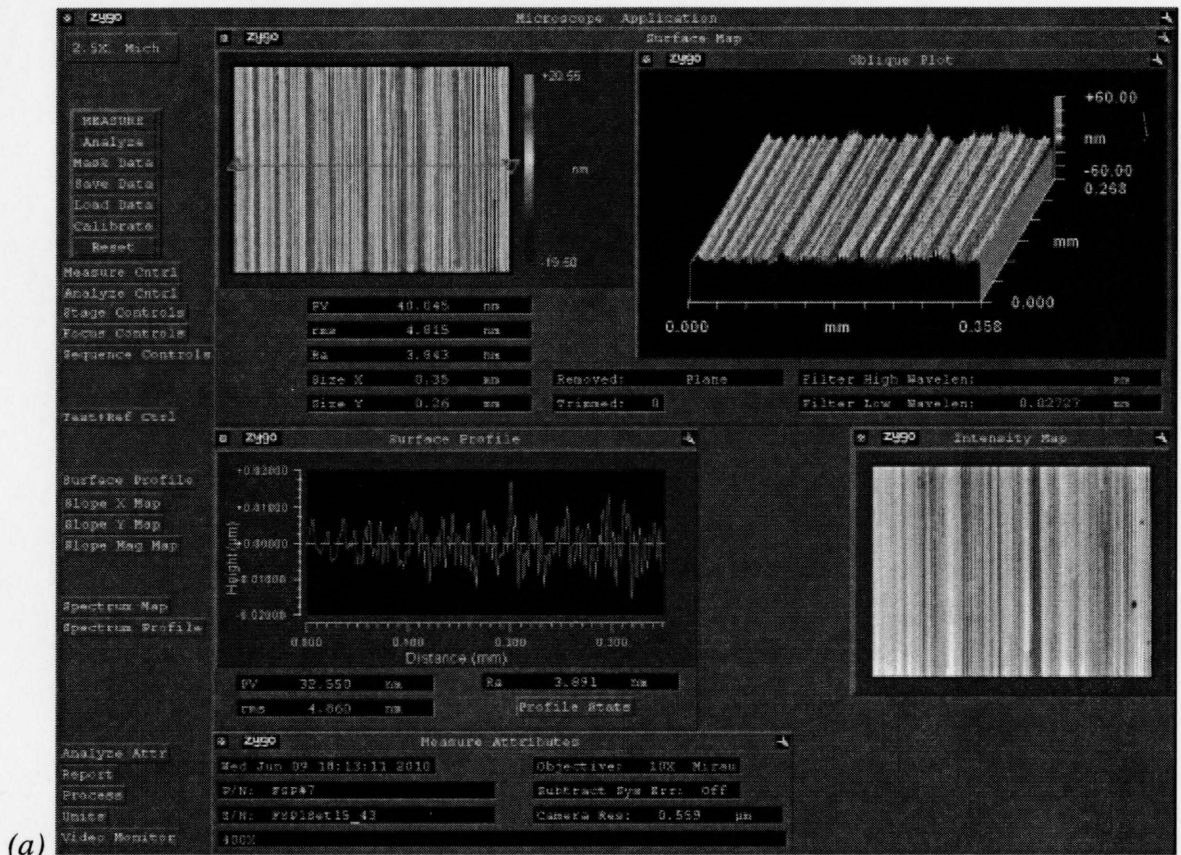


Figure 5-33: Machining of ultra-fine grained material

In Figure 5-33 (a) the relative scale between grains and uncut chip thickness is such that the material behaves as a continuous material. Similarly in Figure 5-33 (b) the effect of grain boundaries are important where a bigger grain may behave as a perfect crystal. Thus, surface roughness only improves with a round nosed tool on the FSP alloy at very low feed rates. Otherwise defects like ductile tearing on the machined surface and grain boundary induced roughness dominates and does not produce a promising surface.

Figure 5-34 (a) shows the interferometer image of a machined FSP alloy at $5\mu\text{m}/\text{rev}$ where the rainbow color is observed. Figure 5-34 (b) shows the amplitude spectrum plot with a distinct spatial frequency of $0.2\mu\text{m}^{-1}$ corresponding to a $5\mu\text{m}/\text{rev}$ feed rate. Despite side flow being eliminated, diffraction of light causes a deterioration of the surface quality and restricts achieving a mirror quality surface.



(a)

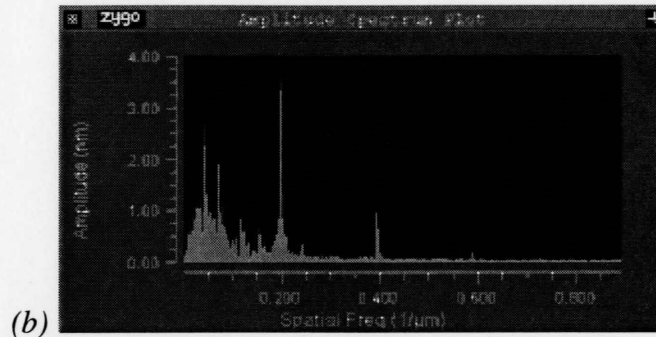
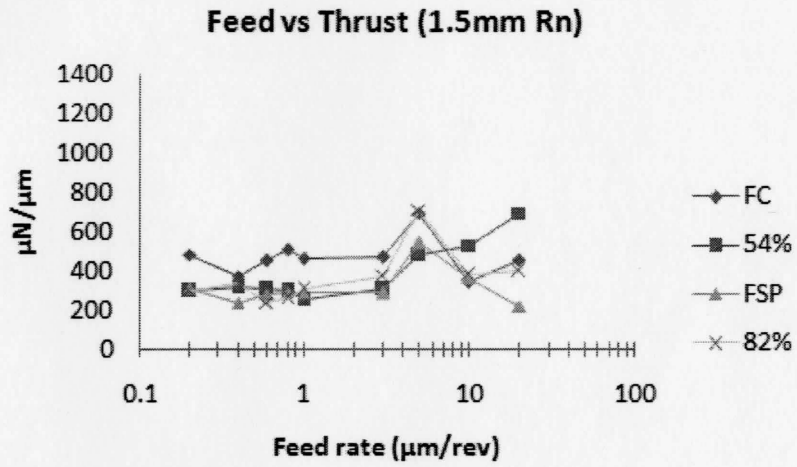
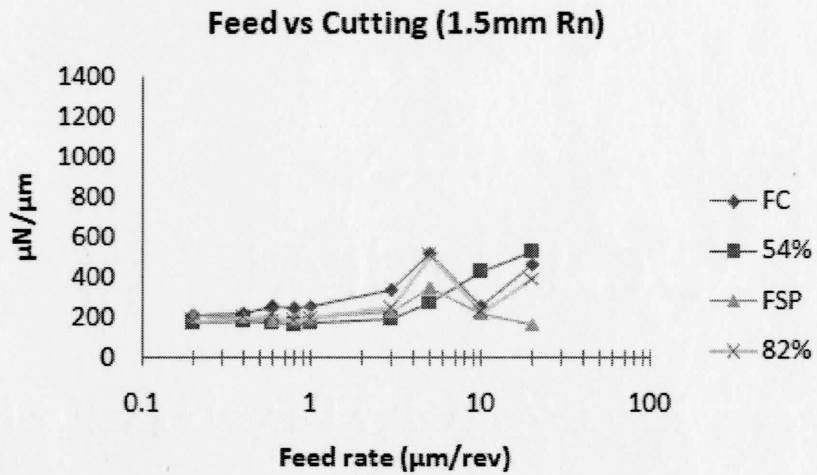


Figure 5-34: Rainbow pattern observed in FSP alloy at 5 μ m/rev

Cutting force data for all the alloys with 1.5mm nose radius tool is shown in Figure 5-35. It can be seen from Figure 5-35 that both the thrust force and cutting force values are higher for the softer furnace cooled alloy. Moreover a similar trend is observed in the ratio of thrust over cutting force. Increased thrust force indicates increased material side flow is taking place which eventually leads to a poorer surface roughness [Ng et al., 2006]. Again, the ratio of thrust force and cutting force is an indirect indication of the friction coefficient. For a known rake angle (α), the friction angle (β) can be estimated according to Figure 2-9. The ratio of thrust force and cutting force is always greater than or equal to 1 in all the cases suggesting size effect resulting from edge roundness (Section 2.3.2).



(a)



(b)

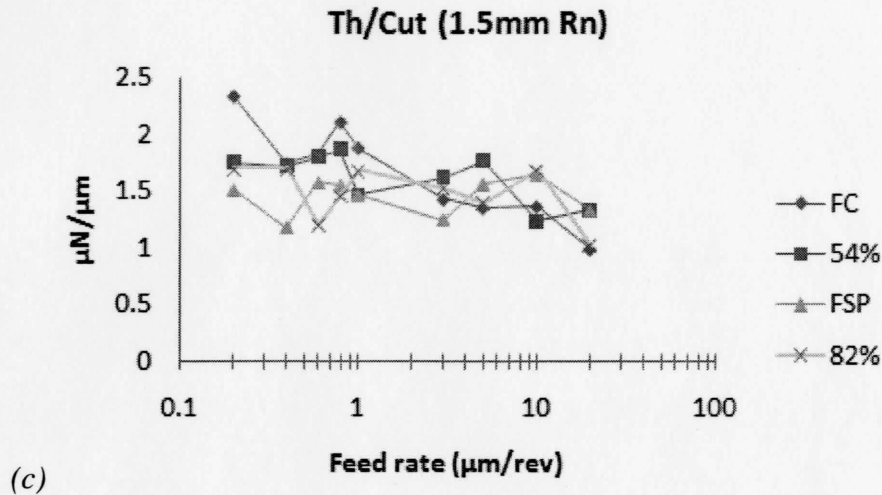


Figure 5-35 Feed rate vs force curves for 1.5mm nose radius tool for FC: Furnace Cooled, 54% CR: 54% Cold rolled, FSP: Friction stir processed and 82% CR: 82% cold rolled aluminum.

Addressing material properties in cutting force models has been a long standing issue until the recent model proposed by Atkins [2003] where the author introduced a new term to address material property (discussed in Section 2.5.4.). Atkins [Atkins, 2003] advised a flow chart on how to apply the model from the force data at different uncut chip thicknesses. A similar approach has been adopted in this SPDT study and it was found that the model can accurately predict how the material is going to respond with the change in microstructure. It has been discussed previously that heavy deformation increases the dislocation density and would eventually lead to higher yield strength of the material as well as ease of chip formation because of an increased number of active slip planes. Figure 5-36 shows the calculated results. The dotted bars show yield strength of the aluminum alloys increasing with the strain hardening and is directly related to surface generation energy. Thus the new model of material separation criteria also supports the

hypothesis and Surface generation energy, R (J/m^2) can now be used as information to describe machinability and can be a direction for future work.

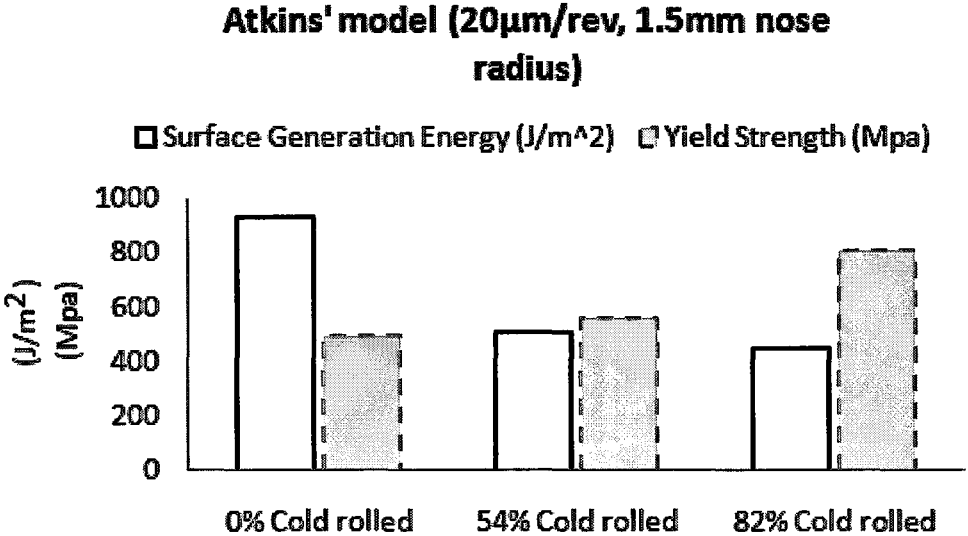
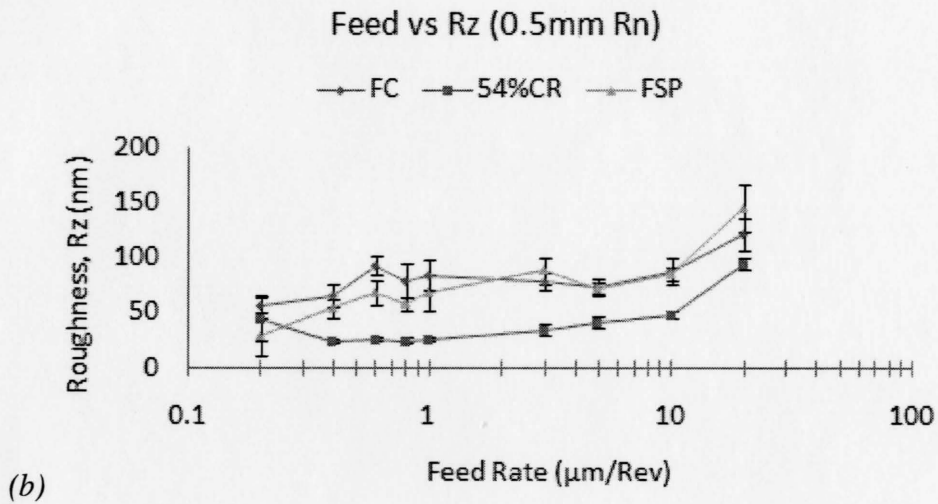
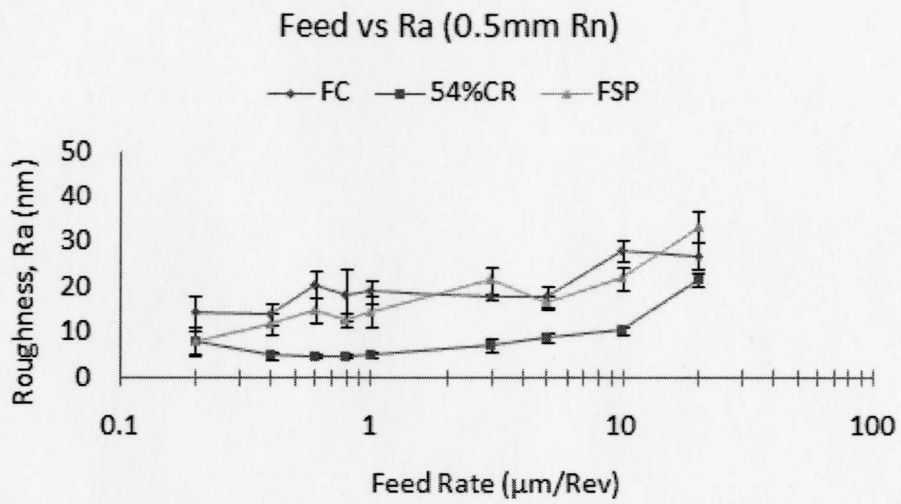
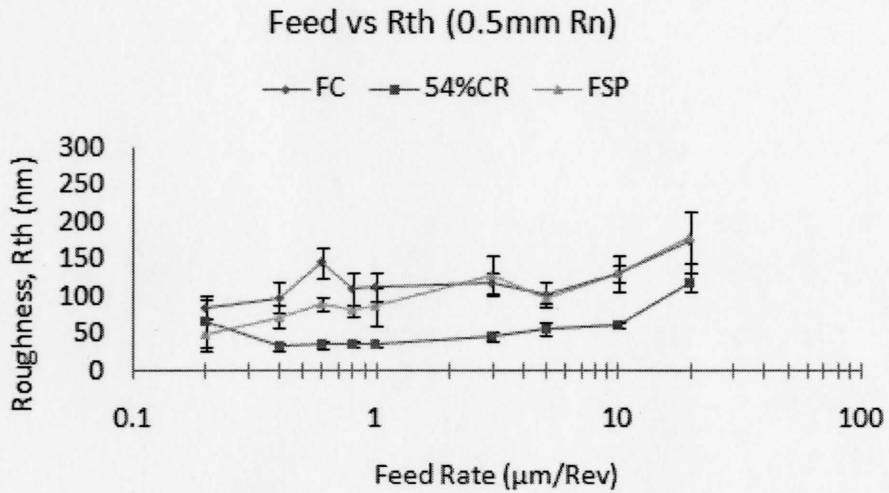


Figure 5-36: Atkins' model verification

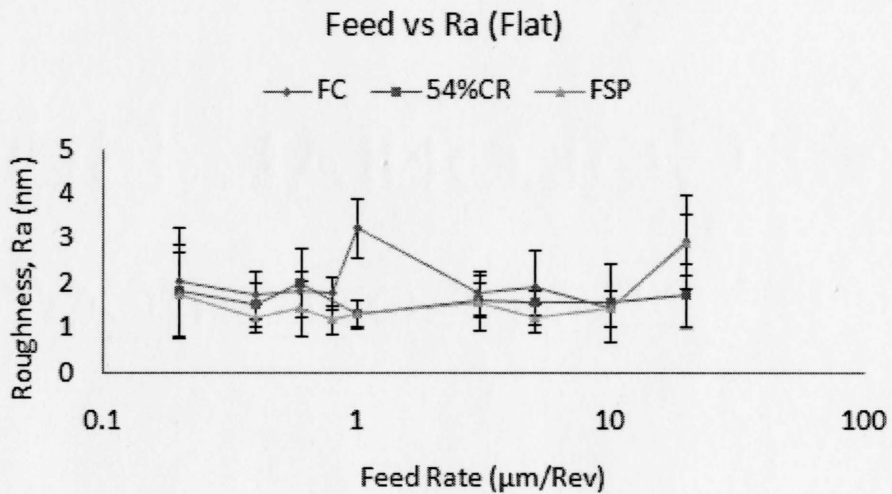
Similar trends in surface roughness have been observed when FC, 54%CR and FSP aluminum alloys are being machined by the 0.5mm nose radius tool (Figure 5-37) and flat end tool (Figure 5-38). 82% cold rolled alloy has not been considered for further study as it did not show any improvement in surface roughness. Irrespective of the feed rate, the furnace cooled alloy produced a poor surface finish because of excessive side flow. The 54% cold rolled sample gives promising surface roughness for all the tool geometries.



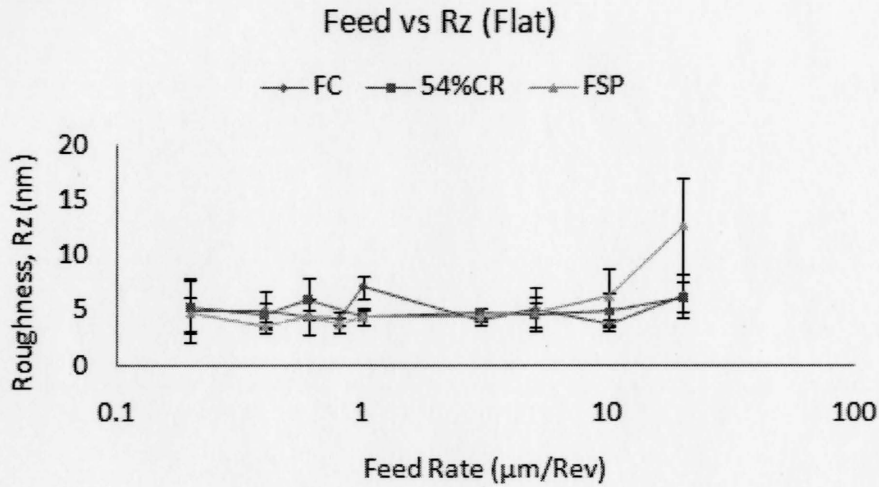


(c)

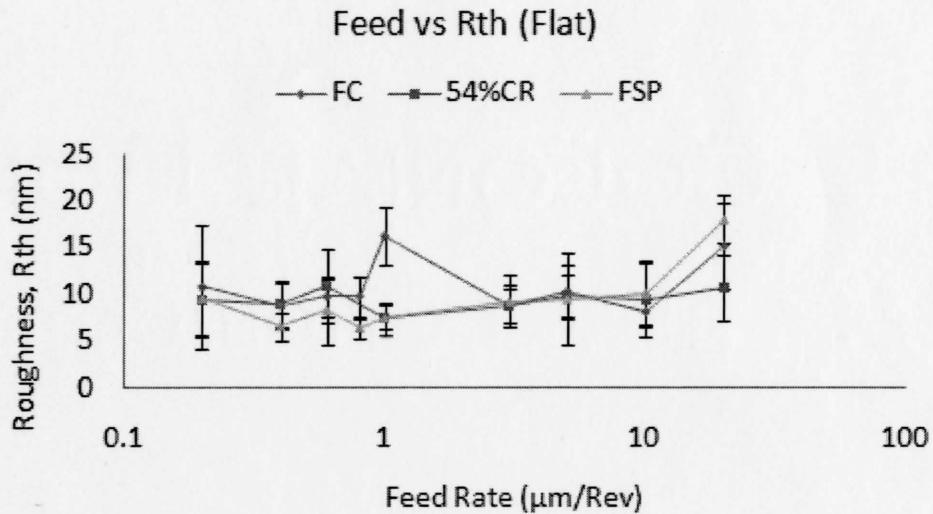
Figure 5-37: Feed rate vs roughness curve for 0.5mm nose radius tool for FC: Furnace Cooled, 54% CR: 54% Cold rolled, FSP: Friction stir processed 99.87% aluminum.



(a)



(b)



(c)

Figure 5-38: Feed rate vs roughness curve for Flat end tool for FC: Furnace Cooled, 54% CR: 54% Cold rolled, FSP: Friction stir processed.

The friction stir alloy shows promising results at very low feed rates with the round nosed tools. However, the significant improvement in surface roughness occurs when a flat end tool is used against a friction stir sample as shown in Figure 5-38. Peak to valley surface roughness less than 5nm and average surface roughness less than 1nm has been achieved with this combination. More details on flat end tools will be discussed in

the following section. For the round nosed tool, the surface roughness is higher for the furnace cooled alloy, followed by FSP alloy and 54% cold rolled alloy. However, with the flat end tool the FSP alloy shows the most promising result produced followed by the 54% cold rolled sample and furnace cooled sample. The reason for such an improvement can also be discussed based on tribological compatibility. Tribological compatibility is related to the capacity of two surfaces to adapt to each other during friction, providing wear stability without surface damage to the two components of the specific tribo-system, for the longest period of time [Bushe and Kopitko, 1981]. During FSP and cold rolling, surface hardening and grain refining takes place. Additional surface hardening and grain refining will occur during machining. The end result is a very hard nano-structured layer. During dynamic formation of this layer adhesive interaction with the cutting tool is diminished as shown by the chips characteristics. This is a typical improvement resulting from a higher degree of tribological compatibility in the tool/chip tribo-system. Because tribological compatibility is achieved in FSP and cold rolled sample, surface finish improves dramatically.

On the other hand the coarse grain boundaries present in furnace cooled and cold rolled alloys plays a vital role in defining surface roughness. It is believed to be taking place because of the anisotropic nature of the material at that small scale of cutting. Lee and Cheung [Lee et al., 1999] studied material induced vibration and observed that different orientations of crystallographic structure has an effect on the diamond turning process. In this study, a strong presence of material induced surface roughness has been

observed while machining 99.87% furnace cooled pure Aluminum which is polycrystalline in structure with a grain size of approximately 300 μm (Figure 5-1). It is well known that for a dislocation to pass from one grain to other, with different orientations, dislocations will have to change their direction of motion. A stress concentration ahead of a slip plane in one grain is most likely the active source of new dislocation in an adjacent grain [Callister, 1997]. Figure 5-39 highlights this statement by showing how the slip lines are being arrested at the grain boundary and at the same time seizure of deformation at the grain boundary is shown with SEM and interferometer images while performing a micro-hardness test on 99.87% furnace cooled Aluminum.

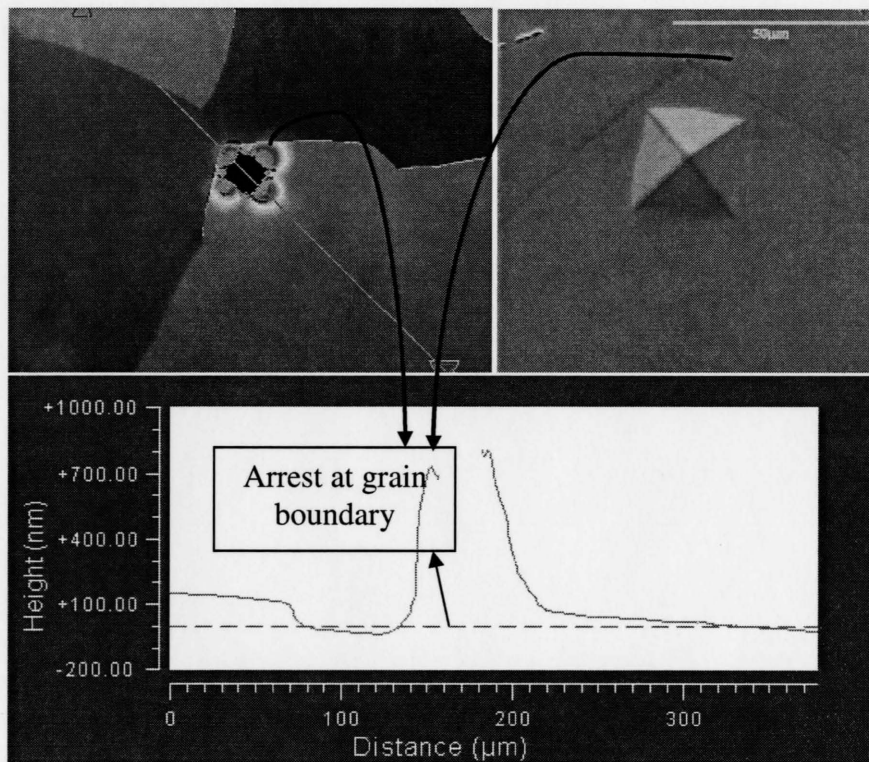


Figure 5-39: Arrest of plastic deformation resulting from micro-indentation on furnace cooled 99.87% Aluminum at grain boundaries.

Figure 5-40 shows the surface roughness induced from a mismatch between the grain boundaries. It has also been concluded that grain boundary induced roughness can be as high as 34.182nm in the cutting direction (1000RPM, 5 μ m depth and 5 μ m/rev feed with 1.5mm nose radius tool).

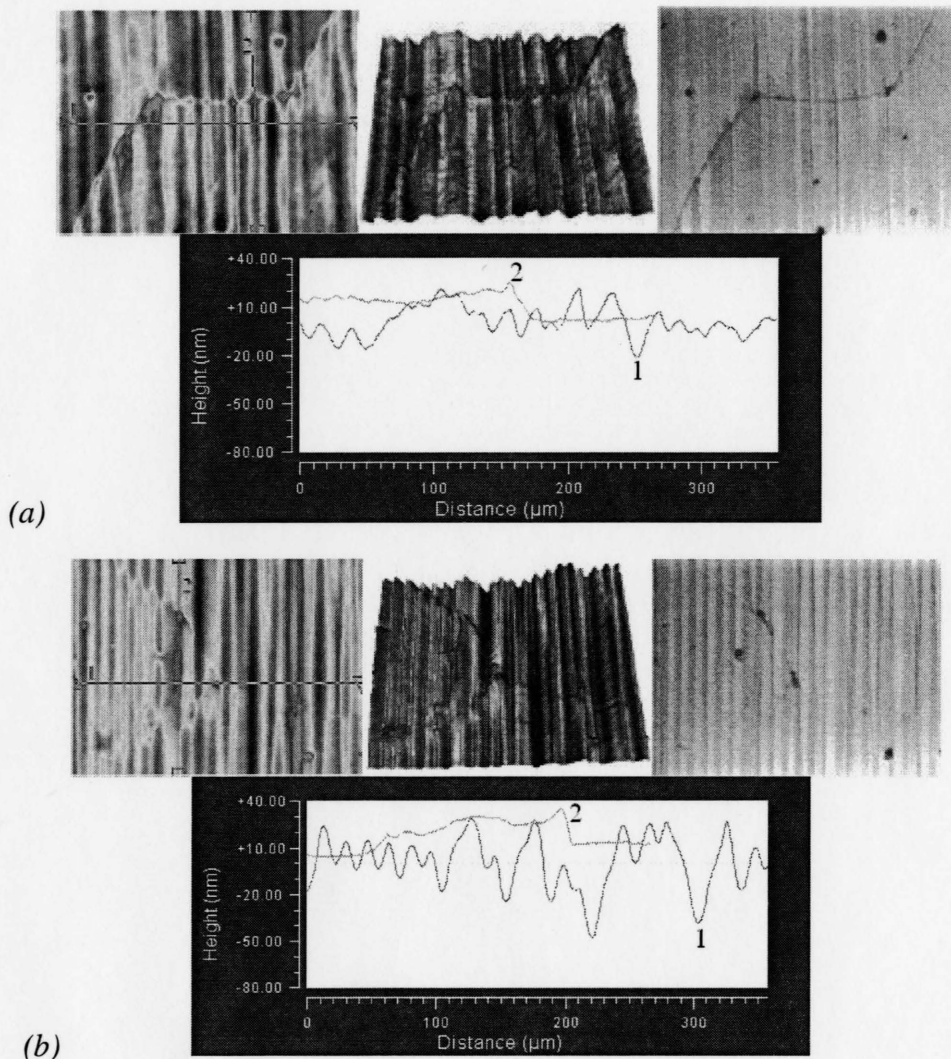


Figure 5-40: Grain boundary induced surface roughness in (a) and (b) on Furnace cooled 99.97% Aluminum; 1. Feed direction, 2. Cutting direction.

Kim et al., [2008] performed constant load (10mN) scratching tests on Al 6061 alloy and observed that near the grain boundary the friction coefficient increases rapidly where there is a shallow penetration depth. This is because the inclusions and defects accumulate at the grain boundary and is harder than the bulk material. In a cutting operation, when the tool encounters that grain boundary, a similar phenomenon takes place as in the case of a constant load scratch test and results in an added surface roughness as can be seen from Figure 5-38. However, when the material is strain hardened, it changes its grain shape (Figure 5-1) and the dislocation density increases. This results in a stress concentration increase which initiates a new dislocation movement in the adjacent grain. For this reason while machining strain hardened 99.87% aluminum, grain boundary induced surface roughness is minimized as shown in Figure 5-41 (a).

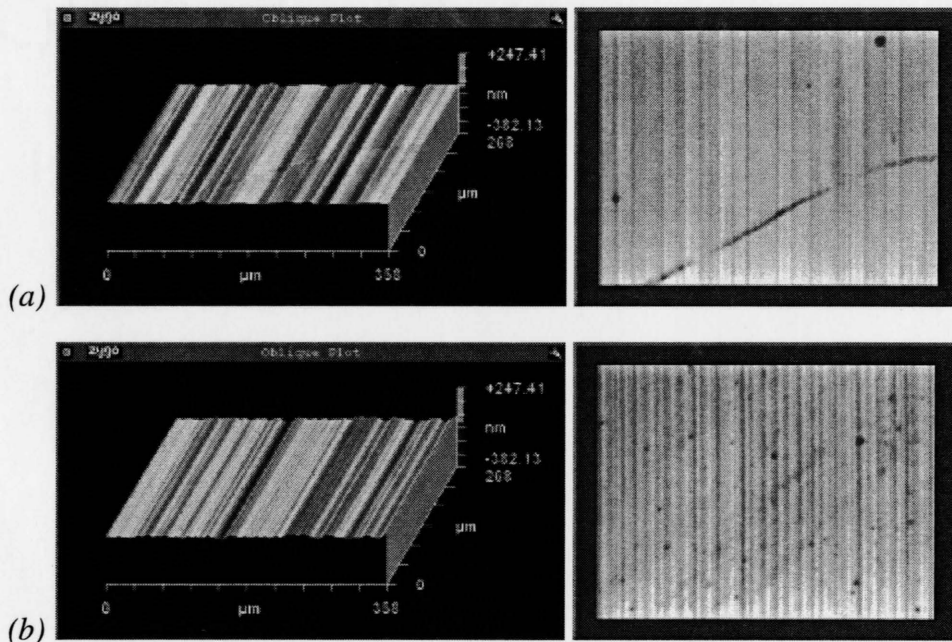


Figure 5-41: Grain boundary induced roughness minimized in (a) 54% cold rolled alloy and eliminated in (b) Friction stir alloy

Material anisotropy is not present in the case of the FSP alloy because of the relative size of the grains and the uncut chip thickness; instead FSP material behaves as a bulk isotropic material as shown in Figure 5-42 using micro indentation test results. Moreover, churning of the material in FSP results in the absence of large grain boundaries and related defects, as shown in Figure 5-41 (b).

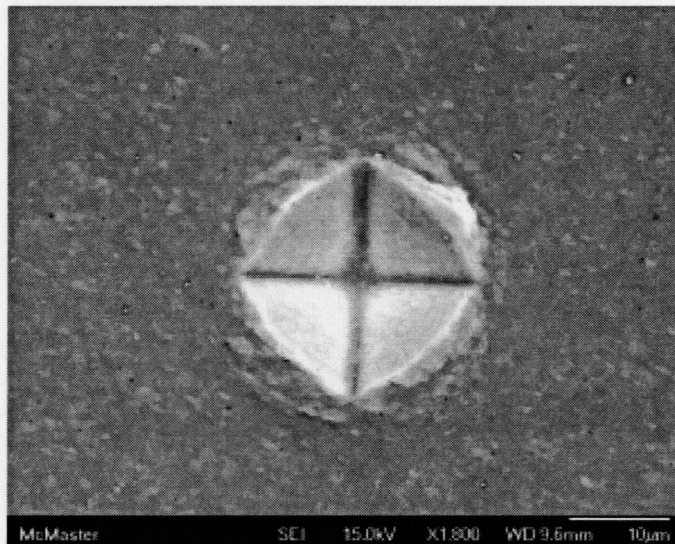
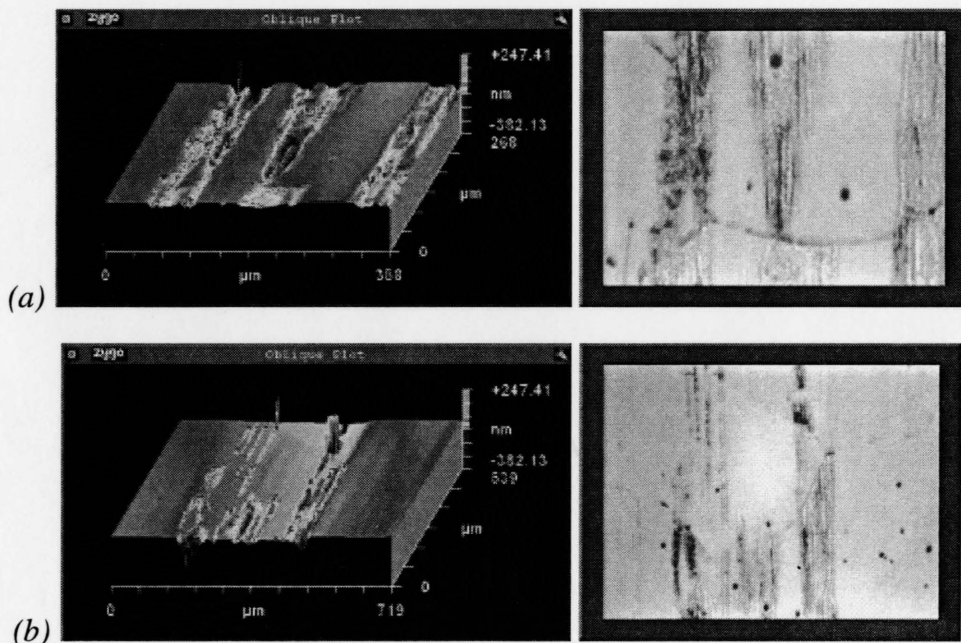
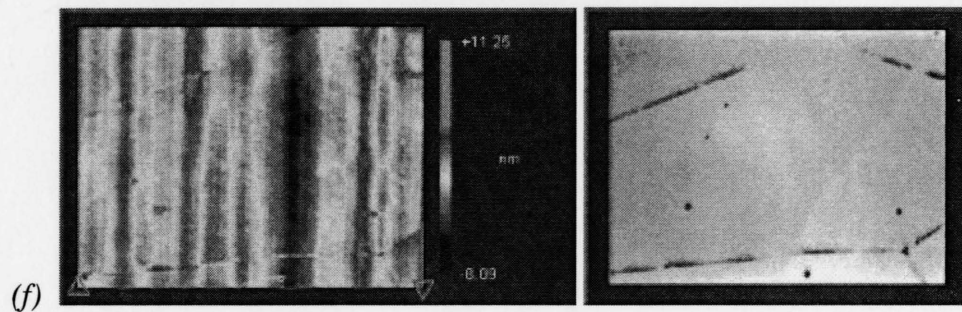
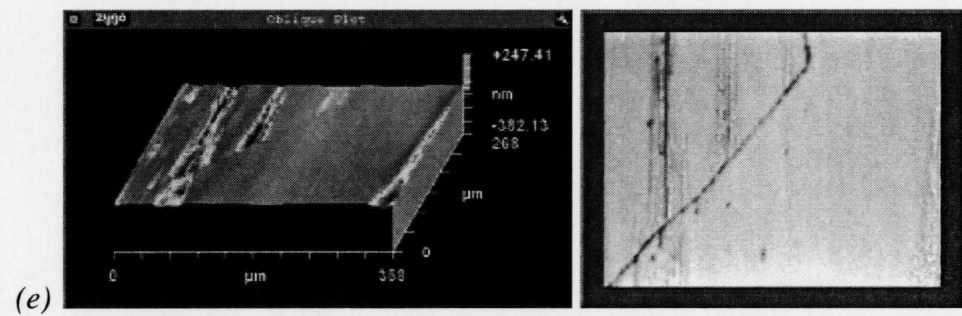
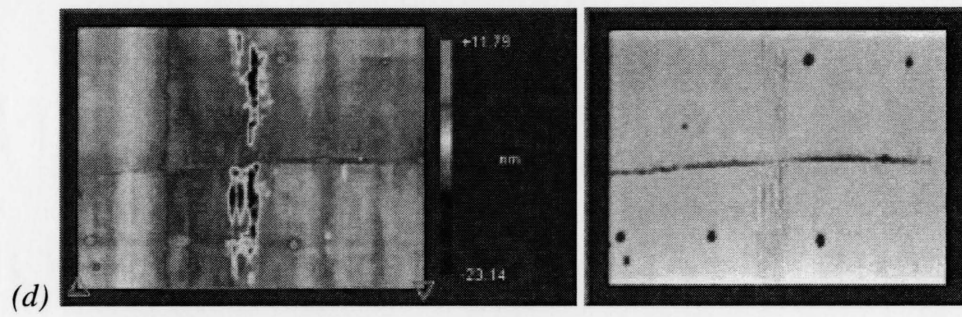
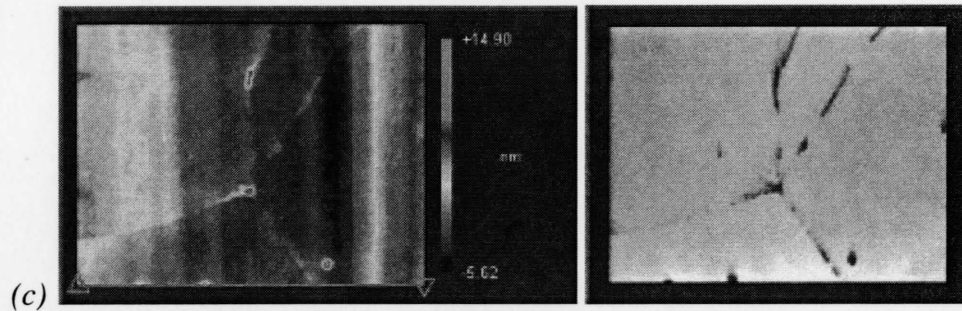


Figure 5-42: Micro indentation on FSP alloy

Cold rolling generates grain refinement and sub-grain formation; however, elongated big grains still remain in the microstructure. Thus when cutting is taking place, material piles up near the grain boundary resulting in a grain boundary induced roughness. Such pile up near the grain boundary is also observed while machining with a round nose radius tool. However, tearing marks are observed on larger grain alloys while machining with a flat end tool. This is probably because of the multiple point engagement of the

cutting tool. In a round nosed single point tool, the tool is physically moving forward with a feed rate and is a point contact. On the other hand, in the case of a flat end tool, when the tool is piling up material, because of the tool setup, the flat trailing edge of the tool address the pile up and tries to remove it. Because of the anisotropic nature of the material, the tool cannot always cut the material. Instead, the material comes out as a torn section that generates irregularities on the surface. Such tearing at the grain boundaries are prominent in soft alloys and the severity is minimized with cold rolling as shown in Figure 5-43 (a-c) for soft furnace cooled alloy and Figure 5-43 (d-f) for the cold rolled alloy. Similar observations are made by other researchers as described in Section 2.5.2. However, this phenomenon is completely eliminated in the case of friction stirred nano grained structure as shown in Figure 5-43 (g). Figure 5-43 (h) shows the machined FSP surface with the flat end tool showing no visible defects at 7500X magnification.





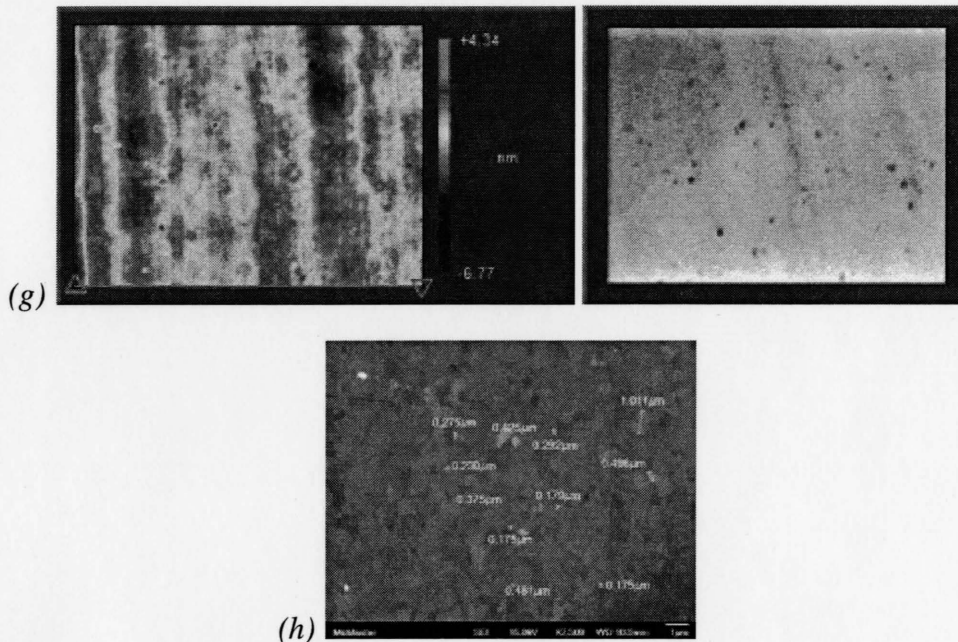


Figure 5-43: Machined surfaces with flat end tool. (a-c) Furnace cooled alloy. (d-f) 54% cold rolled alloy. (g) Frictions stirred alloy. (h) SEM image of a machined friction stirred alloy

5.4.3. Effect of tool geometry on surface roughness

Average roughness and peak to valley roughness graphs are shown in Figure 5-44, Figure 5-45 and Figure 5-46 for furnace cooled, 54% cold rolled and FSP aluminum samples respectively for different tool geometry.

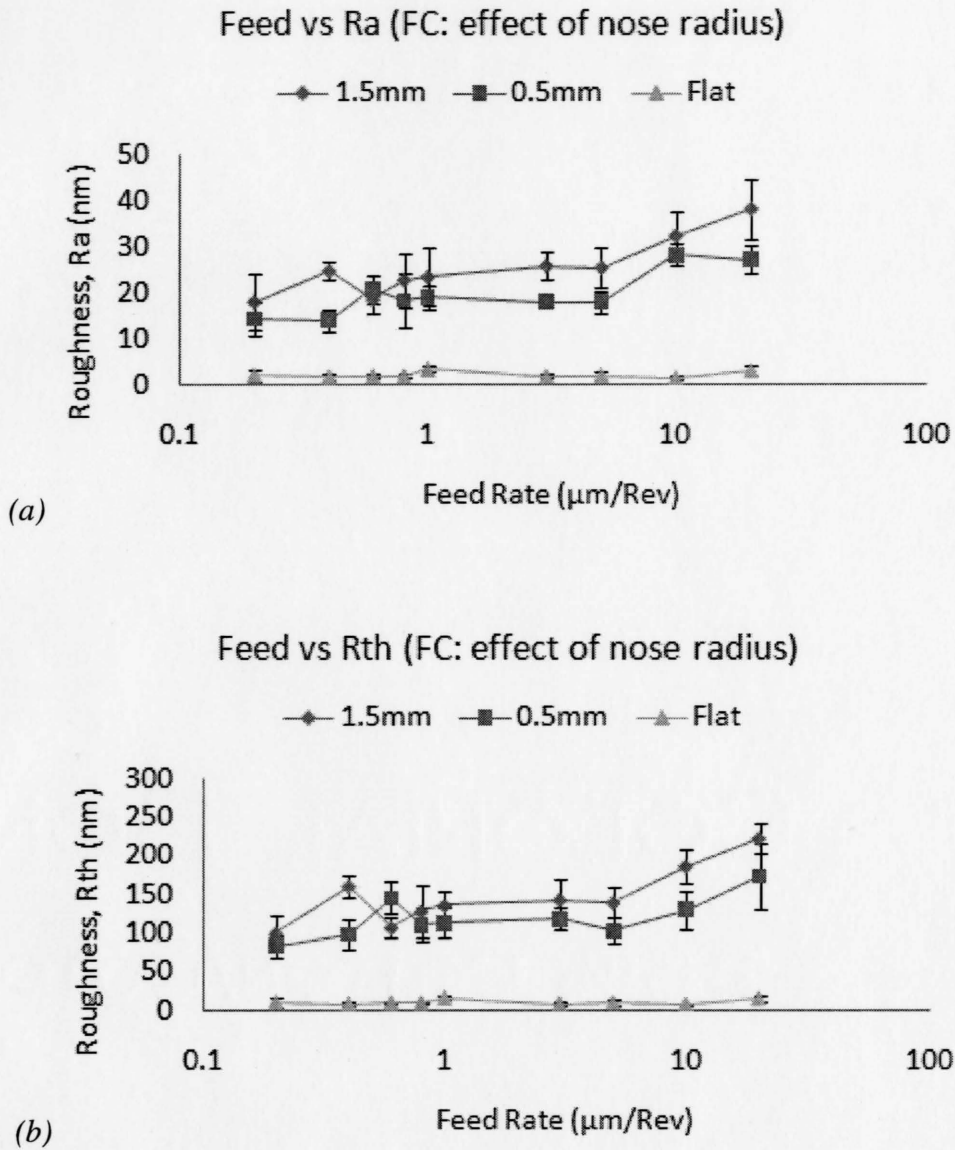
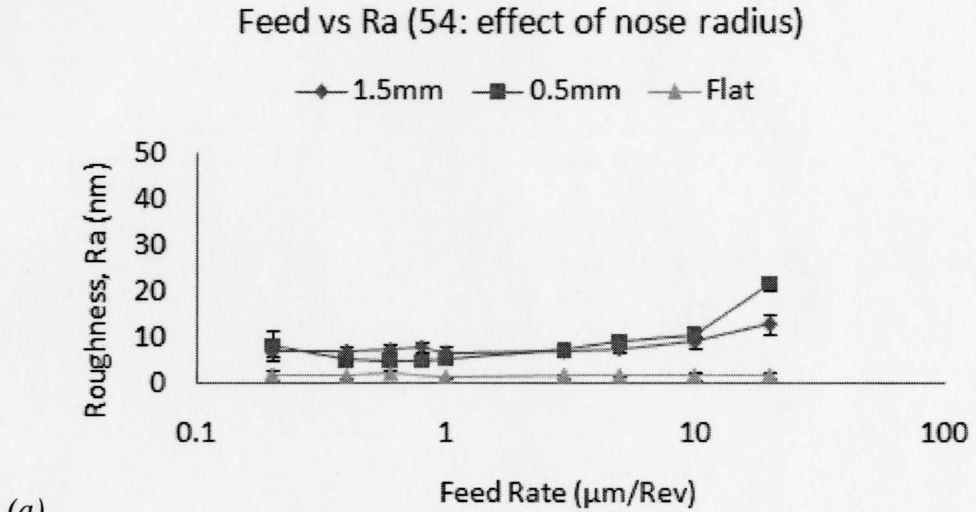
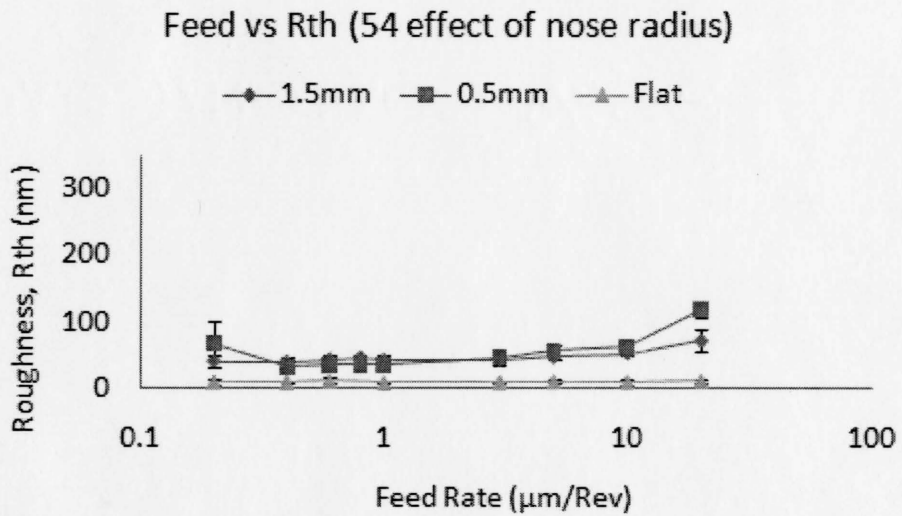


Figure 5-44: Effect of tool geometry on furnace cooled 99.87% aluminum alloy at 1000RPM, 2 μm depth of cut



(a)



(b)

Figure 5-45: Effect of tool geometry on 54% cold rolled 99.87% aluminum alloy at 1000RPM, 2 μm depth of cut

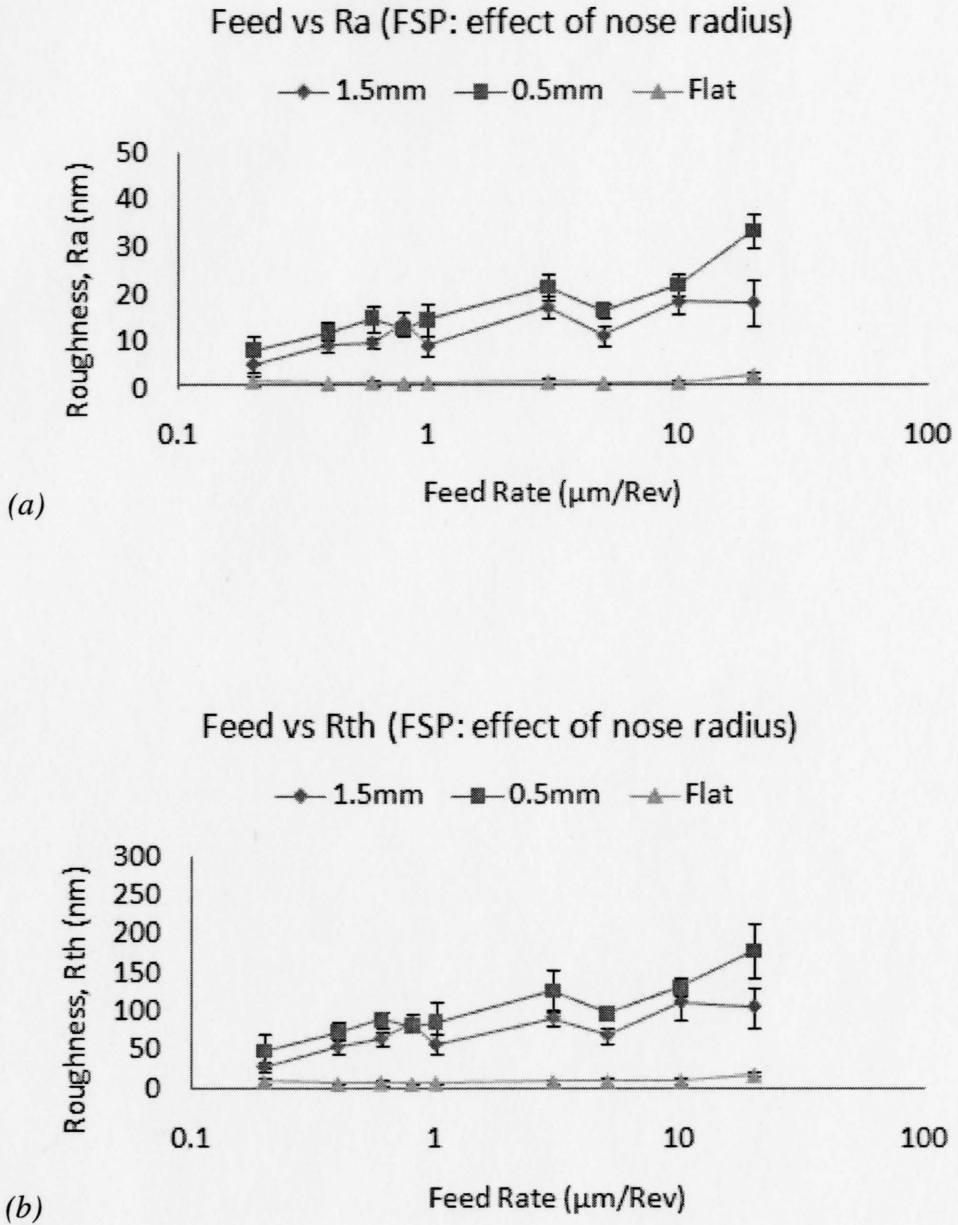


Figure 5-46: Effect of tool geometry on friction stir processed 99.87% aluminum alloy at 1000RPM, 2µm depth of cut

As expected, the flat end tool gives the best surface roughness of all of the combinations. It is interesting to note that in the case of the soft furnace cooled alloy, the

roughness is higher with the larger nose radius tool which is in contradiction with the expected trend. This is because of chip thinning and the reduced presence of defects as the material is carefully solidified. This results in more chip edge serration and side flow. In the case of the 54% cold rolled aluminum alloy, both the tools show similar performance (Figure 5-45). Finally, for the case of the FSP alloy, the roughness pattern matches the theoretical trend where the larger nose radius produces a better surface roughness (Figure 5-46). This is because of the severe plastic deformation that takes place which reduces the side flow. Average surface roughness of 0.75nm has been achieved with the flat end tool and FSP alloy at 1000RPM, 2 μ m depth and 0.4 μ m feed/rev.

It is worth noting that the flat end tool not only improves the surface roughness, but also the productivity by 100 times or more. The roughness achieved with the flat end tool at 20 μ m/rev cannot be achieved with a round nosed tool even at 0.2 μ m/rev. Table 6.1 compiles all the roughness data from this study. From Table 6.1, it can be seen that minimum average surface roughness achieved is Ra: 0.749nm (*Rz*: 3.08nm and *Rth*: 3.995nm) with the combination of FSP alloy and flat end tool. Figure 5-47 shows the measured interferometer image of the surface. The oblique plots of the measured surfaces are shown in APPENDIX C.

Again, due to burnishing effect of the flat secondary edge of the tool on the freshly machined surface, it may also happen that there is a severe deformation at a very

thin layer of the material. This is probably a reason why the flat end tool improves surface finish irrespective of the material microstructures.

Another explanation for the deterioration in the surface roughness is tool wear. A worn tool produces poor surface roughness compared to a sharp tool. There is no standard available for defining SPDT tool wear. In this study, cutting tools were periodically observed optically at approximately 800X magnification to observe tool wear. 800X magnification was selected based on the certificate provided by the tool makers stating that “tool is chip free at 800X.” Diamond tools are re-lapped due to cost of the diamond once tool wear is observed. Figure 5-48 (a) and (b) show the SEM image of a new and used tool respectively where both retain their cutting edge after cutting. Two types of tool wear is observed in this study: 1. Erosive wear resulting in edge roundness as shown in Figure 5-48 (c) and 2. Edge chipping as shown in Figure 5-48 (d). Figure 5-49 plots average and peak to valley surface roughness data while machining 54% cold rolled 99.87% aluminum with a new tool and worn tool (1000RPM, 2 μ m depth of cut).

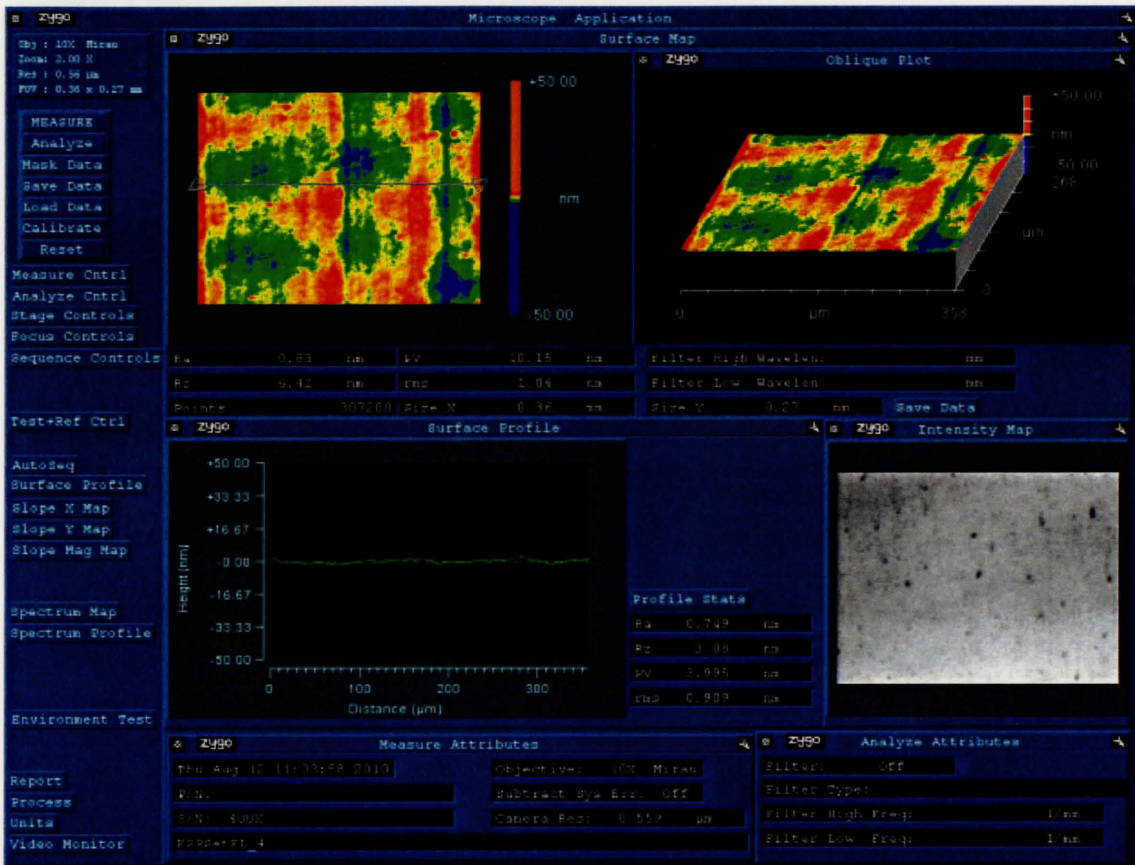


Figure 5-47: Best surface achieved with FSP aluminum alloy and flat end tool at 1000RPM, 2µm depth of cut and 0.4µm/rev feed rate

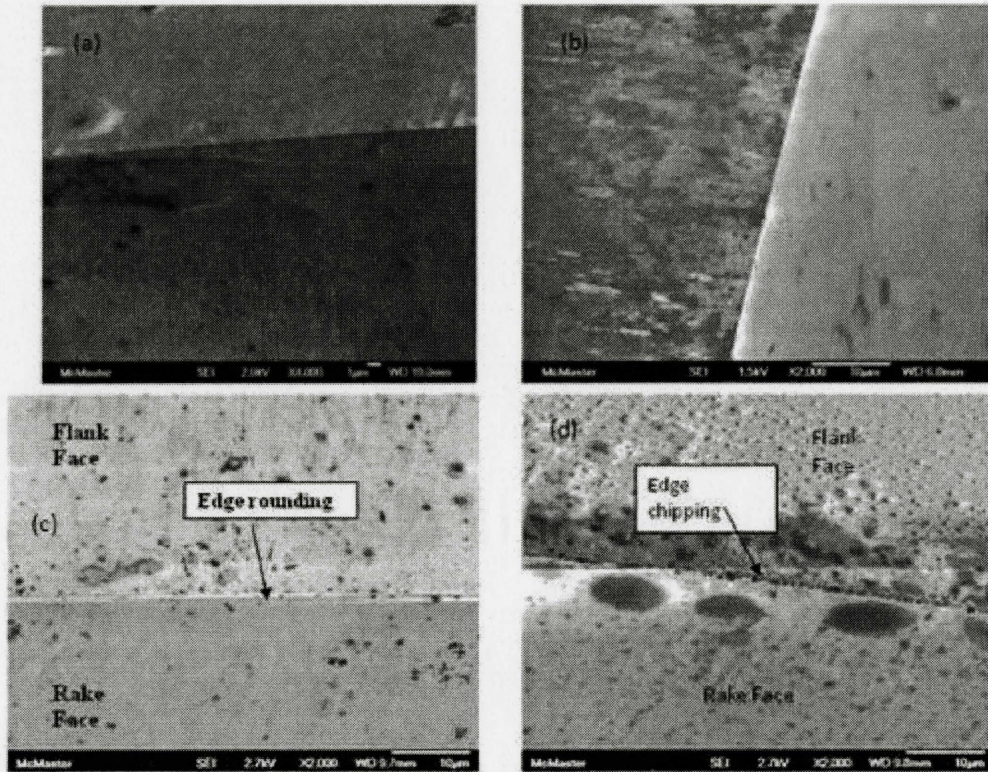


Figure 5-48: New and worn tool

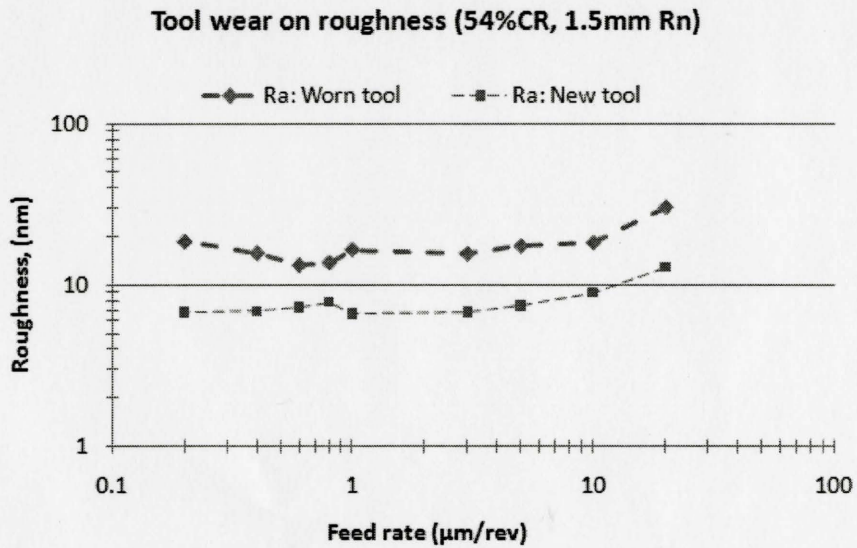


Figure 5-49: Effect of tool wear on surface roughness

CHAPTER 6 CONCLUSIONS AND

RECOMMENDATIONS

The primary objective of this research was to address the surface roughness capability of single point diamond turning. It is well known that below a certain value of feed rate, surface roughness does not improve and further processing of the machined surface is required. Post processing operations like lapping or polishing requires capital investment and increases manufacturing time and cost. Thus, the focus of this project was to address this issue of surface roughness and to produce a surface by SPDT that would require minimum or no post processing.

The reason for this deviation in surface roughness from the theoretically predicted value is the size effect resulting from the relative scale of the cutting tool edge radius to the material microstructure. Realizing the fact that diamond tools have the sharpest cutting edge, effort was given to engineer the workpiece material and cutting tool geometry. Aluminum was selected as the workpiece material as it is widely used for diamond turning in the industry. The available literature shows that there is a lag in the research related to material microstructure. Most of the previous work is done on different material with different mechanical properties and chemical properties. In this research, only one alloy of aluminum was selected to keep the chemical composition

similar. The mechanical property was altered only using mechanical or thermo-mechanical treatments. This was a unique direction for this research.

It has been reported that an average surface roughness less than 3nm is very difficult to achieve with any aluminum alloy. Thus a benchmark was fixed for acceptable average surface which is less than 10nm. However, the focus was to achieve an average surface roughness less than 3nm.

The goal of the research was successfully achieved with a specially designed tool with a flat secondary cutting edge. The flat edge was introduced into the tool design to address the material side flow resulting from the size effect described in this thesis. A proper selection of workpiece material and cutting tool has proven to drastically improve the performance of the SPDT process while generating a planer surface. An average surface roughness value of less than 1nm has been repeatedly produced. This surface would require no post processing for most applications. It is to be noted that engineering the cutting tool or the workpiece material performed in this study does not add significantly to the overall cost of the process. For example, a round nosed tool costs 300\$ and the specially designed flat end tool costs only 500\$ and re-lapping costs only 50\$ for both the tools. The mechanical treatment performed on the workpiece was cold rolling and friction stir process which can be done very easily and with much less expense compared to traditional post processing operations. Moreover, the machining time with the flat end tool can be drastically reduced by hundreds of times due to its large

contact length. This will have an enormous impact on the productivity that can be realized in this industry.

6.1. CONCLUSIONS

Enhancing surface finish is of critical importance for single point diamond turning (SPDT). In this study, efforts have been made to reduce the achievable surface roughness using SPDT by engineering the workpiece material (99.87% aluminum) and cutting tool geometry. Our analysis shows and quantifies that even with the sharpest diamond tool with feed and depth on the micrometer scale, a surface generation mechanism is taking place within the nanometer scale.

With the reduction in scale, the probability of encountering any defect or void reduces and material undergoing the cutting process tends to plough instead of fracture during chip formation. To facilitate chip formation under SPDT operation, strain hardening and ultra-fine grain refinement was utilized as prepared by a friction stir process applied to aluminum. This approach was compared with furnace cooled aluminum alloy. A series of mechanical, optical and cutting tests was performed on all the workpiece materials and chips. Cutting tests were performed with round nosed tools (1.5mm and 0.5mm nose radius) and specially designed flat end tool (0.5mm nose radius

and 0.5mm flat end) while changing the feed rate from 20 μ m/rev down to 0.2 μ m/rev. The conclusions and observations from this study are summarized below:

- I. Increase in micro hardness could indicate dislocation density growth.
- II. Material swelling effect is reduced with strain hardening primarily by reducing side flow and also less spring back. This is a sign of enhanced machinability that could be related to the high dislocation density. Chip edge serration at the trailing edge is a minimum with strain hardened alloy.
- III. Grain boundary induced roughness is severe in the furnace cooled alloy while machining with round nose tool. Grain boundary induced roughness is almost eliminated with the use of strain hardened alloys because of greater number of active slip planes in the adjacent grains.
- IV. Round nose tool gives promising surface roughness with 54% strain hardened aluminum alloy followed by friction stir processed ultra-fine grained aluminum alloy. 82% strain hardened alloy produces voids, fractures and pitting when the material is SPDT. A furnace cooled alloy with a large grain size produces the poorest surface roughness of all of the samples tested.

- V. Ploughing is effectively eliminated with the friction stir processed alloy because of high dislocations and ultra-fine grains. Self deformation of the chips also occurs to address the velocity gradient along the tool workpiece contact length indicating less sticking between tool and chip.
- VI. Nose radius plays an important role at lower feed rates. Severe chip thinning may produce a poor surface roughness at lower feed rates for example at feed rates less than $1\mu\text{m}/\text{rev}$, when a larger nose tool is used.
- VII. Irrespective of the feed rates, larger nose radius tools produce poorer surface roughness values than smaller nose radius tool while machining furnace cooled alloy. This is because of chip thinning and the reduced probability associated with encountering any defect in the furnace cooled alloy. Both of which contribute to increased levels of side flow. At lower feed rates, roughness is comparable for different round nose tools while machining 54% strain hardened alloy. However, chip thinning and the size effect is compromised while machining ultra-fine grained alloy and larger nose radius produces better surface roughness values.
- VIII. Based on the above conclusions a tool was designed with a large nose radius and a flat secondary edge to enhance surface roughness; however the application of this tool is limited to planer surface generation.

- IX. A flat end tool gives the most promising result for all of the materials studied. However, some tearing at the grain boundary along the cutting direction was observed while machining furnace cooled and 54% strain hardened alloy.
- X. Defects generating from grain boundaries while using the flat end tool are completely eliminated when an ultra-fine grained alloy is used. $R_a < 1.0\text{nm}$ has been repeatedly produced without any visible defect with this combination at different feed rates.
- XI. The flat end tool can increase the productivity by hundreds of times.

6.2. SUMMARY

To benefit the reader, a summary of all the measured minimum average surface roughness values are tabulated in Table 6.1. Results are shown for the optimized cutting parameters which are 1000RPM and 2 μm depth of cut. The effect of feed rate on different tool geometres and mechanically and thermo-mechanically processed workpiece materials are highlighted. Finally, Figure 6-1 shows a photograph of a surface produced with the flat end tool showing the zygo interferometer in the reflection with the measurement.

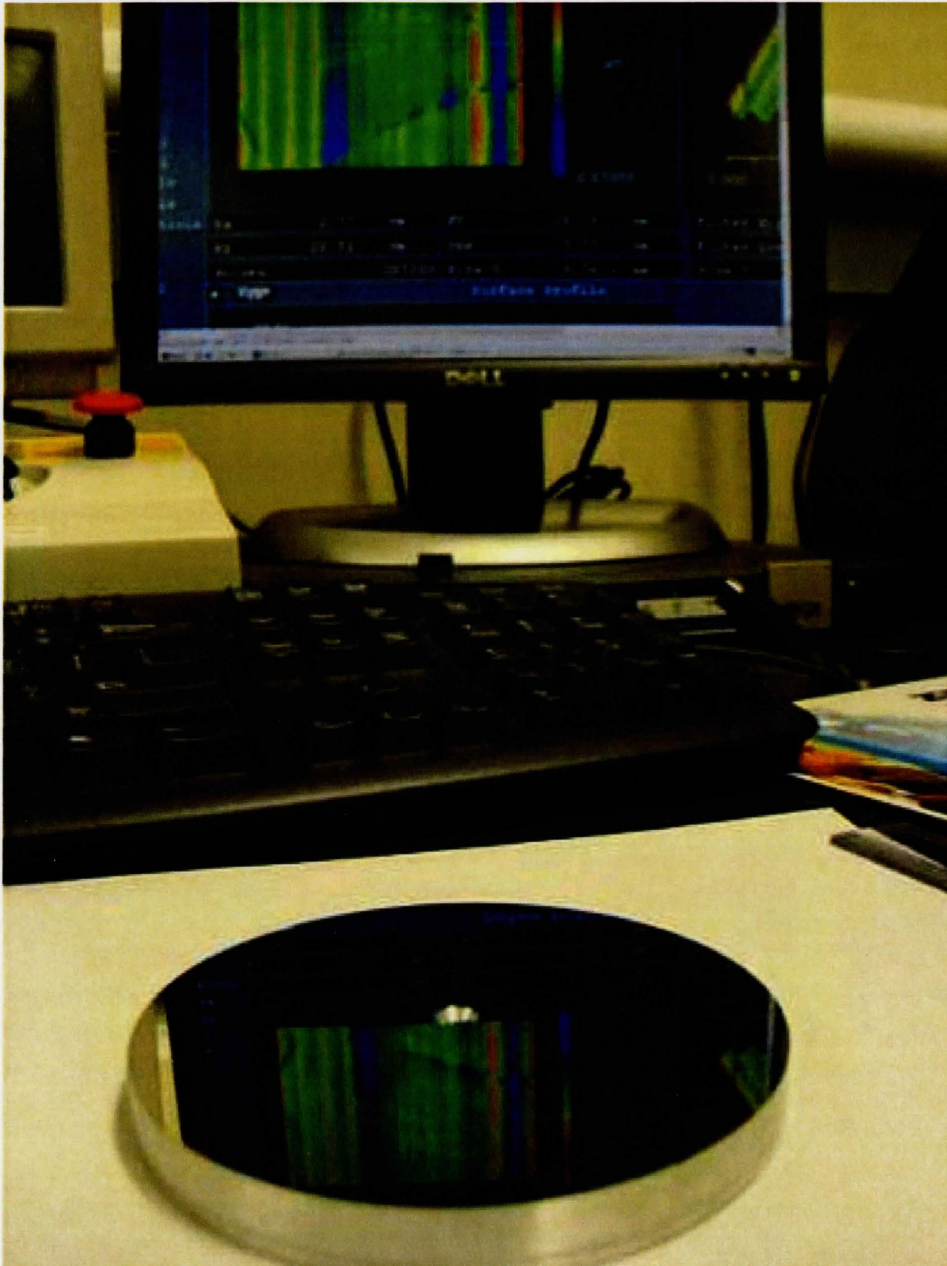


Figure 6-1: A sample produced on 54% cold rolled alloy with flat end tool

Table 6.1: Summary of results

	Minimum measured R_a value, nm			
	Feed rates $\mu\text{m/rev}$	Round nosed tool		0.5mm R_n with 0.5mm flat end
		1.5mm R_n	0.5mm R_n	
Furnace cooled 99.87% aluminum	20	37.3	23.258	1.779
	10	27.2	17.404	0.933
	5	19.242	14.808	2.247
	3	21.06	17.25	1.726
	1	17.76	15.68	2.523
	0.8	17.004	13.51	1.32
	0.6	15.677	17.078	1.442
	0.4	21.836	11.75	1.209
	0.2	10.787	10.842	0.956
54% cold rolled 99.87% aluminum	20	10.081	19.22	1.132
	10	7.379	8.959	0.963
	5	6.498	7.713	1.083
	3	5.054	5.72	1.13
	1	4.277	4.37	0.905
	0.8	6.186	3.806	1.07
	0.6	4.95	4.176	1.23
	0.4	5.665	4.109	0.96
	0.2	4.864	4.402	1.035
Friction stir processed 99.87% aluminum	20	13.241	26.943	2.097
	10	16.19	18.299	0.902
	5	9.141	14.353	0.83
	3	7.895	18.984	0.997
	1	6.092	11.427	0.743
	0.8	11.17	10.935	0.784
	0.6	7.784	10.986	0.846
	0.4	7.205	9.76	0.749
	0.2	3.14	4.606	0.79

6.3. RECOMMENDATIONS

Current work dealt with production of planer surfaces made with aluminum alloys. This study gave a better understanding on the physics of surface generation which was followed by the enhancement of surface roughness. This knowledge can be extended to different materials and geometries. Additional directions of future work are summarized below:

- I. It is important to understand how the mechanical or thermo-mechanical treatments affect the bulk dimensional tolerance of the machined component. This issue can be addressed by observing the form error on a machined part in regular interval, say one week for couple of months. Care may be taken to control the storage environment of the machined sample depending on the end use. If form error is observed, a detailed transmission electron microscopy (TEM) study and X-Ray diffractometry (XRD) study should be done to quantify dislocation density, crystal structure and residual stress on the bulk and machined surface.

- II. While machining 6061 aluminum, the influence of the alloying elements was observed. Alloying elements causes a deterioration of the machined surface quality. The effect of alloying elements on 6061 aluminum is addressed in the industry with rapidly solidified 6061 aluminum where grains are in the range of 2~3 μm ; however, alloying elements are finely distributed. Rapidly solidified

aluminum is highly expensive. The friction stir process can be an interesting cost effective in-house technology that may be a good alternative process to meet the requirements of applications currently met with the rapidly solidification process. A comparative study of both the alloys with different friction stir process can be a potential solution for the diamond turning of 6061 aluminum.

- III. The effect of the friction stir process on any commercial aluminum alloy may be studied and compared. This knowledge of material processing can be applied to copper which shows more anisotropic behavior compared to aluminum.
- IV. It has been observed that grain boundaries offer an added deterioration of surface roughness and higher cutting force. This is probably attributed to more friction at the hard grain boundaries. A suitable alloying element, for example magnesium, copper or Scandium may be added at different percentage to study the grain boundary induced effects and their severity. Additional mechanical processes may offer a better surface roughness on certain suitable new generation alloy in single point diamond turning.
- V. Studies have been done by other researchers on how the machine tool vibration affects surface generation. It has been concluded from present study that mechanical machining also introduces uncertainty in surface roughness

expectations. Combining this knowledge with machine tool dynamics can help one to estimate surface roughness and a model can be developed.

- VI. Effect of engineered material on spherical or aspherical surfaces may be a potential direction of future work. It would be necessary to achieve similar microstructure throughout the cross-section of the workpiece material before machining such a surface.

- VII. It has been observed that cold rolling increases the shearing process and there is an decrease in shear band thickness and are closely packed. This is a qualitative indication of enhancing shearing process and hence machinability. However, a quantitative analysis can be performed by using more sensitive and high frequency sensor for example acoustic emission. FFT or Wavelet analysis may be a useful tool to process the signal and monitor the sharing process. It is recommended that a pure alloy should be used for such study as alloying elements can introduce disturbance into acoustic signal.

REFERENCES

- Alting L., Kimura F., Hansen H.N. and Bissacco G., 2003, Micro engineering, CIRP Annals of Manufacturing Technology 52(2):635-657
- AREFIN, SHAMSUL, 2004. EFFECT OF CUTTING EDGE RADIUS IN DUCTILE MODE CUTTING OF BRITTLE MATERIALS, National University of Singapore, M. Engg. Thesis
- Atkins A.G., 2005, Toughness and cutting: A new way of simultaneously determining ductile fracture toughness and strength, Engineering Fracture Mechanics 72(6):849-860,
- Atkins A.G., 2003, Modelling metal cutting using modern ductile fracture mechanics: Quantitative explanations for some longstanding problems. International Journal of Mechanical Science 45(2):373-396,
- Bau, Alessandro, 2007, Dynamometer for cutting force measurement in micro milling, Department of Manufacturing Engineering, Technical University of Denmark, PhD thesis
- Bhattacharyya A., 2000, Metal cutting theory and practice, New Central Book Agency (P) Ltd. India
- Blackley W.S. and Scattergood R.O., 1991, Ductile-regime machining model for diamond turning of brittle materials, Precision Engineering 13(2):95-103.
- Brinksmeier E., Gläbe R. and Osmer J., 2006, Ultra-precision diamond cutting of steel molds. CIRP Annals of Manufacturing Technology 55(1):551-554
- Bushe N.A. and Kopitko V.V., 1981, Compatibility of rubbing surfaces, Science: Moscow
- Byrne G., Dornfeld D. and Denkena B., 2003, Advancing cutting technology. CIRP Annals of Manufacturing Technology 52(2):483-507.
- Callister J. William D., 1997, Materials science and engineering an introduction. Fourth Edition ed. USA: John Wiley & Sons, Inc
- Chan K.C., Cheung C.F., Ramesh M.V., Lee W.B. and To S., 2001, A theoretical and experimental investigation of surface generation in diamond turning of an Al6061/SiCp metal matrix composite, International Journal of Mechanical Science 43(9):2047-2068

- Chapman, Gavin, Ultra-precision machining systems: an enabling technology for perfect surfaces,
<http://www.nanotechsys.com/images/PDFs/UltraPrecisionMachingSystem.PDF>,
Moore Nanotechnology Systems LLC., Cited November 4, 2010
- Cheung C.F., Chan K.C., To S. and Lee W.B., 2002, Effect of reinforcement in ultra-precision machining of Al6061/SiC metal matrix composites, *Scripta Mater* 47(2):77-82
- Cheung C.F. and Lee W.B., 2000, A multi-spectrum analysis of surface roughness formation in ultra-precision machining, *Precision Eng* 24(1):77-87.
- Childs T.H.C., Dornfeld D., Lee D-, Min S., Sekiya K., Tezuka R. and Yamane Y., 2008a, The influence of cutting edge sharpness on surface finish in facing with round nosed cutting tools, *CIRP Journal of Manufacturing Science and Technology* 1(2):70-75
- Childs T.H.C., Sekiya K., Tezuka R., Yamane Y., Dornfeld D., Lee D-, Min S. and Wright P.K., 2008b, Surface finishes from turning and facing with round nosed tools, *CIRP Annals of Manufacturing Technology* 57(1):89-92
- Corbett J., McKeown P.A., Peggs G.N. and Whatmore R., 2000, Nanotechnology: International developments and emerging products, *CIRP Annals of Manufacturing Technology* 49(2):523-545
- Dornfeld D., Min S. and Takeuchi Y., 2006, Recent advances in mechanical micromachining, *CIRP Annals of Manufacturing Technology* 55(2):745-768
- Demir E., 2008, A taylor-based plasticity model for orthogonal machining of single-crystal FCC materials including frictional effects, *International Journal of Advanced Manufacturing Technology* (2009) 40:847–856
- Fang F.Z. and Zhang G.X., 2003, An experimental study of edge radius effect on cutting single crystal silicon, 22(9):703-707
- Franks A., 1987, Nanotechnology, *Journal of Physics E: Scientific Instruments* 20(12):1442
- Furukawa Y. and Moronuki N., 1988, Effect of material properties on ultra precise cutting processes, *CIRP Annals of Manufacturing Technology* 37(1):113-116
- Fox-Rabinovich, German and Totten George E. editor, 2007, Self-organization during friction- advanced surface-engineered materials and system design, CRC press: Taylor and Francis Group

- Feynman, Richard, 1993, Infinitesimal machinery, *Journal of Microelectromechanical Systems*, 2(1):4
- Grzesik W., 1996, A revised model for predicting surface roughness in turning, *Wear* 194(1-2):143-148.
- Gurson A.L., 1977, Continuum theory of ductile rupture by void nucleation and growth: Part I- yield criteria and flow rules for porous ductile media. *Transactions of ASME* 99:2-15
- Hirata T., Oguri T., Hagino H., Tanaka T., Chung S.W., Takigawa Y. and Higashi K., 2007, Influence of friction stir welding parameters on grain size and formability in 5083 aluminum alloy, *Materials Science and Engineering: A* 456(1-2):344-349
- K & Y diamond, Quebec, Canada. <http://www.kydiamond.ca/>
- Kim H.H., Cho S.H. and Kang C.G., 2008, Evaluation of microstructure and mechanical properties by using nano/micro-indentation and nanoscratch during aging treatment of rheo-forged al 6061 alloy, *Materials Science and Engineering, A* 485(1-2):272-281
- Kishawy H.A. and Elbestawi M.A., 1999, Effects of process parameters on material side flow during hard turning, *International Journal of Machine Tools and Manufacture* 39(7):1017-1030
- Kistler manual (force dynamometer type 9256)
- Knuefermann M.M.W. and McKeown P.A., 2004, A model for surface roughness in ultraprecision hard turning, *CIRP Annals of Manufacturing Technology* 53(1):99-102
- Lee W.B., 1995, Design of meso-structures in materials processing. *Journal of Material Processing Technology* 48(1-4):721-726
- Lee W.B., Cheung C.F., To S., 1999, Materials induced vibration in ultra-precision machining, *Journal of Material Processing Technology*, 89-90:318-325
- Liu K. and Melkote S.N., 2006, Effect of plastic side flow on surface roughness in micro-turning process, *International Journal of Machine Tools and Manufacture* 46(14):1778-1785
- Liu, X., Devor, R. E., Kapoor, S. G. and Ehmann, K. F., 2004, The mechanics of machining at the microscale: Assessment of the current state of the science, *Journal of Manufacturing Science and Engineering* 126(4):666

- Lucca D.A., Seo Y.W., Rhorer R.L. and Donaldson R.R., 1994, Aspects of surface generation in orthogonal ultraprecision machining, *CIRP Annals of Manufacturing Technology* 43(1):43-46
- Luo X., Cheng K., Webb D. and Wardle F., 2005, Design of ultraprecision machine tools with applications to manufacture of miniature and micro components, *Journal of Material Processing Technology* 167(2-3):515-528
- Masuda M., Maeda Y., Nishiguchi T., Sawa M. and Ikawa N., 1989, A study on diamond turning of al-mg alloy — generation mechanism of surface machined with worn tool, *CIRP Annals of Manufacturing Technology* 38(1):111-114
- McDowell D.L., 2000, Modeling and experiments in plasticity, *International Journal of Solids Structures* 37(1-2):293-309
- McKeown P., 1996, From micro-to nano-machining-towards the nanometer era, *Sensor Review* 16(2):4
- Meyer P.A., Veldhuis S.C. and Elbestawi M.A., 2009, Predicting the effect of vibration on ultraprecision machining surface finish as described by surface finish lobes, *International Journal of Machine Tools and Manufacture* 49(15):1165-1174.
- Mishra R.S., Mahoney M.W., McFadden S.X., Mara N.A. and Mukherjee A.K., 2000, HIGH STRAIN RATE SUPERPLASTICITY IN A FRICTION STIR PROCESSED 7075 al ALLOY. *Scripta Mater* 42:163-168
- Moriwaki T., 1989, Machinability of copper in ultra-precision micro diamond cutting, *CIRP Annals of Manufacturing Technology* 38(1):115-118
- Mu Y.H., Hung N.P. and Ngoi K.A., 2000, Monitoring a sub-newton cutting force for ultra-precision machining, 16(4):229-32
- Nanoform 250 ultra, <http://www.hellotrade.com/ametek-precitech/precision-diamond-turning-lathe.html>, cited 2010 October 28, 2010
- National Instruments, <http://www.ni.com>, cited 2010 09/2010
- Ng C.K., Melkote S.N., Rahman M. and Senthil Kumar A., 2006, Experimental study of micro- and nano-scale cutting of aluminum 7075-T6, *International Journal of Machine Tools and Manufacture* 46(9):929-936
- Nikon, Principles and Applications of Two-Beam Interferometry, Available from: <http://www.microscopyu.com/articles/interferometry/twobeam.html>, cited 2010 07/2010

- Nishiguchi T., Maeda Y., Masuda M., Sawa M. and Uehara K., 1988, Mechanism of micro chip formation in diamond turning of al-mg alloy, *CIRP Annals of Manufacturing Technology* 37(1):117-120
- Paul E., Evans C.J., Mangamelli A., McGlaufflin M.L. and Polvani R.S., 1996, Chemical aspects of tool wear in single point diamond turning, *Precision Engineering* 18(1):4-19
- Precitech manual
- Rajeswari, R. Itharaju, 2004, Friction stir processing of aluminum alloys, University of Kentucky, Master's thesis
- Robinson G.M. and Jackson M.J., 2005, A review of micro and nanomachining from a materials perspective, *Journal of Material Processing Technology* 167(2-3):316-337
- Roblee J., 2007, Factors affecting surface finish in diamond turning, Precitech ultra precision technology, <http://precitech.com/FactorsAffectingSurfFinish.pdf>, cited November 04, 2010
- Sata T., Li M., Takata S., Hiraoka H., Li C.Q., Xing X.Z. and Xiao X.G., 1985, Analysis of surface roughness generation in turning operation and its applications, *CIRP Annals of Manufacturing Technology* 34(1):473-476
- Sedláček R., Blum W., Kratochvíl J. and Forest S., 2002, Subgrain formation during deformation: Physical origin and consequence, *METALLURGICAL AND MATERIALS TRANSACTIONS A* 33A (February):319
- Shaw, Milton C., 2005, Metal cutting principles, Second Edition ed., USA: Oxford University Press
- Shaw M.C., 1995, Precision finishing, *CIRP Annals of Manufacturing Technology* 44(1):343-348
- Simoneau A., Ng E. and Elbestawi M.A., 2006a, Chip formation during microscale cutting of a medium carbon steel, *International Journal of Machine Tools and Manufacture* 46(5):467-481
- Simoneau A., Ng E. and Elbestawi M.A., 2006b, Surface defects during microcutting, *International Journal of Machine Tools and Manufacture* 46(12-13):1378-1387
- Simoneau A., Ng E. and Elbestawi M.A., 2006c, The effect of microstructure on chip formation and surface defects in microscale, mesoscale, and macroscale cutting of steel, *CIRP Annals of Manufacturing Technology* 55(1):97-102

- Sreejith P.S. and Ngoi B.K.A., 2001, Material removal mechanisms in precision machining of new materials, *International Journal of Machine Tools and Manufacture* 41(12):1831-1843
- Su J.Q. , Nelson T. W. and Sterling C. J., 2006, Grain refinement of aluminum alloys by friction stir processing, *Philosophical Magazine* 86:1:1-24
- Su J.Q., 2003, A new route to bulk nanocrystalline materials, *Journal of Material Research* 18(8):1758
- Subbiah S.M. and Melkote S.N., 2007, Evidence of ductile tearing ahead of the cutting tool and modeling the energy consumed in material separation in micro-cutting, *Journal of Engineering Materials and Technology* 129(2):321
- Subbiah S. and Melkote S.N., 2007, Evaluation of atkins' model of ductile machining including the material separation component, *Journal of Material Processing Technology* 182(1-3):398-404
- Subbiah, Sathyan, 2006, Some investigations of scaling effects in micro-cutting, G. W. Woodruff School of Mechanical Engineering: Georgia Institute of Technology, PhD Thesis
- Sugita Tahaaki, Ueda Kanji, and Inana Toyojiro, 1984, *Fundamental of machining*, Japan: KOURITU Book Publication
- suppliersonline.com/propertypages/6061.asp, cited 2010 02/2010
- Sutton M.A., Yang B., Reynolds A.P. and Taylor R., 2002, Microstructural studies of friction stir welds in 2024-T3 aluminum, *Materials Science and Engineering A* 323(1-2):160-166
- To S. and Lee W.B., 2001, Deformation behaviour of aluminium single crystals in ultraprecision diamond turning, *Journal of Material Processing Technology* 113(1-3):296-300
- To S., Lee W.B. and Chan C.Y., 1997, Ultraprecision diamond turning of aluminium single crystals. *Journal of Material Processing Technology* 63(1-3):157-162
- Ueda K., Iwata K. and Nakayama K., 1980, Chip formation mechanism in single crystal cutting of β -brass, *CIRP Annals of Manufacturing Technology* 29(1):41-46
- Valiev R., 2004, Nanostructuring of metals by severe plastic deformation for advanced properties, *Nature Materials* 3(August 2004):511-516

Valiev R.Z., 2000, Bulk nanostructured materials from severe plastic deformation, Progress in Materials Science 45(2):103

Valiev R.Z. and Alexandrov I.V., 1999, Nanostructured materials from severe plastic deformation, Nanostructured Materials 12(1-4):35-40.

Whitehouse, David, 2002, Surface and their measurement, 2002 ed., Taylor and Francis Books Inc.

Yuan Z.J., Zhou M. and Dong S., 1996, Effect of diamond tool sharpness on minimum cutting thickness and cutting surface integrity in ultraprecision machining, Journal of Material Processing Technology 62(4):327-330

ZYGO manual, ZYGO corporation

APPENDIX A PRECITECH 700G MOTIONS

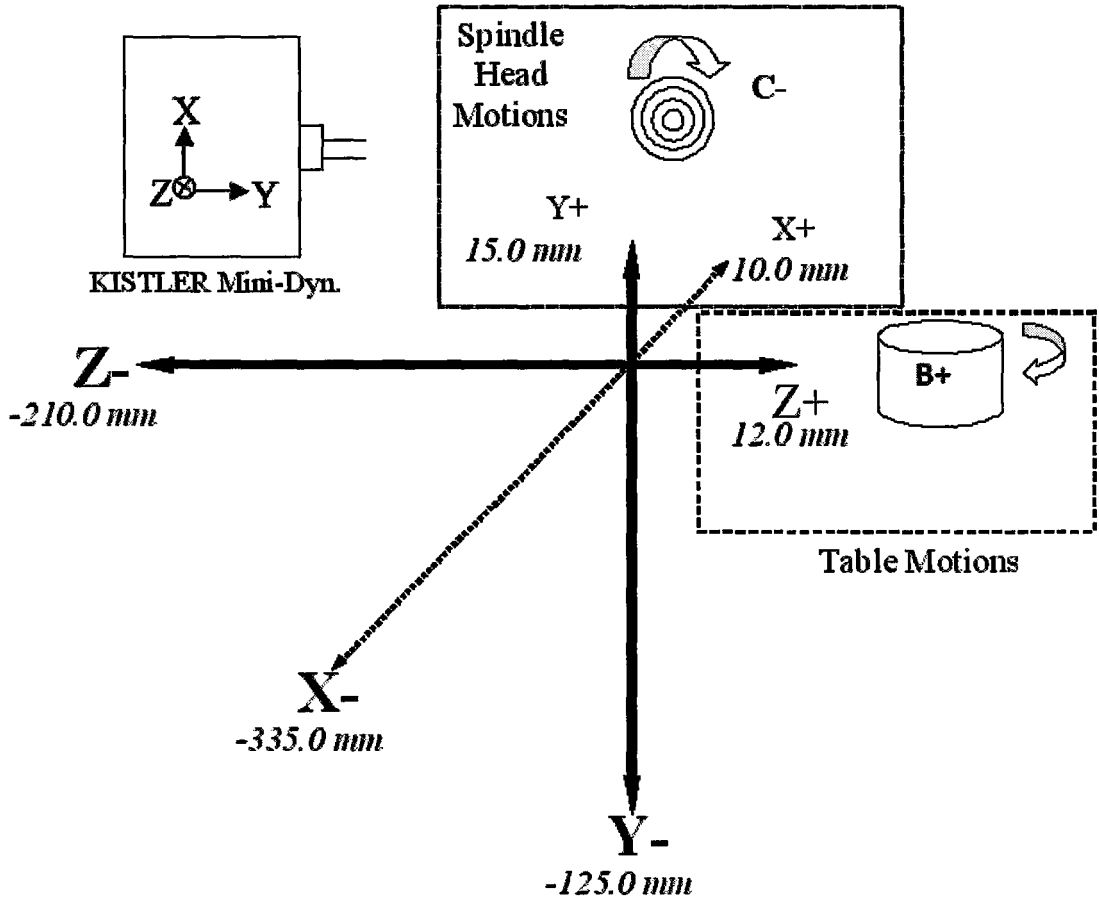


Figure A-1: Machine tool coordinate limits and relative cutting force directions

APPENDIX B PGM AND LABVIEW CODE

G71 ;METRIC UNIT
G90 ;ABSOLUTE SCALE
G92 ;CANCEL PREVIOUS AXIS PRESET POSITION
G01 B-15.0000 C0.0 ;ROTATIONAL AXES POSITION
F100
M07 ;COOLANT “ON”
G00 Y-80.0 X-25.0 Z- ;RAPID LINEAR POSITIONING. Y-AXIS AT CENTER
70.0
M4 S1000 ;CCW ROTATIONAL SPEED (1000RPM)
G01 X-30.218 Z-75.0 ;FINE LINEAR POSITION WITH DEPTH OF CUT.
F75
G04 F0.5 ;0.5 SEC. OF DWELL TIME. READY TO CUT
G01 Z-126.0 F1.0 ;LINEAR FEED MOTION FOR CUTTING (FEED:
1MM/MIN)
G00 X-24.0 Z-70.0 ;RAPID DISENGAGEMENT
M09 ;COOLANT “OFF”
M5 ;SPINDLE “OFF”
M30 ;END PROGRAM

B-1: *.PGM code

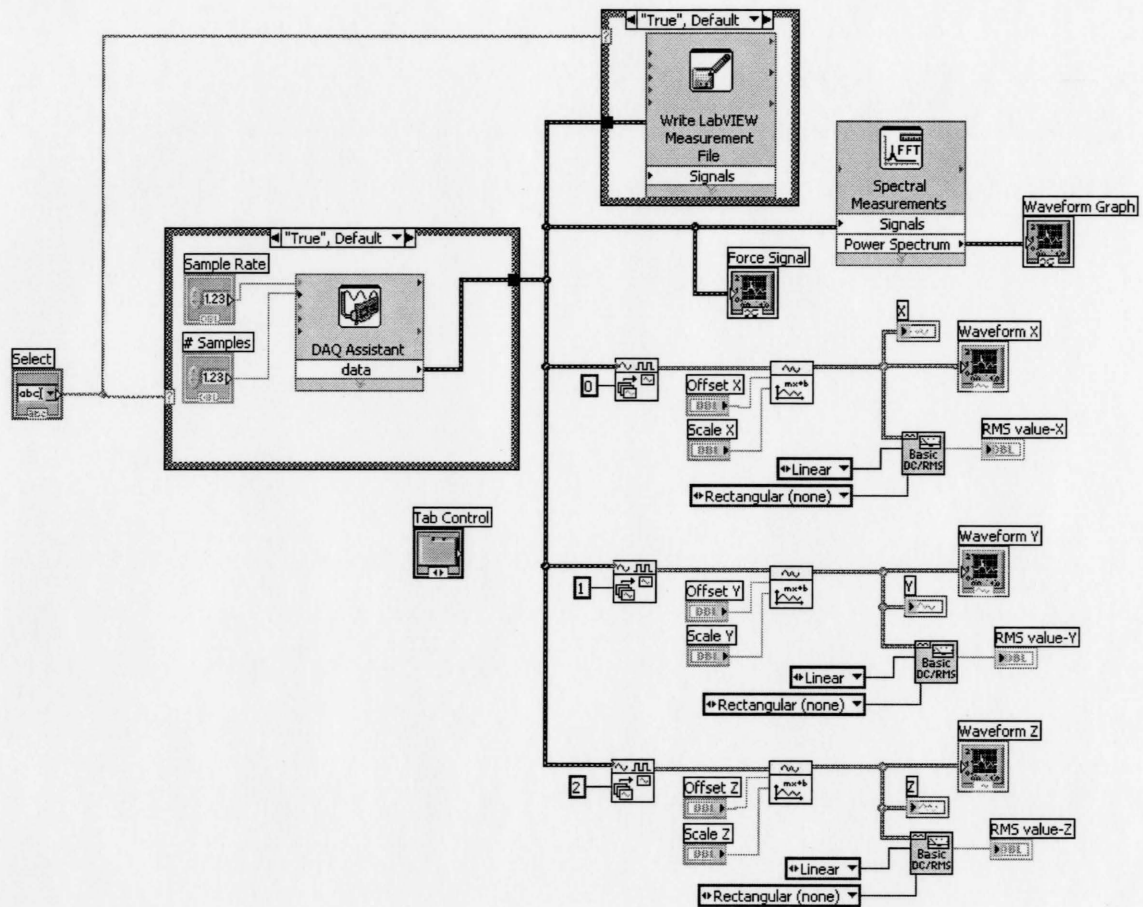


Figure B-2: Graphical representation of LabVIEW data acquisition program

APPENDIX C OBLIQUE PLOTS OF MACHINED SURFACES

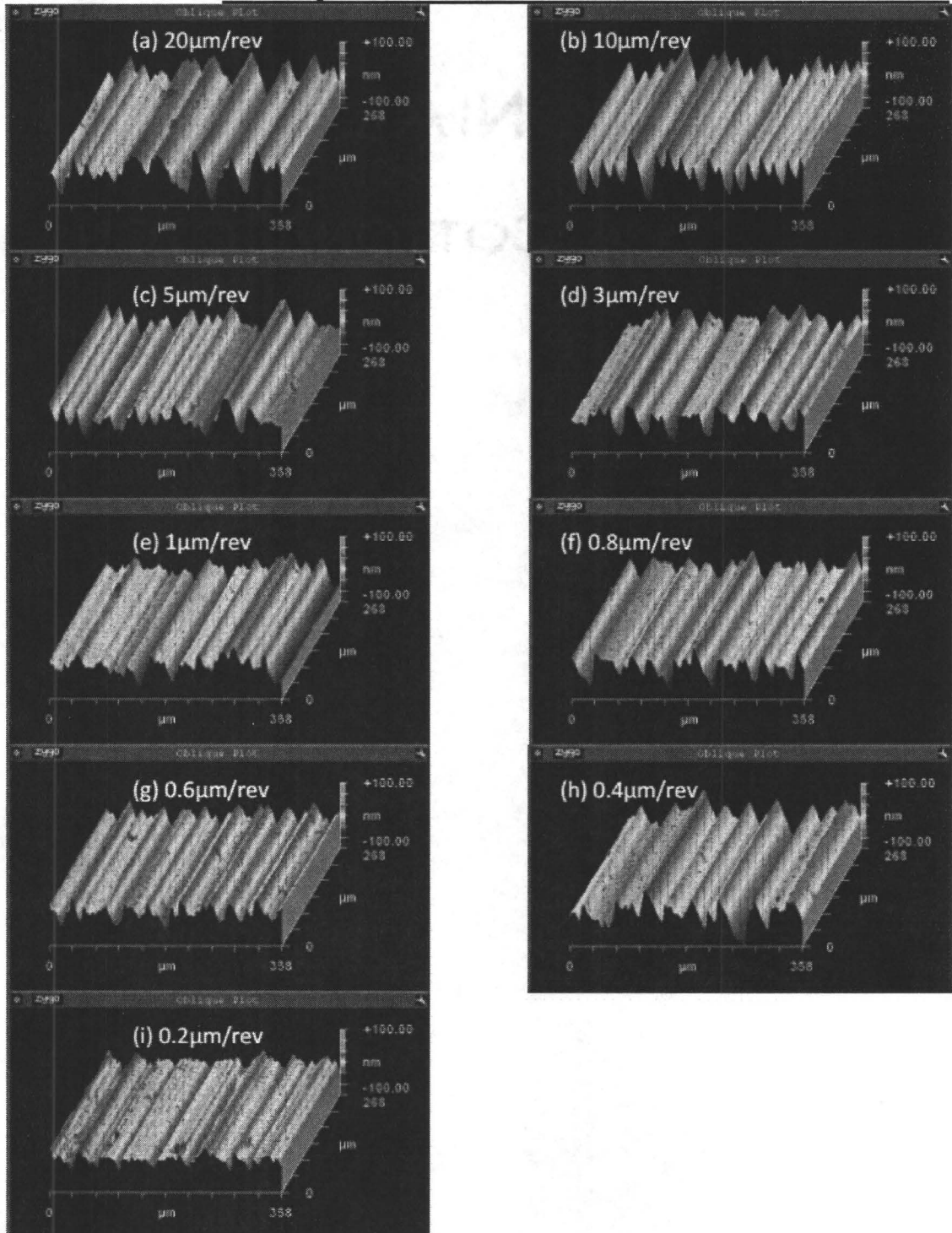


Figure C-1: Furnace cooled 99.87% aluminum (1000RPM, 2µm depth, 1.5mm nose radius)



Figure C-2: 54% cold rolled 99.87% aluminum (1000RPM, 2 μ m depth, 1.5mm nose radius)

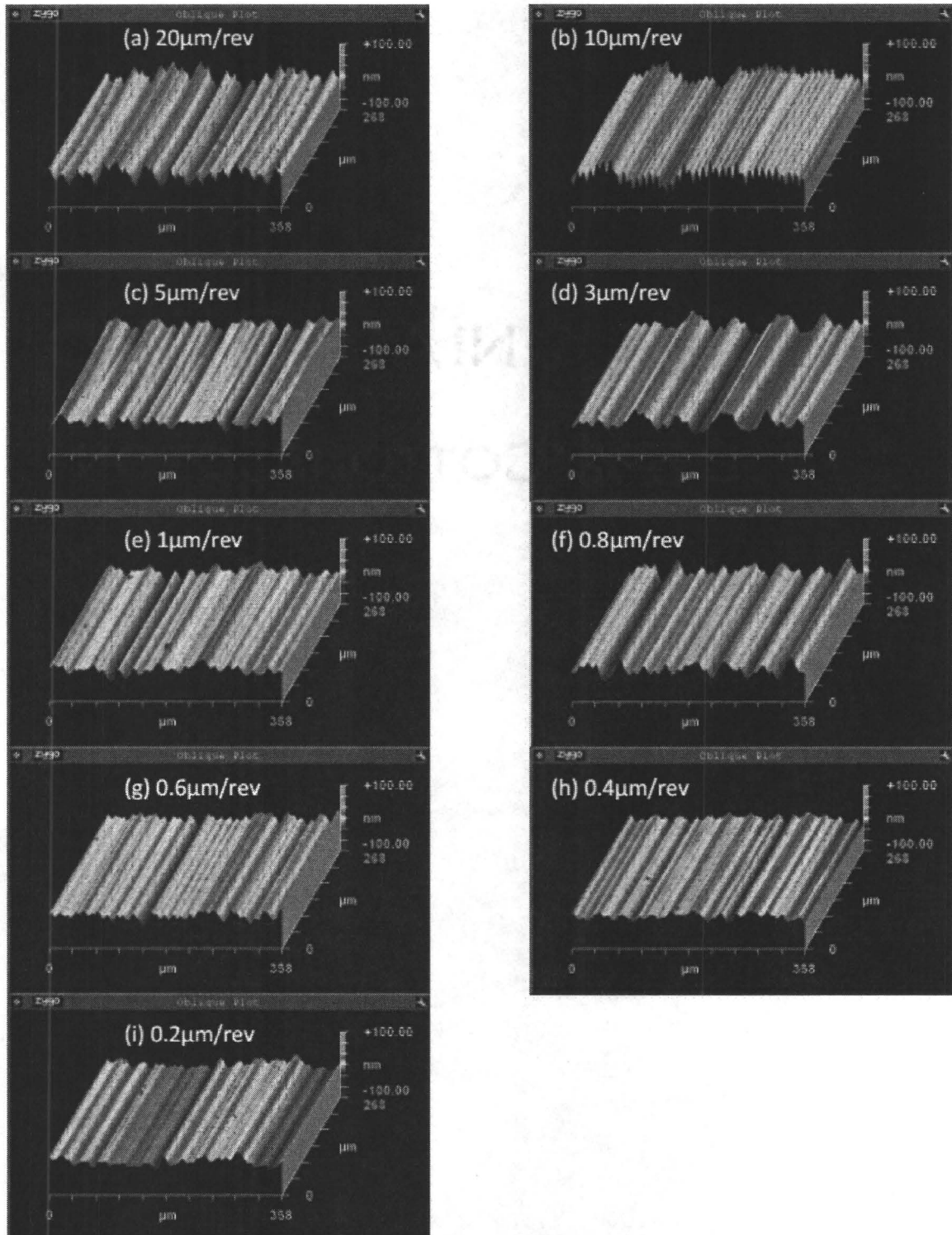


Figure C-3: FSP 99.87% aluminum (1000RPM, 2 μ m depth, 1.5mm nose radius)

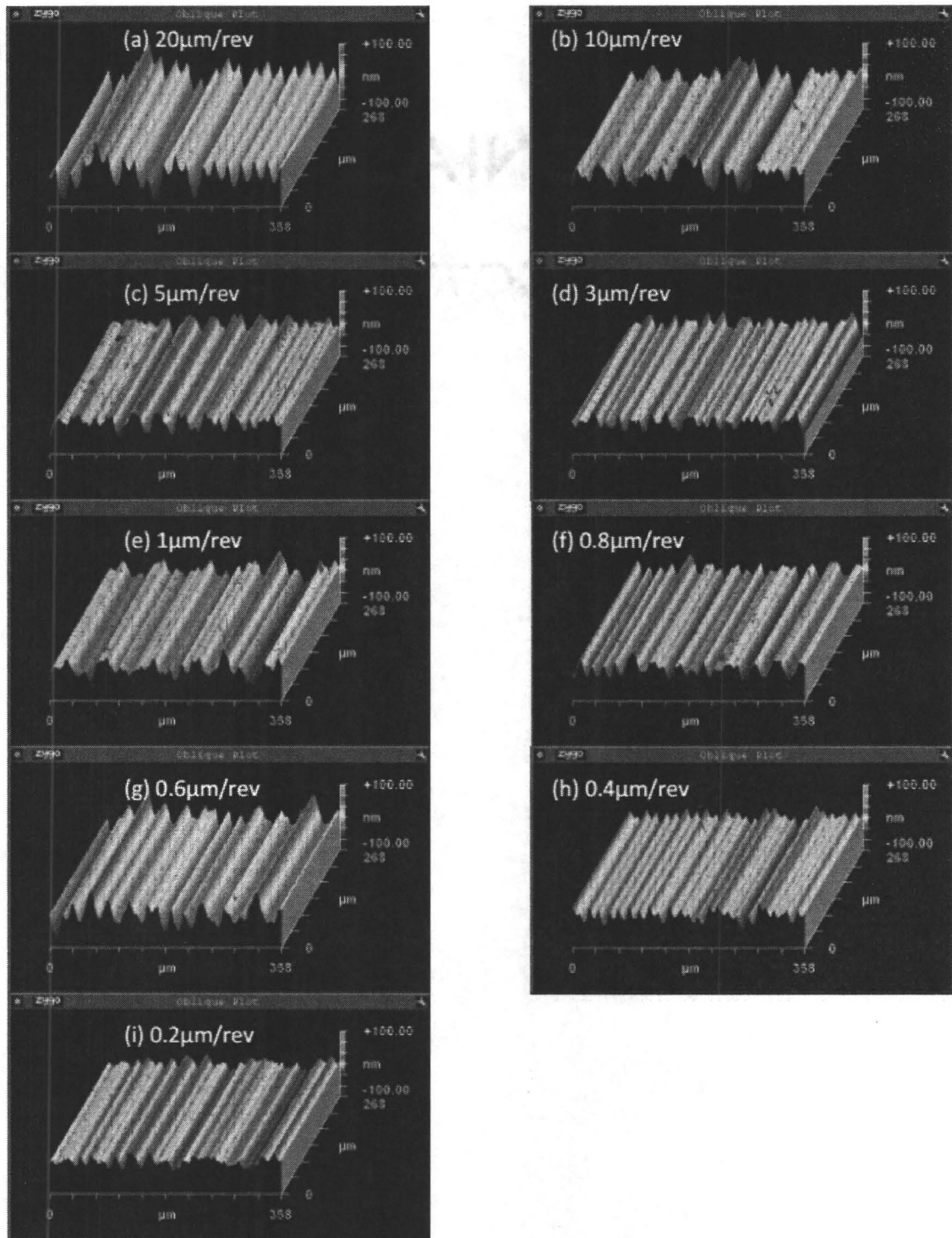


Figure C-4: Furnace cooled 99.87% aluminum (1000RPM, 2 μ m depth, 0.5mm nose radius)

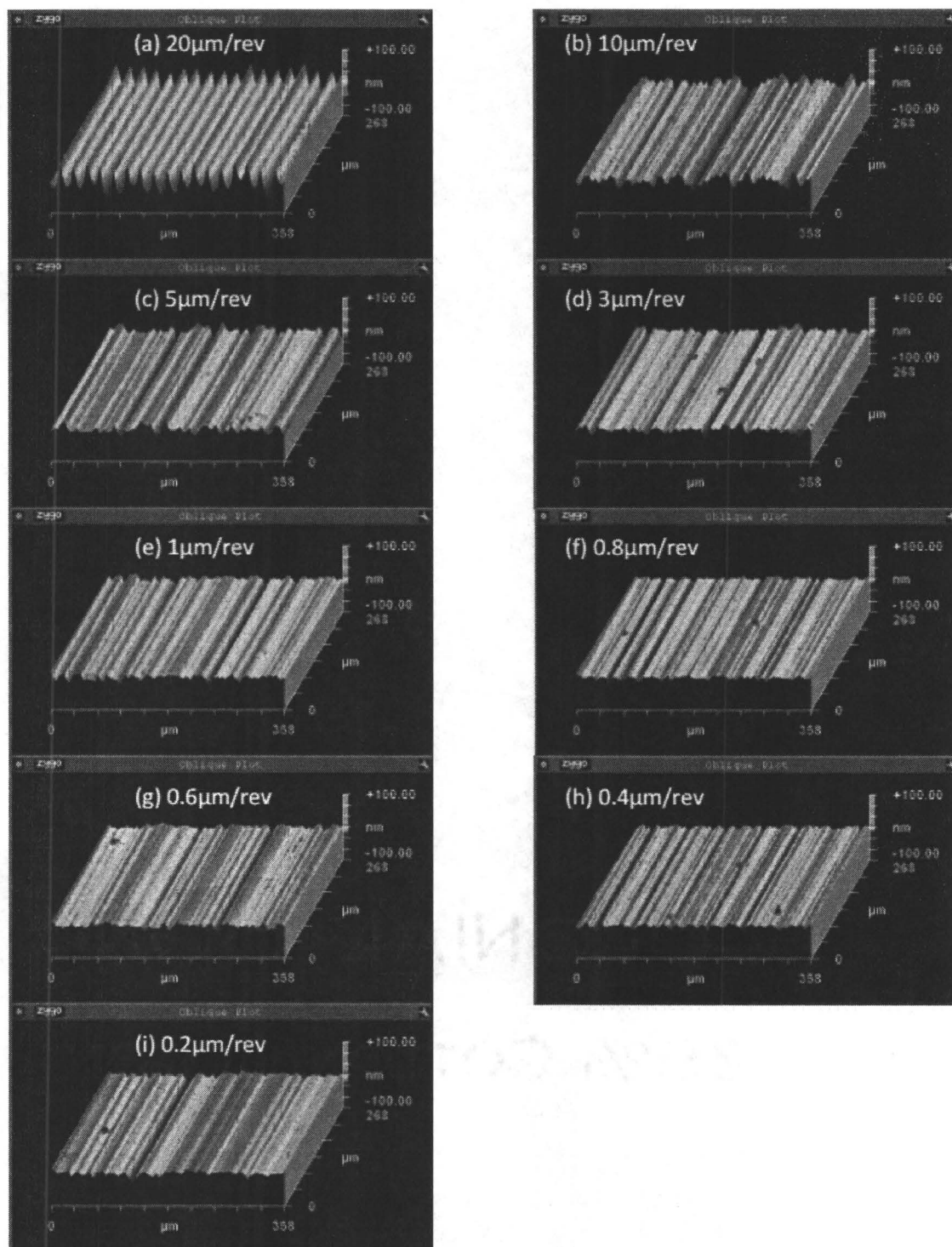


Figure C-5: 54% cold rolled 99.87% aluminum (1000RPM, 2 μ m depth, 0.5mm nose radius)

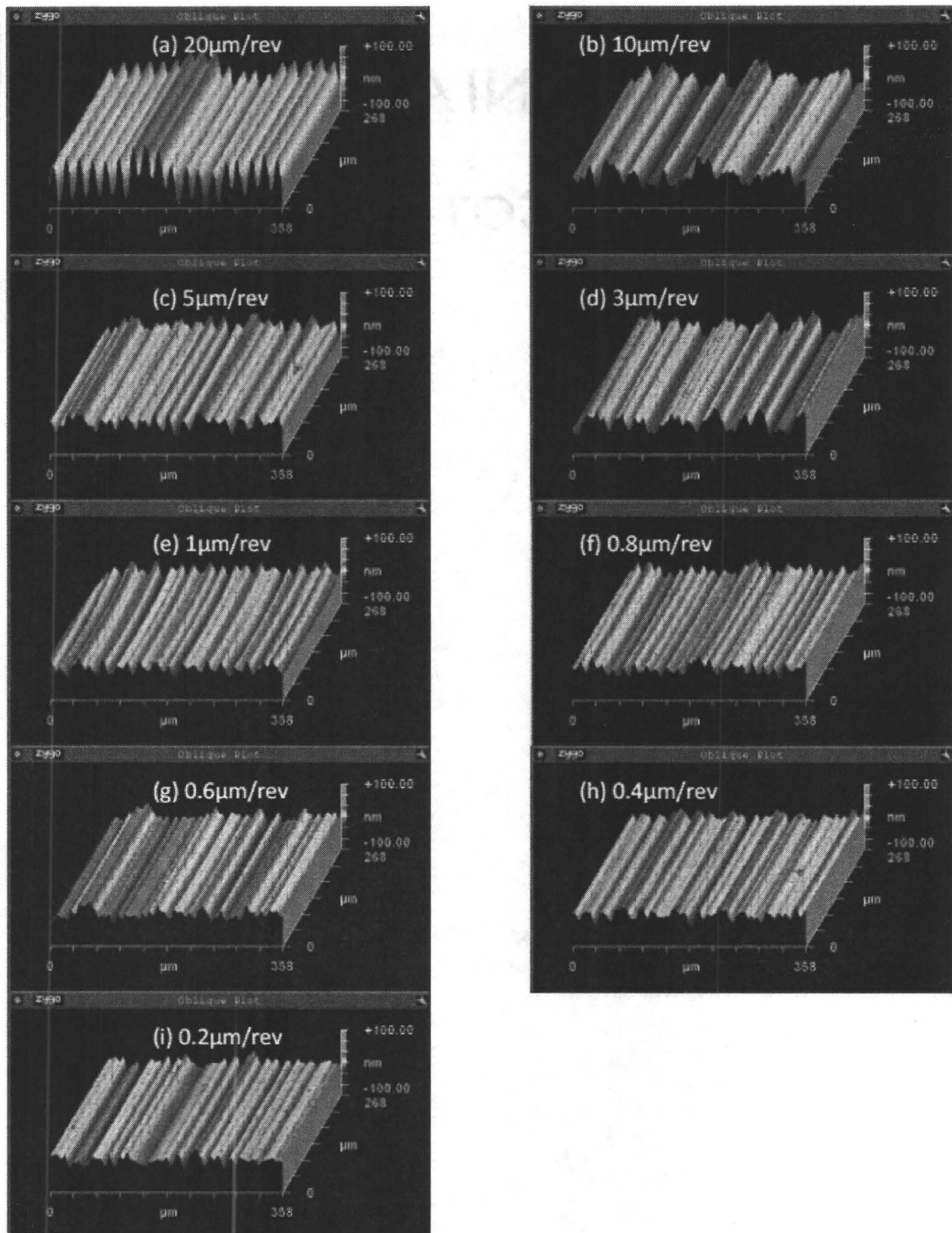


Figure C-6: FSP 99.87% aluminum (1000RPM, 2 μ m depth, 0.5mm nose radius)

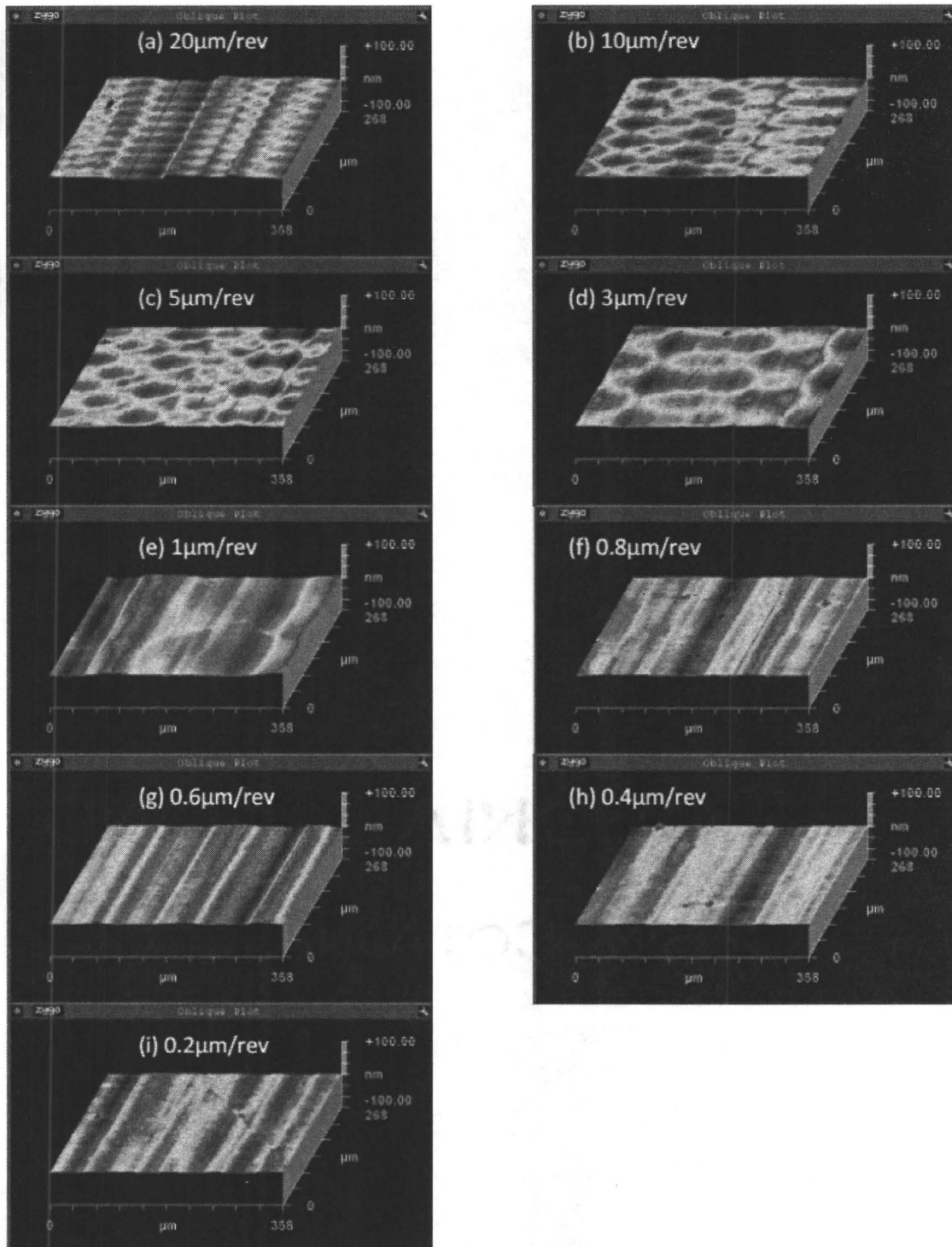


Figure C-7: Furnace cooled 99.87% aluminum (1000RPM, 2μm depth, 0.5mm flat end)

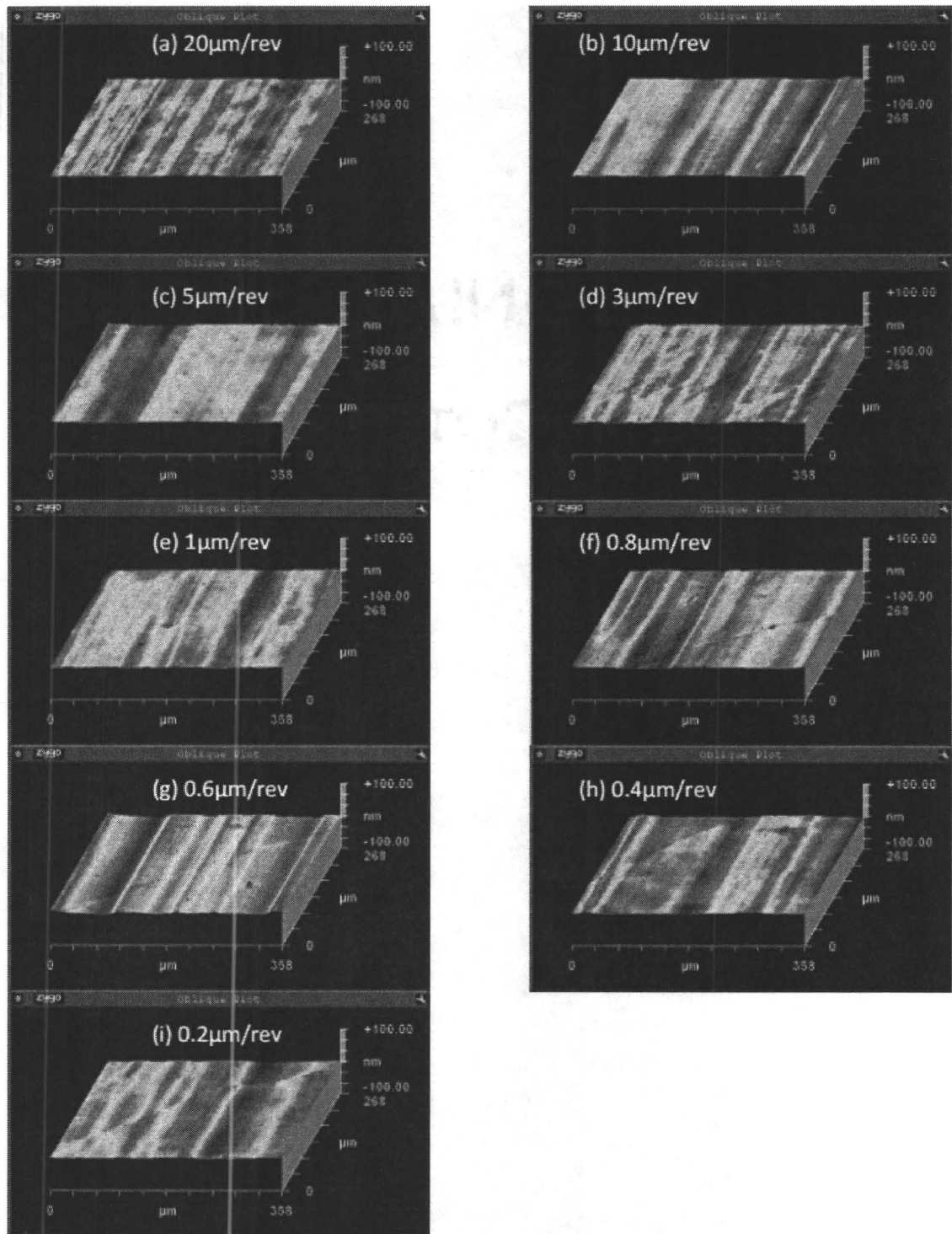


Figure C-8: 54% Cold rolled 99.87% aluminum (1000RPM, 2 μ m depth, 0.5mm flat end)

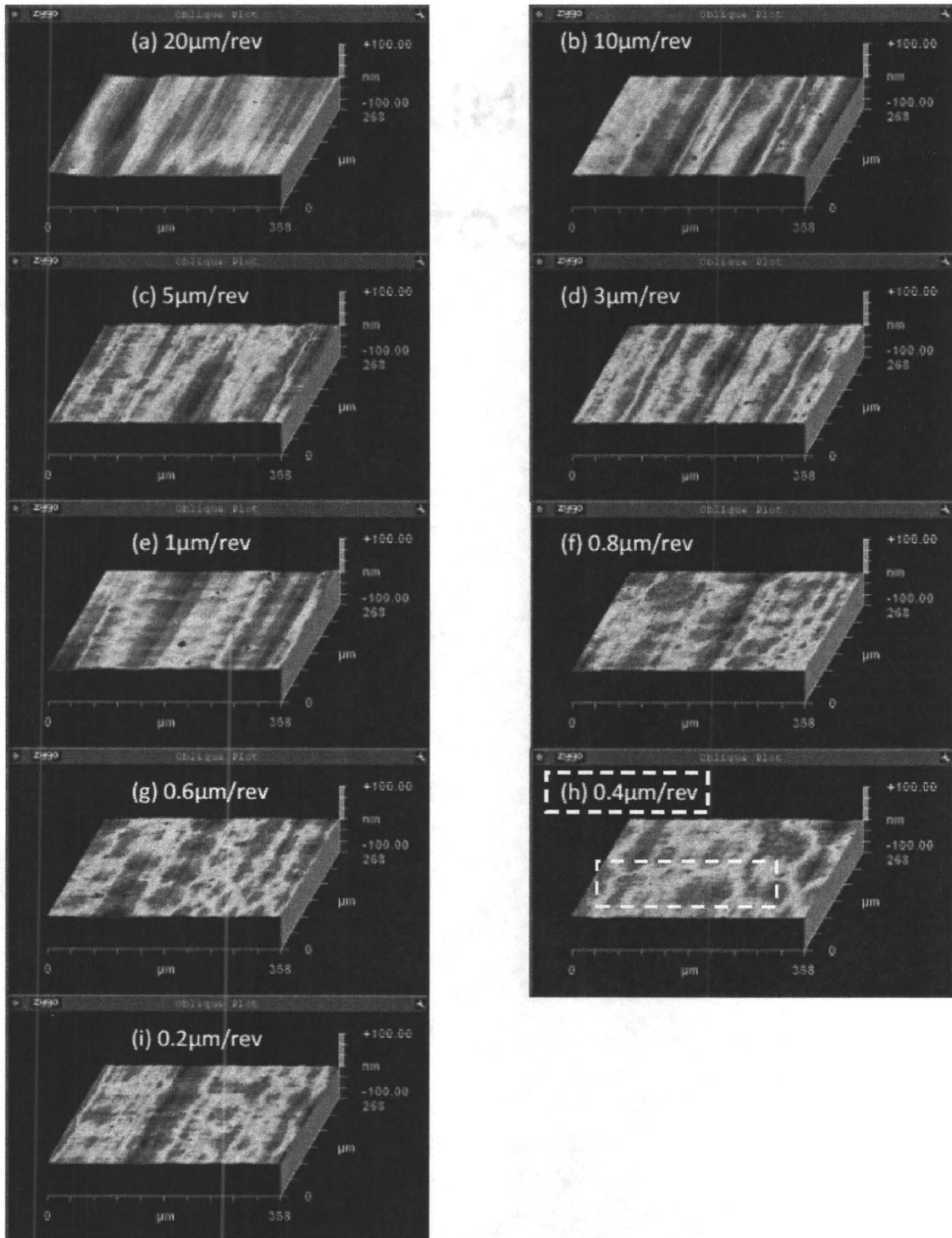


Figure C-9: FSP 99.87% aluminum (1000RPM, 2μm depth, 0.5mm flat end)

APPENDIX D WAVINESS AND FORCE DATA IN THE CUTTING DIRECTION

There is a clear observation of waviness in the cutting direction as can be seen from Appendix C. It is very important in this study to understand the reason for this waviness to further enhance the surface finish of SPDT. This waviness is severe when the furnace cooled soft 99.87% aluminum is used. Effort has been made here to summarize the force data and provide an explanation.

From a spatial frequency analysis based on the Zygo data the wavelength of the patterns in the cutting direction were observed to be 50 μ m, as shown in Figure D-1, when cutting the above mentioned material at 10 μ m/rev. This sample has been selected for this analysis as the waviness patterns are distinctly visible.

For this sample the cutting speed V was approximately:

$$V = r\omega = \frac{2\pi rN}{60} = \frac{2 \times \pi \times 40 \times 1000}{60} = 4188.8 \text{ mm/sec}$$

Where, V is cutting speed, r is the approximate radius of the workpiece where force and surface roughness is measured for this analysis, N is the revolution per min. In this test the workpiece used was the Furnace cooled 99.87% pure aluminum. The radius of cut was approximately 40mm, and the spindle speed was 1000 RPM. The specially

designed flat end tool was used and a 2 μm depth of cut was selected. Based on the periodicity of the surface and the cutting speed the frequency of oscillation was 83 KHz.

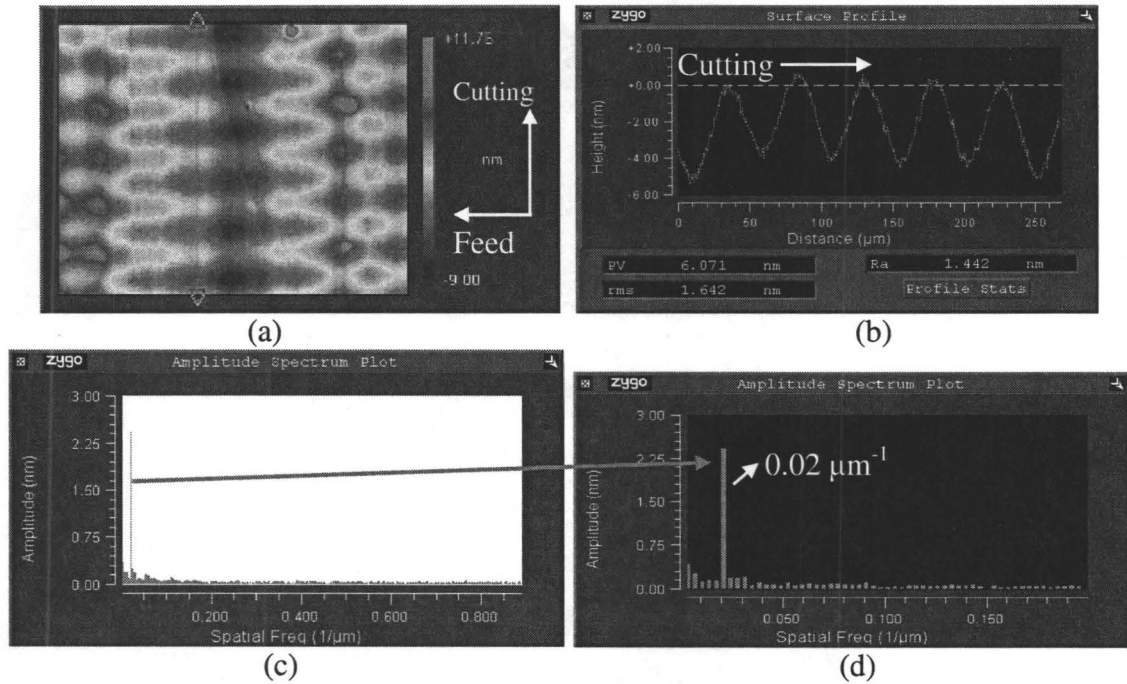


Figure D-1. Zygo images of machined furnace cooled 99.87% pure aluminum alloy at 1000 RPM, 2 μm depth of cut and 20 $\mu\text{m}/\text{rev}$.

Cutting force values observed in this study are in the sub-Newton range. A typical force plot corresponding to the surface shown in Figure D-1 is shown in Figure D-2. The force fluctuation was ± 0.6 N at a frequency of 3700 Hz.

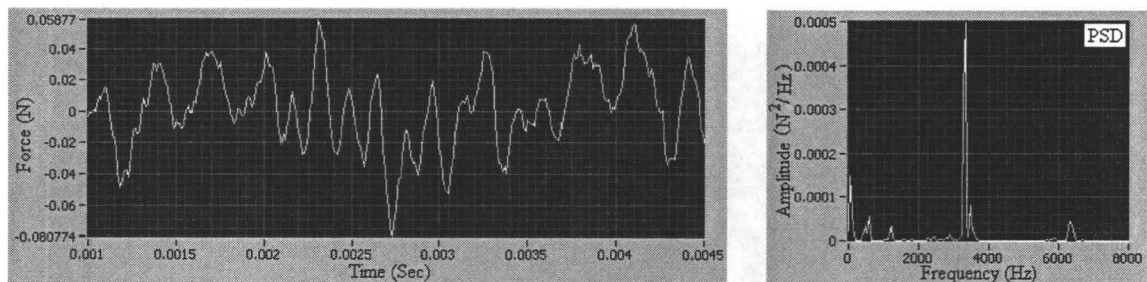


Figure D-2: Thrust force data and frequency analysis of FC 99.87% pure aluminum at 1000RPM, 2 μm depth of cut and 10 $\mu\text{m}/\text{rev}$ feed rate with flat end tool